



universität
wien

DISSERTATION

Titel der Dissertation

DEEPENING OUR UNDERSTANDING OF MEIOTIC PROPHASE I EVENTS IN *C. ELEGANS*
BY THE STUDY OF MUTANTS IN *PROM-1*, *SMC-3*, *RRF-3* AND LIVE IMAGING OF
CHROMOSOME END MOVEMENT

angestrebter akademischer Grad

Doktor/in der Naturwissenschaften (Dr. rer.nat.)

Verfasserin / Verfasser: Antoine Baudrimont
Matrikel-Nummer: 0447209
Dissertationsgebiet (lt. Dr.-Studium der Naturwissenschaften Genetik - Mikrobiologie
Studienblatt):
Betreuerin / Betreuer: Dr. Verena Jantsch
Wien, am 1. Oktober 2010

Table of Contents

Table of Contents

Abstract (English)	3
Kurzfassung (Deutsch)	5
Introduction	7
Meiosis	7
Definition.....	7
Prophase I, a crucial step of meiosis.....	8
The synaptonemal complex	10
Repair of programmed DSBs	11
Cohesins or how to glue the homologues in prophase I	13
Bouquet formation	16
<i>C. elegans</i> as model organism.....	18
Meiosis in <i>C. elegans</i>	20
<i>C. elegans</i> gonads or the recapitulation of the different stages of prophase I.	20
Key players in <i>C. elegans</i> prophase I.....	21
Chromosome axes	22
Central elements of the SC: SYP-1-4.....	23
Identified players of the recombination process in <i>C. elegans</i>	24
Pairing process: pairing centre proteins and SUN-1	25
Regulators of prophase I: CHK-2, PROM-1, HIM-19, CRA-1.....	28
Aims of the Studies.....	29
References	31
Results	41
Chapter 1. <i>Caenorhabditis elegans</i> PROM-1 is Required for Meiotic Prophase Progression and Homologous Chromosome Pairing	43
Chapter 2: Towards a Better Understanding of PROM-1 Function in <i>C. elegans</i>	55
Suppressor screen by EMS mutagenesis	57
Characterization of the suppressor line UV24	58
Extended TZ in the <i>prom-1(ok1140)</i> suppressor and restoration of bivalents	58

Table of Contents

<i>psu-1</i> in <i>prom-1(ok1140)</i> restores the loading of chromosome axis and central element SC components.....	59
In the <i>prom-1(ok1140)</i> suppressor homologues successfully pair and DSBs are timely repaired	60
Mapping of the suppressor mutation <i>psu-1(jf76)</i>	63
References	69
Chapter 3. A <i>Caenorhabditis elegans</i> RNA-Directed RNA Polymerase in Sperm Development and Endogenous RNA Interference	70
Chapter 4. Meiotic Chromosome Homology Search Involves Modifications of the Nuclear Envelope Protein Matefin/SUN-1	98
Chapter 5. Leptotene/Zygotene Chromosome Movement Via the SUN/KASH Protein Bridge in <i>C. elegans</i>	142
Chapter 6. A new Thermo-sensitive <i>smc-3(t2553)</i> Allele Reveals Involvement of Cohesion in Meiotic Repair in <i>C. elegans</i>	216
Methods.....	258
Suppressor screen	260
Mapping.....	261
Sample preparation for solid sequencing	265
Discussion and Outlook	266
Identification and characterization of <i>psu-1(jf76)</i>	268
Catching the PROM-1 suppressor mutation <i>psu-1(jf76)</i>	268
Function of <i>psu-1(jf76)</i> in meiosis.....	269
Gaining new insights into the process of chromosome pairing.	270
Assaying the number of chromosome ends inside SUN-1 foci and patches.....	270
Do paired homologues display different dynamics?	271
Exit from the clustered chromatin conformation.	271
Extending live-imaging to other players of prophase I.....	273
References	275
Acknowledgements.....	276
Curriculum Vitae.....	277

Abstract (English)

Meiosis is the specialized cell division that allows halving of the chromosome content and is required for the formation of haploid gametes. During prophase I homologous chromosomes have to pair, synapse via the synaptonemal complex (SC) and repair programmed double strand breaks (DSBs) by cross over recombination to link homologues. *C. elegans* gonads recapitulate the prophase I of meiosis in a temporal and spatial order.

The inner nuclear protein SUN-1 is one of the key players in the process of meiotic chromosome pairing. We used SUN-1 aggregates to monitor chromosome end movement *in vivo*. SUN-1 aggregates are highly dynamic. They come together, coalesce and disperse. Instead of single chromosome ends looking for their homologous partner, duplets/multiplsets and single chromosome ends are brought to meet. I analyzed the requirements for SUN-1 aggregate formation, wild type kinetics and documented the influence of proper orchestration of meiosis and repair of DSBs on aggregate behavior.

rrf-3 encodes an RNA-directed RNA polymerase involved in endogenous RNAi. Genetic analysis revealed that defective spermatogenesis accounts for the infertility observed in *rrf-3* mutant. I showed that pairing of homologues, meiotic chromosome axes morphogenesis and repair of double strand breaks were normal despite chromosome fragmentation and DNA bridge formation during spermatogenesis. Instead sperm nuclei are surrounded by wreath of tubulin. Deep sequencing analysis of small RNAs comparing wild type and *rrf-3* identified candidate targets regulated by RRF-3 (a collaboration with Jonathan Isaiah Gent).

Cohesin plays an important role by holding sister chromatids together both in meiosis and mitosis. I isolated, cloned and characterized a temperature sensitive allele of *smc-3*. I showed that repair of meiotic DSBs is impaired in this mutant whereas cohesion is normal. The primary defect of this mutant is partial loading of the cohesion complex leading to partial loading of

chromosome axis components and furthermore defective synapsis. This is the first analysis of an *smc-3* disruption in meiosis in *C. elegans*.

PROM-1 is involved in the orchestration of early prophase events. Its absence results in arrest right after meiotic entry. I isolated a suppressor of PROM-1 by EMS mutagenesis. The suppressor allele in the *prom-1* deletion mutant suppresses the meiotic arrest, entails the proper loading of SC proteins and successful pairing resulting in formation of bivalents. I mapped the suppressor mutation by single nucleotide polymorphism to the left arm of chromosome III.

The work presented here covers insight into various aspects of meiotic prophase I in *C. elegans* taking advantage of its amenability to forward genetics and its transparency for *in vivo* time-lapse cell imaging.

Kurzfassung (Deutsch)

Meiose ist eine spezialisierte Zellteilung, bei der der Chromosomengehalt halbiert wird. Sie ist für die Bildung von haploiden Gameten erforderlich. Während der Prophase der ersten Teilung müssen sich homologe Chromosomenpaare finden, weiters mittels des synaptonemalen Komplexes verbinden und programmierte Doppelstrangbrüche über „Cross-over“ Rekombination repariert werden, um Homologe zu verknüpfen. *C. elegans* Gonaden rekapitulieren die meiotische Prophase I in zeitlicher und räumlicher Anordnung.

Das innere Kernhüllenprotein SUN-1 ist einer der wichtigsten Akteure im Prozess der meiotischen Chromosomen-Paarung. Wir verwendeten SUN-1-Aggregate, um die Bewegung der Chromosomenenden *in vivo* zu studieren. SUN-1-Aggregate sind sehr dynamisch. Sie kommen zusammen, vereinigen und zerstreuen sich wieder. Anstatt einzelner Chromosomen-Enden, die ihre „Partner“ suchen, haben wir beobachtet, dass Dupletts/ Multipletts und einzelne Chromosomenenden zusammen gebracht werden. Ich analysierte die Anforderungen für die SUN-1 Aggregatbildung, Wildtyp Kinetik der Bewegung und dokumentierte den Einfluss der richtigen Orchestrierung der Meiose und Reparatur von Doppelstrangbrüchen auf das Verhalten der Aggregate.

rrf-3 kodiert für eine RNA-Polymerase, beteiligt in endogener RNA Interferenz (RNAi). Genetische Analysen zeigten, dass defekte Spermatogenese für die Unfruchtbarkeit in der *rrf-3* Mutante verantwortlich sein könnte. Ich zeigte, dass Paarung der homologen Chromosomen, meiotische Chromosomenachsenmorphogenese und Reparatur von DNA Doppelstrangbrüchen normal waren; nichtsdestotrotz wurden Chromosomenfragmentierung und DNA-

Brückenbildung beobachtet während der Spermatogenese. Stattdessen sind Kerne in Spermien von einem Kranz von Tubulin umgeben. „Deep Sequenzierung“ von kleinen RNAs identifizierte Kandidaten Zielgene (Wildtyp und *rrf-3* vergleichend), welche von RRF-3 reguliert sein könnten (eine Zusammenarbeit mit Jonathan Jesaja Gent).

Cohesin spielt eine wichtige Rolle im Zusammenhalt der Schwesterchromatiden in der Meiose und Mitose. Ich isolierte, klonierte und charakterisierte ein temperaturempfindliches Allel des *smc-3* Gens. Ich zeigte, dass die Reparatur der meiotischen Doppelstrangbrüche in dieser Mutante gestört ist, währenddessen Kohäsion normal ist. Der primäre Defekt dieser Mutante ist die partielle Ladung von Kohäsionmolekülen, dies führt zu partieller Ladung der Komponenten der Chromosomenachsen und weiters zu defekter Synapse. In meiner Arbeit wurde erstmals ein mutiertes *C. elegans smc-3* Allel beschrieben.

PROM-1 spielt bei der Orchestrierung von frühen meiotischen Prophase I Ereignissen eine Rolle. Das Fehlen von *prom-1* führt zu einem meiotischen Arrest gleich nach dem Eintreten in die Meiose. Ich habe einen Suppressor von *prom-1* isoliert mittels eines EMS Mutageneseccreens. Der Suppressor unterdrückt den meiotischen Arrest und führt zu normaler Ladung der Komponenten des synaptonemalen Komplexes. Wiederfunktionierende Paarung im Suppressor resultiert in Ausformung von Bivalenten. Ich habe den Suppressor auf den linken Arme von Chromosome III kartiert.

Die hier vorgestellte Arbeit umfasst Einblicke in verschiedene Aspekte der meiotischen Prophase I in *C. elegans* unter Ausnutzung besonderer Vorteile dieses Modellsystems: der Zugänglichkeit zu genetischer Analyse und Transparenz für *in vivo* Zeitraffer-Zell Aufnahmen.

Introduction

Meiosis

Definition

One difference between prokaryotic and eukaryotic organisms is how they reproduce. Prokaryotes simply divide whereas eukaryotic organisms rely on sexual reproduction. Sexual reproduction has the advantage that genetic information from the parents can be mixed at each generation and this process involves the specialized cell division of meiosis (Figure 1). Meiosis allows diploid organisms to produce haploid gametes or spores. These haploid gametes or spores will fuse upon fertilization and form a new zygote. In other words meiosis halves the chromosome content to compensate for the doubling of the DNA content at each generation.

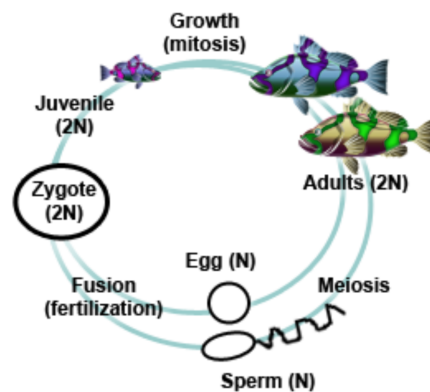


Figure 1. Life cycle of diploid organisms.

Diploid organisms ($2n$) produce haploid gametes or spores (n) that upon fusion form a new diploid cell (zygote). The zygote then divides and grows by mitosis.

Meiosis, or the halving of the ploidy of the cell, consists of two successive divisions after a single round of DNA replication during pre-meiotic S phase (Figure 2). During the first division, meiosis I, the homologous chromosomes pair and exchange genetic information by the means of

crossovers (Figure 2). Paired homologous chromosomes become then physically linked by the crossovers. We refer to this physical link as the formation of chiasmata. At anaphase I, segregation of homologous chromosomes in the two daughter cells halves the ploidy of the cell. The first division of meiosis is therefore called reductional. During the second division, meiosis II, the sister chromatids are segregated and allow the formation of four haploid gametes or spores. As there is no reduction of the ploidy of the cell during, meiosis II, this division is thus equational.

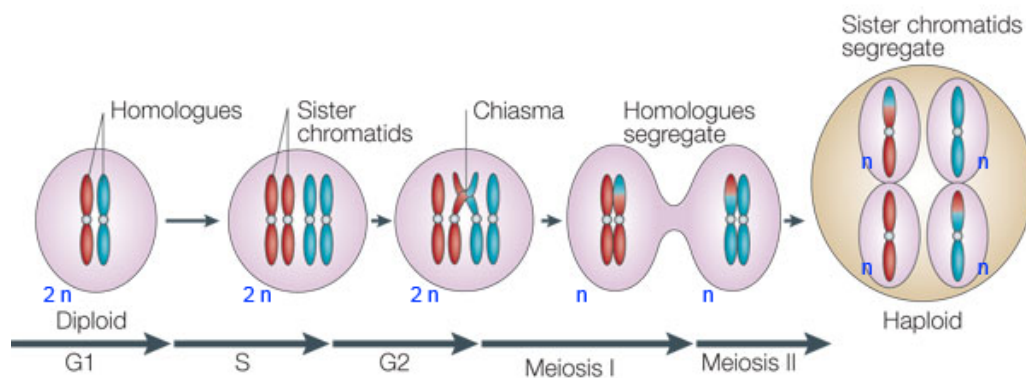


Figure 2. Meiosis consists of two successive rounds of division.

After replicating their DNA during S phase homologous chromosomes pair and chiasmata will be formed in the course of meiosis I (only one chiasma depicted). Meiosis I is reductional as the ploidy of the cell is halved whereas meiosis II is equational, as the ploidy of the cell remains unchanged. The ploidy of the cell is indicated in blue. Adapted from (Marston and Amon, 2004).

The key step of this process is the pairing of homologues. Defects in finding your partner result in random segregation of chromosomes and leads to aneuploidy or polyploidy. Pairing of homologous chromosomes is therefore essential and takes place during the prophase I.

Prophase I, a crucial step of meiosis.

Prophase of meiosis I is subdivided into 5 stages: leptotene, zygotene, pachytene, diplotene and diakinesis (Figure 3). First chromatin starts to condense during leptotene. The search process for the homologous

chromosomes starts at this stage. This search process coincides with the formation of the widely conserved bouquet, which gathers chromosome ends in a restricted area (Scherthan, 2007). In zygotene, the elongation of the tripartite synaptonemal complex (SC) starts between homologous chromosomes, which are successfully paired. Synapsis is the stabilization of the pairing by the polymerization of the central element of the SC between the paired homologues. In all organisms, except *C. elegans* and males *D. melanogaster*, synapsis has been shown to depend on the programmed formation of DSBs (Joyce and McKim, 2007). In pachytene the SC is fully extended and crossovers occur. In the following stage, diplotene, the SC start to depolymerise and chiasmata become visible. In the last stage, diakinesis, chromosomes are fully condensed and linked to their partners via a crossover. We refer to them as bivalents.

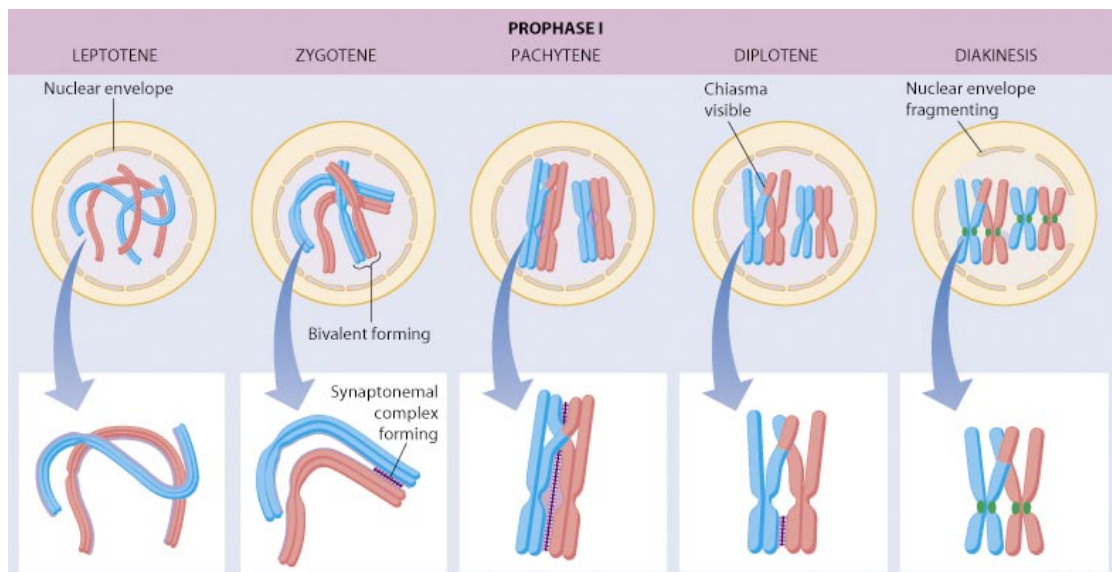


Figure 3. Prophase I is subdivided into 5 stages.

In leptotene duplicated chromosomes start to condense. Synapsis, or stabilization of the pairing by elongation of the synaptonemal complex, is initiated at the zygotene stage and will be complete in pachytene. In pachytene crossovers are occurring. The synaptonemal complex starts to disappear in diplotene and chiasmata become visible. At diakinesis bivalents are linked by one crossover and ready for metaphase. Homologues chromosomes are depicted in blue and red. Copyright © 2005 Pearson Education, Inc. publishing as Benjamin Cummings

The synaptonemal complex

One, if not the most, prominent structure of prophase I is the synaptonemal complex (SC). It was defined as a tripartite structure made of lateral elements bridged by the central element (Figure 4) and it is fully elongated at the pachytene stage (Page and Hawley, 2003). The function of the SC is still under intense investigation despite a clear involvement in stabilization of pairing of the homologues. It was shown to be necessary for the formation of crossovers in all organisms and its polymerization is timely regulated with the progression of DSBs repair in organism in which synapsis depends on DSBs formation (Zickler and Kleckner, 1999). It was proposed to be involved in the process of recombination interference (Pawlowski and Cande, 2005; Hayashi et al., 2010). Recombination interference corresponds to the observations that after a CO is made no other COs are made in the surrounding region. Indeed in *S. pombe*, which lacks a SC, recombination interference is absent and the formation of DSBs is unrestrained (Loidl, 2006).

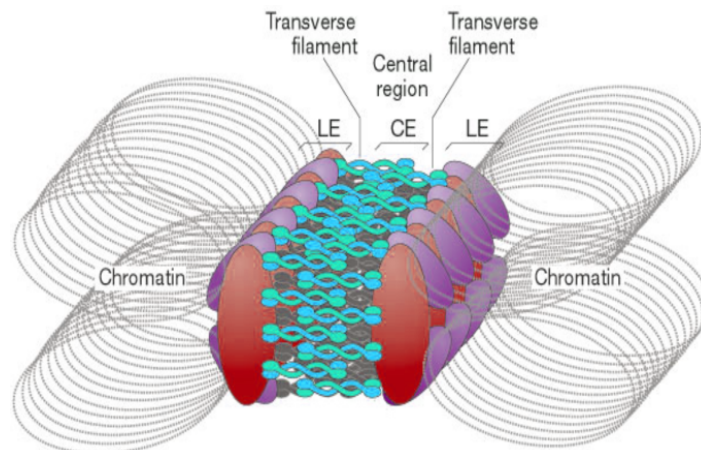


Figure 4. The synaptonemal complex.

The SC is made of lateral elements (red and violet) with adjacent chromatin loops. The lateral elements of the SC are zipped up by the central element (light and bright blue). Adapted from (Castro and Lorca, 2005).

As mentioned earlier, elongation of the SC is dependent on the formation of DSBs by the endonuclease SPO-11 (Pawlowski and Cande, 2005) and DSBs can only be repaired via the homologue if the SC is present.

This point minors the putative function in recombination interference and suggest that the SC could provide the platform for factors necessary for the repair of DSBs using the homologue as a template.

Recent work has provided evidence that the SC is dynamic in its composition instead of being static. Indeed in maize the lateral element are twisted in a left handed helix and the number of twists increasing with progression of prophase I suggests that the central element of the SC would be able to depolymerise allowing thus more torsion to be given on the twist (Wang et al., 2009). In addition in *C. elegans* after photobleaching of the tagged version of the central element SYP-3 of the SC, SYP-3::GFP reappears suggesting that polymerization of the central element of the SC is dynamic (personal communication Anne Villeneuve).

[Repair of programmed DSBs](#)

Proteins involved in DSB repair are quite conserved among eukaryotes (San Filippo et al., 2008). Right after cells enter meiosis DSBs are introduced by the meiosis specific endonuclease SPO-11 (Figure 5). SPO-11 is covalently linked to the 5' end of the cut DNA (Keeney et al., 1997) and will be removed by the MRN complex (MRE-11, RAD-50, NBS-1/Xrs-2)(van den Bosch et al., 2003). In fact the MRN complex in addition to its role in the 5' to 3' end resection process, is also necessary for the formation of DSBs in yeast (Ogawa et al., 1995). This resection will lead to the formation of 3' overhangs. After resection, RAD-51 and DMC-1 will be loaded on the non-resected DNA strand and the homology search will start with the strand invasion. This strand invasion involves RAD-51. The strand invasion will lead to the formation of the D-loop and is followed by new DNA synthesis. Recapture of the extended strand generates a joint molecule containing a double Holliday junction (DHJ). The mode of resolution of DHJs decides whether a DSB results in a crossover or a non-crossover product (Pâques and Haber, 1999). Proteins involve in the resolution process of DHJ are MutS-MutL protein (Figure 5). There is increasing evidence that in fact the fate of a crossover is decided before the

resolution of the DHJ (Bishop and Zickler, 2004). Additionally rapid telomere movements (RPM) are observed in budding yeast during prophase I and it was suggested that these RPMs play a role in specifying the mode of DSBs repair and in resolving entanglements (Conrad et al., 2008; Koszul et al., 2008). Indeed the back and forth movement of chromosome ends could avoid illegitimate interaction between the chromosomes in budding yeast and might represent another layer of quality control for the cell.

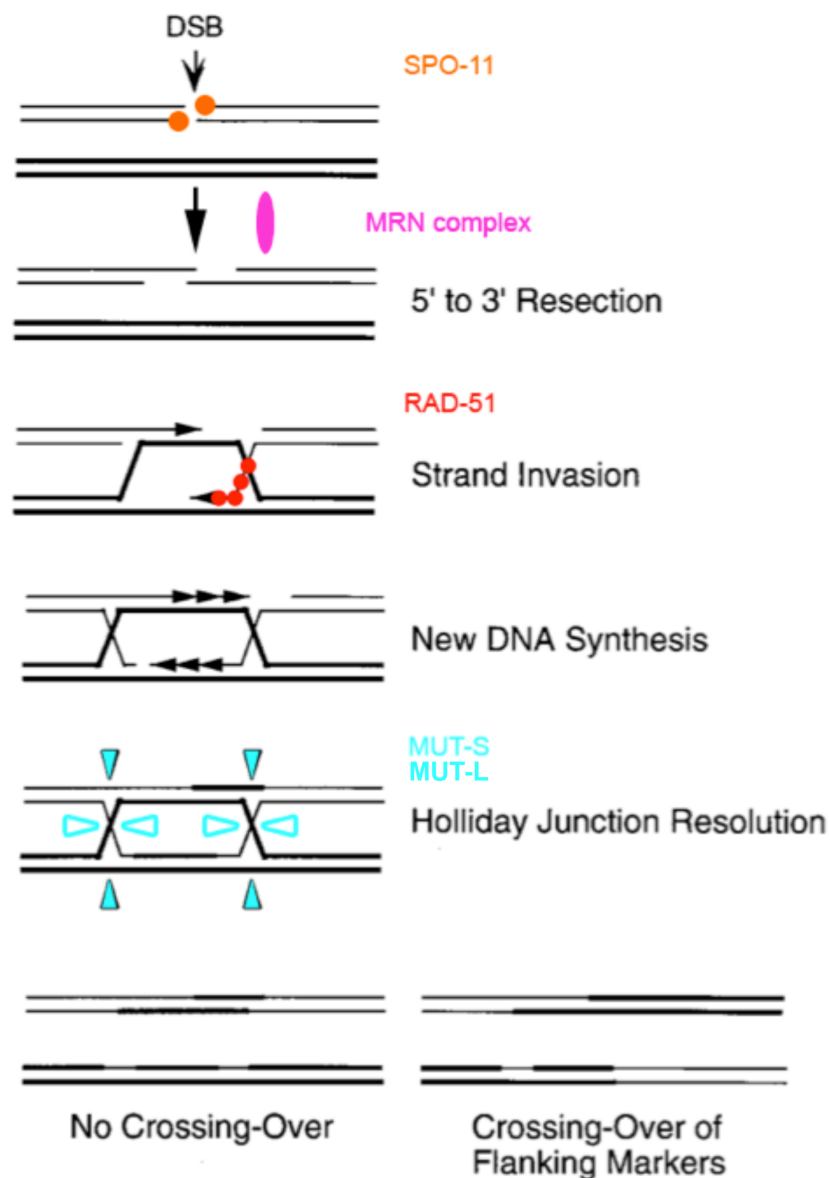


Figure 5. Overview of the repair of DSBs during prophase I.

Briefly, DSBs are made by SPO-11 (orange). SPO-11 is removed by the MRN complex (5' to 3' resection, pink). Strand invasion is mediated by RAD-51 (red) and leads to the formation of the D-loop. After new DNA synthesis the strand recapture leads to the formation of the double

Holliday junction (DHJ). At the end the MutS-MutL complex (light blue) resolve the DHJ. The position of the introduced cuts decides whether the repair product is a crossover product or a non-cross-over product. (Pâques and Haber, 1999).

Therefore formation of crossover during meiosis links the homologous chromosomes together. Furthermore sister chromatids have to be held together to allow segregation of homologous chromosome and the proteins involved in this process are cohesins.

Cohesins or how to glue the homologues in prophase I

Cohesins are made of two Structural Maintenance Components, SMC-1 and SMC-3 that are closed by two non-SMC proteins (kleisins and SCC-3) (Figure 6). Kleisins differ in mitosis and meiosis, with Scc1 being used in mitosis and Rec8 in meiosis whereas Scc-3 stabilizes the complex in both stages (mitosis, meiosis). Cohesins form a ring that traps DNA (Haering et al., 2002). How DNA is trapped is still a question of debate and multiple models have been proposed (Onn et al., 2008). In addition to provide cohesion, cohesins are involved in many cellular processes such as recombination and gene expression in eukaryotes (Wood et al., 2010).

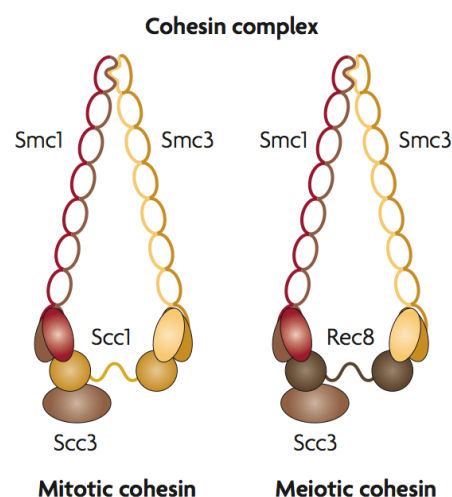


Figure 6. The mitotic and meiotic cohesin complexes.

Cohesin are composed of Smc1 –Smc-3 dimmers, which are close by the kleisin (Scc1 during mitosis, Rec8 during meiosis). The complex is finally stabilized by Scc-3 in both cases. (Wood et al., 2010).

During mitosis, cohesins hold chromosomes together and permit the bipolar orientation of the spindle kinetochores. Cohesins are then removed during the transition from metaphase to anaphase from all the chromosomes (Figure 7A). This removal involves the separase, activated by the Anaphase Promoting Complex (APC) and will lead to the cleavage of the mitotic kleisin Scc1 (Marston and Amon, 2004). This allows sister chromatids to be segregated to the daughter cell.

The main difference between mitosis and meiosis is that during meiosis removal of cohesin loaded on chromosome is sequential (Figure 7B). Indeed the protein Sugoshin protects cohesins at the centromere from cleavage of the meiotic kleisin Rec8 by the separase during meiosis I (Kitajima et al., 2004). Additionally, the monopolin complex supports the establishment of co-orientated kinetochores of paired chromosomes linked by COs (Monje-Casas et al., 2007). This non-removal of centromeric cohesins with the help of the monopolin complex allows bi-orientation of the chromosome and promotes segregation of homologous chromosomes instead of sister chromatids as in mitosis (Marston and Amon, 2004). In meiosis II this protection of centromeric cohesins by Sugoshin is lost, making thus the kleisin Rec8 available for cleavage by the separase. This loss of cohesins on the full length of the chromosomes leads to segregation of sister chromatids in meiosis II.

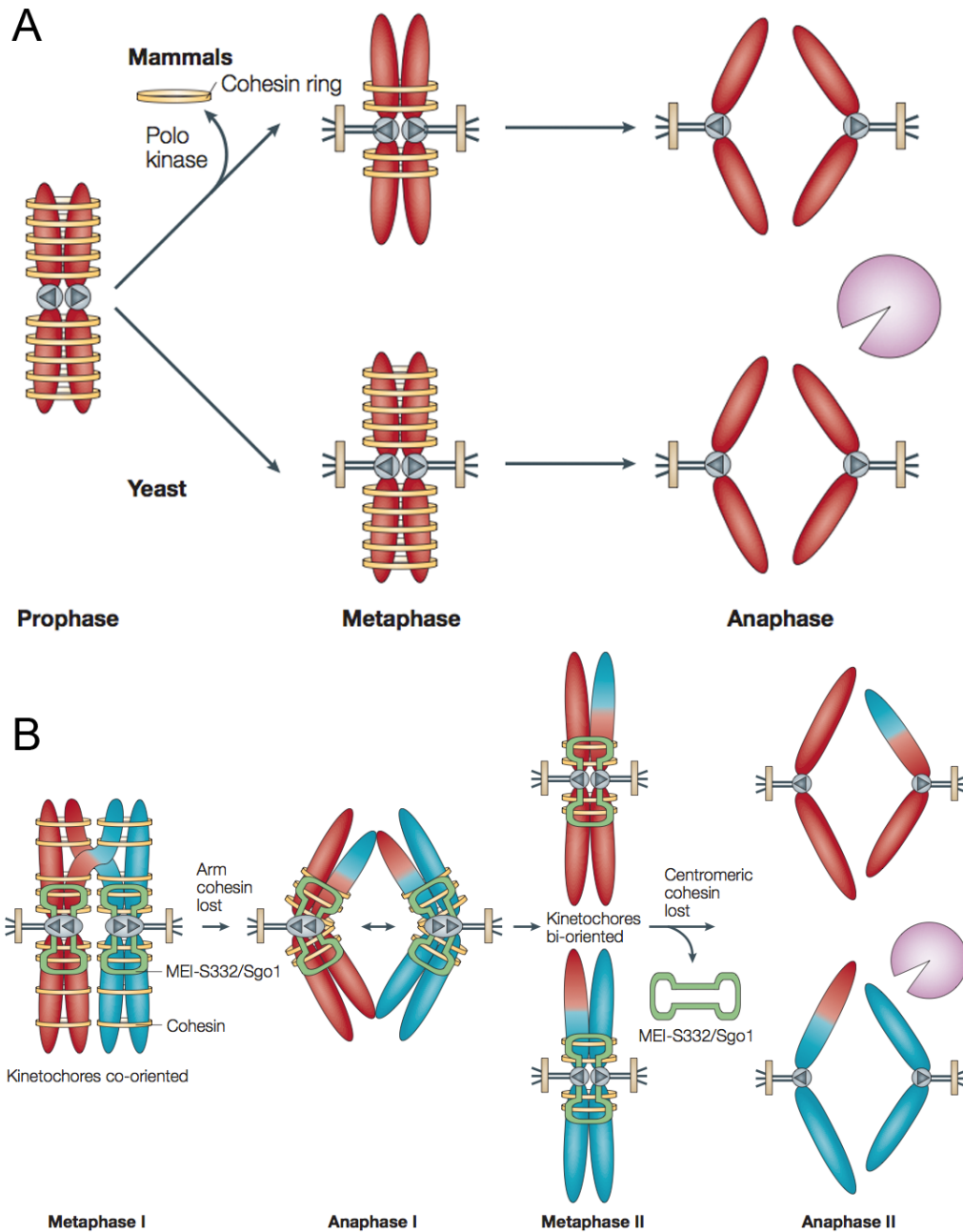


Figure 7. Difference in cohesin removal in mitosis and meiosis.

A. At the transition from prophase to metaphase the cohesin rings will be kept between the sister chromatids (it is removed non centromeric regions in mammals). At the transition of metaphase to anaphase, separase will cleave the cohesin ring. This loss of the cohesin ring will allow separation of the sister chromatids. B. During meiosis cohesins rings are also loaded on sister chromatids of paired chromosomes linked by one crossover. Sugoshin protects centromeric cohesins from cleavage by the separase allowing homologues to be segregated in anaphase I. In meiosis II, Sugoshin protection is lost allowing the separase to cleave centromeric cohesins. It leads to the separation of the sister chromatids in anaphase II. Adapted from (Marston and Amon, 2004).

Bouquet formation

The meiotic bouquet designates the clustering of chromosome ends in a defined region of the nucleus (Figure 8A). It was first described in *Batrachoseps* (Eisen, 1900) and found in most of the model organism studied so far (Scherthan, 2001). Tethering of the chromosome ends to the nuclear membrane has been shown to involve SUN domain proteins (Alsheimer, 2009). The abbreviation SUN domain stands for Sad1p, UNC-84 domains. SUN domains are greatly conserved amongst phyla and proteins bearing this domain are anchored in the inner nuclear membrane (INM). SUN proteins are involved in many processes (Fridkin et al., 2008). In fission yeast the Sad1 protein connects chromosome ends to cytoplasmic forces in meiosis (Figure 8B) via Kms1 protein. The protein complex Bqt1-Bqt2-Rap1-Taz1 links telomeres to Sad1. Kms1p interacts with Sad1 through its KASH domain. The connection made by Sad1p and Kms1p is referred as the SUN/KASH bridge (Fridkin et al., 2008).

In budding yeast, chromosome end movement driven by the SUN domain protein Mps3p is involved in the formation of rapid telomere movement (RPM). These RPMs are thought to contribute to the recombination process by destabilizing illegitimate interactions between chromosomes. Movement of the chromatin during prophase I has also been reported in maize where two kinds of rotational movements are observed. A slow paced rotational movement is observed throughout the stages of zygonema to pachynema with a quiescence phase in between, whereas rapid and short-range chromosome end movements are restricted to the zygonema stage. These rapid and short-range chromosome end movement are thought to help the pairing process of homologues (Sheehan and Pawlowski, 2009).

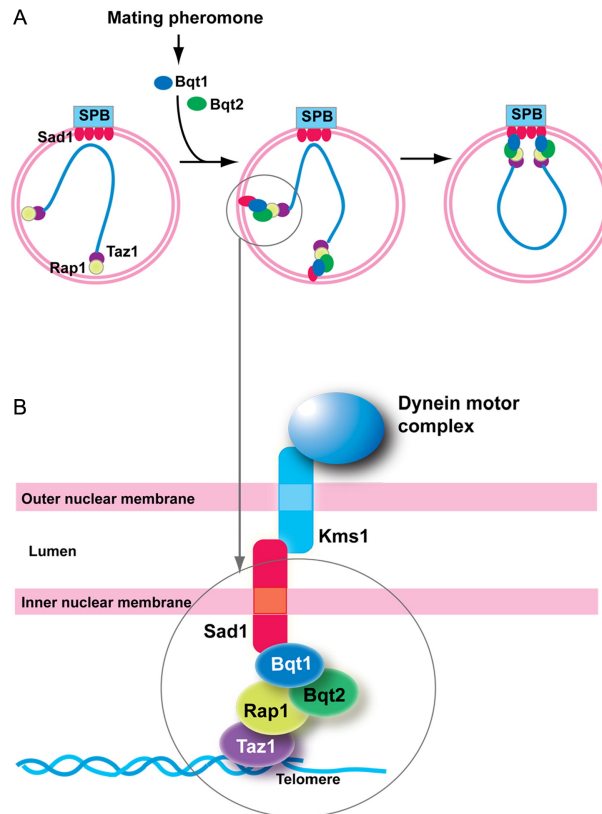


Figure 8. Bouquet formation in *S. pombe*.

A. Following the trigger of pheromones, Bqt1 and Bqt2 will allow the migration of chromosome ends to the spindle pole body (SPB). B. Close up of the molecular components involved in the process of migration of chromosome ends to the SPB. (Chikashige et al., 2006).

In summary the prophase I of meiosis can be subdivided into 5 different stages during which chromosome structure is tremendously changed to coordinate the different events. First chromosomes have to pair with their homologues, likely with the assistance of the meiotic bouquet. Second the elongation of the central elements of the SC over the full length of the chromosomes will stabilize pairing (leptotene/zygotene). Programmed DSBs are introduced in leptotene and their repair will last until mid pachytene. Paired homologues are then physically linked by the chiasmata. At the end of meiosis I homologous chromosomes are segregated thanks to the sequential removal of the cohesin from the chromosome arms and chiasmata linking homologues.

C. elegans as model organism.

C. elegans is a small roundworm (1mm long) and belongs to the Nematoda phylum. It has a short life cycle (2.5 days at 22°C, Figure 8). The RNAi pathway was first characterized in this organism (Fire et al., 1998) and since 1998 the *C. elegans* genome has been sequenced (Consortium, 1998), making it thus possible to inactivate any gene of interest by RNAi. *C. elegans* worms are hermaphrodites and produce males in 0.02% of the progeny. The presence of males in the progeny permits forward genetics using *C. elegans*. *C. elegans* hermaphrodites are highly fertile and can lay 300 eggs and up to 1000 eggs when inseminated with males. In addition worms can be frozen at the larval stage L1 making it possible to keep stocks of worms.

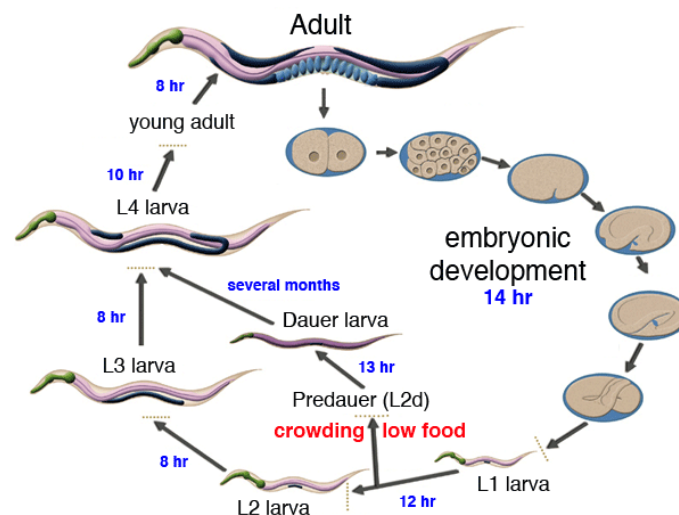


Figure 9. The *C. elegans* life cycle at 22°C.

Eggs develop and form the L1 larva (14 hours). After 12 hours L1 larva molts into L2 larva. It is between these two larval stages that *C. elegans* can enter the dauer stage. Worms enter the dauer stage upon starvation or overpopulation. In the dauer stage worms can survive up to several months. The next larval stage is the L3 stage and it lasts for 8 hours. At this stage gonads start to develop. After 8 hours worms reach the L4 stage. Gonads are formed. After this larval stage, worms molt to the adult stage and produce eggs. (Altun, 2009)

During the growth of worms through the larval stages L1 to L4, meiotic precursor cells Z2 and Z3 multiply (Figure 9). From the L1 to the L2 stage

mitotic germ cell and somatic gonad cells are produced. Gonad arms are formed between the L3 and L4 stages and lead to the generation of the rachis. Meiosis starts at the mid L4 stage and culminated in the production of spermatids at the late L4 stage. Looking at L4 worms allows thus the study of spermatogenesis. During the transition from L4 to young adult, a switch from spermatogenesis to oogenesis takes place. The first egg produced, pushes the spermatids into the spermatheca. This entails the maturation of spermatids into spermatozoa. Releasing gonads of adult worms permits the study of oogenesis.

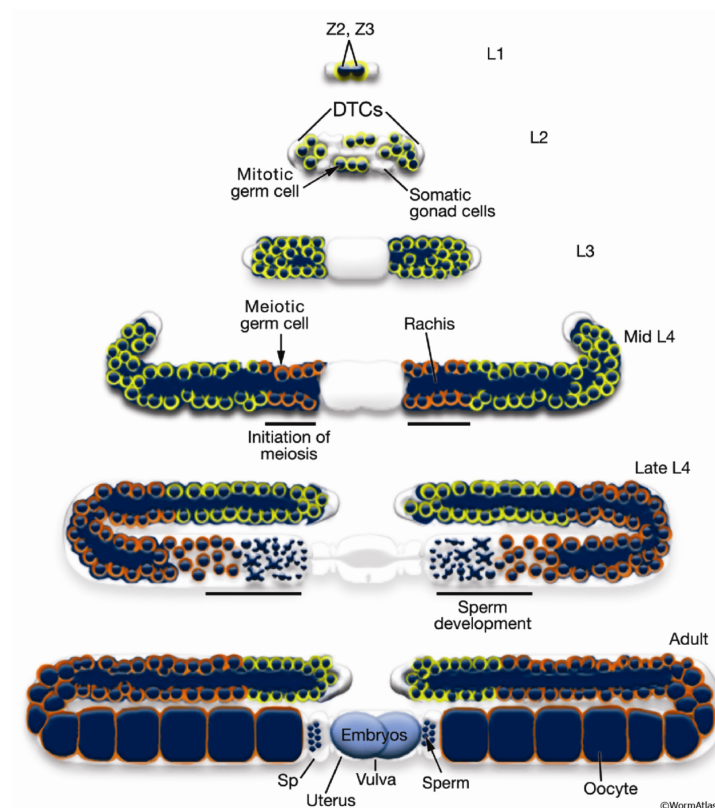


Figure 10. Gonadogenesis in the larval stages of *C. elegans*.

In L1 larvae, the meiotic precursor cells Z2 and Z3 divide and this leads to the formation of mitotic and somatic gonad cells (L2 stage). Division continues until the larval stage L3. Upon entry into the larval stage L4 gonad cells start to undergo meiosis and formation of spermatids. At the late L4 stage gonad switches from spermatogenesis to oogenesis. In the young adult the first egg induces maturation of the spermatids into spermatozoa; which fertilize the oocytes when passing by. (Altun, 2009)

In addition to offer the possibility to study both meiotic process (spermatogenesis and oogenesis) *C. elegans* gonads recapitulate the different stages of prophase I. *C. elegans* is therefore a powerful tool to study the process of homologous chromosome pairing.

Meiosis in *C. elegans*

***C. elegans* gonads or the recapitulation of the different stages of prophase I.**

A released gonad of *C. elegans* recapitulates the different stages of prophase I in a temporal and spatial manner (Figure 11).

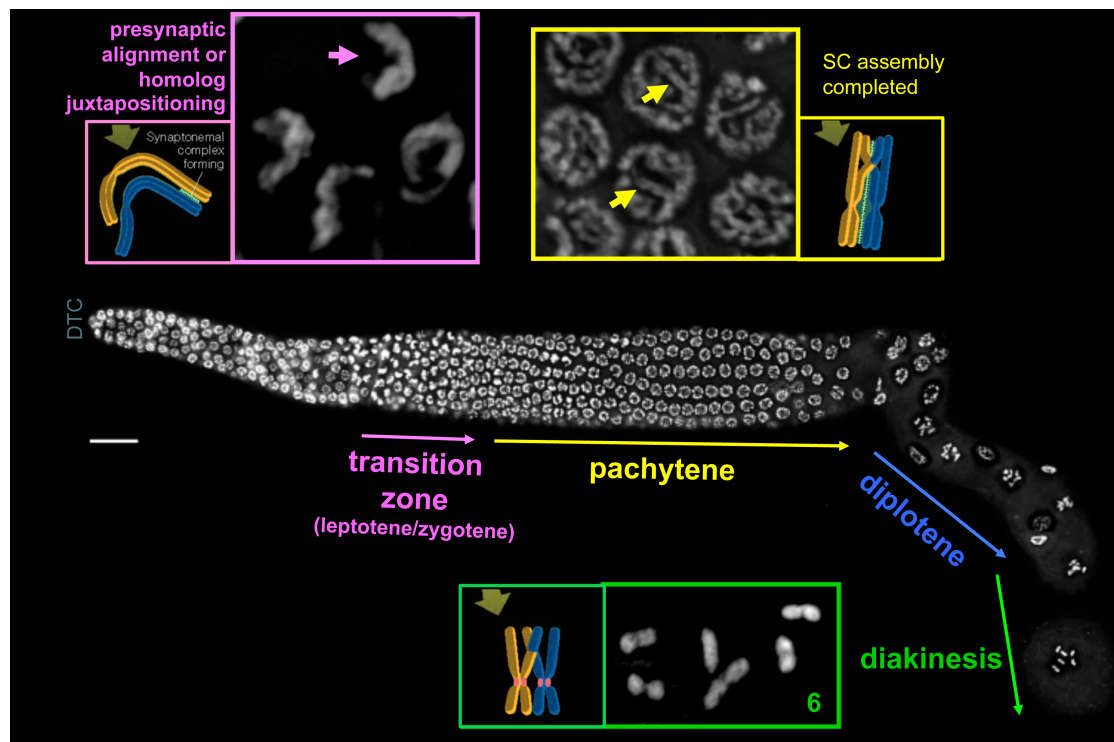


Figure 11. Different stages of prophase I in *C. elegans*.

The gonad is temporally ordered from the distal tip to the proximal end. First we find the mitotic zone (MZ) where DNA is replicated in response to signals emanating from the distal tip cell (DTC). It is followed by the transition zone, which corresponds to the leptotene/zygotene (pink text and boxes). Later on in pachytene, synapsis is achieved and we can recognize parallel tracks of DNA (yellow text and boxes). Then follows diplotene with the depolymerisation of the SC (blue text). Finally, diakinesis with 6 bivalents formed which are

linked by one crossover (green text and boxes). Released gonads stained with DAPI. DTC: Distal Tip Cells. Adapted from Copyright © 2005 Pearson Education, Inc. publishing as Benjamin Cummings

The search process starts in the transition zone (TZ). It is at this stage that first contacts between homologues are initiated (Colaiácovo, 2006). During this stage, leptotene/zygotene, chromatin adopts a polarized conformation that can be described as a crescent shape (Figure 11, pink text and box). Programmed DSBs are made by the endonuclease SPO-11 at this stage (Dernburg et al., 1998). Later on in pachytene, synapsis is achieved and we can recognize parallel tracks of DNA (yellow text and box). Crossovers are taking place at this time. Whereas in most organisms synapsis depends on formation of DSBs, synapsis is independent of formation of DSBs in *C. elegans* (Dernburg et al., 1998), similar as in male meiosis of *D. melanogaster* (Joyce and McKim, 2007). This idea of independence between synapsis and DSBs formation is being challenged by the isolation of a new mutant (Smolikov et al., 2008). In diplotene the SC starts to depolymerise and chromosomes condense. At diakinesis the 6 bivalents are linked by one crossover (Figure 11, green text and box).

Key players in *C. elegans* prophase I

In *C. elegans* many proteins involved in prophase I have been isolated and functionally characterized (Figure 12). Next, I will go thoroughly through most of the players known so far and summarize their function in meiosis I in *C. elegans*- with an special emphasis on those important for the studies I undertook during my PhD.

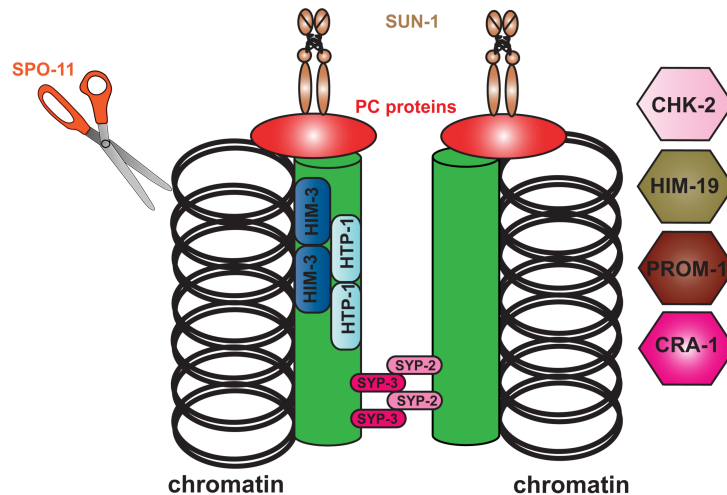


Figure 12. Prophase I players in *C. elegans* (essential to my studies).

Cartoon depicting the different proteins involved in the formation of the SC (HIM-3, HTP-1, SYP-2-3), proteins involved in pairing (SUN-1, PC proteins), meiotic regulators (CHK-2, HIM-19, PROM-1, CRA-1) and the endonuclease SPO-11.

Chromosome axes

I grouped under the term chromosome axes the meiotic cohesin components (SMC-3, SMC-1, REC-8) and lateral elements of the SC (HTP-3, HTP-1-2, HIM-3). We will next focus on the different components of the chromosome axes.

REC-8 is the meiosis specific kleisin, which locks SMC-1 and SMC-3. It was identified through a database screen and was confirmed by RNAi (Pasierbek et al., 2001). The screen also isolated 3 other potential candidates, which were termed COH-1-3 (COhesin protein Homolog). REC-8 is loaded on chromosome axis upon entry into meiosis and delineates chromosome axis. Depletion of REC-8 by RNAi leads to the formation of univalents and some DNA fragmentation at diakinesis suggesting a role for the cohesins in the repair process (Pasierbek et al., 2001). It has been shown that loading of cohesins relies on the protein HTP-3 (Him-Three Paralog) during meiosis (Severson et al., 2009). RNAi mediated depletion of SCC-3 showed that SCC-3 is required for synapsis and segregation of chromosomes both in meiosis and mitosis (Pasierbek et al., 2003). Until now the study of SMC-3 function

was limited to its immunodetection in meiosis as its inactivation by RNAi leads to embryonic lethality with full penetrance (Mito et al., 2003). Lateral elements of the SC rely on loading of the cohesins; without cohesins lateral elements are not loaded (Colaiácovo, 2006).

HTP-3 appears to be the first brick for the construction of the chromosome axis. Indeed its depletion result in defects of cohesin loading and lateral elements of the SC are missing (Severson et al., 2009). As REC-8, HTP-3 delineates chromosome axis and is detected at the beginning of the TZ. HTP-3 was additionally shown to link DSBs formation with homologues pairing and synapsis (Goodyer et al., 2008). Two homologues of HTP-3 are found in *C. elegans*: HTP-1 and 2. HTP-1 and 2 are part of the lateral element of the SC and co-localize with other components of chromosome axis (Couteau and Zetka, 2005; Martinez-Perez and Villeneuve, 2005). HTP-1 in addition to its structural role inhibits synapsis between non-homologous chromosomes. Another component of the lateral element is HIM-3. Like HTP-1, 2 and 3 HIM-3 encodes a Horma-domain bearing HOP-1-like protein and co-localize with other axial elements (Couteau et al., 2004; Zetka et al., 1999). Additionally HIM-3 is involved in the inhibition of the repair of DSBs via the sister chromatids. Indeed foci of the strand invasion protein RAD-51 do not accumulate in *him-3(gk149)* worms as in other pairing mutants (Couteau et al., 2004) suggesting that HIM-3 exerts a barrier to DNA repair via the sister chromatid. HIM-3 is also required for formation of chromosomal attachment plaques of chromosome ends at the nuclear envelope (Penkner et al., 2009; Baudrimont et al., in press).

Central elements of the SC: SYP-1-4

Central elements of the SC zip up the lateral elements of the SC. HTP-1 and chromosome movement mediated by the SUN/KASH bridge restrict synapsis exclusively between paired homologues (Couteau and Zetka, 2005; Martinez-Perez and Villeneuve, 2005; Penkner et al., 2007; Penkner et al., 2009; Sato et al., 2009). Deletion alleles of SYP-1-4 show an extended zone

where chromatin is clustered to one pole of the nucleus (Colaiácovo, 2006). This extension of the TZ is characteristic of synapsis mutants. These proteins can be detected between the chromosome axis by immunostaining and delineate the zone of synapsis. Analysis of *syp-3(me42)* revealed an additional role of SYP-3 in specifying the mode of repair used (Smolikov et al., 2007). Indeed whereas repair of DSBs visualized with the strand invasion RAD-51 is delayed in *syp-2(ok307)*, in *syp-3(me42)* most of the RAD-51 foci disappear. This suggests that in *syp-3(me42)* background DSBs are not repaired with the conventional mode (repair via the homologue). Recently a yeast two-hybrid screen using SYP-3 as bait identified SYP-4 and SYP-4 appears involved in the maturation process of the SC (Smolikov et al., 2009).

[Identified players of the recombination process in *C. elegans*.](#)

DSBs are introduced by the endonuclease SPO-11 in *C. elegans* (Dernburg et al., 1998). Studies using the *spo-11* deletion allele *ok79* revealed that synapsis and pairing are independent of DSB formation. At diakinesis, instead of 6 bivalents linked by one crossover, 12 univalents are found. As in yeast, formation of DSBs requires the MRN complex (MRE-11, RAD-50, NBS-1/XRS-2) in *C. elegans*. Deletion of MRE-11 or RAD-50 results in the formation of 12 univalents at diakinesis whereas synapsis and pairing are achieved (Chin and Villeneuve, 2001; Hayashi et al., 2007). Analysis of *rad-50(ok197)* revealed that two modes of DSBs formation exist in *C. elegans* and that the MRN complex sustains a constraint for the mode of repair using the sister chromatid as a template. It is lost when chromosome axis formation is impeded (Hayashi et al., 2007).

Mutational analysis of the strand invasion protein RAD-51 revealed that instead of 6 fully condensed bivalents, undefined chromatin masses are found at the diakinesis (Alpi et al., 2003; Rinaldo et al., 2002). Antibodies raised against RAD-51 allow the visualization of the repair process and are a widely used tool to monitor repair of DSBs. Other components of the repair pathway have been isolated in *C. elegans*. MSH-5 functions as crossover promoting

heteroduplex (Kelly et al., 2000) and is involved in promoting the strand invasion step together with HIM-14, the MSH-4 paralogue (Colaiácovo et al., 2003). At diakinesis 12 univalents are formed in these backgrounds. It is worth mentioning that MSH-5 was found to play a role in the exit of the clustered conformation of the chromatin characteristic of the TZ (Carlton et al., 2006). HEL-308, and rfs-1 play a redundant role in the removal of the strand invasion protein RAD-51 (Ward et al., 2010). ZHP-3 plays a crucial role in bivalent restructuring in response to crossover formation in addition to an active role in crossover formation itself. At diakinesis ZHP-3 marks the chromosome arms where the crossover occurred (Bhalla et al., 2008; Jantsch et al., 2004).

Synapsis and pairing are independent of formation of DSBs in *C. elegans* and two major players in the pairing process are the pairing centre (PC) proteins and SUN-1.

[Pairing process: pairing centre proteins and SUN-1](#)

In *C. elegans*, heterochromatic repeats located at the end of each chromosome define the homolog recognition regions (HRRs). These HRRs, also called pairing centre (PC) regions, were shown to be required for initiation of synapsis and crossover recombination (MacQueen et al., 2005; McKim et al., 1988; Rosenbluth and Baillie, 1981). Pairing centre (PC) proteins (ZIM-1-3, HIM-8) have a Zn-finger domain, which enables them to bind specifically to HRRs and recognize one or two chromosome ends (Figure 13) (Phillips et al., 2009; Phillips and Dernburg, 2006; Phillips et al., 2005).

When any of these PC proteins is removed, synapsis is abolished for the corresponding chromosomes (Phillips and Dernburg, 2006). Therefore it has been proposed that PC proteins are necessary for stabilization of the pairing process by synapsis. Additionally PC proteins co-localize with SUN-1 and ZYG-12 to the periphery of the nucleus and could be co-IP with SUN-1 (Penkner et al., 2009; Phillips et al., 2009).

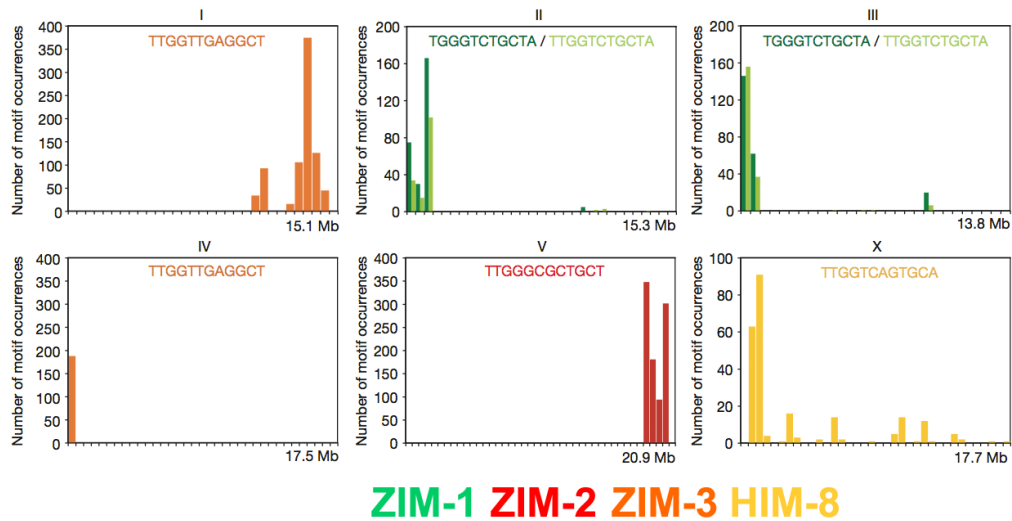


Figure 13. Localization of the PC proteins on the 6 chromosomes of *C. elegans*.

In each box the sequence recognized by the PC protein is indicated and they are concentrated to one end of each chromosome. Note that ZIM-1 and ZIM-3 bind to 2 different chromosomes but their binding patterns do not overlap. Adapted from (Phillips et al., 2009).

SUN domain proteins have been involved in the process of pairing homologues during meiosis (Fridkin et al., 2008). Inside the lumen of the nuclear membrane SUN-1 interacts with the KASH domain of ZYG-12 (Figure 14) (Zhou et al., 2009). ZYG-12 is anchored in the outer nuclear membrane (ONM) and interacts via dynein motors with the cytoskeleton (Malone et al., 2003). Inside the nucleus SUN-1 is bound to chromosome ends via the PC proteins. This SUN/KASH bridge supports the connection between forces located in the cytoplasm and chromosomes in the nucleoplasm (Figure 14). Cytoplasmic forces drive movement of chromosome ends via the SUN/KASH protein bridge.

SUN-1 forms movement competent aggregates inside the TZ that can be categorized into two classes by their size: foci and patches. Foci are circular and small aggregates of SUN-1 whereas patches are bigger and mostly elongated in one dimension (Penkner et al., 2009). Analysis of the ratio between SUN-1 foci and patches suggested that SUN-1 foci likely represent single chromosome ends whereas more than two ends are found in SUN-1

patches. We would like to consider SUN-1 aggregates as attachment plaques (Alsheimer, 2009). As mentioned earlier HIM-3 loading is a prerequisite for the formation of these attachment plaques. Indeed in *him-3(gk149)* formation of SUN-1 aggregates on autosomal chromosomes is abrogated (Penkner et al., 2009).

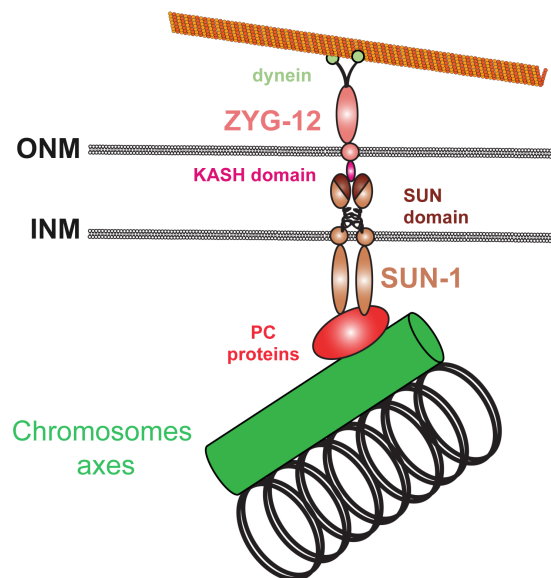


Figure 14. Model of SUN-1 interactions.

SUN-1 protein (brown ellipse) is anchored in the inner nuclear membrane. Inside the nucleus SUN-1 interact with the PC proteins, which bind to the chromosomes end. In the lumen of the nuclear membrane SUN-1 interacts with the KASH domain of ZYG-12. ZYG-12 likely moves via a dynein motor along microtubules. This SUN/KASH bridge triggers movement of chromosome ends.

Furthermore SUN-1 is phosphorylated upon entry into meiosis at multiple positions on its nuclear N-terminus (Penkner et al., 2009). Phosphorylation of SUN-1 at serine 8 marks entry into meiosis and decreases progressively during progression of meiosis. Phosphorylation of serine 12 (S12) on the contrary is specific for the leptotene/zygotene stage. As transgenic lines mimicking a constitutive phosphorylation of S12 display an extended zone with polarized conformation of the chromatin it is thought that loss of phosphorylation state of S12 is one of the factors triggering the exit of the polarized conformation (Penkner et al., 2009).

As we saw prophase I of meiosis involves many players acting at different levels (formation of axial elements, pairing of homologous chromosomes, introduction of DSBs and their repair, synapsis between paired homologues). All these processes need to be tightly regulated.

[Regulators of prophase I: CHK-2, PROM-1, HIM-19, CRA-1](#)

CHK-2 is a checkpoint protein kinase and controls polarization of chromatin, synapsis, formation of DSBs and phosphorylation of SUN-1 (MacQueen and Villeneuve, 2001). Indeed *chk-2(me64)* mutants lack a TZ and 12 univalents are found at the diakinesis. Deleting PROM-1, which contains a domain similar to an F-box, results in an extended meiotic entry zone and delayed non-homologous synapsis (Jantsch et al., 2007). This highlights the necessity for the orchestration of the meiotic program. HIM-19 is a newly identified meiotic regulator and is involved in polarization of chromatin, formation of DSBs and elongation of the SC (Tang et al., 2010). Analysis of CRA-1 mutants challenged the view that synapsis is independent of DSBs formation. Indeed in this mutant full extension of the SC required completion of repair (Smolikov et al., 2008).

Aims of the Studies

Our laboratory is investigating meiosis and its regulation in *C. elegans*. *C. elegans* is a small roundworm on which forward and reverse genetics are available as experimental approaches to dissect meiosis. The main challenge of meiosis is the faithful pairing of homologous chromosomes so that after the first division of meiosis the ploidy of the cell will be halved. This step of pairing must be tightly regulated. Defects in chromosome segregation lead to aneuploidy and are one of the most prominent causes for pregnancy loss and bring about clinical syndromes linked to mental retardation.

PROM-1 is a recently isolated regulator of progression of meiosis. In *prom-1* mutants, the meiotic entry zone is extended and the delayed synapsis is non homologous (Chapter 1). With the aim of identifying interacting partners of PROM-1 a suppressor screen was conducted in addition to the biochemical approach done by Lucia Riedmann (see her diploma thesis for details). This suppressor screen of *prom-1* mutation allowed me to isolate a genetic suppressor that I further characterized and mapped (chapter 2).

RNA-directed RNA polymerases (RdRPs) belong to the RNAi machinery and are involved in regulation of gene expression. The requirement of one of the two essential RdRPs, RRF-3, was shown to be temperature dependent (Simmer et al., 2002). Previous work demonstrated that inseminating *rrf-3* hermaphrodite mutants with wild-type sperm rescued the reduced viability observed at 25°C, pointing to a defect in spermatogenesis in *rrf-3* mutants (Duchaine et al., 2006). To further investigate the role of RRF-3 during spermatogenesis, we combined high-throughput sequencing to isolate genes up regulated in *rrf-3* mutants (work done by Jonathan I. Gent) with the cytological characterization of *rrf-3* spermatogenesis in hermaphrodites (my task). Thereby we intended to link a cytological defect with the deregulation of mRNAs during spermatogenesis dependent on *rrf-3* (Chapter 3).

The isolation and characterization of the *sun-1(jf18)* mutant, revealed that disrupting the SUN/KASH bridge led to non-homologous synapsis suggesting that chromosome end-led movement counteracts non-homologous synapsis (Penkner et al., 2007). The successful generation of a functional SUN-1::GFP transgenic line, allowed us to show that SUN-1 was phosphorylated at multiple positions and additionally to analyze the ratio of the two classes of SUN-1 aggregates (foci and patches) in wild type and most of the known pairing mutants (Chapter 4). My task was to use the SUN-1::GFP line to establish conditions for the *in vivo* imaging of SUN-1 in leptotene/zygotene (the TZ), the time window when first homologous contacts are established. SUN-1::GFP aggregates in the TZ likely represent an equivalent to “chromosomal attachment plaques”. I wanted to understand how chromosome end movement drives pairing of homologous chromosomes in *C. elegans* and to prove that non-homologous synapsis in *sun-1(jf18)* mutants was the result of lack of chromosome ends movement. Furthermore I wanted to analyze the behavior of SUN-1::GFP aggregates in most available pairing mutants and the recombination mutant *spo-11*. I set out to characterize movement in the wild type and all those mutants and tried to set up parameters to describe the movement in various different genetic backgrounds. Furthermore I sought to define parameters to quantify deviations from the wild-type behavior (Chapter 5).

A screen of a temperature sensitive maternal effect lethal mutant collection allowed me the isolation of a mutant showing fragmentation of DNA at the diakinesis. My task was to molecularly clone the mutant allele and subject the novel mutant to thorough cytological analysis. With this newly isolated *smc-3* allele I set out to study the role of *C. elegans* SMC-3 in the repair of DSBs for the first time (Chapter 6).

References

- Alpi, A., P. Pasierbek, A. Gartner, and J. Loidl. 2003. Genetic and cytological characterization of the recombination protein RAD-51 in *Caenorhabditis elegans*. *In Chromosoma*. Vol. 112. 6-16.
- Alsheimer, M. 2009. The dance floor of meiosis: evolutionary conservation of nuclear envelope attachment and dynamics of meiotic telomeres. *In Genome dynamics*. Vol. 5. 81-93.
- Altun, Z.F.a.H., D.H. 2009. Introduction. *In WormAtlas*.
- Bhalla, N., D.J. Wynne, V. Jantsch, A.F. Dernburg, and R.S. Hawley. 2008. ZHP-3 Acts at Crossovers to Couple Meiotic Recombination with Synaptonemal Complex Disassembly and Bivalent Formation in *C. elegans*. *In PLoS Genet*. Vol. 4. e1000235.
- Bishop, D.K., and D. Zickler. 2004. Early decision; meiotic crossover interference prior to stable strand exchange and synapsis. *In Cell*. Vol. 117. 9-15.
- Carlton, P.M., A.P. Farruggio, and A.F. Dernburg. 2006. A link between meiotic prophase progression and crossover control. *In PLoS Genet*. Vol. 2. e12.
- Castro, A., and T. Lorca. 2005. Exploring meiotic division in *Cargèse*. Meeting on meiotic divisions and checkpoints. *In EMBO Rep*. Vol. 6. 821-5.
- Chikashige, Y., C. Tsutsumi, M. Yamane, K. Okamasa, T. Haraguchi, and Y. Hiraoka. 2006. Meiotic proteins bqt1 and bqt2 tether telomeres to form the bouquet arrangement of chromosomes. *In Cell*. Vol. 125. 59-69.

References

- Chin, G.M., and A.M. Villeneuve. 2001. *C. elegans mre-11* is required for meiotic recombination and DNA repair but is dispensable for the meiotic G(2) DNA damage checkpoint. *In Genes Dev.* Vol. 15. 522-34.
- Colaiácovo, M.P. 2006. The many facets of SC function during *C. elegans* meiosis. *In Chromosoma.* Vol. 115. 195-211.
- Colaiácovo, M.P., A.J. MacQueen, E. Martinez-Perez, K. McDonald, A. Adamo, A. La Volpe, and A.M. Villeneuve. 2003. Synaptonemal complex assembly in *C. elegans* is dispensable for loading strand-exchange proteins but critical for proper completion of recombination. *In Dev Cell.* Vol. 5. 463-74.
- Conrad, M.N., C.-Y. Lee, G. Chao, M. Shinohara, H. Kosaka, A. Shinohara, J.-A. Conchello, and M.E. Dresser. 2008. Rapid telomere movement in meiotic prophase is promoted by NDJ1, MPS3, and CSM4 and is modulated by recombination. *In Cell.* Vol. 133. 1175-87.
- Consortium, C.e.S. 1998. Genome sequence of the nematode *C. elegans*: a platform for investigating biology. *In Science.* Vol. 282. 2012-8.
- Couteau, F., K. Nabeshima, A. Villeneuve, and M. Zetka. 2004. A component of *C. elegans* meiotic chromosome axes at the interface of homolog alignment, synapsis, nuclear reorganization, and recombination. *In Curr Biol.* Vol. 14. 585-92.
- Couteau, F., and M. Zetka. 2005. HTP-1 coordinates synaptonemal complex assembly with homolog alignment during meiosis in *C. elegans*. *In Genes Dev.* Vol. 19. 2744-56.
- Dernburg, A.F., K. McDonald, G. Moulder, R. Barstead, M. Dresser, and A.M. Villeneuve. 1998. Meiotic recombination in *C. elegans* initiates by a conserved mechanism and is dispensable for homologous chromosome synapsis. *In Cell.* Vol. 94. 387-98.

References

- Duchaine, T.F., J.A. Wohlschlegel, S. Kennedy, Y. Bei, D. Conte, K. Pang, D.R. Brownell, S. Harding, S. Mitani, G. Ruvkun, J.R. Yates, and C.C. Mello. 2006. Functional proteomics reveals the biochemical niche of *C. elegans* DCR-1 in multiple small-RNA-mediated pathways. *In Cell*. Vol. 124. 343-54.
- Eisen, G. 1900. The spermatogenesis of *Batrachoseps*. *J. Morphol.* . 17:1–117.
- Fire, A., S. Xu, M.K. Montgomery, S.A. Kostas, S.E. Driver, and C.C. Mello. 1998. Potent and specific genetic interference by double-stranded RNA in *Caenorhabditis elegans*. *In Nature*. Vol. 391. 806-11.
- Fridkin, A., A. Penkner, V. Jantsch, and Y. Gruenbaum. 2008. SUN-domain and KASH-domain proteins during development, meiosis and disease. *In Cell Mol Life Sci*. Vol. 66. 1518-33
- Goodyer, W., S. Kaitna, F. Couteau, J.D. Ward, S.J. Boulton, and M. Zetka. 2008. HTP-3 Links DSB Formation with Homolog Pairing and Crossing Over during *C. elegans* Meiosis. *In Dev Cell*. Vol. 14. 263-74.
- Haering, C.H., J. Löwe, A. Hochwagen, and K. Nasmyth. 2002. Molecular architecture of SMC proteins and the yeast cohesin complex. *In Mol Cell*. Vol. 9. 773-88.
- Hayashi, M., G. Chin, and A. Villeneuve. 2007. *C. elegans* Germ Cells Switch between Distinct Modes of Double-Strand Break Repair During Meiotic Prophase Progression. *In PLoS Genet*. Vol. 3. e191.
- Hayashi, M., S. Mlynarczyk-Evans, and A.M. Villeneuve. 2010. The Synaptonemal Complex Shapes the Crossover Landscape Through Cooperative Assembly, Crossover Promotion and Crossover Inhibition During *Caenorhabditis elegans* Meiosis. *In Genetics*. doi:10.1534/genetics.110.115501

References

- Jantsch, V., P. Pasierbek, M. Mueller, D. Schweizer, M. Jantsch, and J. Loidl. 2004. Targeted gene knockout reveals a role in meiotic recombination for ZHP-3, a Zip3-related protein in *Caenorhabditis elegans*. *In Mol Cell Biol.* Vol. 24. 7998-8006.
- Jantsch, V., L. Tang, P. Pasierbek, A. Penkner, S. Nayak, A. Baudrimont, T. Schedl, A. Gartner, and J. Loidl. 2007. *Caenorhabditis elegans* prom-1 is required for meiotic prophase progression and homologous chromosome pairing. *In Mol Biol Cell.* Vol. 18. 4911-20.
- Joyce, E.F., and K.S. McKim. 2007. When specialized sites are important for synapsis and the distribution of crossovers. *In Bioessays.* Vol. 29. 217-26.
- Keeney, S., C.N. Giroux, and N. Kleckner. 1997. Meiosis-specific DNA double-strand breaks are catalyzed by Spo11, a member of a widely conserved protein family. *In Cell.* Vol. 88. 375-84.
- Kelly, K.O., A.F. Dernburg, G.M. Stanfield, and A.M. Villeneuve. 2000. *Caenorhabditis elegans* msh-5 is required for both normal and radiation-induced meiotic crossing over but not for completion of meiosis. *In Genetics.* Vol. 156. 617-30.
- Kitajima, T.S., S.A. Kawashima, and Y. Watanabe. 2004. The conserved kinetochore protein shugoshin protects centromeric cohesion during meiosis. *In Nature.* Vol. 427. 510-7.
- Kozul, R., K.P. Kim, M. Prentiss, N. Kleckner, and S. Kameoka. 2008. Meiotic chromosomes move by linkage to dynamic actin cables with transduction of force through the nuclear envelope. *In Cell.* Vol. 133. 1188-201.
- Loidl, J. 2006. *S. pombe* linear elements: the modest cousins of synaptonemal complexes. *In Chromosoma.* Vol. 115. 260-71.

References

- MacQueen, A., and A. Villeneuve. 2001. Nuclear reorganization and homologous chromosome pairing during meiotic prophase require *C. elegans* chk-2. *In* *Genes Dev.* Vol. 15. 1674-87.
- MacQueen, A.J., C.M. Phillips, N. Bhalla, P. Weiser, A.M. Villeneuve, and A.F. Dernburg. 2005. Chromosome sites play dual roles to establish homologous synapsis during meiosis in *C. elegans*. *In* *Cell.* Vol. 123. 1037-50.
- Malone, C.J., L. Misner, N. Le Bot, M.-C. Tsai, J.M. Campbell, J. Ahringer, and J.G. White. 2003. The *C. elegans* hook protein, ZYG-12, mediates the essential attachment between the centrosome and nucleus. *In* *Cell.* Vol. 115. 825-36.
- Marston, A.L., and A. Amon. 2004. Meiosis: cell-cycle controls shuffle and deal. *In* *Nat Rev Mol Cell Biol.* Vol. 5. 983-97.
- Martinez-Perez, E., and A.M. Villeneuve. 2005. HTP-1-dependent constraints coordinate homolog pairing and synapsis and promote chiasma formation during *C. elegans* meiosis. *In* *Genes Dev.* Vol. 19. 2727-43.
- McKim, K.S., A.M. Howell, and A.M. Rose. 1988. The effects of translocations on recombination frequency in *Caenorhabditis elegans*. *In* *Genetics.* Vol. 120. 987-1001.
- Mito, Y., A. Sugimoto, and M. Yamamoto. 2003. Distinct developmental function of two *Caenorhabditis elegans* homologs of the cohesin subunit Scc1/Rad21. *In* *Mol Biol Cell.* Vol. 14. 2399-409.
- Monje-Casas, F., V.R. Prabhu, B.H. Lee, M. Boselli, and A. Amon. 2007. Kinetochores orientation during meiosis is controlled by Aurora B and the monopolin complex. *In* *Cell.* Vol. 128. 477-90.

References

- Ogawa, H., K. Johzuka, T. Nakagawa, S.H. Leem, and A.H. Hagihara. 1995. Functions of the yeast meiotic recombination genes, MRE11 and MRE2. *In* *Adv Biophys.* Vol. 31. 67-76.
- Onn, I., J. Heidinger-Pauli, V. Guacci, and e. al. 2008. Sister chromatid cohesion: a simple concept with a complex reality. *In* *Annual review of cell and developmental biology.* Vol. 24. 105-29.
- Page, S.L., and R.S. Hawley. 2003. Chromosome choreography: the meiotic ballet. *In* *Science.* Vol. 301. 785-9.
- Pâques, F., and J.E. Haber. 1999. Multiple pathways of recombination induced by double-strand breaks in *Saccharomyces cerevisiae*. *In* *Microbiol Mol Biol Rev.* Vol. 63. 349-404.
- Pasierbek, P., M. Födermayr, V. Jantsch, M. Jantsch, D. Schweizer, and J. Loidl. 2003. The *Caenorhabditis elegans* SCC-3 homologue is required for meiotic synapsis and for proper chromosome disjunction in mitosis and meiosis. *In* *Exp Cell Res.* Vol. 289. 245-55.
- Pasierbek, P., M. Jantsch, M. Melcher, A. Schleiffer, D. Schweizer, and J. Loidl. 2001. A *Caenorhabditis elegans* cohesion protein with functions in meiotic chromosome pairing and disjunction. *In* *Genes Dev.* Vol. 15. 1349-60.
- Pawlowski, W.P., and W.Z. Cande. 2005. Coordinating the events of the meiotic prophase. *In* *Trends Cell Biol.* Vol. 15. 674-81.
- Penkner, A., L. Tang, M. Novatchkova, M. Ladurner, A. Fridkin, Y. Gruenbaum, D. Schweizer, J. Loidl, and V. Jantsch. 2007. The Nuclear Envelope Protein Matefin/SUN-1 Is Required for Homologous Pairing in *C. elegans* Meiosis. *In* *Dev Cell.* Vol. 12. 873-85.

References

- Penkner, A.M., A. Fridkin, J. Gloggnitzer, A. Baudrimont, T. Machacek, A. Woglar, E. Csaszar, P. Pasierbek, G. Ammerer, and Y. Gruenbaum. 2009. Meiotic Chromosome Homology Search Involves Modifications of the Nuclear Envelope Protein Matefin/SUN-1. *In Cell*. Vol. 139. 920-933.
- Phillips, C., X. Meng, L. Zhang, J. Chretien, F. Urnov, and A. Dernburg. 2009. Identification of chromosome sequence motifs that mediate meiotic pairing and synapsis in *C. elegans*. *In Nat Cell Biol*. Vol. 11, 934-42
- Phillips, C.M., and A.F. Dernburg. 2006. A family of zinc-finger proteins is required for chromosome-specific pairing and synapsis during meiosis in *C. elegans*. *In Dev Cell*. Vol. 11. 817-29.
- Phillips, C.M., C. Wong, N. Bhalla, P.M. Carlton, P. Weiser, P.M. Meneely, and A.F. Dernburg. 2005. HIM-8 binds to the X chromosome pairing center and mediates chromosome-specific meiotic synapsis. *In Cell*. Vol. 123. 1051-63.
- Rinaldo, C., P. Bazzicalupo, S. Ederle, M. Hilliard, and A. La Volpe. 2002. Roles for *Caenorhabditis elegans* rad-51 in meiosis and in resistance to ionizing radiation during development. *In Genetics*. Vol. 160. 471-9.
- Rosenbluth, R.E., and D.L. Baillie. 1981. The genetic analysis of a reciprocal translocation, eT1(III; V), in *Caenorhabditis elegans*. *In Genetics*. Vol. 99. 415-28.
- San Filippo, J., P. Sung, and H. Klein. 2008. Mechanism of eukaryotic homologous recombination. *In Annu Rev Biochem*. Vol. 77. 229-57.
- Sato, A., B. Isaac, C. Phillips, R. Rillo, P. Carlton, D. Wynne, R. Kasad, and A. Dernburg. 2009. Cytoskeletal Forces Span the Nuclear Envelope to Coordinate Meiotic Chromosome Pairing and Synapsis. *In Cell*. Vol. 139. 907-19

References

- Scherthan, H. 2001. A bouquet makes ends meet. *In Nat Rev Mol Cell Biol.* Vol. 2. 621-7.
- Scherthan, H. 2007. Telomere attachment and clustering during meiosis. *In Cell Mol Life Sci.* Vol. 64. 117-24.
- Severson, A.F., L. Ling, V. van Zuylen, and B.J. Meyer. 2009. The axial element protein HTP-3 promotes cohesin loading and meiotic axis assembly in *C. elegans* to implement the meiotic program of chromosome segregation. *In Genes Dev.* Vol. 23. 1763-78.
- Sheehan, M., and W. Pawlowski. 2009. Live imaging of rapid chromosome movements in meiotic prophase I in maize. *In Proc Natl Acad Sci USA.* Vol. 106. 20989-94
- Simmer, F., M. Tijsterman, S. Parrish, S.P. Koushika, M.L. Nonet, A. Fire, J. Ahringer, and R.H.A. Plasterk. 2002. Loss of the putative RNA-directed RNA polymerase RRF-3 makes *C. elegans* hypersensitive to RNAi. *In Curr Biol.* Vol. 12. 1317-9.
- Smolikov, S., A. Eizinger, K. Schild-Prufert, A. Hurlburt, K. McDonald, J. Engebrecht, A.M. Villeneuve, and M.P. Colaiácovo. 2007. SYP-3 restricts synaptonemal complex assembly to bridge paired chromosome axes during meiosis in *Caenorhabditis elegans*. *In Genetics.* Vol. 176. 2015-25.
- Smolikov, S., K. Schild-Prüfert, and M.P. Colaiácovo. 2008. CRA-1 uncovers a double-strand break-dependent pathway promoting the assembly of central region proteins on chromosome axes during *C. elegans* meiosis. *In PLoS Genet.* Vol. 4. e1000088.
- Smolikov, S., K. Schild-Prüfert, and M.P. Colaiácovo. 2009. A yeast two-hybrid screen for SYP-3 interactors identifies SYP-4, a component

References

- required for synaptonemal complex assembly and chiasma formation in *Caenorhabditis elegans* meiosis. *In PLoS Genet.* Vol. 5. e1000669.
- Tang, L., T. Machacek, Y.M. Mamnun, A. Penkner, J. Gloggnitzer, C. Wegrostek, R. Konrat, M.F. Jantsch, J. Loidl, and V. Jantsch. 2010. Mutations in *Caenorhabditis elegans* him-19 show meiotic defects that worsen with age. *In Mol Biol Cell.* Vol. 21. 885-96.
- van den Bosch, M., R.T. Bree, and N.F. Lowndes. 2003. The MRN complex: coordinating and mediating the response to broken chromosomes. *In EMBO Rep.* Vol. 4. 844-9.
- Wang, C.-J.R., P.M. Carlton, I.N. Golubovskaya, and W.Z. Cande. 2009. Interlock formation and coiling of meiotic chromosome axes during synapsis. *In Genetics.* Vol. 183. 905-15.
- Ward, J.D., D.M. Muzzini, M.I.R. Petalcorin, E. Martinez-Perez, J.S. Martin, P. Plevani, G. Cassata, F. Marini, and S.J. Boulton. 2010. Overlapping Mechanisms Promote Postsynaptic RAD-51 Filament Disassembly during Meiotic Double-Strand Break Repair. *In Molecular cell.* Vol. 37. 259-272.
- Wood, A.J., A.F. Severson, and B.J. Meyer. 2010. Condensin and cohesin complexity: the expanding repertoire of functions. *In Nat Rev Genet.* Vol. 11. 391–404
- Zhou, K., M.M. Rolls, D.H. Hall, C.J. Malone, and W. Hanna-Rose. 2009. A ZYG-12-dynein interaction at the nuclear envelope defines cytoskeletal architecture in the *C. elegans* gonad. *In The Journal of Cell Biology.* Vol. 186. 229-41.
- Zickler, D., and N. Kleckner. 1999. Meiotic chromosomes: integrating structure and function. *In Annu Rev Genet.* Vol. 33. 603-754.

Results

Chapter 1. *Caenorhabditis elegans* PROM-1 is Required for Meiotic Prophase Progression and Homologous Chromosome Pairing

Caenorhabditis elegans *prom-1* Is Required for Meiotic Prophase Progression and Homologous Chromosome Pairing^D

Verena Jantsch,* Lois Tang,* Pawel Pasierbek,† Alexandra Penkner,*
Sudhir Nayak,‡ Antoine Baudrimont,* Tim Schedl,‡ Anton Gartner,§
and Josef Loidl*

*Department of Chromosome Biology and Max F. Perutz Laboratories, Faculty of Life Sciences, University of Vienna, A-1030 Vienna, Austria; †Biooptics Department, Research Institute of Molecular Pathology, A-1030 Vienna, Austria; ‡Department of Genetics, Washington University School of Medicine, St. Louis, MO 63110; and §School of Life Sciences, University of Dundee, Dundee DD1 5EH, United Kingdom

Submitted March 22, 2007; Revised September 19, 2007; Accepted September 25, 2007
Monitoring Editor: Yixian Zheng

A novel gene, *prom-1*, was isolated in a screen for *Caenorhabditis elegans* mutants with increased apoptosis in the germline. *prom-1* encodes an F-box protein with limited homology to the putative human tumor suppressor FBXO47. Mutations in the *prom-1* locus cause a strong reduction in bivalent formation, which results in increased embryonic lethality and a Him phenotype. Furthermore, retarded and asynchronous nuclear reorganization as well as reduced homologous synapsis occur during meiotic prophase. Accumulation of recombination protein RAD-51 in meiotic nuclei suggests disturbed repair of double-stranded DNA breaks. Nuclei in *prom-1* mutant gonads timely complete mitotic proliferation and premeiotic replication, but they undergo prolonged delay upon meiotic entry. We, therefore, propose that *prom-1* regulates the timely progression through meiotic prophase I and that in its absence the recognition of homologous chromosomes is strongly impaired.

INTRODUCTION

Meiosis is the specialized nuclear division in which the diploid chromosomal complement is reduced to a haploid gametic chromosome set to compensate for the duplication of chromosome number that occurs at fertilization. During meiosis, pairs of homologous chromosomes (one from each parent) separate in a first round of nuclear division (meiosis I), and each chromosome splits into its two sister chromatids during a second round of nuclear division (meiosis II). Before homologous chromosomes disjoin at meiosis I, they reciprocally exchange corresponding portions, which results in each chromosome becoming a mosaic consisting of parts of the original parental chromosomes. This process, which is called crossing over, contributes to the genetic diversity of the four meiotic products, and as a consequence, to the variability of offspring. To allow for the orderly segregation of homologues at meiosis I and crossing over to occur, chromosomes have to pair during meiotic prophase.

Meiotic pairing is a multistep process during which homologous chromosomes first recognize each other, then align, and finally engage in an intimate association along their entire lengths. The final, close apposition is mediated by a ribbon-like proteinaceous structure, referred to as the synaptonemal complex (SC). Crossing over, which takes place within the framework of the SC, produces chiasmata. Together with the cohesion of sister chromatids, chiasmata connect homologues after the disassembly of the SC, allowing them to persist as bivalents until their separation in the first anaphase of meiosis (for review, see Petronczki *et al.*, 2003).

The establishment of bivalents needs the accurate coordination of all the events that are taking place during prophase I. Many aspects of the meiotic cell cycle are regulated by the interplay between cyclin-dependent kinase activity and ubiquitin-mediated proteolysis of inhibitory factors similar to the mitotic cell cycle (Harper *et al.*, 2002; Henderson *et al.*, 2006). To date, little is known about the orchestration and cell cycle dependence of meiotic events of prophase I such as chromatin condensation, homologue recognition, axis formation, and SC formation.

In *C. elegans*, various defects in meiotic pairing and recombination lead to the elimination of a major portion of affected cells by germ cell apoptosis (Gartner *et al.*, 2000; Bhalla and Dernburg, 2005). Here, we describe a novel gene, *progression of meiosis (prom-1)*, which was originally identified in a screen for increased apoptosis in the germline and which plays a role in the orderly progression of meiotic prophase I and in full homologous chromosome pairing and recombination.

This article was published online ahead of print in *MBC in Press* (<http://www.molbiolcell.org/cgi/doi/10.1091/mbc.E07-03-0243>) on October 3, 2007.

^D The online version of this article contains supplemental material at *MBC Online* (<http://www.molbiolcell.org>).

Address correspondence to: Josef Loidl (josef.loidl@univie.ac.at).

Abbreviations used: DSB, double-strand break; FISH, fluorescence in situ hybridization; SC, synaptonemal complex; SNP, single-nucleotide polymorphism.

MATERIALS AND METHODS

Worm Strains and Culture Conditions

The wild-type N2 Bristol, the Hawaiian strain CB4856, and strain DC1079 [*ces-1(n703) qDf8/hT2[blt-4(e937) let-3(q728) qIs48]* (L:III)] were obtained from the *Caenorhabditis* Genetics Center (University of Minnesota, St. Paul, MN). The *prom-1* deletion allele *ok1140* (strain RB1183) was generated by the *C. elegans* Gene Knockout Consortium. AV106 *spo-11(ok79)* (Dernburg *et al.*, 1998) and AV393 *htp-1(gk174)* (Martinez-Perez and Villeneuve, 2005) were kindly provided by Anne M. Villeneuve. Worms were grown on NGM plates with *Escherichia coli* OP50 (Brenner, 1974). To create *prom-1/qDf8* heterozygotes, *prom-1(ok1140)* males were mated to DC1079 hermaphrodites. F1 progeny, which do not carry the *myo-2::GFP*, were selected.

Screen for Mutants with Increased Meiotic Cell Death

A synchronized population of wild-type worms at the L4 larval stage was mutagenized with ethyl methanesulfonate (EMS) under standard conditions, and it was subsequently allowed to grow to adulthood. These adults were bleached and the F₂ generation was stained with acridine orange (Gartner *et al.*, 2004), and live animals were screened under a standard fluorescence dissection microscope for increased apoptosis.

Candidate mutants were outcrossed four to five times and tested for the viability of offspring and for a high incidence of males (Him) among the progeny. Mapping of the mutant alleles was performed with single-nucleotide polymorphism (SNP) markers as described in Wicks *et al.* (2001). The mutation was mapped to an interval between an SNP on cosmid F14B4 (position 13524) and an SNP on M04C9 (position 11470), and the remaining candidate open reading frames were sequenced.

Protein Depletion by Double-stranded RNA (dsRNA) Interference (RNAi)

F54D5.9p and CUL-1 proteins were depleted by double-stranded RNAi by feeding hermaphrodites with dsRNA-producing bacteria (Timmons *et al.*, 2001). Target sequences were polymerase chain reaction (PCR)-amplified from *C. elegans* genomic DNA and cloned into feeding vector pPD129.36. The following primers were used: MJ959 5'-ctccttgaggattgacgag-3' and MJ960 5'-catttggagctggaagcct-3' for F54D5.9, and MJ901 5'-atgacaatagcgaaccgag-3' and MJ902 5'-acaattctgtctgcaactc-3' for *cul-1* (D2045.6).

Measurement of Genetic Recombination in the Oocytes

To assay crossing over in nonviable *prom-1* mutant progeny, we tested recombination between loci polymorphic for SNP markers as in Hillers and Villeneuve (2003). First, a strain homozygous for *prom-1Δ* and heterozygous for two SNP markers on chromosome V was created by crossing the Bristol *prom-1Δ* strain to a *prom-1Δ* strain carrying Hawaiian chromosome V. The markers polymorphic for DraI restriction sites were at position base pairs 7973 on cosmid F36H9 (primers 5'-CGGAAAATTGCGACTGTC-3' and 5'-ATTAGGACTGCTTGCTCC-3') and at position base pairs 92865 on cosmid Y51A2A (primers 5'-TTTATCCGACGGACTTGAC-3' and 5'-TCTCCTCCTCATGGTTAAC-3'). Hermaphrodites were individually mated to Bristol males carrying a green fluorescent protein (GFP) transgene. The eggs laid by these individuals were collected at ~4-h intervals to avoid decomposition of dead eggs, and they were individually lysed. PCR was performed on the lysates and restriction digests were performed. Products were run on 2% agarose gels to detect restriction patterns diagnostic of recombination between the SNP markers. Only eggs positive for GFP or PROM-1 (contributed by the males) were evaluated.

In Situ Detection of DNA Replication by Incorporation of dUTP

Gonads of immobilized animals were injected with a solution of 300 pM Cy3-labeled dUTP (GE Healthcare, Chalfont St. Giles, United Kingdom) in phosphate buffer, pH 7.0 (Mello *et al.*, 1991). Worms were allowed to recover in M9 buffer (0.3% KH₂PO₄, 0.6% Na₂HPO₄, 0.5% NaCl, and 1 mM MgSO₄) for 30 min, and then they were transferred to a fresh plate. Gonads were dissected and 4,6-diamidino-2-phenylindole (DAPI)-stained (see below) after ~1.5 h of exposure to the nucleotides. The incorporation of labeled nucleotides into nuclear DNA was directly observed by fluorescence microscopy.

Cytological Preparation of Gonads

Hermaphrodites were cut open to release the gonads in 5 μl of M9 buffer on a microscope slide and fixed by the addition of an equal volume of 7.4% formaldehyde. The material was immediately covered with a coverslip, and gentle pressure was applied. The coverslip was removed after freezing the preparations in liquid nitrogen and the slides were then transferred to 1× phosphate-buffered saline (PBS). For the staining of chromatin and chromosomes, slides were mounted in Vectashield anti-fading medium (Vector Laboratories, Burlingame, CA) containing 2 μg/ml DAPI.

Immunostaining

For immunostaining, gonads prepared in M9 buffer on a microscope slide were fixed in a series of methanol, methanol:acetone (1:1), and acetone for 5 min each at -20°C, and then they were immediately transferred to 1× PBS without drying. Preparations were transferred to fresh 1× PBS twice for 5 min each and were blocked with 3% bovine serum albumin (BSA) in 1× PBS for 30 min at 37°C in a humidity chamber. The primary antibody was applied and the specimen was incubated overnight at 4°C in a humidity chamber. Antibodies were diluted in 1× PBS containing 3% BSA as follows: 1:100 anti-REC-8 (Pasierbek *et al.*, 2001), 1:100 anti-RAD-51 (Colaiácovo *et al.*, 2003), 1:50 anti-SYP-1 (MacQueen *et al.*, 2002), 1:100 anti-HIM-3 (Zetka *et al.*, 1999), and 1:500 anti-HIM-8 (Phillips *et al.*, 2005). After washing three times in 1× PBS plus 0.1% Tween 20, secondary antibodies were applied at the following dilutions: anti-rabbit Cy3 (1:250), anti-rabbit fluorescein isothiocyanate (FITC) (1:500) or anti-rat FITC (1:500). After 60-min incubation at room temperature, slides were washed and mounted in Vectashield supplemented with DAPI (see above). Fixation and staining for phosphorylated histone H3 was performed as described previously (Jones *et al.*, 1996).

Fluorescence In Situ Hybridization (FISH)

Pooled cosmids C53D5 and R119, and PCR-amplified 5S rDNA, were used as probes for the left end of chromosome I and the right arm of chromosome V, respectively (Pasierbek *et al.*, 2001). Cosmid DNA was directly labeled with Cy3 by using the BioNick Labeling System (Invitrogen, Carlsbad, CA) according to the manufacturer's instructions. The 5S rDNA was labeled by PCR with digoxigenin-11-dUTP during PCR amplification.

Slides prepared according to the above-mentioned protocol were dehydrated by incubation in increasing ethanol concentrations, dried on air, and kept in the freezer until use for FISH. Labeled probe DNA and cytological preparations were denatured separately before the probe was added to the slides for hybridization. The protocol is described in detail in Pasierbek *et al.* (2001). Hybridized digoxigenin-labeled probes were detected with FITC-conjugated anti-digoxigenin, and FITC (green) and Cy3 (red) fluorescence was emitted by excitation with light of appropriate wavelengths. Slides were mounted in Vectashield containing 2 μg/ml DAPI.

Microscopy and Evaluation

Preparations were examined with a Zeiss Axioskop epifluorescence microscope. Images were recorded with a cooled charge-coupled device camera (Photometrics, Tucson, AZ). Evaluation of cytological phenotypes was performed in animals kept at 20°C 16–24 h after larval stage 4 (L4). For multicolor immunostaining and FISH pictures, monochrome images were captured separately for each emission wavelength. Artificial coloring and merging were undertaken using IPLab Spectrum software (Scanalytics, Fairfax, VA). In some cases, three-dimensional stacks of images were taken (MetaVue software; Molecular Devices, Sunnyvale, CA), deconvolved (AutoDeblur software; AutoQuant Imaging, Troy, NY), and projected (Helicon Focus software; <http://helicon.com.ua/heliconfocus/>).

RESULTS

Isolation and Characterization of *prom-1* Mutant Alleles

In animals, defects in meiotic recombination and/or meiotic pairing can lead to the elimination of affected cells by apoptotic cell death (Gartner *et al.*, 2000). We exploited this phenotype for the screening for *C. elegans* meiotic mutants, taking advantage of the preferential uptake of the dye acridine orange by apoptotic corpses (Gartner *et al.*, 2004; Schumacher *et al.*, 2005). Two alleles, *op240* and *jf3*, of a novel gene (*prom-1*) were identified. In addition to increased apoptosis, these mutants exhibited high embryonic lethality and a high incidence of males (Him) phenotype (see below). After backcrossing the mutant animals, the corresponding gene (*prom-1*) was mapped to open reading frame F26H9.1 on chromosome I by using morphological and SNP markers. Sequencing of these alleles revealed a D₂₄₂ to N missense mutation in *op240* and a Q₃₆₃ to premature stop codon mutation in *jf3* (see Supplemental Figures S1 and S2 for cDNA sequence, intron–exon boundaries, and mutation sites). A third allele, *ok1140*, was provided by the *C. elegans* Gene Knockout Consortium. Complementation testing confirmed that *jf3*, *op240*, and *ok1140* are indeed allelic (data not shown). *ok1140* is a deletion of 1229 base pairs encompassing the first five and a half exons and 63 base pairs of the promoter region. Because *prom-1(ok1140)* is the most se-

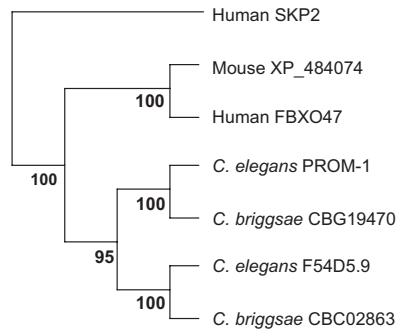


Figure 1. Phylogenetic tree of *C. elegans* PROM-1 and related proteins. The human F-box protein SKP2 is displayed as a member of the outgroup. The phylogenetic tree was derived from a multiple protein sequence alignment by the ClustalX program (Thompson *et al.*, 1997). The resulting tree was tested by resampling (bootstrapping) by using the programs seqboot, protpars, and consense from the PHYLIP package (Felsenstein, 1989), executed on a server of the Department of Molecular Evolution, Uppsala University (<http://artedi.ebc.uu.se/programs/>). The numbers at the forks indicate in how many trees (out of 100) the grouping to the right of the fork occurred.

verely mutated allele, most quantitative mutant analyses were performed using progeny of homozygous backcrossed *ok1140* (hereafter *prom-1Δ*) mothers, unless indicated otherwise. Similar phenotypes, and in particular strong phenotypic variability between individuals (see below) were observed in the other alleles as well (data not shown).

The F26H9.1 transcript shows a three- to fourfold germline enrichment relative to somatic tissues (Reinke *et al.*, 2000). It encodes a 524-amino acid (aa) protein with an F-box motif (Kipreos and Pagano, 2000; Supplemental Figure S1). A *C. elegans* paralogue, F54D5.9, with an amino acid identity of 22% and a similarity of 39% is listed in WormBase (www.wormbase.org). F54D5.9 and, to a lesser degree, F26H9.1 show homology to the human F-box protein 47 (FBXO47), which is a putative tumor suppressor (Simon-Kayser *et al.*, 2005) and to FBXO47-related proteins in various vertebrates. Although there seems to exist only one FBXO47-like protein in all vertebrates examined, this locus seems to be duplicated in nematodes (Figure 1). Intriguingly, we were unable to find homologues of FBXO47 in *Drosophila*, plants, or yeast. An RNAi phenotype was not detected for F54D5.9 by Kamath *et al.* (2003) and Rual *et al.* (2004), whereas Piano *et al.* (2002) reported 10–29% embryonic lethality. We found RNAi of F54D5.9 to result in embryos with hyperproliferating tissues, whereas meiosis was not notably affected (data not shown).

Mutation of *prom-1* Causes Reduced Fertility and Increased Production of Males

Brood size was strongly reduced in the mutants, and it was highly variable from animal to animal, with all three backcrossed alleles. *prom-1Δ* homozygous hermaphrodites laid 143 ± 70 (SD) embryos (ranging from 44 to 256; $n = 17$ animals) compared with an average brood size of 282 ± 22 ($n = 8$) of the wild type. *prom-1Δ* worms also displayed high embryonic lethality. The average viability was 10.2% (70 of 688 laid eggs developed further than to the L1 stage) compared with 99.8% in the wild type ($n = 2257$ eggs), but it was highly variable between individual hermaphrodites, ranging from 1.4 to 54.2%. Of the surviving mutant offspring, 22% (72 of 328 L3–adult worms in a different experiment) were males. Most of the viable progeny were vigorous and

morphologically normal, suggesting that embryonic lethality was due to chromosomal defects in the wake of disturbed meiosis (see below), and that animals receiving a balanced, intact chromosome set were not affected. Deletion of *prom-1*, therefore, seems to have only a mild, if any, somatic phenotype.

To test whether both female and male meioses are affected and whether the combined defects contribute to the lethality of hermaphrodite progeny, we crossed *prom-1Δ* hermaphrodites to wild-type (WT) males and *fog-2(oz40)* female-only worms to *prom-1Δ* males. Progeny from *prom-1Δ* hermaphrodites \times WT males showed 33% viability (1610 eggs scored). Progeny from *fog-2* females \times *prom-1Δ* males showed 28% viability (1309 eggs scored), which is not significantly different (*t* test). (*fog-2* females \times WT males produced 99% viable offspring; $n = 1622$ eggs.) Thus, the involvement of either *prom-1* mutant eggs or sperm in zygote formation considerably reduces viability, suggesting that formation of both types of gametes is compromised in *prom-1Δ* hermaphrodites.

Apoptosis Is Increased in the *prom-1Δ* Mutant

We scored for apoptotic nuclei by differential interference contrast microscopy in animals 16–24 h past L4. In accordance with the apoptosis phenotype by which *prom-1* was initially identified, up to 21 (mean \pm SD, 11.6 ± 4.7 ; $n = 30$) nuclei in the ovary of the *prom-1Δ* mutant, at any given time, show morphological features indicative of apoptosis, compared with a maximum of three nuclei (1.4 ± 0.6 ; $n = 23$) in the wild type. We tested whether impaired repair of meiotic double-strand breaks (DSBs) contributed to increased germ cell apoptosis by scoring for apoptotic nuclei in a *prom-1 spo-11* double mutant. We found that in the absence of SPO-11 (which catalyzes meiotic DSB formation; Dernburg *et al.*, 1998), on average, only 1.9 nuclei \pm 1.9 ($n = 19$) per gonad were apoptotic. Thus, the apoptosis phenotype was bypassed in the absence of DSBs, indicating that incomplete or delayed repair of meiotic DSBs, which is a possible consequence of delayed meiotic progression (see below) may trigger DNA damage checkpoint-dependent apoptosis in a *prom-1Δ* mutant. Moreover, we found that apoptosis was reduced to almost wild-type levels in a *prom-1 cep-1* double mutant (2.7 ± 2.2 apoptotic nuclei per gonad, $n = 25$). The dependency of apoptosis on CEP-1 (the p53 homologue of the worm) also suggests that it is not due to a recently discovered checkpoint that monitors meiotic chromosome synapsis (Bhalla and Dernburg, 2005). It is conceivable that nonhomologous synapsis (which occurs in the *prom-1* mutant; see below) is sufficient to escape this checkpoint (Penkner *et al.*, 2007).

Mutation of *prom-1* Causes a Transient Arrest of Nuclei on Meiotic Entry

Cytological inspection of mutant gonads revealed that in addition to elevated apoptosis, the normal progression of meiotic stages was perturbed (Figure 2a). In wild-type ovaries, the distal region of the gonad where germ cells are produced by a series of mitoses, is characterized by spherical DAPI-stained nuclei. It is commonly referred to as the mitotic zone, although its most proximal nuclei start to express meiotic genes (MacQueen *et al.*, 2002; Hansen *et al.*, 2004; Crittenden *et al.*, 2006; see below) and hence satisfy the classical cytological definition of leptotene. This “meiotic entry zone” (marking the switch from proliferation to meiotic determination (Hansen *et al.*, 2004) possesses somewhat larger nuclei than the genuine mitotic zone. It is followed by several rows of cells that comprise the transition zone,

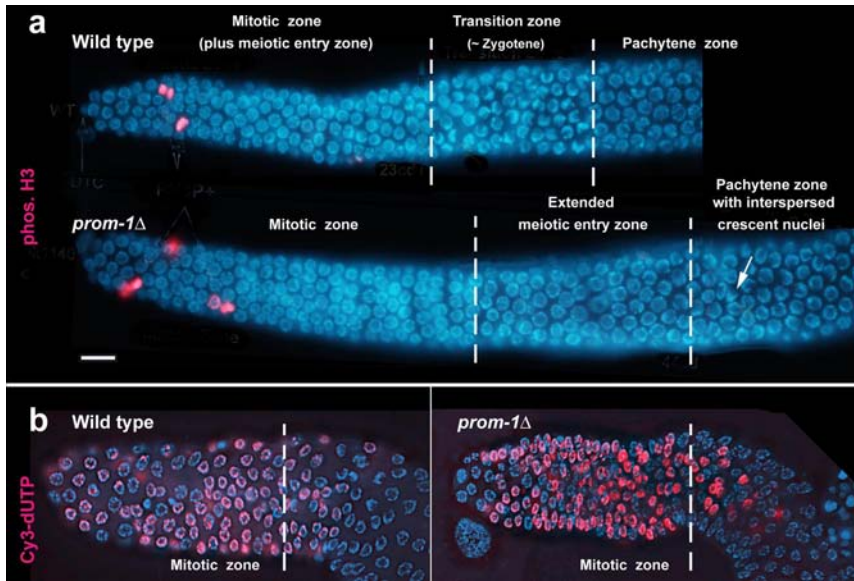


Figure 2. Organization of gonads in the wild type and in *prom-1Δ* (*ok1140*). (a) In the wild type, the mitotic zone of the germline (with mitotic nuclei immunostained for phosphorylated histone H3 depicted in red) and a narrow meiotic entry zone (see text) is followed by the transition zone containing crescent-shaped nuclei and then by the pachytene zone. In the *prom-1Δ* mutant, the mitotic zone is followed by an extended meiotic entry zone with large nuclei that are not crescent shaped. The pachytene zone contains some crescent-shaped nuclei (arrow). The vertical broken lines indicate the boundaries between different regions, defined by DAPI staining (see text). (b) Incorporation of Cy3-labeled dUTP (red) is limited to the mitotic zone in wild-type and mutant gonads. Chromatin is stained blue with DAPI. Bar, 10 μm .

where leptotene nuclei become replaced by nuclei with chromatin arranged in a crescent, which correspond to early zygotene. The region next to the transition zone is occupied by late zygotene and pachytene nuclei, followed by cells in diplotene and diakinesis (Schedl, 1997).

In *prom-1* mutants, the zone with small DAPI-bright nuclei, resembling the wild-type mitotic zone, extended for 19.69 ± 4.40 ($n = 56$) nuclear diameters from the distal tip cell (DTC), which is comparable with the 20.75 ± 1.62 ($n = 56$) nuclear diameters from the DTC in the wild type. Within this mitotic zone, mitoses were identified by immunostaining for phosphorylated histone H3 (Figure 2a). It was followed by a zone with slightly larger and less bright nuclei, ~ 16 nuclear diameters in width (Figure 2a), which was missing in the wild type. This zone did not contain mitoses (Supplemental Figure S3). To determine whether DNA replication was ongoing in these putative postmitotic cells, we monitored DNA synthesis by the incorporation of Cy3-labeled dUTP. Young adult hermaphrodites were injected with high concentrations of Cy3-labeled dUTP, and incorporation was scored in fixed DAPI-stained gonads. After 1.5-h exposure to Cy3-labeled dUTP, it was found that labeled nucleotides had been incorporated for the same number of distal cell rows both in the wild type (27.2 ± 2.1 ; $n = 13$) and in the mutant (27.5 ± 3.4 ; $n = 13$) (Figure 2b). Further down in the gonad, only stray cells with some Cy3 label were detected. This indicates that DNA synthesis takes place mostly within the first ~ 27 cell rows of the wild type and the mutant, and we assume that it corresponds to S phase in proliferative cells (~ 20 cell rows) plus a few adjacent cell rows where cells undergo meiotic DNA replication (compare Crittenden *et al.*, 2006). This result suggests that the mitotic zone is normal and that meiotic S phase is essentially complete in the additional cell rows that follow this zone in the mutant.

A distinct transition zone was missing in the mutant. Instead, sporadic nuclei with chromatin arranged in a crescent were scattered over the proximal area (the pachytene zone) of the gonad (Figure 2a). (For simplicity, the area of the *prom-1Δ* mutant gonad that corresponds to the pachytene zone of the wild type will be also called pachytene zone throughout the article, despite the fact that chromosome pairing may be incomplete; see below.) The occurrence of

such transition zone-like nuclei in the pachytene zone of the gonad may reflect delayed and asynchronous initiation of homologous chromosome pairing in the *prom-1Δ* mutant (see below).

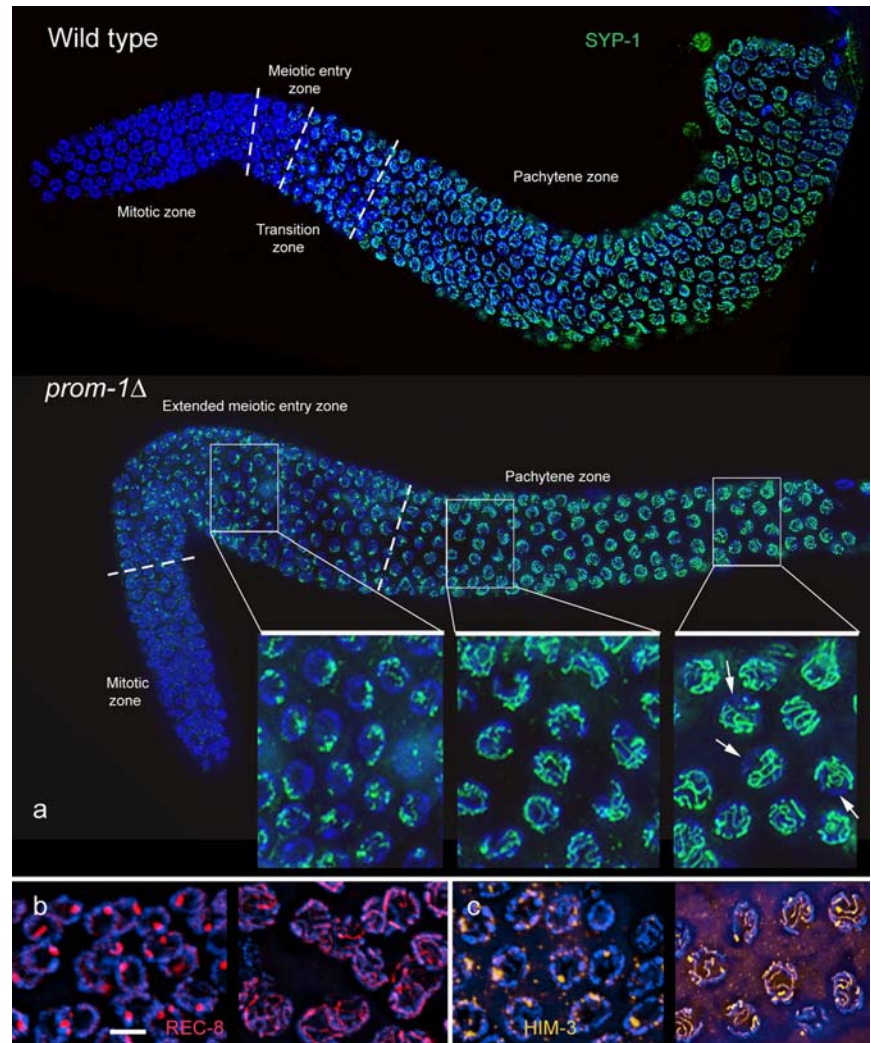
To further determine the nature of the cells following the zone where mitoses and DNA replication take place, we studied the expression of SC proteins. In the wild type, SCs form between pairs of homologous chromosomes along their entire length, and they can be visualized as thread-like structures corresponding to the haploid chromosome number when immunostained for SC components or associated proteins such as SYP-1 (MacQueen *et al.*, 2002), HIM-3 (Zetka *et al.*, 1999), and REC-8 (Pasierbek *et al.*, 2001) (Figure 3; Supplemental Figure S4). In the *prom-1Δ* mutant, SYP-1, a protein that connects the synapsed partners; HIM-3, an axial element component; and the cohesin subunit REC-8 were present in a few patches inside nuclei proximal to the mitotic zone. This observation confirms our interpretation that these nuclei have entered the meiotic program and hence they represent an extended meiotic entry zone (Figure 3, b and c), and it suggests that PROM-1 functions very early in meiotic prophase.

Reduced Levels of Bivalent Formation and Crossing Over in the *prom-1Δ* Mutant

In the pachytene zone of the *prom-1Δ* mutant, all three SC-associated proteins progressively developed into long lines (Figure 3, b and c), indicating the occurrence of rather extensive although incomplete synapsis. Consistent with partial synapsis, we found a high level of univalents at diakinesis of mutant hermaphrodites. Whereas six bivalents are present in the wild type, in the *prom-1Δ* animals a range of six to 12 DAPI-positive entities were detected (Figure 4, a and b). Of the 1074 homologue pairs in the 179 diakineses scored, 367 formed bivalents (i.e., the frequency of bivalents was 34%), amounting to an average of approximately two bivalents per meiosis.

The number of bivalents was highly variable. Although 39% of diakinesis cells had no bivalents, a complete set of six bivalents was formed in 7% of cells (Figure 4b). To exclude the possibility that the product of the close paralogue F54D5.9 could partially substitute PROM-1, we performed RNAi for F54D5.9 in the *prom-1Δ* mutant. Depletion of the

Figure 3. (a) Immunostaining of SC component SYP-1 (green) in the wild type and in the *prom-1* Δ mutant. In the images of whole ovaries, the broken lines mark the borders between the zones with distinguishable nuclear morphologies (see Figure 2a), namely, the mitotic zone, the meiotic entry zone and the pachytene zone. In the wild type, small spots of SYP-1 first occur in a narrow meiotic entry zone just upstream of the transition zone, and then they develop into continuous lines along the pachytene zone. In the *prom-1* Δ mutant, the meiotic entry zone with SYP-1 spots is greatly expanded; SYP-1 starts to form lines in the distal pachytene zone. Insets are enlarged details of the regions indicated. By the end of the pachytene zone, SC formation in some nuclei is quite extensive, as is evident from the formation of long SYP-1 lines, but incomplete (arrows denote DAPI-positive chromatin regions devoid of SYP-1). (For blow up images of corresponding regions of the wild-type gonad, see Supplemental Figure S4.) (b) REC-8 in the extended meiotic entry zone (left) and the pachytene zone (right) of the *prom-1* Δ mutant showing increasing formation of linear structures. (c) HIM-3 in the extended meiotic entry zone (left) where it only forms spots, and the pachytene zone (right) where in some nuclei thick HIM-3 lines suggest the presence of synapsed regions in the *prom-1* Δ mutant. Bar, 5 μ m (b, c, and insets in a are shown at the same magnification).



F54D5.9 protein caused >90% embryonic lethality, but it did not further reduce the frequency of bivalents (data not shown), indicating that the two genes do not function redundantly in meiotic progression. Because reverse transcription-PCR showed a transcript of the remaining open reading frame in the *prom-1(ok1140)* mutant, there exists the possibility that the mutant expresses low levels of a severely truncated product which could exert some residual function and perhaps cause variable expression of the mutant phenotype. We, therefore, studied the consequence of halving its dosage in a *prom-1(ok1140) prom-1(qDf8)* heterozygote. *qDf8* is a deletion from position 1.14–4.67 cM on chromosome I, which encompasses the *prom-1* locus. Bivalent formation was still highly variable and not significantly different (*t* test, $p > 0.05$) from the homozygous mutant (Figure 4b).

Because bivalent formation was reduced in the female germline of the *prom-1* Δ mutant, we wanted to compare it to the crossover frequency in female meioses. Recombination frequencies calculated from rare viable offspring may be biased due to the preferential survival of embryos derived from germ cells in which crossing over was highest and hence faithful segregation of most chromosomes was ensured. Recombination was, therefore, assayed using freshly laid embryos by scoring for the production of recombinant progeny of parents carrying SNPs. To this end, we crossed *prom-1* $\Delta/prom-1$ Δ hermaphrodites heterozygous for two

SNP markers on chromosome V to *prom-1+/prom-1+* males homozygous for both SNP loci. (Mating was confirmed by PCR testing the presence of a paternal GFP marker or a wild-type copy of *prom-1* in the embryos; see *Materials and Methods*). All recombination scored in this experiment must have taken place in the ovaries of *prom-1* Δ mothers. The frequency of recombination was calculated by counting the fraction of embryos where a recombination event caused homozygosity of one of the two SNP markers in the progeny (Table 1; Supplemental Figure S5). The control experiment was done with *prom-1+/prom-1+* hermaphrodites. The reduction in recombination in *prom-1* Δ female meiosis to ~32% of the wild type corresponds reasonably well with the reduction in chromosome V bivalent formation, with bivalents found in 24% of diakinesis nuclei (see below).

Reduced Homologous Pairing and Nonhomologous Synapsis in the *prom-1* Δ Mutant

Univalent formation during diakinesis can be caused by defects in 1) homologous chromosome pairing, 2) chromosome synapsis, 3) recombination, and/or in 4) chiasmata maintenance. We performed experiments to assess for potential defects in these processes in *prom-1* Δ .

To quantify homologous pairing, we highlighted homologous chromosomal loci by FISH (Figure 4, c and d) with probes corresponding to loci near the left end of chromo-

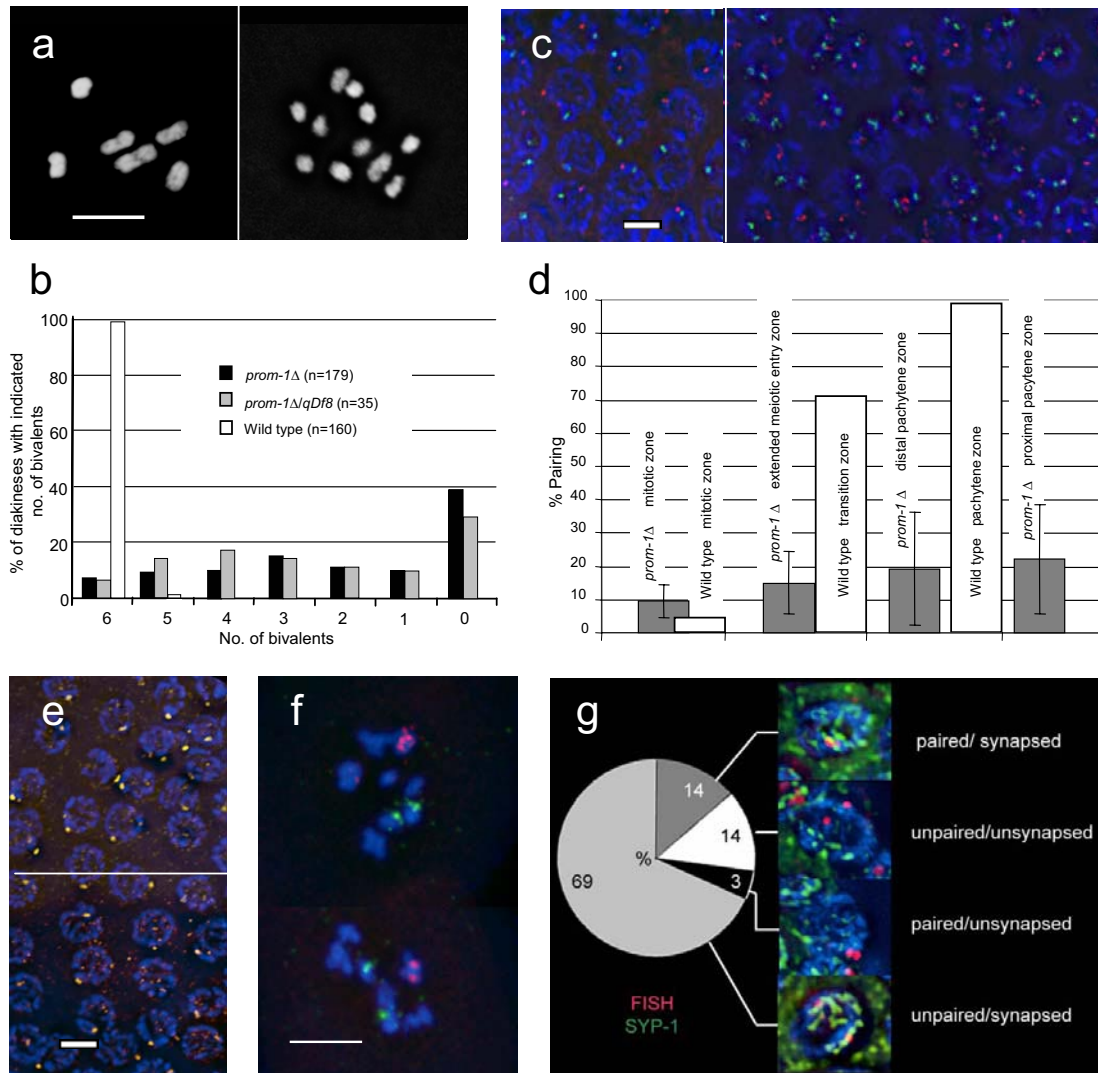


Figure 4. Reduced homologous pairing and bivalent formation in the *prom-1Δ* mutant. (a) A variable number of univalents is formed in the *prom-1Δ* mutant. Although six bivalents are formed in diakinesis in the wild type (left), univalents are abundant in the mutant. In this particular *prom-1Δ* mutant cell (right), 10 univalents and one bivalent are present (DAPI staining). (b) Bivalent frequencies in *prom-1Δ* mutant, *prom-1Δ/qDf8* heterozygous, and wild-type diakineses. Shown is the percentage of diakinesis nuclei with the number of bivalents indicated. n = number of diakineses scored. (c and d) Homologous pairing was tested by FISH of a locus near the left end of chromosome I (Cy3, red) and of the 5S rDNA region on the right arm of chromosome V (FITC, green). (c) In the pachytene zone of the wild type (left), a single signal or a closely associated pair of signals is mostly observed for both loci. In the pachytene zone of the *prom-1Δ* mutant (right), homologous loci on autosomes remain mostly unpaired. (d) Homologous pairing frequencies of the rDNA locus in different zones of the wild-type and *prom-1Δ* gonads as indicated by the association of FISH signals. The percentages of nuclei with paired loci (represented by a single dot or two dots touching each other) are shown. The raw data for this figure are given in Supplemental Table S6. (e) Immunostaining of the X chromosome-associated protein HIM-8 (orange) produces mostly a single signal in wild-type (top) and in *prom-1Δ* mutant (bottom) pachytene. (f) Examples of *prom-1Δ* mutant diakinesis nuclei with X chromosomes (red, FISH signal) and chromosomes V (green, FISH signal). The X chromosomes are more often involved in bivalent formation (as indicated by signals sharing a DAPI-positive entity) than the autosomes (see text). (g) Frequencies of homologous pairing and synapsis of the 5S rDNA locus determined by simultaneous FISH and SYP-1 staining. This experiment shows that most of the time synapsis is nonhomologous. Bars, 5 μ m.

some I and the right end of chromosome V. In the wild type, there was almost no association of homologous FISH signals in the mitotic zone, but 72 and 99% of FISH signal doublets were homologously associated in the transition zone and pachytene zones, respectively (Figure 4d and Supplemental Table S6). In the mutant, we evaluated the frequencies of associated FISH signals in the mitotic zone, in the extended meiotic entry zone, in the distal pachytene zone just proximal to the extended meiotic entry zone, and in the proximal pachytene zone just proximal to the first diplotene nuclei.

Homologous pairing of autosomes was found to vary considerably between gonads, but it was, in general, reduced compared with the wild type (Figure 4d and Supplemental Table S6). *C. elegans* chromosomes possess a pairing center near one end that has been implicated in the maintenance of pairing and promotion of SC formation (McKim, 2005). We did not observe an obvious difference in the pairing of a chromosome region near the pairing center (5S rDNA locus) and a region at the left end of chromosome I which is distant from it (data not shown).

Table 1. Recombination frequencies observed on embryos between SNP markers in cosmids F36H9 and Y51A2A on chromosome V

	No. of recombinants	No. of embryos tested	%
<i>prom-1Δ</i>	9	65	13.8
Wild type	48	112	42.8

The number of recombinants corresponds to the number of embryos homozygous for the wild-type (Bristol) or the Hawaiian SNP pattern on either side of the interval.

Next, we studied the pairing of X chromosomes by immunostaining of the HIM-8 protein that is associated with the pairing centers on the X chromosomes (Phillips *et al.*, 2005) (Figure 4e). We scored the association of HIM-8 foci in a total of 350 nuclei (in 6 different gonads) from the proximal pachytene zone. In 69% of *prom-1Δ* nuclei, we found a single focus or two associated foci (WT control: 99% single or associated; $n = 208$), suggesting that the pairing of X chromosomes is affected to a lesser degree than that of autosomes. Likewise, when we determined bivalent formation in diakinesis for specific chromosomes by FISH (Figure 4f), it turned out that the X chromosomes were involved in bivalent formation more often than the autosomes. X chromosome bivalents were found in 74% of the nuclei ($n = 38$), whereas chromosome V bivalents were present in only 24% of the nuclei ($n = 21$).

Because SYP-1 thread formation indicated extensive synapsis, whereas the association of homologous FISH signals was limited, we tested to which extent synapsis in the *prom-1Δ* mutant was homologous. To this end, simultaneous FISH of 5S rDNA loci on chromosome V and SYP-1 immunostaining were performed (compare Couteau *et al.*, 2004). In the wild type, paired loci were associated with SYP-1 (i.e., synapsed) tracts in 73 of 74 nuclei scored. In the *prom-1Δ* mutant, however, one or both unpaired homologous loci were associated with SYP-1 tracts in 69% of the nuclei ($n = 213$ pachytene nuclei from 7 different gonads), indicating that they were synapsed with a nonhomologous region (Figure 4g). This suggests that nonhomologous synapsis is extensive in the *prom-1Δ* mutant.

Defective DSB Processing in the *prom-1Δ* Mutant

The recombination protein, RAD-51, assembles at sites of meiotic DSBs (Shinohara *et al.*, 1992), and immunostaining of RAD-51 produces foci in late zygotene to midpachytene nuclei, just proximal to the transition zone in wild-type *C. elegans* meiosis (Alpi *et al.*, 2003; Colaiácovo *et al.*, 2003). In the *prom-1Δ* mutant, RAD-51 foci appeared near the beginning of the pachytene zone and they did not disappear before diplotene (Figure 5). Moreover, their number greatly increased toward the end of the pachytene zone. The mean number of foci in nuclei within the RAD-51-positive region of the *prom-1Δ* mutant was 22.0 ± 10.0 ($n = 234$ nuclei from 7 different gonads), whereas in the wild type this number was only 6.0 ± 3.5 ($n = 263$ nuclei from 5 different gonads). We cannot exclude the possibility that more DSBs than in the wild type are formed in the first place, but the persistence of RAD-51 foci suggests that DSBs may be formed normally but accumulate because of their delayed repair in the absence of PROM-1. Moreover, the ~ 4 times increased mean number of RAD-51 foci is comparable with other mutants where the repair of DSBs is delayed or abolished (Alpi *et al.*, 2003; Colaiácovo *et al.*, 2003).

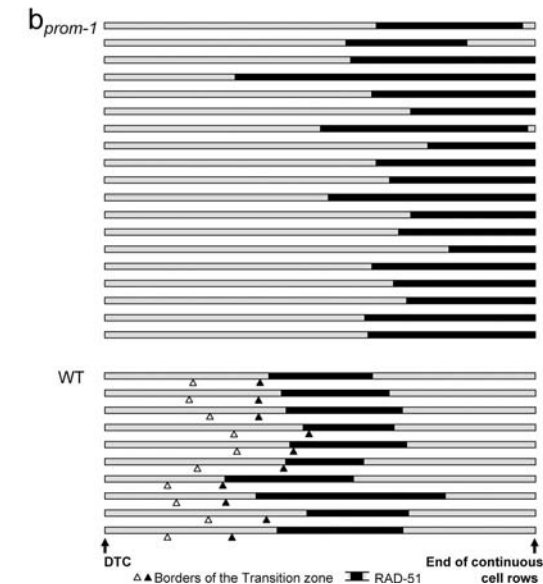
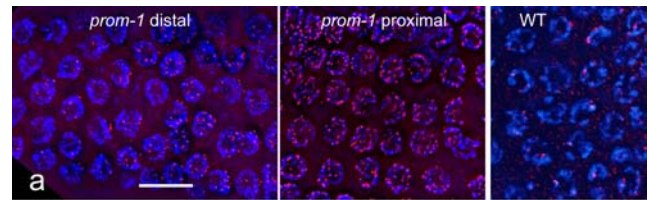


Figure 5. The abundance and distribution of recombination sites visualized by immunostaining of RAD-51. (a) RAD-51 foci (red) in the *prom-1Δ* mutant and wild-type (WT) animals. For the *prom-1Δ* mutant, the distal and the proximal border of a RAD-51-positive region are shown, where RAD-51 foci appear and are most abundant, respectively. In the wild type, there is not very much variation in the number of RAD-51 foci along the RAD-51-positive region of which a representative section is shown. (b) The position and extent of the RAD-51-positive region (black bars) in the gonads (shaded bars) of *prom-1Δ* mutant and wild-type (WT) animals. Gonads were measured from the DTC to the end of continuous cell rows (roughly coinciding with the end of the pachytene zone) and normalized, and the borders of the RAD-51-positive region were entered. This region is striking due to the abundance of RAD-51 foci. In quantitative terms, it is defined as the zone in which $>90\%$ of nuclei have more than two prominent foci by RAD-51 immunostaining. The open and solid arrowheads indicate the distal and proximal borders of the transition zone of the wild type, respectively (for a classification of meiotic stages in the gonad; see MacQueen *et al.*, 2002), whereas the transition zone is absent from the *prom-1Δ* mutant gonads. Bar, 10 μm .

prom-1 Acts Earlier Than *htp-1*

prom-1 mutants resemble *htp-1* mutants with respect to nonhomologous synapsis, with the difference that *htp-1* loads SC components prematurely (Couteau and Zetka, 2005; Martinez-Perez and Villeneuve, 2005). We produced a *prom-1Δ htp-1* double mutant to study the genetic interaction between *prom-1* and *htp-1*. REC-8 staining highlighted the aggregations of SC proteins typical for the extended meiotic entry zone (Figure 6). In the *prom-1Δ htp-1* double mutant, the extended meiotic entry zone of *prom-1Δ* was still present. This means that the delayed entry into zygotene cannot be suppressed by inducing premature synapsis in the *htp-1* mutant, and it confirms that *prom-1* acts early in the leptotene/zygotene commitment upstream of *htp-1*. The scattered transition zone-like nuclei found in the pachytene zone of *prom-1Δ* were missing (Figure 6) and only univalents were



Figure 6. Analysis of the epistatic relationship between *prom-1* and *htp-1*. Dissected *prom-1*, *htp-1* and *prom-1 htp-1* gonads are shown. MZ, mitotic zone; TZ, transition zone; MEZ, meiotic entry zone; PZ, pachytene zone. In the *prom-1* mutant, a transition zone is missing, but there is an extended meiotic entry zone. This zone is characterized by the expression of SC proteins, but they do not organize into axial elements but form nuclear spots, such as seen here for REC-8. In the pachytene zone axial elements and SCs do form but some of the spots remain. The pachytene zone is interspersed with nuclei with chromatin arranged in a crescent shape. In the *htp-1* mutant, there is onset of axial element formation and precocious synapsis immediately downstream of a narrow and poorly developed transition zone. There are no nuclei with crescent-shaped chromatin in the pachytene zone. In the *prom-1 htp-1* double mutant, the extended meiotic entry zone is present and spots of SC proteins remain in pachytene. Nuclei with crescent-shaped chromatin are no longer found.

formed during diakinesis of the double mutant. This supports our assumption that the limited homologous pairing observed in *prom-1Δ* is initiated in these transition zone-like nuclei.

DISCUSSION

prom-1Δ Mutants Display a Complex Meiotic Phenotype

The *prom-1Δ* mutation causes aberrant meiotic progression in the ovary. Following the mitotic zone of the gonad, there was an elongated tract of cells (an expanded meiotic entry zone) in which cells were transiently arrested right after entry into the meiotic pathway. These cells had completed mitotic and presumably also premeiotic DNA synthesis, and they expressed the meiosis-specific structural proteins HIM-3 and SYP-1. A transition zone with cells synchronously initiating chromosome pairing was missing, instead, the presence of transition zone-like nuclei in the proximal region of the gonad seems to reflect asynchronous and retarded onset of homology search. Homologous pairing and synapsis were reduced and the number of RAD-51 foci was increased, indicating that the repair of DSBs was abnormal.

The increased incidence of apoptotic germline cells and the reduced brood size suggest that in *prom-1* mutants a substantial portion of faulty pachytene nuclei is discarded.

By the very end of the pachytene zone the RAD-51 foci disappeared (Figure 5). This, together with the fact that ~10% of embryos are viable, suggests that although the repair of DSBs was delayed, it must eventually have taken place efficiently. It has been proposed that DSB repair via the sister chromatid becomes possible at the pachytene–diplotene transition once a barrier (possibly created by lateral elements) has disappeared (Colaiácovo *et al.*, 2003). Therefore, it is possible that in the *prom-1Δ* mutant where chiasma formation and recombination are reduced to about one third of the frequency in the wild type, most of the repair occurs via the sister chromatid.

A remarkable feature of the *prom-1* mutants, including the deletion mutant, was the extreme variability of phenotypes between individuals with respect to brood size and the viability of their offspring, between gonads with respect to homologous pairing, and between the cells of a gonad with respect to bivalent formation. All these parameters were evaluated under controlled conditions and in descendants from homozygous *prom-1Δ* mothers to avoid a possible maternal rescue as a source of variability. (In fact, the viability of embryos laid by homozygous *prom-1Δ* hermaphrodites, which directly derived from heterozygous mothers was notably higher (21% of laid eggs; $n = 1813$), which suggests some maternal rescue in the first generation.) The tested parameters continued to vary among later descendants with no obvious tendency to recapitulate high or low brood size, hatch rate, pairing, or bivalent formation of their mothers (data not shown). We do not have at present an explanation for the variable expressivity of the mutant genotype.

PROM-1 Has a Role in Meiotic Chromosome Pairing

In *prom-1Δ* hermaphrodites, homologous pairing was reduced and only few nuclei with crescent chromatin arrangement indicative of initial chromosome pairing were scattered in the pachytene zone of the gonad. Thus, PROM-1 adds to the list of proteins that have been identified as essential regulators of the establishment of initial pairing in *C. elegans*. The protein kinase CHK-2, for example, promotes homologous pairing (MacQueen and Villeneuve, 2001). In contrast to *prom-1Δ* however, absence of CHK-2 also inhibits SC formation, suggesting that the CHK-2 kinase is not directly involved in homology search and recognition but rather plays a central role as a more upstream regulator of meiosis, which allows it to govern both homology recognition and SC formation, which are two independent processes in *C. elegans*. Also, deletion of *him-3*, which encodes a meiosis-specific axial element protein causes a pairing defect (Couteau *et al.*, 2004). It is, therefore, conceivable that chromosomal axis components have to be loaded and/or modified in time to establish a chromosomal organization, which supports homology search. HTP-1 is another protein with a role in initial chromosome pairing. It was shown that in addition to its more prominent function in coordinating pairing with SC formation, HTP-1 contributes to pairing because in a *htp-1 syp-2* double mutant initial homologous alignment is reduced compared with a *syp-2* mutant in which alignment occurs but is not enforced by synapsis (Martinez-Perez and Villeneuve, 2005).

Recently, the chromosome binding ZIM proteins (ZIM-1, -2, and -3 and HIM-8) were identified as factors that facilitate homologous contacts and SC formation. Because individual ZIM proteins are responsible for the pairing of more than one chromosome pair, it is unlikely that the ZIM proteins

confer the specificity for the recognition of homologous chromosomes (Phillips and Dernburg, 2006). Together with the ZIM proteins, SUN-1 and ZYG-12 seem to impose a certain chromosomal arrangement within the nucleus as a precondition for pairing (Penkner *et al.*, 2007). It remains to be shown how PROM-1 interacts with the mentioned factors to ensure the encounter of homologues or its manifestation as homologous alignment.

Coordinated Meiotic Entry Is Essential for Downstream Meiotic Events

In the wild type, only few cells of the hermaphrodite gonad pass through the meiotic entry zone at any given time. Hence, the older literature failed to recognize the meiotic nature of the cells immediately upstream of the transition zone and assigned them to the "mitotic zone." Only more recent accounts (MacQueen *et al.*, 2002; Hansen *et al.*, 2004; Crittenden *et al.*, 2006) associate these cells with early meiotic prophase. The lack of informative mutants aggravated detailed analysis of nuclei at this stage. To date, only the protein kinase CHK-2 was ascribed functions already at very early steps in meiosis that are crucial for downstream meiotic events culminating in faithful chromosome segregation (MacQueen and Villeneuve, 2001).

Germ cells of *prom-1Δ* mutants readily proceed through mitosis and premeiotic DNA replication. Although they are competent for timely entering the meiotic program as judged by the expression of meiosis-specific proteins, *prom-1Δ* nuclei display a pronounced delay in the meiotic entry stage resulting in a dramatic extension of this zone. Once *prom-1* nuclei have passed the meiotic entry zone, axial and central components of the SC are loaded and chromosome condensation, homologous interactions, and recombination are initiated asynchronously, consistent with the lack of a distinct transition zone. As a consequence, *prom-1* mutants undergo extensive nonhomologous synapsis, a feature shared with the weak *him-3(vv6)* and the *htp-1* null mutants (Couteau *et al.*, 2004; Couteau and Zetka, 2005; Martinez-Perez and Villeneuve, 2005). In cases (such as in haploids) where homologous chromosomes are not available but where the SC machinery is intact, it has been observed that the failure to find a homologous partner leads to indiscriminate nonhomologous synapsis (Loidl and Jones, 1986; Loidl, 1994). We think that SC polymerization along chromosomes is a default process that can readily involve nonhomologous chromosomes if homologous alignment has not been achieved by the time SC development starts (Loidl, 1991). Thus, HTP-1 and HIM-3 prevent nonhomologous synapsis, because they may sufficiently delay the onset of synapsis or otherwise coordinate alignment and synapsis to ensure that only prealigned homologues will synapse (Couteau and Zetka, 2005; Martinez-Perez and Villeneuve, 2005). Although untimely synapsis in the *htp-1* and *him-3* mutants precedes the homologous pairing step, synapsis is delayed in the *prom-1Δ* mutant. The *prom-1Δ htp-1Δ* double mutant shows the Prom-1 delayed synapsis phenotype, which indicates that the early onset nonhomologous synapsis in the *htp-1Δ* mutant requires PROM-1.

A notable difference between the *prom-1Δ* and the *htp-1* mutant is that in the latter RAD-51 foci do not accumulate. Whereas in the *prom-1Δ* mutant, a possible alternative DSB repair via the sister might be implemented only at the pachytene–diplotene transition after the axial elements become disassembled (see above), in the *htp-1* (and in the *him-3* null) mutant, the sister chromatid may be efficiently used for DSB repair in pachytene (Martinez-Perez and Villeneuve, 2005).

It is worth mentioning that bivalent formation of the X chromosomes is less affected compared with the autosomes in the *prom-1* mutant. This behavior of the X resembles the one in weak *him-3* mutants (Couteau *et al.*, 2004; Nabeshima *et al.*, 2004) and in the *htp-1* null mutant (Couteau and Zetka, 2005; Martinez-Perez and Villeneuve, 2005), and it suggests redundant or less susceptible pathways ensuring X chromosome pairing. A different regulation of X chromosome pairing is also revealed by the fact that the concentration at the nuclear envelope of the X chromosome specific pairing protein HIM-8 is independent of CHK-2, whereas the behavior of its autosomal counterparts is affected in a *chk-2* mutant (Phillips and Dernburg, 2006).

PROM-1 May Play a Role in the Ubiquitination of a Meiotic Regulator

Many F-box proteins have been implicated to act as the substrate-recognizing component of Skp1-Cullin-F-box protein ubiquitin–protein ligase complexes (e.g., Schulman *et al.*, 2000; Hochstrasser, 2002). PROM-1 contains an F-box-like motif, and it is possible that it is involved in ubiquitination. Indeed, components of the ubiquitination pathway have been implicated in meiotic prophase control in various organisms. In budding yeast, meiosis is impaired in mutants of the E2 ubiquitin conjugating enzyme RAD6 (Borts *et al.*, 1986). In mice, loss of ubiquitin-conjugating activity by HR6B, one of the two mammalian RAD6 homologues, results in a damaged SC structure and other meiotic anomalies (Baarends *et al.*, 2003). Likewise, homologous synapsis is impaired by a mutation in the *ASK1* gene of *Arabidopsis*, which encodes a Skp1p homologue (Wang *et al.*, 2004). In *C. elegans*, depletion of Skp-related proteins 1 and 2 results in univalent formation at diakinesis (Nayak *et al.*, 2002), as does depletion of CUL-1 (cullin) (our preliminary data). A mutation in *cul-1* was previously shown to cause hyperplasia of all tissues (Kipreos *et al.*, 1996). Thus, the pairing defect displayed by *C. elegans prom-1Δ* mutant animals could well be explained by a defect in ubiquitin-dependent degradation of one or several meiotic regulators yet to be identified.

ACKNOWLEDGMENTS

We are indebted to Michael Hengartner (University of Zurich) in whose laboratory the *op240* allele was initially isolated. Materials were generously provided by Abby Dernburg (University of California, Berkeley), Andrew Fire (Stanford University, CA), Adriana La Volpe (Istituto di Genetica, Consiglio Nazionale delle Ricerche, Naples), Jill Schumacher (University of Texas, Houston), Anne Villeneuve (Stanford University, CA), and Monique Zetka (McGill University, Montreal). We thank the *C. elegans* Gene Knockout Consortium for the deletion allele *ok1140* and the *C. elegans* Genetic Center (University of Minnesota) for strains. We are grateful to Michael Jantsch (University of Vienna), Maria Novatchkova (Research Institute of Molecular Pathology, Vienna), and Maria Siomos (Gregor Mendel Institute, Vienna) for valuable suggestions and to Christian Pflügl for technical assistance. This work was supported by grant P-17329 of the Austrian Science Fund (Fonds zur Förderung der wissenschaftlichen Forschung), by a WWTF (Wiener Wissenschafts-, Forschungs- und Technologiefonds) grant (to V.J.), by a Cancer Research UK career development award (to A.G.), and by National Institutes of Health grant GM-063310 (to T.S.).

REFERENCES

- Alpi, A., Pasierbek, P., Gartner, A., and Loidl, J. (2003). Genetic and cytological characterization of the recombination protein RAD-51 in *Caenorhabditis elegans*. *Chromosoma* 112, 6–16.
- Baarends, W. M., Wassenaar, E., Hoogerbrugge, J. W., van Cappellen, G., Roest, H. P., Vreeburg, J., Ooms, M., Hoeyjmakers, J.H.J., and Grootegoed, J. A. (2003). Loss of HR6B ubiquitin-conjugating activity results in damaged synaptonemal complex structure and increased crossing-over frequency during the male meiotic prophase. *Mol. Cell Biol.* 23, 1151–1162.

- Bhalla, N., and Dernburg, A. F. (2005). A conserved checkpoint monitors meiotic chromosome synapsis in *Caenorhabditis elegans*. *Science* 310, 1683–1686.
- Borts, R. H., Lichten, M., and Haber, J. E. (1986). Analysis of meiosis-defective mutations in yeast by physical monitoring of recombination. *Genetics* 113, 551–567.
- Brenner, S. (1974). The genetics of *Caenorhabditis elegans*. *Genetics* 77, 71–94.
- Colaiácovo, M. P., MacQueen, A. J., Martinez-Perez, E., McDonald, K., Adamo, A., La Volpe, A., and Villeneuve, A. M. (2003). Synaptonemal complex assembly in *C. elegans* is dispensable for loading strand-exchange proteins but critical for proper completion of recombination. *Dev. Cell* 5, 463–474.
- Couteau, F., Nabeshima, K., Villeneuve, A., and Zetka, M. (2004). A component of *C. elegans* meiotic chromosome axes at the interface of homolog alignment, synapsis, nuclear reorganization, and recombination. *Curr. Biol.* 14, 585–592.
- Couteau, F., and Zetka, M. (2005). HTP-1 coordinates synaptonemal complex assembly with homolog alignment during meiosis in *C. elegans*. *Genes Dev.* 19, 2744–2756.
- Crittenden, S. L., Leonhard, K. A., Byrd, D. T., and Kimble, J. (2006). Cellular analyses of the mitotic region in the *Caenorhabditis elegans* adult germ line. *Mol. Biol. Cell* 17, 3051–3061.
- Dernburg, A. F., McDonald, K., Moulder, G., Barstead, R., Dresser, M., and Villeneuve, A. M. (1998). Meiotic recombination in *C. elegans* initiates by a conserved mechanism and is dispensable for homologous chromosome synapsis. *Cell* 94, 387–398.
- Felsenstein, J. (1989). PHYLIP: phylogeny inference package (version 3.2). *Cladistics* 5, 164–166.
- Gartner, A., MacQueen, A. J., and Villeneuve, A. M. (2004). Methods for analyzing checkpoint responses in *Caenorhabditis elegans*. *Methods Mol. Biol.* 280, 257–274.
- Gartner, A., Milstein, S., Ahmed, S., Hodgkin, J., and Hengartner, M. O. (2000). A conserved checkpoint pathway mediates DNA damage-induced apoptosis and cell cycle arrest in *C. elegans*. *Mol. Cell* 5, 435–443.
- Hansen, D., Hubbard, E.J.A., and Schedl, T. (2004). Multi-pathway control of the proliferation versus meiotic development decision in the *Caenorhabditis elegans* germline. *Dev. Biol.* 268, 342–357.
- Harper, J. W., Burton, J. L., and Solomon, M. J. (2002). The anaphase-promoting complex: it's not just for mitosis any more. *Genes Dev.* 16, 2179–2206.
- Henderson, K. A., Kee, K., Maleki, S., Santini, P. A., and Keeney, S. (2006). Cyclin-dependent kinase directly regulates initiation of meiotic recombination. *Cell* 125, 1321–1332.
- Hillers, K. J., and Villeneuve, A. M. (2003). Chromosome-wide control of meiotic crossing over in *C. elegans*. *Curr. Biol.* 13, 1641–1647.
- Hochstrasser, M. (2002). New proteases in a ubiquitin stew. *Science* 298, 250–252.
- Jones, A. R., Francis, R., and Schedl, T. (1996). GLD-1, a cytoplasmic protein essential for oocyte differentiation, shows stage- and sex-specific expression during *Caenorhabditis elegans* germline development. *Dev. Biol.* 180, 165–183.
- Kamath, R. S. *et al.* (2003). Systematic functional analysis of the *Caenorhabditis elegans* genome using RNAi. *Nature* 421, 231–237.
- Kipreos, E. T., Lander, L. E., Wing, J. P., He, W. W., and Hedgecock, E. M. (1996). *cul-1* is required for cell cycle exit in *C. elegans* and identifies a novel gene family. *Cell* 85, 829–839.
- Kipreos, E. T., and Pagano, M. (2000). The F-box protein family. *Genome Biol.* 1, 3002.1–3002.7.
- Loidl, J. (1991). Coming to grips with a complex matter. A multidisciplinary approach to the synaptonemal complex. *Chromosoma* 100, 289–292.
- Loidl, J. (1994). Cytological aspects of meiotic recombination. *Experientia* 50, 285–294.
- Loidl, J., and Jones, G. H. (1986). Synaptonemal complex spreading in *Allium*. I. Triploid *A. sphaerocephalon*. *Chromosoma* 93, 420–428.
- MacQueen, A. J., Colaiácovo, M. P., McDonald, K., and Villeneuve, A. M. (2002). Synapsis-dependent and -independent mechanisms stabilize homolog pairing during meiotic prophase in *C. elegans*. *Genes Dev.* 16, 2428–2442.
- MacQueen, A. J., and Villeneuve, A. M. (2001). Nuclear reorganization and homologous chromosome pairing during meiotic prophase require *C. elegans* *chk-2*. *Genes Dev.* 15, 1674–1687.
- Martinez-Perez, E., and Villeneuve, A. M. (2005). HTP-1-dependent constraints coordinate homolog pairing and synapsis and promote chiasma formation during *C. elegans* meiosis. *Genes Dev.* 19, 2727–2743.
- McKim, K. S. (2005). When size does not matter: pairing sites during meiosis. *Cell* 123, 989–992.
- Mello, C. C., Kramer, J. M., Stinchcomb, D., and Ambros, V. (1991). Efficient gene transfer in *C. elegans*: extrachromosomal maintenance and integration of transforming sequences. *EMBO J.* 10, 3959–3970.
- Nabeshima, K., Villeneuve, A. M., and Hillers, K. J. (2004). Chromosome-wide regulation of meiotic crossover formation in *Caenorhabditis elegans* requires properly assembled chromosome axes. *Genetics* 168, 1275–1292.
- Nayak, S., Santiago, F. E., Jin, H., Lin, D., Schedl, T., and Kipreos, E. T. (2002). The *Caenorhabditis elegans* Skp1-related gene family: diverse functions in cell proliferation, morphogenesis, and meiosis. *Curr. Biol.* 12, 277–287.
- Pasierbek, P., Jantsch, M., Melcher, M., Schleiffer, A., Schweizer, D., and Loidl, J. (2001). A *Caenorhabditis elegans* cohesion protein with functions in meiotic chromosome pairing and disjunction. *Genes Dev.* 15, 1349–1360.
- Penkner, A., Tang, L., Novatchkova, M., Ladurner, M., Fridkin, A., Gruenbaum, Y., Schweizer, D., Loidl, J., and Jantsch, V. (2007). The nuclear envelope protein *matefin/SUN-1* is required for homologous pairing in *C. elegans* meiosis. *Dev. Cell* 12, 873–885.
- Petronczki, M., Siomos, M. F., and Nasmyth, K. (2003). Un ménage à quatre: the molecular biology of chromosome segregation in meiosis. *Cell* 112, 423–440.
- Phillips, C. M., and Dernburg, A. F. (2006). A family of zinc-finger proteins is required for chromosome-specific pairing and synapsis during meiosis in *C. elegans*. *Dev. Cell* 11, 817–829.
- Phillips, C. M., Wong, C., Bhalla, N., Carlton, P. M., Weiser, P., Meneely, P. M., and Dernburg, A. F. (2005). HIM-8 binds to the X chromosome pairing center and mediates chromosome-specific meiotic synapsis. *Cell* 123, 1051–1063.
- Piano, F., Schetter, A. J., Morton, D. G., Gunsalus, K. C., Reinke, V., Kim, S. K., and Kempthues, K. J. (2002). Gene clustering based on RNAi phenotypes of ovary-enriched genes in *C. elegans*. *Science* 1959–1964.
- Reinke, V. *et al.* (2000). A global profile of germline gene expression in *C. elegans*. *Mol. Cell* 6, 605–616.
- Rual, J.-F. *et al.* (2004). Toward improving *Caenorhabditis elegans* phenome mapping with an ORFeome-based RNAi library. *Genome Res.* 14, 2162–2168.
- Schedl, T. (1997). *Developmental Genetics of the Germ Line*. In: *C. elegans II*, ed. D. L. Riddle, T. Blumenthal, B. J. Meyer, and J. R. Priess, Plainview, NY: Cold Spring Harbor Laboratory Press, 241–269.
- Schulman, B. A., Carrano, A. C., Jeffrey, P. D., Bowen, Z., Kinnucan, E. R., Finnin, M. S., Elledge, S. J., Harper, J. W., Pagano, M., and Pavletich, N. P. (2000). Insights into SCF ubiquitin ligases from the structure of the Skp1-Skp2 complex. *Nature* 408, 381–386.
- Schumacher, B., Hanazawa, M., Lee, M.-H., Nayak, S., Volkmann, K., Hofmann, R., Hengartner, M., Schedl, T., and Gartner, A. (2005). Translational repression of *C. elegans* p53 by GLD-1 regulates DNA damage-induced apoptosis. *Cell* 120, 357–368.
- Shinohara, A., Ogawa, H., and Ogawa, T. (1992). Rad51 protein involved in repair and recombination in *Saccharomyces cerevisiae* is a RecA-like protein. *Cell* 69, 457–470.
- Simon-Kayser, B., Scoul, C., Renaudin, K., Jezequel, P., Bouchot, O., Rigaud, J., and Bezieau, S. (2005). Molecular cloning and characterization of FBXO47, a novel gene containing an F-box domain, located in the 17q12 band deleted in papillary renal cell carcinoma. *Genes Chromos. Cancer* 43, 83–94.
- Thompson, J. D., Gibson, T. J., Plewniak, F., Jeanmougin, F., and Higgins, D. G. (1997). The ClustalX windows interface: flexible strategies for multiple sequence alignment aided by quality analysis tools. *Nucleic Acids Res.* 25, 4876–4882.
- Timmons, L., Court, D. L., and Fire, A. (2001). Ingestion of bacterially expressed dsRNAs can produce specific and potent genetic interference in *Caenorhabditis elegans*. *Gene* 263, 103–112.
- Wang, Y. X., Wu, H., Liang, G. Q., and Yang, M. (2004). Defects in nucleolar migration and synapsis in male prophase I in the *ask1-1* mutant of *Arabidopsis*. *Sex. Plant Reprod.* 16, 273–282.
- Wicks, S. R., Yeh, R. T., Gish, W. R., Waterston, R. H., and Plasterk, R.H.A. (2001). Rapid gene mapping in *Caenorhabditis elegans* using a high density polymorphism map. *Nat. Genet.* 28, 160–164.
- Zetka, M. C., Kawasaki, I., Strome, S., and Muller, F. (1999). Synapsis and chiasma formation in *Caenorhabditis elegans* require HIM-3, a meiotic chromosome core component that functions in chromosome segregation. *Genes Dev.* 13, 2258–2270.

Chapter 2: Towards a Better Understanding of PROM-1 Function in *C. elegans*

Suppressor screen by EMS mutagenesis

With the aim to isolate interacting partners of PROM-1 I conducted a suppressor screen with the *prom-1(ok1140)* deletion allele. In order to easily follow *prom-1 (ok1140)*, it was linked to *unc-55(e402)*. We performed mutagenesis and the screen, as described in the methods section.

This screen led to the successful isolation of 8 suppressor lines that suppressed embryonic lethality caused by *prom-1(ok1140)*. The suppressor mutation was named *psu* (*prom-1* suppressor). Figure 15 shows the viability of control (*unc-55(e402)*), mutant worms (*prom-1(ok1140) unc-55(e402)*) and suppressor worms (isolated line UV24) (*psu-1(jf76); prom-1(ok1140) unc-55(e402)*).

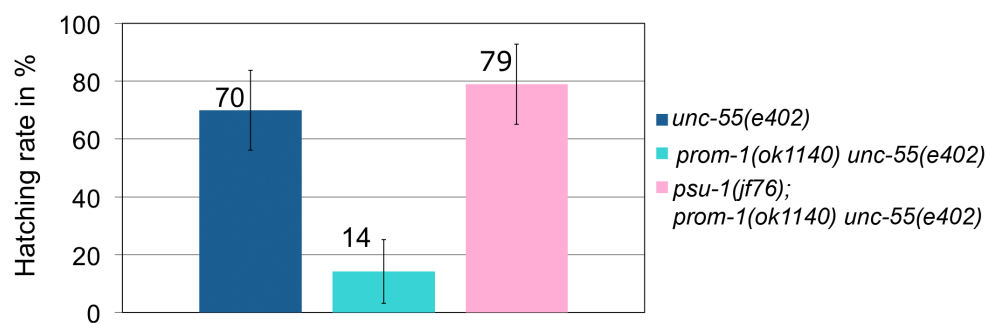


Figure 15. Increased viability of the *psu-1 (jf76)* suppressor line

Hatch rate of *unc-55(e402)* (dark blue), *prom-1(ok1140) unc-55(e402)* (light blue) and *psu-1(jf76), prom-1(ok1140) unc-55(e402)* (pink, suppressor line chosen for further characterization)

We chose the suppressor mutant line with the best viability for further characterization. This strain was named UV24. All of the isolated lines displayed an extended transition zone (TZ) and restored the formation of bivalents at diakinesis (see below). Since our screen was not clonal, it is possible that the suppressor lines are related.

Characterization of the suppressor line UV24

Extended TZ in the *prom-1(ok1140)* suppressor and restoration of bivalents

In the *prom-1(ok1140)* mutant a zone with loosely clustered chromatin follows a very prominent prolonged meiotic entry zone. In the suppressor line a clear TZ is restored, nevertheless the suppressor mutation *psu-1(jf76)* induced an extended TZ in *prom-1(ok1140)* (Figure 16A). I quantified the length of this TZ (Figure 16B) and it is on average 6 cell rows more extended than in the wild type.

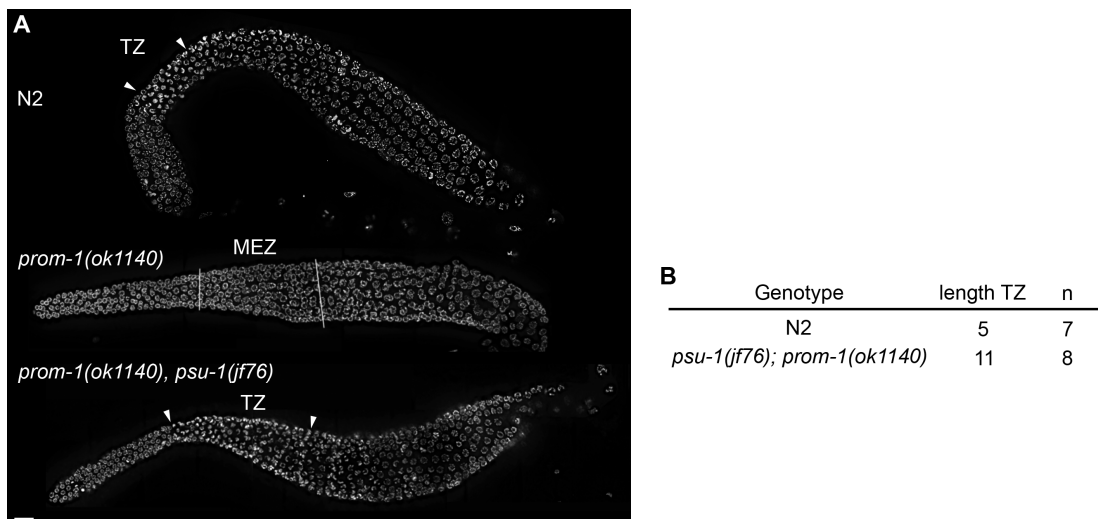


Figure 16. The suppressor of *prom-1* mutation displayed an extended TZ.

A. DAPI staining of gonads for the please insert. Arrows indicate the extension of the TZ and the white line the extended MEZ. Bar: 10 μ m. B. Table with the length of the TZ for wild type (N2) and *psu-1(jf76), prom-1(ok1140)*. n indicated the number of gonads counted.

Next I looked at the diakinesis. In the *prom-1(ok1140) unc-55(e402)* mutant univalents are found (Figure 17, left part), whereas in *psu-1; prom-1(ok1140) unc-55(e402)* the formation of bivalents is restored (Figure 17, right part)

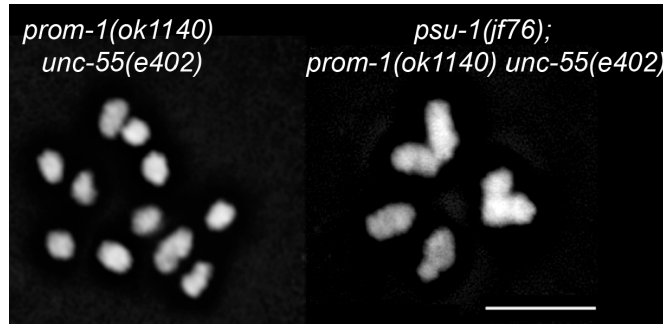


Figure 17. Formation of bivalents is restored in the *prom-1* suppressor line UV24.

High magnification of nuclei at the diakinesis stage. Bar: 5 μ m.

Formation of bivalents was restored in 86% of *psu-1; prom-1(ok1140) unc-55(e402)* gonad whereas 14% of the gonads had univalents (as judged by at least 7-12 DAPI positive configurations). This is in agreement with the high incidence of males (HIM) phenotype still observed in *prom-1(ok1140)* suppressor worms (not quantified).

To summarize, the *psu-1(jf76)* mutation in the *prom-1(ok1140)* background restored the occurrence of the TZ and formation of bivalents at diakinesis which are two features definitely missing in *prom-1(ok1140)* mutant worms.

[psu-1 in prom-1\(ok1140\) restores the loading of chromosome axis and central element SC components.](#)

In *prom-1(ok1140) unc-55(e402)* the loading of chromosomes axis components and the polymerization of the central element proteins of the SC are delayed. In the extended MEZ, chromosome axis and central element proteins of the SC both form polycomplexes before being extended into linear structures in pachytene (Figure 18). In the suppressor line those proteins rather formed polycomplexes in the distal part of the extended TZ. These polycomplexes readily disappeared in the proximal part of the TZ and then chromosome axis and central element of the SC were found extended on chromosomes like in *unc-55(e402)* control (Figure 18). Later on, in pachytene

fully extended stretches of chromosomes axis and central elements of the SC are found in the suppressor line, as seen in *unc-55(e402)* and *prom-1(ok1140)* mutants.

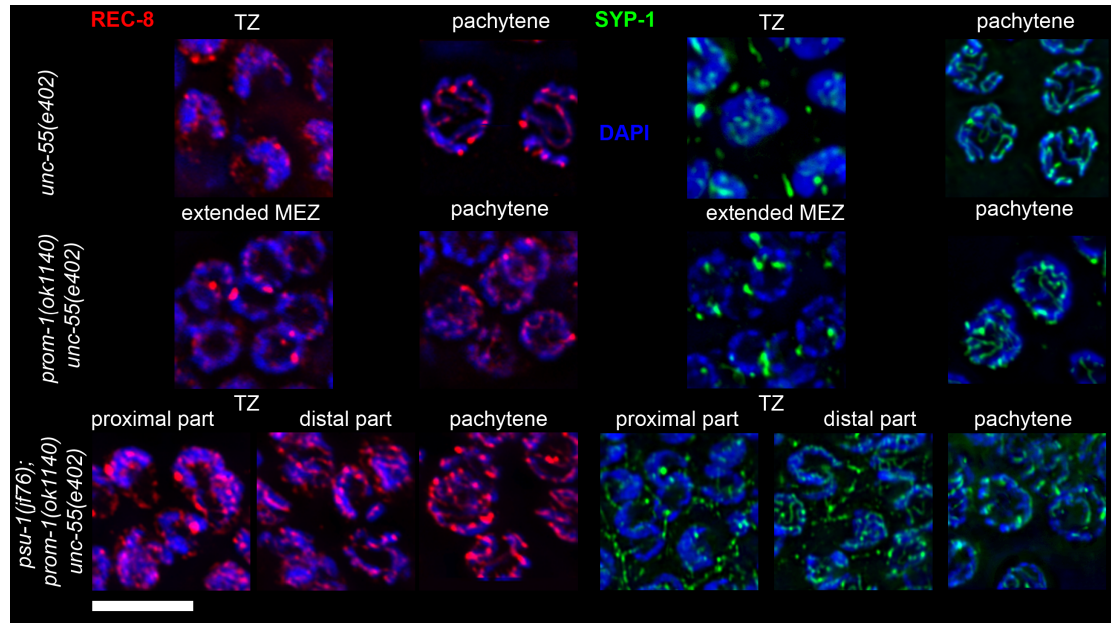


Figure 18. Loading of REC-8 and polymerization of the SC are restored in the suppressor line.

Immunostaining of REC-8 (red) and SYP-1 (green) in *unc-55(e402)*, *prom-1(ok1140) unc-55(e402)* and *psu-1(jf76); prom-1(ok1140) unc-55(e402)*. Pictures were taken from the MEZ, the TZ and pachytene. Bar: 5µm

In the *prom-1(ok1140)* suppressor homologues successfully pair and DSBs are timely repaired

Formation of univalents at the diakinesis can reflect a defect in repairing the programmed DSBs formed by the endonuclease SPO-11 when the homologous chromosome is not paired with its partner. In the suppressor line mostly bivalents are found at diakinesis suggesting that most probably homologues are paired allowing thus the repair of the DSBs via the homologous chromosomes. To control that pairing was effective in the

suppressor line, pairing of homologous chromosomes was assayed by FISH with a probe highlighting the 5S rDNA located on the right arm of chromosome V (Figure 19).

To assess pairing, gonads were subdivided into 6 zones of equal length and in each zone the association of the FISH probes was counted (Figure 19A). In *prom-1(ok1140)* pairing level of homologues did not show any significant increase until zone 3 and in the next zone (4-6) rose to around 50% (Figure 19C). In contrast in *psu-1(jf76); prom-1(ok1140)* pairing was as effective (90% paired signals in zone 6, Figure 19D) as in the wild type (Figure 19B) despite a slight delay (zone 3-5, Figure 19D). In fact the zone where pairing was delayed in the *prom-1* suppressor corresponds to the place where the extended TZ is found.

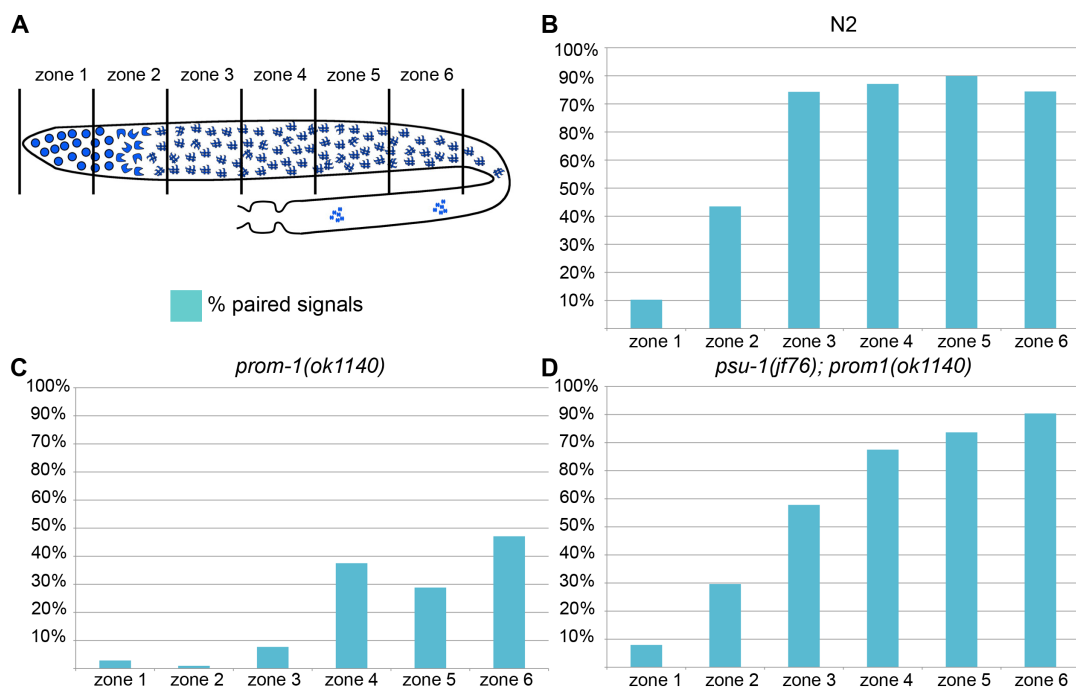


Figure 19. Homologues effectively pair in the suppressor lines.

Gonads were divided in 6 zones of equal lengths (A, upper part) and in each zone the number of paired foci inside a nucleus was scored (A, lower part). This time course was done for wild type (B), *prom-1(ok1140)* (C) and *psu-1(jf76); prom-1(ok1140)* (D). For each zone over 200 nuclei were counted.

As pairing was effective in *psu-1(jf76); prom-1(ok1140)* we would expect that DSB accumulation observed in *prom-1(ok1140)* mutants would be lost in this background. We visualized ongoing repair of DSBs with the strand invasion protein RAD-51 and divided gonads into 6 zones of equal lengths (Figure 20A). In each zone the number of RAD-51 foci/nucleus was scored. Time course revealed that indeed RAD-51 foci do not accumulate in *psu-1(jf76); prom-1(ok1140)* (Figure 20D).

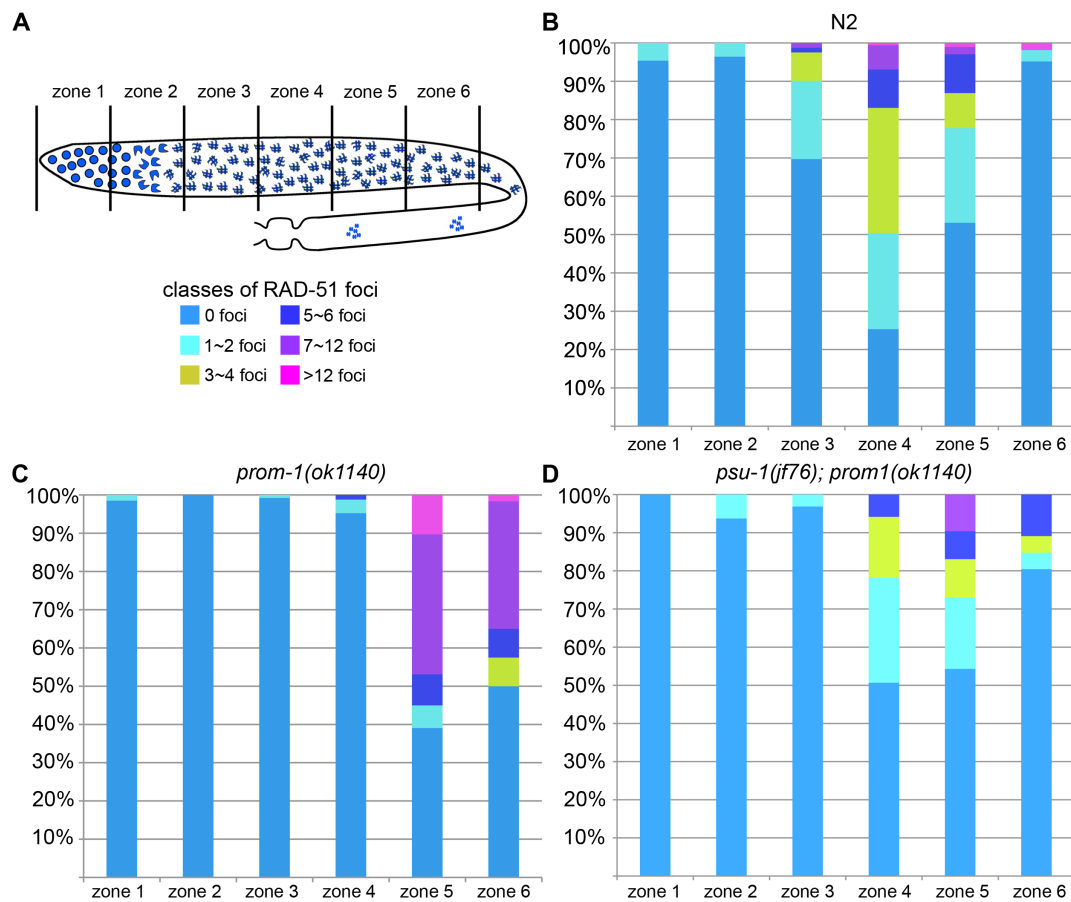


Figure 20. DSB intermediates do not accumulate in the suppressor line.

Gonads were divided into 6 zones of equal lengths (A, upper part) and in each zone the number of RAD-51 foci inside a nucleus was scored and classified (A, lower part). This time course was done for wild type (B), *prom-1(ok1140)* (C) and *psu-1(jf76); prom-1(ok1140)* (D). For each zone over 200 nuclei were counted.

In summary, the suppressor mutation *psu-1(jf76)* restored the non-homologous synapsis observed in *prom-1(ok1140)* to proper synapsis

between the homologues. Synapsis was slightly delayed and pairing is effective. In the suppressor line UV24, repair of DSBs was slightly delayed in comparison to wild type but no accumulation of DSBs was observed as seen in *prom-1(ok1140)*.

Mapping of the suppressor mutation *psu-1(jf76)*

Next I set out to map the suppressor mutation in the UV24 line. I did this with the commonly used SNIP mapping technique (Wicks et al., 2001).

First I tried to cross *psu-1(jf76)* away from the *prom-1* deletion allele. Unfortunately the suppressor did not display a phenotype on its own. Therefore we decided to map the suppressor in the *prom-1* deletion background after confirmation that the suppressor mutant behaved recessively (*psu-1(jf76)/+; prom-1(ok1140) unc-55(e402)* worms have an extended MEZ and univalents at diakinesis, not shown).

The rough mapping was done by pooling lysates and probing them by PCR with SNP primers followed by enzymatic restriction as described (Wicks et al., 2001). As control I used lysates from Hawaiian worms, *prom-1(ok1140) unc-55(e402)* and the siblings of the positive worms from the cross with Hawaiian. Specific primers defining left, centre and right parts of the 6 chromosomes, allowed us to map the suppressor mutation to the left arm of chromosome III (Figure 21). Indeed chromosome III, left arm is the only region where Hawaiian DNA is not present in the suppressor digests (Figure 21, pink rectangle). Note that the loss of Hawaiian DNA in the central part of chromosome I is expected as worms were selected for [Unc-55] (*prom-1(ok1140) unc-55(e402)*) and *prom-1* is located on the central part of chromosome I.

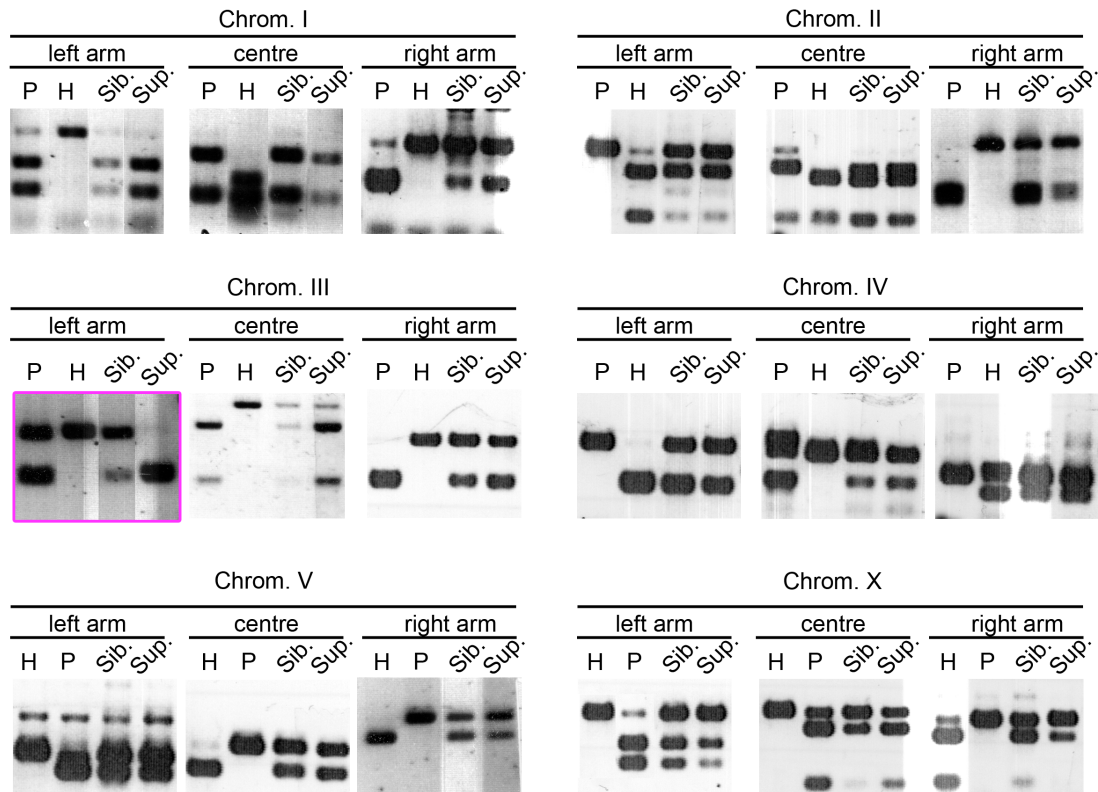


Figure 21. *psu-1(jf76)* is located on chromosome III, left arm.

SNP results of the digested PCR products for *prom-1(ok1140) unc-55(e402)* (P), Hawaiian (H), siblings (Sib.) and *psu-1(jf76); prom-1(ok1140) unc-55(e402)* (Sup.) on the indicated chromosome regions.

Fine mapping was done using single lysates and probing segments 1 to 17 of chromosome III. Repeatedly, we were able to map the suppressor to chromosome III (genomic position: 763,293 ... 804,202) (Figure 22).



Figure 22. Region where the suppressor mutation was mapped with fine mapping.

The candidate region on chromosome III: position: 763,293 ... 804,202), as defined by the loss of the Hawaiian signal in the lysates (violet for lysates from first cross, dark green for lysates from second cross), placing the position of the suppressor into this interval.

Genes present in the candidate region (Figure 23) were amplified, cloned and sequenced. Unfortunately no deviations from the sequence of the starting strain *prom-1 unc55* could be detected.

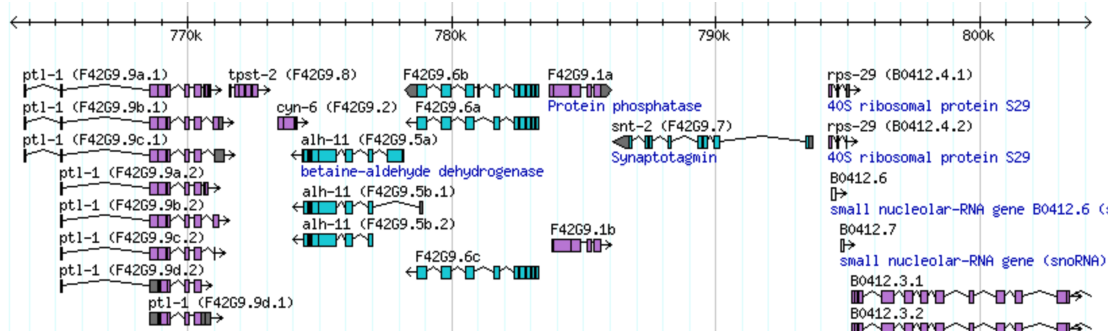


Figure 23. Genes found in III: 763,293 ... 804,202 bp interval.

This region was completely sequenced and revealed no changes in *psu-1(jf76)*; *prom-1(ok1140) unc-55(e402)* DNA sequence when compared to *prom-1(ok1140) unc-55(e402)*.

Therefore, I confirmed the mapping a third time. *psu-1(jf76)*; *prom-1(ok1140) unc-55(e402)* worms were outcrossed 5 more times and from the last outcross *psu-1(jf76)*; *prom-1(ok1140)* and *prom-1(ok1140)* were recovered. Isolated DNA from the out-crossed strains was then sent to Solid sequencing (see methods).

Solid sequencing results revealed that 1778 SNPs existed between the 2 samples. Out of these 1778 SNPs only 45 were found homozygote in the suppressor line. When looking at chromosome III, left no SNPs were homozygous in the region defined by the mapping (III: 763,293 ... 804,202 bp). Therefore we extended the borders and found 2 mutations, which were homozygous (see below). No homozygous SNP was found on chromosome I. The solid sequencing results also included a second table listing small deletions. Only 1 homozygous deletion was found in the middle of the 3rd intron of *cdh-12* in the region defined by fine SNP mapping on chromosome III and its border. On chromosome I, 1 deletion was found in the middle of the 6th intron of the gene *png-1*. As these deletions did not remove any splice sites I continued to focus on the SNP mutation.

The first SNP is a single nucleotide deletion and is at the position III: 691,185. It is located in the last intron of W02B3.7 gene and results in a longer version of the protein (Figure 24).

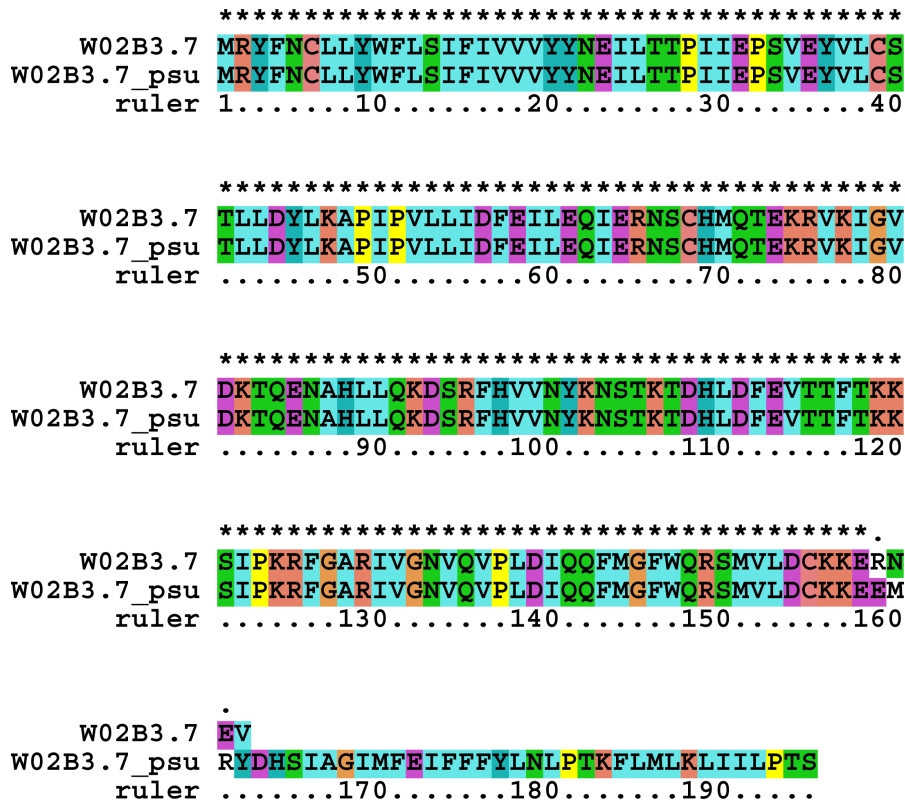


Figure 24. Alignment of W02B3.7 in the suppressor line and the wild type.

In the suppressor line a single base pair deletion in W02B3.7 occurred at position 159 and results in the addition of 35 amino acids.

W02B3.7 is an unknown protein with unknown function. It is predicted to encode an integral membrane protein (Ashburner et al., 2000). No mutant strains are available.

The second SNP is located at III: position 118,298 and is a one-nucleotide deletion (T to -). It is located in the 3rd intron of C29F9.5. This change results in a truncated version of the protein (Figure 25).

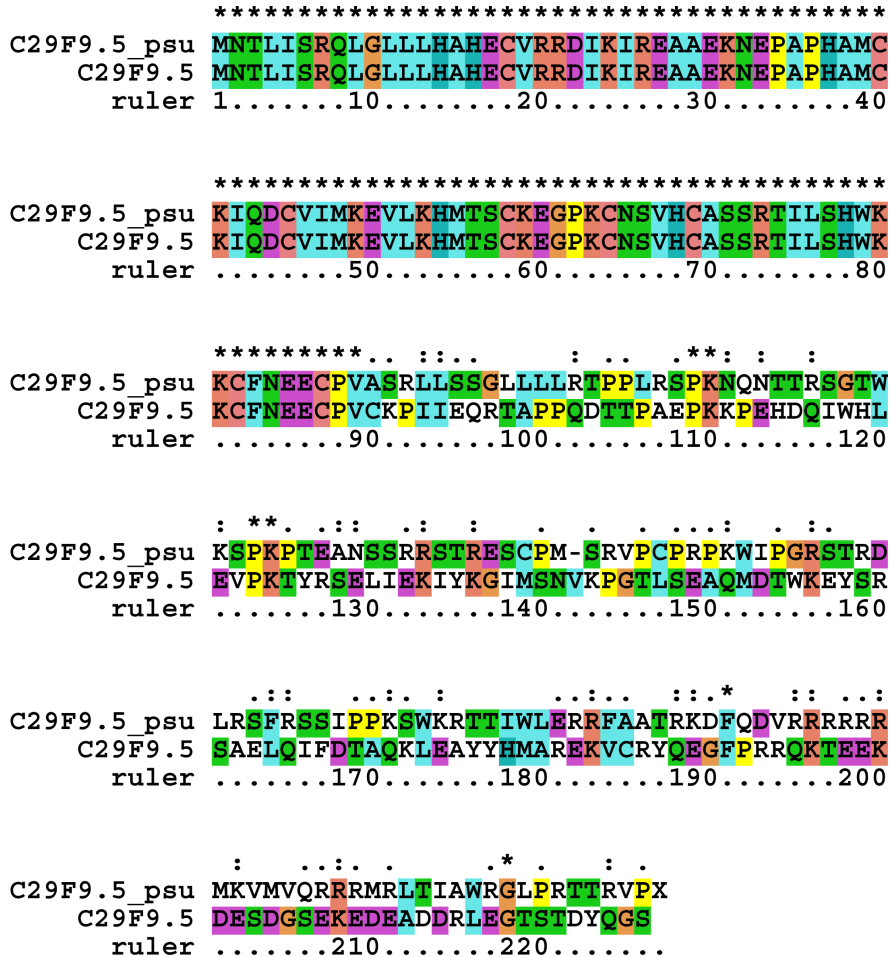


Figure 25. Alignment of C29F9.5 in suppressor line and wild type.

In the suppressor line C29F9.5 is truncated at the position 142 (leading to a change of reading frame at position 90).

C29F9.5 has a Zn-finger domain and is predicted to have histone acetyltransferase activity and to reside in the nucleus (Ashburner et al., 2000). Surprisingly, the Hawaiian strain used for the mapping carries a deletion in the last intron of this gene. This could potentially explain why the last borders of the initial fine mapping were not correct (I did not find any deviations in sequence in that interval, when I compared the starting with the suppressor strain). The deletion in the Hawaiian background, niDF66, includes 4 other genes, which were all free of mutations in the solid sequencing result.

References

Ashburner, M., C.A. Ball, J.A. Blake, D. Botstein, H. Butler, J.M. Cherry, A.P. Davis, K. Dolinski, S.S. Dwight, J.T. Eppig, M.A. Harris, D.P. Hill, L. Issel-Tarver, A. Kasarskis, S. Lewis, J.C. Matese, J.E. Richardson, M. Ringwald, G.M. Rubin, and G. Sherlock. 2000. Gene ontology: tool for the unification of biology. The Gene Ontology Consortium. *In Nature Genetics*. Vol. 25. 25-9.

Wicks, S.R., R.T. Yeh, W.R. Gish, R.H. Waterston, and R.H. Plasterk. 2001. Rapid gene mapping in *Caenorhabditis elegans* using a high density polymorphism map. *In Nat Genet*. Vol. 28. 160-4.

Chapter 3. A *Caenorhabditis elegans* RNA-Directed RNA Polymerase in Sperm Development and Endogenous RNA Interference

A *Caenorhabditis elegans* RNA-Directed RNA Polymerase in Sperm Development and Endogenous RNA Interference

Jonathan I. Gent,* Mara Schvarzstein,[†] Anne M. Villeneuve,*[†] Sam Guoping Gu,[‡] Verena Jantsch,[§] Andrew Z. Fire*^{*,†,1} and Antoine Baudrimont[§]

*Department of Genetics, [†]Department of Developmental Biology, and [‡]Department of Pathology, Stanford University School of Medicine, Stanford, California 94305 and [§]Department of Chromosome Biology, Max F. Perutz Laboratories, University of Vienna, A-1030 Vienna, Austria

Manuscript received September 11, 2009

Accepted for publication October 1, 2009

ABSTRACT

Short interfering RNAs (siRNAs) are a class of regulatory effectors that enforce gene silencing through formation of RNA duplexes. Although progress has been made in identifying the capabilities of siRNAs in silencing foreign RNA and transposable elements, siRNA functions in endogenous gene regulation have remained mysterious. In certain organisms, siRNA biosynthesis involves novel enzymes that act as RNA-directed RNA polymerases (RdRPs). Here we analyze the function of a *Caenorhabditis elegans* RdRP, RRF-3, during spermatogenesis. We found that loss of RRF-3 function resulted in pleiotropic defects in sperm development and that sperm defects led to embryonic lethality. Notably, sperm nuclei in mutants of either *rrf-3* or another component of the siRNA pathway, *eri-1*, were frequently surrounded by ectopic microtubule structures, with spindle abnormalities in a subset of the resulting embryos. Through high-throughput small RNA sequencing, we identified a population of cellular mRNAs from spermatogenic cells that appear to serve as templates for antisense siRNA synthesis. This set of genes includes the majority of genes known to have enriched expression during spermatogenesis, as well as many genes not previously known to be expressed during spermatogenesis. In a subset of these genes, we found that RRF-3 was required for effective siRNA accumulation. These and other data suggest a working model in which a major role of the RRF-3/ERI pathway is to generate siRNAs that set patterns of gene expression through feedback repression of a set of critical targets during spermatogenesis.

REPRESSION of gene expression by small RNAs of ~20–30 nt in length is important for many aspects of multicellular eukaryotic development. A variety of classes of small RNA with distinct structural features, modes of biogenesis, and biological functions have been identified (reviewed in HUTVAGNER and SIMARD 2008). We are particularly interested in a class of small RNAs, called endogenous short interfering RNAs (siRNAs), that are similar to intermediates in exogenously triggered RNA interference (RNAi) in their perfect complementarity to mRNA targets. High-throughput sequencing technology has provided a valuable tool for characterization of endogenous siRNA populations from many diverse sources, including mouse embryonic stem cells (BABIARZ *et al.* 2008), *Drosophila* heads (GHILDIYAL *et al.* 2008), and *Arabidopsis* pollen (SLOTKIN *et al.* 2009). These siRNAs have been proposed to function in the regulation of both cellular processes and genome defense through downregulation of gene

expression. *Caenorhabditis elegans*, like plants and fungi, utilizes RNA-copying enzymes called RNA-directed RNA polymerases (RdRPs) as part of the RNAi machinery (SMARDON *et al.* 2000; SIJEN *et al.* 2001). While two of the *C. elegans* RdRPs are nonessential (RRF-1 and RRF-2), mutations in either of the remaining two (EGO-1 or RRF-3) lead to fertility defects (SMARDON *et al.* 2000; SIMMER *et al.* 2002). RRF-3 is functionally distinct from EGO-1 in that the RRF-3 requirement in fertility is temperature dependent. In addition, RRF-3 activity has an inhibitory effect on exogenously triggered RNAi (resulting in an ERI, or enhanced RNAi, mutant phenotype in *rrf-3* mutants). Mutants lacking either RRF-3 or another ERI factor, ERI-1, have been used as experimental tools because of their enhanced sensitivity in RNAi-based screens. One proposed mechanism for the enhancement in RNAi in *rrf-3* and *eri* mutants has been a competition for cofactors between the exogenously triggered RNAi pathway and an endogenous RNAi pathway. Consistent with this hypothesis, siRNAs corresponding to several genes have been shown by Northern analysis to depend upon RRF-3 and other ERI factors for their accumulation (DUCHAINE *et al.* 2006; LEE *et al.* 2006; YIGIT *et al.* 2006). Global microarray analyses have also

Supporting information is available online at <http://www.genetics.org/cgi/content/full/genetics.109.109686/DC1>.

¹Corresponding author: Stanford University, 300 Pasteur Dr., Room L235, Mail Stop M5324, Stanford, CA 94305-5324. E-mail: afire@stanford.edu

been undertaken to identify messenger RNAs whose expression is affected by *RRF-3* and *ERI-1* (LEE *et al.* 2006; ASIKAINEN *et al.* 2007).

A functional significance of the *RRF-3*/*ERI* pathway has been inferred by the inability of *rrf-3*, *eri-1*, *eri-3*, and *eri-5* mutant strains to propagate at a high growth temperature (SIMMER *et al.* 2002; DUCHAINE *et al.* 2006). Rather than producing temperature-sensitive mutant protein effects, *RRF-3* and other *ERI* proteins are thought to act in a temperature-sensitive process, as evidenced by the predicted truncated and presumed nonfunctional protein fragments that would result from the available deletion alleles and by their shared temperature-sensitive phenotypes. *rrf-3* mutant animals have been observed to exhibit X-chromosome missegregation (SIMMER *et al.* 2002) and an unusual persistence of a chromatin mark on the X chromosome during male spermatogenesis (MAINE *et al.* 2005). X-chromosome missegregation and defective spermatogenesis have been referred to in previous studies of *eri-1* (KENNEDY *et al.* 2004) and *eri-3* and *eri-5* (DUCHAINE *et al.* 2006). Furthermore, *eri-3* mutant sterility can be rescued by insemination with wild-type sperm (DUCHAINE *et al.* 2006).

Here we investigated the role of *RRF-3* during spermatogenesis. We found defects evident at multiple stages, including after fertilization, where defects in *rrf-3* mutant sperm can produce subsequent nonviable embryos. By using high-throughput sequencing, we characterized a large population of siRNAs present in spermatogenic cells and found a strong enrichment for antisense siRNAs from genes with known mRNA expression during spermatogenesis. While the majority of siRNA production during spermatogenesis does not require *RRF-3*, we found a set of genes for which siRNA production was dependent upon *RRF-3*. Existing data indicate increased expression for these genes in *rrf-3* and/or *eri-1* mutants. Taken together, our analyses suggest a working model in which the *RRF-3*/*ERI* pathway generates siRNAs that downregulate specific genes during spermatogenesis, with this regulation playing a key role in generating functional sperm.

MATERIALS AND METHODS

C. elegans strains, growth conditions, and spermatogenic cell isolation

Strains: Except as noted, *C. elegans* Bristol N2 (BRENNER 1974) was used as the wild-type strain for these studies. The other strains used in this study were the following: GE24—*pha-1(e2123)* I (SCHNABEL and SCHNABEL 1990); GR1378—*eri-1(mg366)* IV (KENNEDY *et al.* 2004); JK816—*fem-3(q20)* IV (BARTON *et al.* 1987); JK987—*tra-2(q276)/mmC1 dpy-10(e128) unc-52(e444)* II (OKKEMA and KIMBLE 1991); NL2099—*rrf-3(pk1426)* II (STJEN *et al.* 2001); PD3303—*rrf-3(pk1426)* II; *pha-1(e2123)* III; PD3330—*rrf-3(pk1426)* II; *him-8(e1489)* IV; PD3331—*him-8(e1489)* IV; VC407—*rrf-3(ok629)/mIn1[mIs14 dpy-10(e128)]* II (<http://www.celeganskoconsortium.omrf.org>); WM48—*rde-4(ne299)* III (TABARA *et al.* 1999); and WM161—*prg-1(tm872)* I (YIGIT *et al.* 2006), *tra-2(q122)* II (SCHEDEL and KIMBLE 1988).

Growth conditions: As stated in the description of each experiment, animals were grown at 16°, 23°, or 25°. The *rrf-3* and *eri-1* mutant fertility phenotypes were strongest at 25°, but certain experiments were carried out at the milder temperature of 23° due to the insufficient numbers of embryos produced at 25°. Self-fertilized *rrf-3(pk1426)* hermaphrodites had an approximate surviving brood size of 2 at 25°, but 30 at 23°. *rrf-3(pk1426)* males were also significantly more fertile at 23°. Self-fertilized *rrf-3(ok629)* hermaphrodites also showed temperature-sensitive decreased fertility (they also exhibited a temperature-independent egg-laying-defective phenotype). Animals used for RNA extraction and sequencing were grown and harvested at 25° (see below).

Spermatogenic cell isolation: A population of mixed stage *fem-3(q20)* hermaphrodites grown at 16° was treated with a 1.2% sodium hypochlorite, 0.5 N NaOH solution with periodic vortexing to dissolve everything but eggs. After washing in M9 buffer to remove hypochlorite, eggs were hatched overnight in M9 solution and allowed to starve as L1 larva. These were put onto OP50-seeded, peptone-enriched plates at 25° to mature to early adult stage (55 hr), when animals were washed off plates with M9 buffer. After repeated washes to remove bacteria, the animals were diced with a razor blade in a 10-cm tissue culture dish to release spermatogenic cells into solution (other cells remained attached to carcasses). The mixture of carcasses and released spermatogenic cells was filtered through a double layer of 10 µm Nitex bolting cloth (Wildlife Supply) and washed three times in M9 buffer before flash freezing in liquid N₂. Visual inspection of a portion that was transferred to a microscope slide prior to freezing indicated that the sample contained a mix of spermatogenic cell types, including primary spermatocytes, secondary spermatocytes, residual bodies, and spermatids (supporting information, Figure S5). This procedure is optimized for small-scale isolation of mixed-stage spermatogenic cells to be immediately frozen [we note that studies of mature sperm function optimally utilize a Percoll gradient and SM buffer (L'HERNAULT and ROBERTS 1995; MACHACA *et al.* 1996) rather than M9 buffer (KLASS and HIRSH 1981; MILLER 2006)].

Male isolation: Set 1: After sodium hypochlorite treatment of mixed stage animals grown at 16°, released eggs were hatched overnight in M9 solution to starve as L1 larva. Fifty-one hours after being put onto OP50-seeded NGM plates at 25°, the starved L1's had reached adulthood, and males were separated from hermaphrodites by filtration through 35-µm Nitex bolting cloth (Wildlife Supply). Embryos that passed through the filter were separated from males by putting both males and embryos on an unseeded area of a plate and allowing males to crawl toward food. Adult males were washed off plates in EN buffer (0.1 M NaCl, 10 mM EDTA) and filtered a second time immediately prior to freezing in liquid N₂, 53 hr after initially being put on seeded plates as L1's. Approximately 95% of the *him-8(e1489)* sample and 90% of the *rrf-3(pk1426)*; *him-8(e1489)* sample was male.

Set 2: After sodium hypochlorite treatment of mixed stage animals grown at 16°, released eggs were put on OP50-seeded NGM plates at 25° directly without being starved as L1's. Fifty-six hours later, when they had reached adulthood, males were separated from hermaphrodites by filtration through 35-µm Nitex bolting cloth (Wildlife Supply). Embryos that passed through the filter were separated from males by putting both males and embryos on an unseeded area of a plate and allowing males to crawl toward food. Adult males were washed off the plates in EN buffer and frozen in liquid N₂ 60 hr after initially being put on seeded plates as eggs. Approximately 90% of the *him-8(e1489)* and 95% of the *rrf-3(pk1426)*; *him-8(e1489)* sample was male.

Assaying embryonic viability

Mated *tra-2(q122)* females were allowed to lay eggs for several hours on NGM plates with thin, clear lawns of OP50 (≤ 1 day after seeding). After removing the mothers from the plates, the newly laid embryos were immediately counted. The surviving progeny were counted when they had reached L4 or adult stage. For temperature-shift experiments, matings were set up between L4 stage *tra-2(q122)* females and L4 or adult males raised at the starting temperature, where they were allowed to mate overnight. The gravid females were then separated from the males and shifted to the new temperature, where they were left for sufficient time to flush out previously fertilized embryos (6 hr at 23° and 25° or 12 hr at 16°). After this period they were allowed to lay eggs for several more hours (3 hr at 23° and 25° or 6 hr at 16°). In each experiment, multiple matings were set up, and a minimum of four gravid hermaphrodites were evaluated at each growth temperature. Males were raised at 23° rather than at 25° [because matings with *rrf-3(pk1426)* males at 25° are inefficient in terms of embryo production]. Twenty-three degrees represents an intermediate temperature at which enough competent sperm are produced to allow for continued egg production many hours after mating.

Cytological techniques

RAD-51, REC-8, HIM-8, and SYP-1 immunostaining: Hermaphrodite gonads were dissected and fixed as previously described for anti-RAD-51, anti-HIM-8, anti-SYP-1 (MARTINEZ-PEREZ and VILLENEUVE 2005), and anti-REC-8 (PASIERBEK *et al.* 2001) stainings. Animals were synchronized by bleaching to kill everything but embryos. Embryos were then allowed to hatch overnight on NGM plates seeded with *Escherichia coli* (OP50) at 16°, after which time embryos were shifted to grow at 25° until the animals were ready for dissection. After fixation, samples were washed three times in 1× PBS for 5 min and then blocked with 3% bovine serum albumin (BSA) in 1× PBS for 20 min at room temperature. Antibodies were diluted in 1× PBS containing 3% BSA as follows: 1:80 anti-RAD-51 (ALPI *et al.* 2003), 1:100 anti-REC-8 (PASIERBEK *et al.* 2001), 1:500 anti-HIM-8 (PHILLIPS *et al.* 2005), and 1:200 anti-SYP-1 (MACQUEEN *et al.* 2002). Samples were then incubated overnight at 4° in a humid chamber. After washing three times in 1× PBS plus 0.1% Tween 20, secondary antibodies were applied at the following dilutions: anti-rabbit DyLight 547 nm (1:200), anti-rabbit Alexa Fluor 568 (1:500), and anti-guinea pig Alexa Fluor 488 (1:500). After 2 hr at room temperature, slides were washed three times in 1× PBS plus 0.1% Tween 20 and mounted in Vectashield antifading medium (Vector Laboratories, Burlingame, CA) containing 2 µg/ml DAPI. Samples were examined with a Zeiss Axio Imager M1 microscope. Images were recorded with a Spot camera (Diagnostics Instruments). For multicolor immunostaining, monochrome stacks of images were captured separately for each emission wavelength (MetaView software; Molecular Devices, Sunnyvale, CA). Three-dimensional stacks of images were deconvolved (AutoQuant software; AutoQuant Imaging, Troy, NY) and projected (Helicon Focus software; <http://helicon.com.ua/heliconfocus/>).

α-Tubulin immunostaining: We used fixation procedures optimized for preservation of microtubules (GONCZY *et al.* 1999; OEGEMA *et al.* 2001), with modifications as previously described (MARTINEZ-PEREZ *et al.* 2008). FITC-conjugated anti-α-tubulin monoclonal antibody DM 1A (Sigma) was used at a concentration of 1 µg/ml. Images were acquired as stacks of optical sections at 0.2-µm intervals using a DeltaVision deconvolution microscopy system. We quantified the inci-

dence of microtubule wreaths surrounding sperm nuclei in reproductive tracts (gonads and spermathecae) dissected either from self-fertilizing hermaphrodites or from *tra-2(q122)* females that had been mated with either wild-type or *rrf-3(pk1426)* mutant males. Quantification was performed using animals that had been raised and maintained at 23°. Microtubule wreaths were frequent in sperm from both *rrf-3* self-fertilizing hermaphrodites (15 worms; 237/287 sperm nuclei with microtubule wreaths) and *tra-2(q122)* females that had been mated with *rrf-3* males (1 worm; 17/20 nuclei with microtubule wreaths). Self-fertilized *eri-1* hermaphrodite sperm had microtubule wreaths in 59% of their sperm (5 worms; 152/256 nuclei with tubulin wreaths). Microtubule wreaths were not detected in either control N2 self-fertilizing hermaphrodites (2 worms; 0/93 nuclei with tubulin wreaths) or control *tra-2(q122)* females mated with N2 males (4 worms; 0/86 nuclei with tubulin wreaths). Although discrete tubulin wreaths were not detected in control sperm, some hazy/diffuse tubulin staining was detected in 4/179 control sperm. For experiments analyzing wild-type sperm, successful microtubule staining in mitotic germ cells from the same gonad served as an internal positive control.

Preparation of libraries of small RNAs for sequencing

Small RNA was extracted from frozen tissue samples with the mirVana microRNA (miRNA) isolation kit (Ambion). Libraries of small RNAs were prepared using a protocol similar to one previously described for miRNA cloning (LAU *et al.* 2001), in which small RNA species were flanked by adapter sequences to allow for PCR and sequencing. We modified the original protocol at several key steps to allow for capture of triphosphorylated species and for sequencing with the Illumina genome analyzer system. To remove the bias for 5' monophosphorylated species but preserve the bias toward 3' hydroxylated species, we removed both monophosphates and polyphosphates from the 5'-end of the small RNA with Antarctic Phosphatase (New England Biolabs) following the addition of the 3' adapter with T4 RNA ligase 1 (New England Biolabs). The resulting hydroxylated 5'-ends were phosphorylated by treatment with T4 polynucleotide kinase (New England Biolabs) and ATP to form a substrate for T4 RNA ligase 1-mediated addition of the 5' adapter. T4 polynucleotide kinase treatment after addition of the 3' adapter is important because of its 3' phosphatase and 2',3' cyclic phosphodiesterase activity, which can convert unwanted RNA degradation products into a substrate for the 3' adapter ligation reaction. After ligation of both the 3' and 5' adapters, the adapters were extended during the reverse transcription and PCR steps to include complete primer binding sites for subsequent amplification and sequencing reactions. To protect against cross-contamination and to allow for pooling of samples, we modified the 5' adapter sequence to include the Illumina genomic sequencing primer immediately followed by a 4-nt barcode. The pair of barcodes used in the set 1 wild-type and mutant samples was switched in the set 2 wild-type and mutant samples to guard against any potential biases introduced by adapter sequences. The samples were PAGE purified at three stages: after initial RNA extraction and after each ligation step (except with the isolated spermatogenic cell sample, where the first PAGE purification was skipped to conserve material). Additional details for each sample are provided in Table S1. The following oligos were used:

3' adapter (IDT linker-1 with 5' adenylation and 3' dideoxyC):
rAppCTGTAGGCACCATCAATC;

5' adapter (*i.e.*, AF-PP-341 DNA/RNA hybrid oligo with a 5' amino modifier and 4-nt barcode at the 3'-end): ACGCTCTCCGATCTrGrUrUrA;
 Dual reverse transcription primer and PCR primer (AF-JIG-37, complementary to IDT linker-1): CAAGCAGAAGACGGCA TACGAattgatggtgcctacag;
 PCR primer (AF-JIG-40, containing 5' adapter sequence): AATGATACGGCGACCACCGACACTCTTTCCCTACACGA CGCTCTCCGATCT.

Sequence analyses

Thirty-six-nucleotide sequencing reads were generated using the Illumina Genome Analyzer system. The 3' adapter sequences were trimmed off *in silico* by scanning from the 3'-end of the sequence for the first instance of the first 4 nt of the adapter: CTGT. Sequence reads that lacked CTGT in the 3' most 13 nt were excluded from further analysis. After barcode sorting, the 4 nt of barcode were trimmed off the 5'-ends to yield 19- to 28-nt reads corresponding to the captured small RNAs. siRNA alignment counts were produced by aligning the reads to a cDNA reference set using a local installation of BLAT (Kent 2002), with default parameters, except tileSize was set to 10 and stepSize to 5. The term "siRNA alignment count" (above) refers to the number of matches to an individual cDNA obtained from the set of reads. The cDNA data set, derived from the *C. elegans* WS190 genome assembly, was downloaded from <http://www.wormbase.org:80/biomart/martview>. The data set of known transposon sequences was downloaded from http://www.sanger.ac.uk/Projects/C_elegans/REPEATS/elegans.lib. Read counts and alignment counts are listed in Table S1.

Statistical methods

P-value calculations for identification of genes with RRF-3-dependent siRNAs: Gene-by-gene siRNA alignment counts were tallied and compared for each sample. To measure fold-changes in alignment count between samples for a particular gene, the alignment count was first converted to a proportion by dividing the alignment count of that gene by the sum of the alignments of the complete cDNA reference set. To obtain a measure of the statistical significance of differences between samples, we assumed that there was no difference in population proportions for each gene and then calculated the probability (*P*-value) of measuring a difference in sample proportions at least as extreme as the one observed. A one-tailed test was used since we had prior expectations that the proportions for certain genes would decrease in the *rrf-3(pk1426)* samples (see File S1 for a representative calculation). The standard errors of the means for sample proportion differences were calculated on the basis of predicted normal distributions of the sample proportions, which is justified by the large sample size and the central limit theorem (the proportions here are equivalent to means). The sample proportion differences were standardized to *Z*-scores by dividing by the standard errors of the means for the proportion differences.

P-values and fold-enrichment calculations for overlap between sets of genes with RRF-3-dependent siRNAs and genes with elevated mRNA levels in *rrf-3* and *eri-1* mutants: *P*-values were derived using Fisher's exact test from the following numbers: 16,887 of the genes represented in the cDNA data set had probes on the microarray used by ASIKAINEN *et al.* (2007). Of the 21 genes that we identified as spermatogenesis candidate RRF-3 targets, 18 were included in this set. Of the

16,887 total genes, 178 had increased mRNA levels in *rrf-3(pk1426)*, while 46 had decreased levels. Of the 18 spermatogenesis candidate RRF-3 targets, 3 had increased mRNA levels in *rrf-3(pk1426)* (15.8-fold enrichment; *P*-value = 8.8×10^{-4}); none had decreased levels. Of the 16,887 genes, 706 had increased mRNA levels in *eri-1(mg366)*, while 263 had decreased levels. Of the 18 spermatogenesis candidate RRF-3 targets, 8 had increased mRNA levels in *eri-1(mg366)* (10.6-fold enrichment; *P*-value = 2.9×10^{-7}). These 8 included the 3 with elevated mRNA levels in *rrf-3(pk1426)*. None of the 18 had decreased levels in *eri-1(mg366)*. When we considered all 44 candidate RRF-3 targets rather than just the 18 with siRNAs present in the spermatogenic cell sample, the numbers were still highly significant: fold enrichments of 6.5 and 4.4 with *P*-values of 1.5×10^{-2} and 4.4×10^{-4} for *rrf-3(pk1426)* and *eri-1(mg366)*, respectively.

RESULTS

Compromised spermatogenesis accounts for reduced brood size and X-chromosome loss from *rrf-3(pk1426)* hermaphrodites: We first set out to determine whether the *rrf-3(pk1426)* reduced brood size and X-chromosome missegregation phenotypes were attributable to defects in sperm or oocytes. *C. elegans* exists in two sexes: males, which produce only sperm, and hermaphrodites, which produce first sperm and then oocytes in the same gonad. Defects in either gamete line can result in sterility of self-fertilizing hermaphrodites. *rrf-3(pk1426)* self-fertilizing hermaphrodites produced very few fertilized embryos at 25°, with 90% of these nonviable (Figure 1A). Here and in subsequent experiments, we defined "nonviable" as failure to give rise to L4 stage larva or adults. We found that a preponderance (or all) of the nonviability was accounted for by embryonic lethality prior to hatching. To determine the source of the reduced embryo count and viability, we set up matings between *rrf-3(pk1426)* hermaphrodites and wild-type N2 males at 25°. Fertilization by wild-type sperm rescued the *rrf-3(pk1426)* brood size reduction in terms of both numbers of embryos produced and embryonic viability (Figure 1, A and B), indicating that both phenotypes can be attributed to defects during spermatogenesis.

To determine whether X-chromosome missegregation is linked to spermatogenesis in *rrf-3(pk1426)* hermaphrodites, we utilized a genetic test that takes advantage of the *C. elegans* sex determination system. The ratio of X-chromosomes to autosomes in *C. elegans* determines the sex: animals with two X chromosomes and two sets of autosomes are hermaphrodites; animals with one X and two sets of autosomes are male (NIGON 1951; MADL and HERMAN 1979). Hence, in a normal self-fertilization, a hermaphrodite contributes one X from each sperm and from each ovum so that the resulting embryos are virtually all (~99.8%) XX hermaphrodites. Generation of XO males from XX hermaphrodite self-fertilization is indicative of X-chromosome loss or non-disjunction in either the sperm or oocyte lineage. To test for X-chromosome loss in *rrf-3(pk1426)* oogenesis, we set

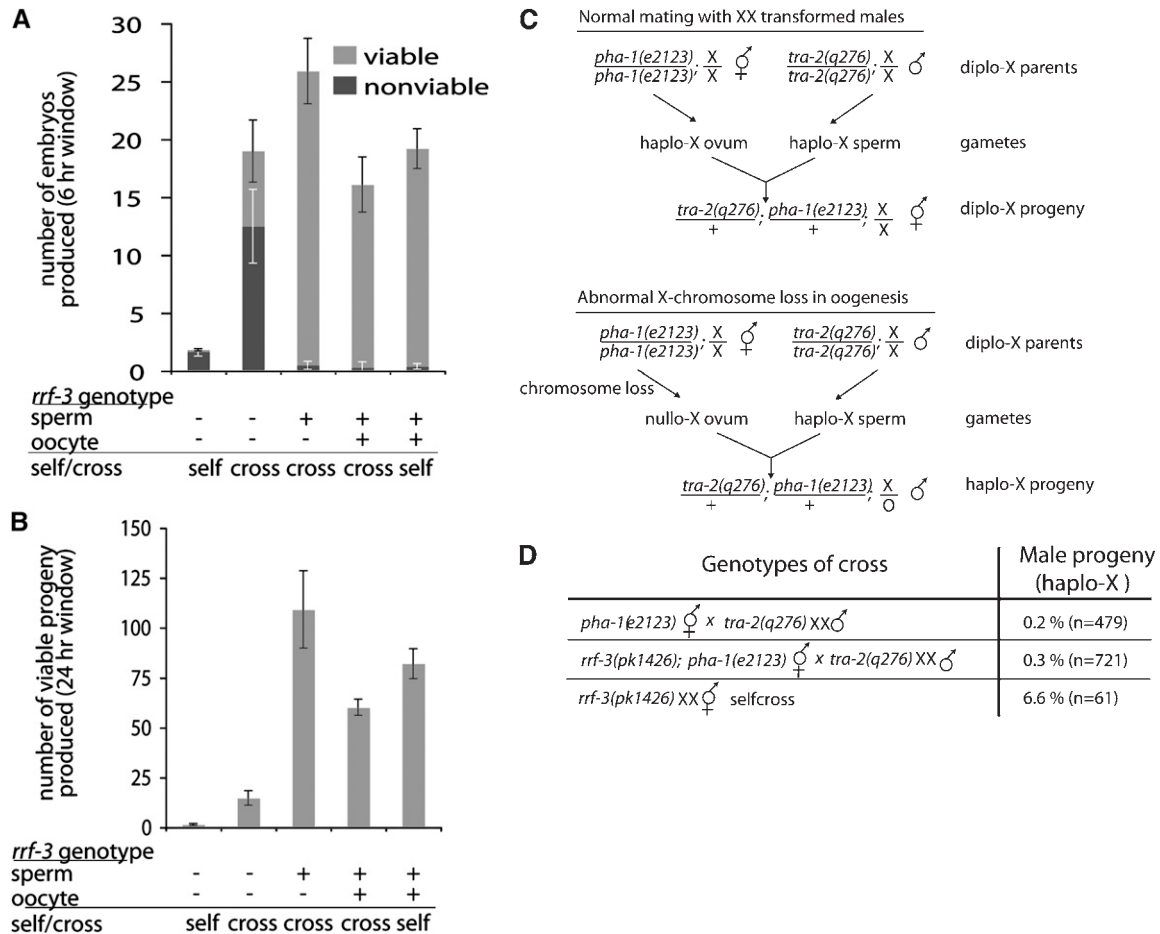


FIGURE 1.—Lack of embryos, nonviable embryos, and X-chromosome loss are attributable to defective spermatogenesis in *rrf-3* mutants. Individual hermaphrodites either were allowed to self-fertilize or were crossed with males at 25° and then allowed to lay eggs during a 6-hr window followed by an 18-hr window. The progeny from both periods were counted when they had reached L4 and adult stage. Cases where the matings were unsuccessful, as evidenced by few embryos or a lack of male progeny, were not counted. Multiple matings were set up and progeny from at least five gravid hermaphrodites were counted in every case. (A) Rescue of *rrf-3(pk1426)* embryo production and viability of wild-type sperm (6-hr window). The embryos laid during the first 6 hr were counted in addition to the surviving progeny to estimate the number of nonviable embryos. Error bars denote standard errors of the means. (B) Rescue of the *rrf-3(pk1426)* brood size (24-hr window). The number of surviving progeny from both the 6- and 18-hr windows were combined. Error bars denote standard errors of the means. (C) Diagram of assay for loss of the X chromosome during oogenesis. *pha-1(e2123)* is a temperature-sensitive, recessive, embryonic lethal mutation that ensures that only outcrossed progeny survive at 23°. The *tra-2(q276)* mutation causes XX animals, which would normally be hermaphrodites, to develop into partially fertile males. (D) Wild-type levels of X-chromosome loss in *rrf-3(pk1426)* oogenesis. Multiple matings were set up, each with five hermaphrodites and at least five males, with the exception of the *rrf-3(pk1426)* self-fertilizations, which were done with individual hermaphrodites. The number of male progeny was scored when they had reached L4 or adult stage. The total number of progeny counted, *n*, is smaller than would be expected from wild-type matings due to the inefficiency of *tra-2(q276)* males. These crosses were set up at 23° rather than 25° for increased success.

up matings with *tra-2(q276)* XX-transformed males, which contribute an X from each sperm (like a hermaphrodite). Unless the X chromosome is lost during oogenesis, hermaphrodites mated with *tra-2(q276)* males give rise to almost entirely XX hermaphrodite progeny (Figure 1C) (OKKEMA and KIMBLE 1991). We set up matings between either *rrf-3(pk1426)* or wild-type hermaphrodites with *tra-2(q276)* males. To select for outcrossed progeny, the hermaphrodites also carried a temperature-sensitive mutation in *pha-1* that causes self-fertilized progeny to die as embryos (SCHNABEL and SCHNABEL 1990). The progeny from this cross

exhibited extremely low numbers of spontaneous males (wild type: 1 of 479; *rrf-3(pk1426)*: 2 of 721) (Figure 1D). These results indicate that oogenesis is not the source of X-chromosome loss in *rrf-3(pk1426)* propagation, implicating spermatogenesis as the affected process. While RRF-3 may have additional functions in oogenesis, these results indicate that most or all of the fertility and X-chromosome segregation mutant phenotypes can be accounted for by roles for RRF-3 during spermatogenesis.

RRF-3 is required for spermatocyte cell division: To further investigate the nature of the sperm defect, we examined germlines of *rrf-3(pk1426)* hermaphrodites

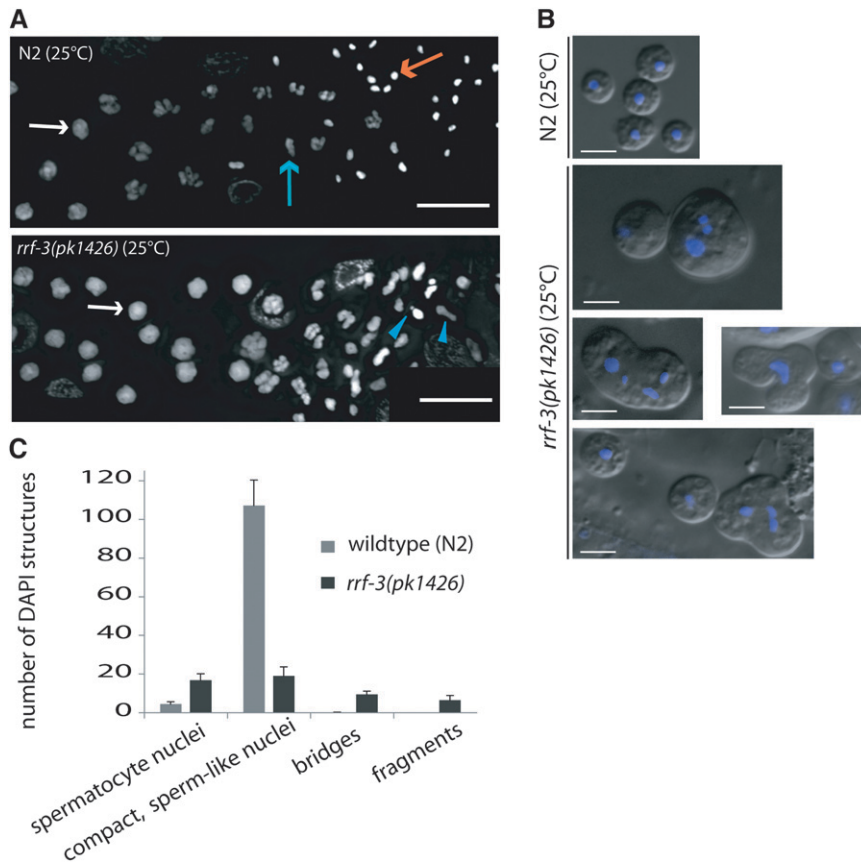


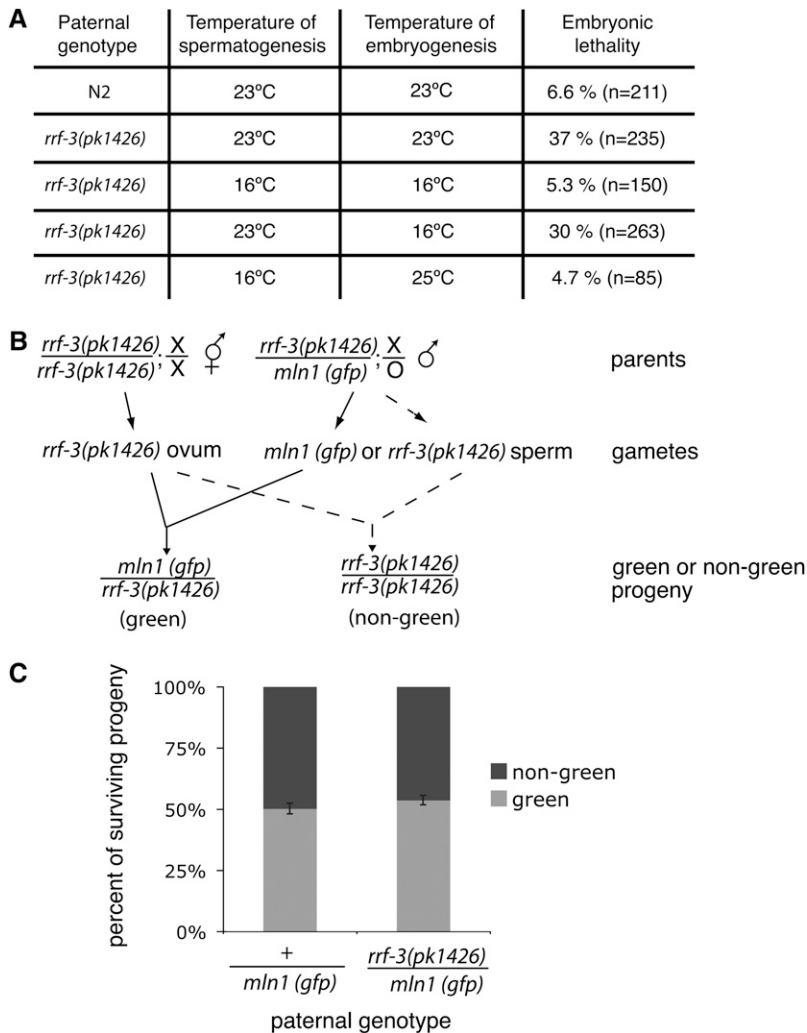
FIGURE 2.—RRF-3 is required for normal spermatocyte cell division. (A) Abnormal nuclear structures and lack of sperm visible by DAPI staining of fixed hermaphrodite gonads undergoing spermatogenesis at 25°. Nuclei in both wild-type and mutant spermatocytes (white arrows) appeared visibly normal, but nuclei in subsequent stages often appeared fragmented or bridged in the mutant (blue arrowheads). A wild-type dividing spermatocyte nuclei (blue arrow) and spermatid nuclei (orange arrow) are also indicated. Bar, 10 μ m. (B) Multiple and misshapen Hoechst-staining structures in mutant spermatocytes at 25°. Unfixed sperm and spermatocytes released from *rrf-3(pk1426)* dissected gonads and stained with Hoescht 33342 show multiple nuclear structures within individual cells (bottom four panels), often of inconsistent sizes and shapes compared to N2 control sperm nuclei (top). Mutant worms also produced sperm that were visibly similar to the N2 (*e.g.*, upper left corner of bottom panel). (C) Quantification of DAPI-staining structures in fixed hermaphrodite gonads at 25°. Nuclear structures were counted in the proximal gonad at the expected timing of spermatogenesis completion (after the appearance of the first oocyte but prior to ovulation; at this stage the sperm have not yet moved into the spermatheca). Compact, sperm-like nuclei are not equiv-

alent to cell counts because of the presence of multiple DNA structures within some individual cells in the mutant. Values shown are averages obtained from 9 N2 gonads and 10 *rrf-3(pk1426)* gonads. Error bars denote standard errors of the means.

prior to and during completion of spermatogenesis at 25°. We investigated chromosome organization during meiotic prophase using antibodies labeling RAD-51, which functions in recombination and decorates chiasmata (ALPI *et al.* 2003; COLAIACOVO *et al.* 2003); the synaptonemal complex components REC-8 and SYP-1 (PASIERBEK *et al.* 2001; MACQUEEN *et al.* 2002); and HIM-8, which marks a specific domain on the X chromosome (PHILLIPS *et al.* 2005). This analysis did not reveal any overt defects in meiotic prophase (Figure S1 and Figure S2). In addition, DAPI-stained nuclei in the process of transitioning between prophase and the first meiotic division appeared normal in *rrf-3* mutants (Figure 2A). Cytological abnormalities in *rrf-3* mutant germ cells first started to become evident after the primary spermatocyte stage, where DAPI staining revealed nuclear abnormalities such as small or bridged structures (Figure 2A). Further analysis of unfixed late-stage spermatocytes by DIC and Hoechst staining revealed both unusual cell morphology and the presence of multiple nuclear structures within individual mutant spermatocytes (Figure 2B). Other spermatocytes within the same gonads appeared to develop without obvious morphological abnormalities and to produce residual bodies and sperm of the normal size and shape, although in smaller

numbers than wild type. Additional DAPI staining of released gonads revealed that the production of compact sperm-like nuclei was both delayed and decreased. At the expected time of spermatogenesis completion (prior to ovulation but after appearance of oocytes), *rrf-3* mutants had a fivefold reduction in compact, sperm-like nuclei relative to N2 (Figure 2C). By the time of the first ovulation, the number in *rrf-3* mutants of sperm-like nuclei relative to N2 increased to half of the N2 levels (data not shown), but these gonads still contained cells with multiple or misshapen nuclei. Together, these phenotypes indicate defects in developmental progression and cell division processes during spermatogenesis in *rrf-3(pk1426)*.

An *rrf-3* paternal effect on embryogenesis: Since *rrf-3(pk1426)* animals at elevated temperatures yield a high percentage of nonviable embryos, we asked whether RRF-3 functions directly in embryos or in a spermatogenesis process linked to embryogenesis. To test this, we set up matings between *rrf-3(pk1426)* males and *tra-2(q122)* females, which genetically are XX hermaphrodites but have feminized germlines that produce only oocytes (SCHEDL and KIMBLE 1988). We found that *rrf-3(pk1426)* males produced sperm that were capable of fertilization, but many of the resulting embryos were



nonviable (~37% at 23°). This effect on embryos depended on the temperature at which spermatogenesis occurred but was independent of the temperature at which embryogenesis occurred (Figure 3A). The paternally derived lethality was not due to the presence of a second, unrelated recessive mutation because *trans*-heterozygous males bearing *rff-3(pk1426)* and another deletion allele, *rff-3(ok629)*, also produced nonviable embryos. Such males should be heterozygous for any extraneous mutations outside *rff-3*, so the contribution of any such mutations, if any, should be minimized. In setting up the test for the *rff-3* requirement, we utilized *trans*-heterozygote rather than *ok629* homozygotes because of a male-tail-defective phenotype in the strain (which we have not definitively assigned to *ok629*). In matings between *tra-2(q122)* females and *ok629/pk1426* *trans*-heterozygote males at 25°, the resulting embryos showed similar levels of nonviability as embryos sired by *pk1426* homozygous males: 84% nonviability from *pk1426/pk1426* and 72% nonviability from *ok629/pk1426*, contrasted with 2% nonviability from N2 (Figure S3).

To distinguish a paternal effect from an embryonic requirement for a paternally delivered *rff-3(+)* allele,

we used the scheme in Figure 3B, setting up matings between *rff-3(pk1426)* homozygous hermaphrodites and *rff-3(pk1426)/mIn1* heterozygous males. *mIn1* is a chromosome inversion of chromosome II containing the wild-type *rff-3* locus and a transgene insertion that drives pharyngeal GFP expression (EDGLEY and RIDDLE 2001), enabling us to determine which paternal allele is inherited by the progeny. We found that survival was not affected by physical inheritance of the wild-type *rff-3* allele (on *mIn1*), indicating that *rff-3* expression is not required after separation of joined secondary spermatocytes into spermatids nor in embryogenesis (Figure 2 and Figure 3C). Together with the early temperature-sensitive period (prior to fertilization of the embryo as shown in Figure 3A), this result implicates spermatogenesis as the crucial timing for both RRF-3 expression and activity.

Roles for *rff-3* and *eri-1* in preventing microtubule accumulation in sperm and abnormal microtubule structures in one-cell embryos: To examine the basis of the embryonic lethality, we stained wild-type and *rff-3(pk1426)* self-fertilized embryos with an antibody against α -tubulin. One particularly notable defect was

FIGURE 3.—RRF-3 is involved in a temperature-sensitive spermatogenic process with effects on embryonic viability. (A) The viability of embryos sired by *rff-3(pk1426)* males is determined by temperature of spermatogenesis. *rff-3(pk1426)* or N2 males raised at the indicated temperatures were mated with *tra-2(q122)* females. The level of embryonic viability was estimated by counting both the total number of eggs laid (*n*) and the number of surviving progeny (as described in MATERIALS AND METHODS). (B) Diagram of assay for an embryonic requirement for a paternally delivered, wild-type copy of *rff-3*. *rff-3(pk1426)* homozygous hermaphrodites were mated with males that were heterozygous for *rff-3(pk1426)* and the *mIn1* inversion (which carries the wild-type *rff-3* locus and a transgene driving pharyngeal GFP expression). Inheritance of the mutant and wild-type *rff-3* allele could be tracked by GFP expression. No marker for outcrossed progeny was necessary because of the sperm defect in *rff-3(pk1426)* hermaphrodites. Animals were raised and matings set up at 25°. (C) A wild-type copy of *rff-3* is dispensable for embryogenesis. GFP- and non-GFP-expressing progeny were counted at L4 or adult stage to determine the proportion with paternally inherited *mIn1*. To provide a control for the potential effects of the inversion and the dominant transgene marker, +/*mIn1* males were used. A total of 526 progeny resulting from five matings were counted for +/*mIn1*, and a total of 675 progeny resulting from four matings were counted for *rff-3(pk1426)/mIn1*. Error bars denote standard error of the means.

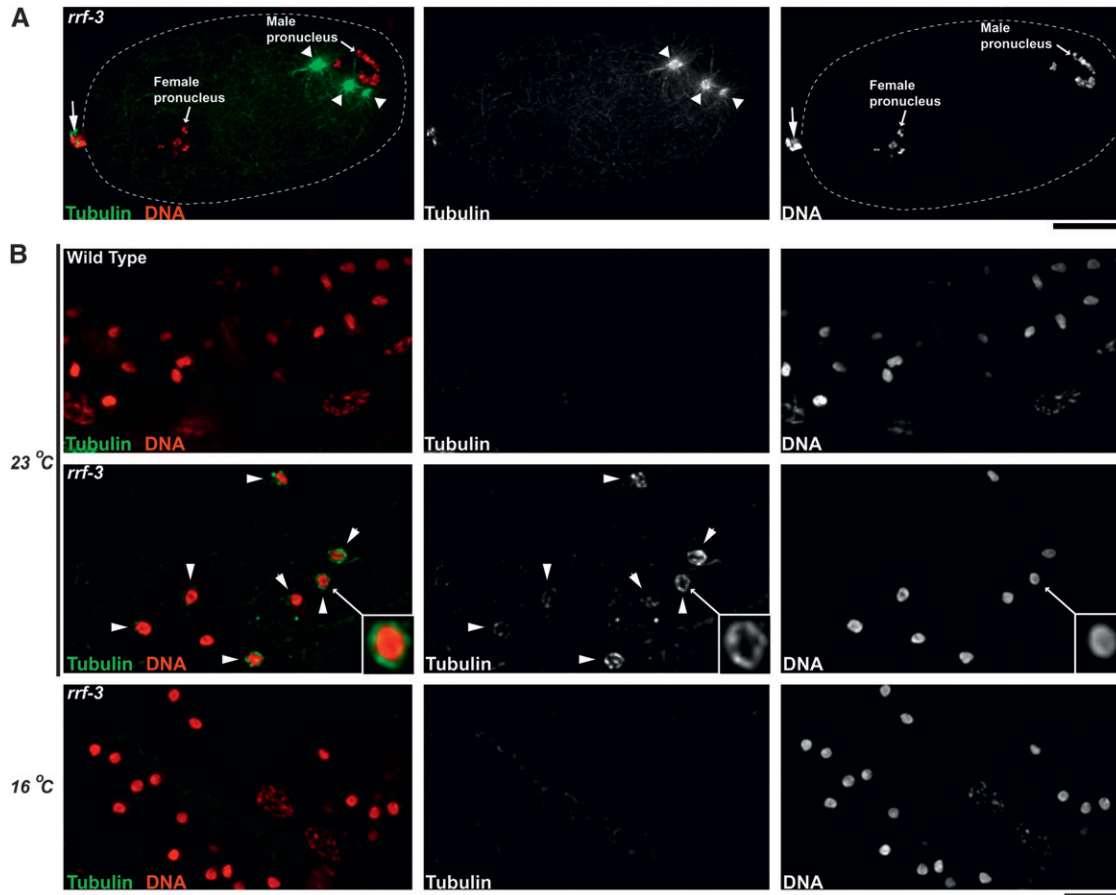


FIGURE 4.—Abnormal microtubule structures in *rrf-3* mutant embryos and sperm. An embryo (A) and sperm (B) stained with Hoechst to label chromosomes (red) and immunostained with antitubulin antibody to label microtubules (green). (A) One-cell embryo (prior to meeting of male and female pronuclei) laid by an *rrf-3(pk1426)* hermaphrodite at 23°. Although two asters are normally associated with the male pronucleus at this stage in wild-type embryos, this mutant embryo has three asters (marked by arrowheads) associated with the male pronucleus. An arrow marks the polar bodies, which are located at the anterior end of the embryo. Bar, 10 μm . (B) Sperm from either a wild-type hermaphrodite (top row) or *rrf-3(pk1426)* hermaphrodites (bottom three rows), raised at the indicated temperatures. Arrowheads highlight sperm nuclei surrounded by tubulin wreaths that were observed in *rrf-3* mutant sperm at 23°. The insets in the middle row show an enlarged view of the tubulin wreath encasing the nucleus of an *rrf-3* mutant sperm. Bar, 5 μm .

the presence of abnormal microtubule structures in a subset of the mutant embryos at the one-cell stage (*i.e.*, from formation of the maternal meiotic spindle through metaphase of the first mitotic division). Specifically, we detected supernumerary microtubule asters associated with the sperm pronucleus or tripolar spindles in 5 of 35 *rrf-3* mutant one-cell embryos (Figure 4A), whereas such structures were never observed in control embryos (0 of 34; *P*-value: 0.029).

Immunofluorescence analysis also revealed striking microtubule-based abnormalities in *rrf-3* mutant sperm. At 23°, we observed bright wreaths of microtubules surrounding the nuclei of both hermaphrodite and male-derived sperm (Figure 4B and Figure S4). These microtubule wreaths were clearly visible in 83% ($n = 307$) of *rrf-3* mutant sperm. In contrast, only 2% of wild-type sperm exhibited any detectable tubulin staining (which had a diffuse appearance) other than the sperm centrioles. Microtubule wreath structures were never

observed in wild-type sperm ($n = 179$). The fact that tubulin was largely undetectable is expected on the basis of previous observations that microtubules in secondary spermatocytes are effectively segregated to an enucleated cytoplasm called the residual body (ROBERTS *et al.* 1986; WARD 1986; WARD *et al.* 1986). At 16°, where we did not see dead embryos, the mutant sperm lacked the microtubule wreath phenotype.

Because meiotic DNA damage resulting from compromised small RNA machinery in *Drosophila* results in microtubule polarization defects (CHEN *et al.* 2007; KLATTENHOFF *et al.* 2007; PANE *et al.* 2007), we tested the possibility that the microtubule wreaths in *rrf-3* mutant sperm might be a consequence of unrepaired meiotic DNA double-strand breaks (DSBs). (Although the normal kinetics of RAD-51 foci in *rrf-3* mutants suggests successful DSB repair, our data could not exclude the possibility of persistent meiotic DNA damage.) Specifically, we looked for microtubule wreaths

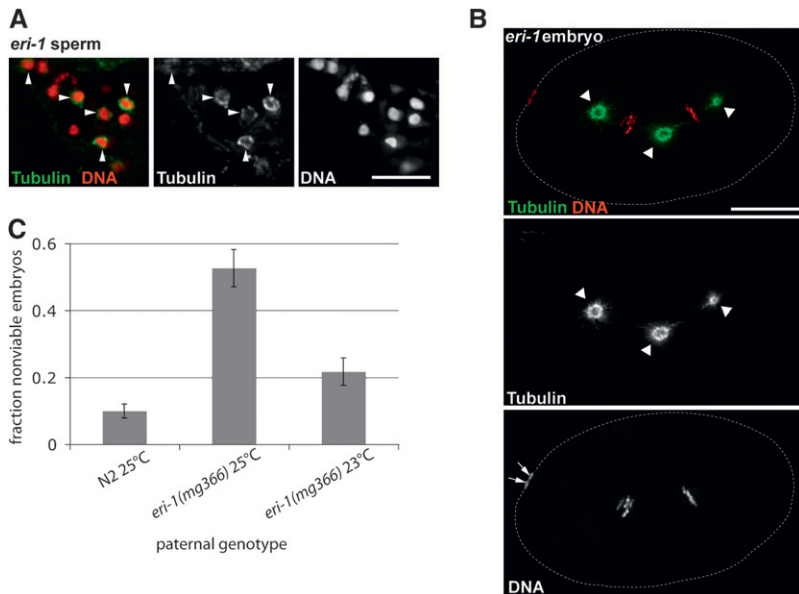


FIGURE 5.—Abnormal microtubule structures in *eri-1* mutant embryos and sperm and paternal-effect nonviability from *eri-1* mutant males. (A) *eri-1(mg366)* sperm and (B) embryo from hermaphrodites grown at 23° and stained with Hoechst to label chromosomes (red) and antitubulin antibody to label microtubules (green). (A) Some *eri-1(mg366)* sperm contain abnormal microtubule wreath structures (arrowheads) similar to those observed in *rrf-3* mutant sperm. Bar, 5 μ m. (B) One-cell *eri-1* mutant embryo with a tripolar spindle. Arrowheads mark each of the three spindle poles. Arrows mark the polar bodies, which indicate the anterior of the embryo. Bar, 10 μ m. (C) *eri-1(mg366)* males sire nonviable embryos at elevated temperatures. The fraction of nonviable embryos was estimated by counting both the number of eggs laid and the resulting number of surviving progeny. Matings were set up at both 23° and 25°. Error bars denote standard errors of the means.

around sperm nuclei at 23° in double-mutant worms lacking SPO-11 (the enzyme required for inducing meiotic DSBs) (KEENEY *et al.* 1997; DERNBURG *et al.* 1998) and RRF-3. Microtubule wreaths were present in sperm from the double mutant, indicating that these structures do not depend on meiotic DSBs induced by SPO-11 (data not shown).

Given the similarities between the fertility and RNAi phenotypes of *rrf-3* and *eri-1* mutants, we examined tubulin distribution in sperm and embryos from *eri-1(mg366)* hermaphrodites raised at 23°. We found both microtubule wreaths in sperm (59%, $n = 256$) and microtubule/spindle defects in embryos (4/20) produced by *eri* mutants (Figure 5, A and B). We further confirmed a role for ERI-1 in producing functionally normal sperm by showing that mating *eri-1(mg366)* males with *tra-2(q122)* females resulted in nonviable embryos at elevated temperatures (Figure 5C).

Identification of siRNAs present in spermatogenic cells: During the progression through the distinct stages of spermatogenesis from a premeiotic syncytium to a mature sperm, a large number of genes must be choreographed to ensure that the proper genes are expressed at the appropriate level and developmental stage (*e.g.*, JOHNSTON *et al.* 2008). Since several RNAi-related factors have been implicated in spermatogenesis through mutant studies, we expected that RNA-based regulatory machinery might contribute at several levels to this choreography. Consequently, we characterized the small RNAs present in the male germline. We took a sequencing-based approach to this, adapting sperm isolation and optimizing high-throughput sequencing methods to generate an extensive data set of small RNA sequences from isolated spermatogenic cells. Spermatogenic cells were isolated from adult *fem-3(q20)* XX animals using a technique that yields a large proportion of sperm precursors in addition to mature sperm (adapted from LAMUNYON and

WARD 1995, which describes a dicing method, and from MILLER 2006, which uses M9 buffer and does not require a Percoll step to obtain sperm for biochemical analysis). *fem-3(q20)* animals produce an excess of sperm and no oocytes or embryos at 25° (BARTON *et al.* 1987). Functionality of *fem-3(gf)* XX sperm has been demonstrated previously by their ability to sire live embryos following artificial insemination (LAMUNYON and WARD 1994). The population of cells isolated and used for sequencing is shown in Figure S5.

We prepared sequencing libraries using a method that allows for capture of small RNAs independently of the 5' phosphorylation status. In *C. elegans*, the majority of RdRP products have a 5' triphosphate (RUBY *et al.* 2006; PAK and FIRE 2007; SIJEN *et al.* 2007), but standard high-efficiency library preparation methods (*e.g.*, LAU *et al.* 2001) rely on a 5' monophosphate, which is characteristic of microRNAs and other DCR-1 products. The ability to capture 5'-triphosphorylated siRNAs was critical for this analysis, since this terminus structure is expected to be present on any initial RdRP transcript and would be retained unless there is covalent 5'-end processing. In MATERIALS AND METHODS, we describe our procedure for preparing such libraries using a modification of LAU *et al.* (2001) with the addition of a dephosphorylation and a single phosphate addition step following 3' adapter ligation. The resulting libraries of small RNAs were of diverse sequence composition, and we obtained large numbers of distinct small RNA species including microRNAs, piwi-interacting RNAs (also called piRNAs or 21U-RNAs), and siRNAs. These sequences are available at the NCBI short read archive (GEO accession number GSE18429). We aligned the small RNA sequences to a cDNA data set downloaded from <http://www.wormbase.org> to generate a list of siRNA alignment counts for each annotated gene (where "siRNA alignment count" for each gene is the

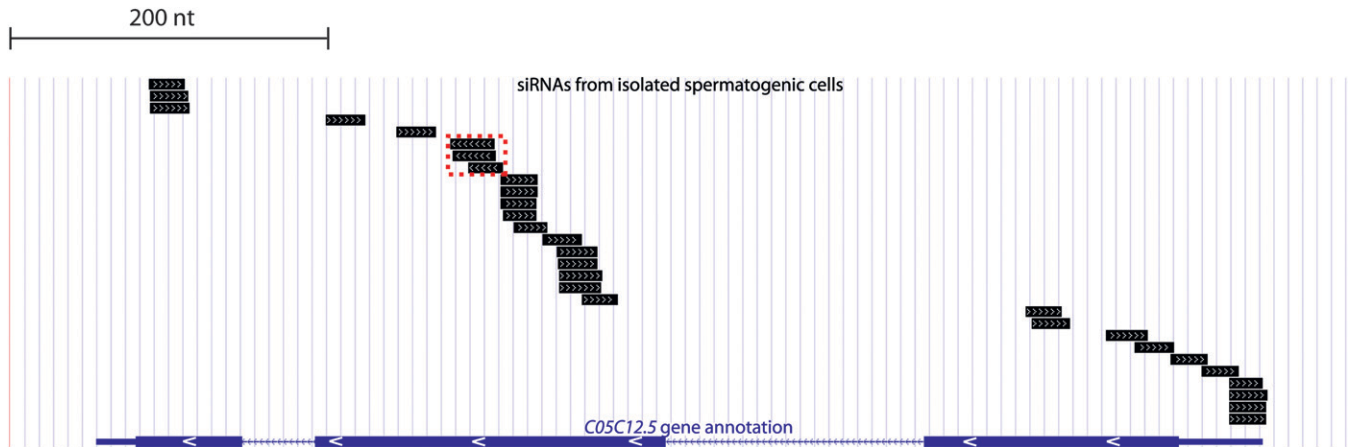


FIGURE 6.—siRNA alignments to an mRNA: antisense predominance and diversity of intragenic locations. A modified UCSC Genome Browser Display illustrates the *C05C12.5* annotation and siRNAs from the spermatogenic cell sample. For the *C05C12.5* annotation, thin solid end segments denote untranslated regions, thick solid segments denote exons, and line segments denote introns. White arrows within exons indicate the gene's orientation. siRNA alignments are represented by short black segments. All but the three siRNA alignments outlined by a dashed red box are antisense to *C05C12.5*. Note that siRNAs that span exon–exon boundaries do not produce genomic alignments.

number of alignments that it produced from the complete set of small RNA sequences) These data are tabulated in File S1. Also included in the NCBI short read archive are alignment files in psl format, which can be directly uploaded onto the UCSC Genome Browser (<http://www.genome.ucsc.edu>) for viewing. Two notable features of the siRNA alignments are a bias toward antisense orientation relative to the annotated mRNA and a diversity of positions within the individual target genes, as illustrated by siRNAs of the gene *C05C12.5* (Figure 6). The antisense orientation of the spermatogenesis siRNAs suggests synthesis by RdRP and is consistent with potential modulatory roles of these small RNAs through a “standard” gene-silencing model in which an Argonuate-bound short antisense RNA segment catalytically locates and silences mRNAs with extended regions of homology (reviewed in HUTVAGNER and SIMARD 2008).

The full small RNA-ome from sperm is large, complex, and likely to reflect numerous distinct regulatory processes. We began by analyzing small RNAs with likely roles in the regulation of specific mRNAs by compiling siRNA alignment counts for each annotated mRNA-encoding gene in this data set. While a comprehensive list of spermatogenesis-expressed mRNAs is unavailable for *C. elegans*, several studies have categorized mRNAs with higher relative expression in spermatogenic cells than in other tissues. We compared the list of genes with siRNAs present in the spermatogenic cell sample with two gene lists, “spermatogenesis-enriched” and “mountain 4.” The spermatogenesis-enriched category was derived by comparison of mRNA expression from mutant hermaphrodites that were either masculinized to produce only sperm or feminized to produce only oocytes (REINKE *et al.* 2004). Mountain 4 was derived from a study that grouped genes according to correlated

expression patterns over multiple growth conditions, developmental time points, and mutant backgrounds (KIM *et al.* 2001). For a gene to be categorized as having siRNAs in spermatogenic cells, we required that the number of alignments to its mRNA from our isolated spermatogenic cell siRNAs be at least three. A total of 4723 of the 21,133 genes in our cDNA reference set met this criterion. These 4723 genes show a 3.7- and 3.5-fold greater-than-expected overlap with the spermatogenesis-enriched and mountain 4 expression category, respectively (accounting for 84% of the total spermatogenesis-enriched category and 77% of the mountain 4 category, Figure 7A). Conversely, genes from the spermatogenesis-enriched and mountain 4 categories were significantly underrepresented among the group of mRNAs identified in our isolated spermatogenic cell sample with siRNA alignment counts of fewer than 3 (4.8- and 3.3-fold less-than-expected, respectively). These results indicate that siRNA abundance in spermatogenic cells correlates with mRNA expression during spermatogenesis and that siRNA production is a general feature of gene activity during spermatogenesis, involving the majority of genes with enriched expression during spermatogenesis.

Identification of RRF-3-dependent siRNAs: To identify siRNAs that depend upon RRF-3 for their production, we analyzed siRNA expression profiles from *rrf-3* mutant samples. To avoid any possible confounding effects of the *fem-3* mutant background (since FEM-3 affects the control of spermatogenesis), we carried these experiments out using populations of karyotypically normal XO males. For both *rrf-3* mutant and wild-type control samples, a *him-8(e1489)* mutation that compromises X-chromosome pairing primarily in oocytes was used to generate populations with large numbers of males (HODGKIN *et al.* 1979).

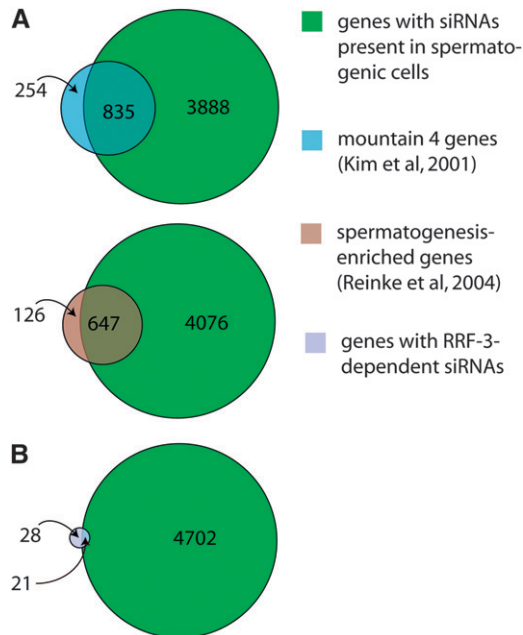


FIGURE 7.—Overlap between siRNA- and mRNA-based gene expression categories. (A) The genes with siRNAs present in spermatogenic cells are the majority of genes whose mRNAs have enriched expression during spermatogenesis. Venn diagrams display the numbers of genes either shared between two categories or exclusive to either category. Genes with siRNAs present in spermatogenic cells had an siRNA count of at least three from the isolated spermatogenic cell sample. Genes in mountain 4 (KIM *et al.* 2001) and spermatogenesis-enriched (REINKE *et al.* 2004) categories are associated with enriched mRNA expression during spermatogenesis as measured by comparative microarray analyses. Only genes that had probes on the microarrays and were present in the cDNA data set used for aligning small RNA sequences were counted in each category. (B) The candidate RRF-3 regulatory targets are enriched for genes with siRNAs present in spermatogenic cells. Relative siRNA expression levels were measured by siRNA sequencing from two sets of *him-8(e1489)* adult males (mutant and wild type for *rf-3*). Forty-nine genes whose siRNA alignment counts were decreased by at least threefold with a *P*-value of <0.005 in *rf-3(pk1426)* in both sets were categorized as candidate RRF-3 regulatory targets.

siRNA profiles from the *him-8(e1489)* whole males and from the isolated *fem-3(q20)* hermaphrodite spermatogenic cells were generally similar in that genes with abundant siRNAs in one sample tended to be abundant in the other, but a number of genes did show genotype/tissue specificity (Figure S6). To increase the stringency of our analysis, we prepared two sets of males of each genotype at 25° using different population synchronization methods for each set. We aligned the sequences from each sample to the cDNA data set and compared the siRNA alignment count for each gene in the *rf-3* mutant and control male sample. For the vast majority of genes, we saw little or no effect of *rf-3(pk1426)* on siRNA levels in these assays: $<5\%$ of the genes had reproducible, greater-than-twofold decreases in siRNAs levels. A subset of genes showed dramatic effects, however, and

we chose to track 49 genes whose expression is likely dependent upon RRF-3 by the criterion of a threefold-reduced alignment count with a *P*-value of <0.005 in both sets of experiments (Table 1; MATERIALS AND METHODS).

This list of 49 genes is intended as exemplary rather than complete: other genes appear to have similar properties without quite reaching our arbitrary statistical threshold criteria, while still more may produce siRNAs that are expressed at levels insufficient for statistical significance in these analyses. In addition, alignment of the small RNA sequences to the genome without regard to predicted coding status revealed additional unannotated loci with small RNAs dependent upon RRF-3, such as the previously identified RRF-3-dependent locus on the X chromosome called the X cluster (AMBROS *et al.* 2003; DUCHAINE *et al.* 2006). The two genes on the list of 49 with the highest siRNA levels, *C44B11.6* and *K02E2.6*, have previously been shown by siRNA Northern analysis to require RRF-3 for siRNA accumulation, providing an independent confirmation of our experimental approach (DUCHAINE *et al.* 2006; LEE *et al.* 2006).

For any of these genes to be regulated by an RRF-3-driven mechanism during spermatogenesis, one would expect that both their mRNAs and siRNAs would be expressed during spermatogenesis. We found 5.2-fold enrichment for the mountain 4 expression category and 4.6-fold enrichment for the spermatogenesis-enriched category in our list of 49 candidate RRF-3 target genes, indicating that a substantial fraction of RRF-3-regulated genes are expressed during spermatogenesis (Table 1; Figure 7B). We also used an siRNA alignment count from spermatogenic cells as a means of ranking the candidate gene list in terms of the likelihood of spermatogenesis gene regulation. As before, we split the list into two categories using a spermatogenesis siRNA alignment count of 3 as the threshold, resulting in 21 genes with spermatogenesis siRNAs and 28 without (Table 1). These 21 genes with spermatogenesis siRNAs and dependency on RRF-3 represent a sample of candidate RRF-3 regulatory targets during spermatogenesis. An important result of this analysis was that RRF-3 had little or no effect on gene-specific siRNA counts for the majority of the 4723 genes with spermatogenesis siRNAs (Figure 8): $<4\%$ of the genes had reproducible, greater-than-twofold decreases in siRNA levels in *rf-3(pk1426)* relative to control *him-8(e1489)* males (69 of 1784 genes; to exclude background noise from genes with low siRNA alignment counts, only genes with counts of at least 25 in both sets of control males were included). This result is consistent with the existence of many other RNAi-related factors with substantial germline phenotypes (COX *et al.* 1998; SMARDON *et al.* 2000; KNIGHT and BASS 2001; TOPS *et al.* 2005; CHEN *et al.* 2007).

In addition to mRNA-encoding genes, we examined small RNAs corresponding to a large number of repeated

TABLE 1
Candidate RRF-3 regulatory targets

Gene name	Annotation	siRNA alignment count from isolated spermatogenic cells	Expression mountain (Kim <i>et al.</i> 2001)	Expression category (REINKE <i>et al.</i> 2004)	Fold increase in <i>rrf-3</i> and <i>eri-1</i> mutants (ASKAINEN <i>et al.</i> 2007)	
					<i>rrf-3</i>	<i>eri-1</i>
<i>K09G1.2</i>		141	4	Unassigned	5.44	5.16
<i>Y47D3A.30 (elo-8)</i>	Polyunsaturated fatty acid elongase	91	4	Mixed spermatogenesis: somatic	CND	CND
<i>C05C12.5</i>		31	Unassigned	Spermatogenesis-enriched	2.44	2.91
<i>R10F2.1 (adhl-1)</i>	Cadherin	29	9, 10, 3, 0	Unassigned	CND	CND
<i>C36H8.1</i>	MSP domain	25	4	Spermatogenesis-enriched	CND	CND
<i>B0523.1 (him-31)</i>	Protein kinase	22	4	Spermatogenesis-enriched	CND	CND
<i>W09G10.6 (lec-125)</i>	C-type lectin	22	26	Male soma: enriched	CND	CND
<i>C44B11.6</i>		17	—	—	—	—
<i>B0348.5</i>		15	7, 1	Unassigned	CND	CND
<i>F18C5.4</i>		12	4	Spermatogenesis: enriched	CND	CND
<i>F37E3.3</i>	Protein kinase	11	4	Intrinsic	CND	1.92
<i>K02E2.6</i>	Retroviral aspartyl protease	11	6	Unassigned	CND	1.86
<i>Y41C4A.13</i>		11	Unassigned	Unassigned	CND	CND
<i>F55H12.1 (snf-2)</i>	Sodium:neurotransmitter symporter	10	4	Spermatogenesis-enriched	CND	3.10
<i>E01G4.7</i>		8	—	—	—	—
<i>K11C4.1</i>	Protein kinase	7	4	Spermatogenesis-enriched	CND	2.15
<i>K08D10.7 (scrm-8)</i>	Phospholipid scramblase	6	4	Spermatogenesis-enriched	CND	2.16
<i>W05H12.2</i>		5	Unassigned	Unassigned	CND	CND
<i>Y82E9BL.18</i>	Cyclin-like F-box, FTH domain	4	—	—	—	—
<i>F36A2.11</i>		3	4	Spermatogenesis-enriched	4.06	4.13
<i>H16D19.4</i>		3	2	Unassigned	CND	CND
<i>Y37E11B.2</i>		2	6	Unassigned	CND	CND
<i>Y17D7C.1</i>		1	3	Unassigned	CND	CND
<i>T08B6.2</i>		1	0	Unassigned	CND	CND
<i>Y17D7B.4</i>	7-Transmembrane receptor	1	8	Unassigned	CND	CND
<i>C36A4.11</i>		1	—	—	—	—
<i>K06B9.6</i>		1	—	—	—	—
<i>W04B5.2</i>		1	0	Unassigned	CND	CND
<i>F52D2.6</i>		1	7	Mixed oogenesis-somatic	CND	CND
<i>C01G8.2 (chr-3.2)</i>	Transmembrane protein	1	2	Unassigned	CND	CND
<i>W04B5.1</i>		1	Unassigned	Unassigned	CND	CND
<i>E01G4.5</i>	Protease inhibitor 14, serpin	1	1	Mixed oogenesis-somatic	CND	CND
<i>Y116A8A.3 (lec-193)</i>	C-type lectin	1	Unassigned	Mixed oogenesis-somatic	CND	CND
<i>Y116A8A.1 (lec-192)</i>	C-type lectin (pseudogene)	1	10	Male sex- enriched	CND	CND
<i>F39E9.7</i>	Staufen double-stranded RNA binding	0	12	Unassigned	CND	CND

(continued)

TABLE 1
(Continued)

Gene name	Annotation	siRNA alignment count from isolated spermatogenic cells	Expression mountain (Kim <i>et al.</i> 2001)	Expression category (REINKE <i>et al.</i> 2004)	Fold increase in <i>rrf-3</i> and <i>eri-1</i> mutants (ASIKAINEN <i>et al.</i> 2007)	
					<i>rrf-3</i>	<i>eri-1</i>
F55A4.4	Staufen double-stranded RNA binding	0	Unassigned	Unassigned	CND	CND
Y43F8B.9		0	15	Unassigned	CND	CND
Y7A5A.8	Nepriylisin	0	0	Male sex-enriched	CND	CND
C18D4.4		0	15	Unassigned	CND	CND
F39E9.6		0	12	Male sex-enriched	CND	CND
Y7A5A.3		0	3, 0	Male soma: enriched	CND	CND
F14F7.5	WSN domain	0	0	Unassigned	CND	CND
F07G6.6 (<i>fbxa-52</i>)	FTH domain	0	0	Unassigned	CND	CND
Y46D2A.1		0	—	Unassigned	CND	CND
Y26D4A.17		0	3	—	—	—
Y9D1A.1		0	12	Unassigned	CND	CND
H09G03.1		0	3	Unassigned	CND	CND
ZK380.5		0	—	—	—	—
M142.1 (<i>unc-119</i>)	GMP phosphodiesterase, Δ-subunit	0	1	Unassigned	CND	CND

The 49 genes with reduced siRNA alignment counts in *rrf-3(pk1426)* in both sets of whole-male samples were ranked according to siRNA alignment count from the isolated spermatogenic cell sample. The 21 genes with siRNA alignment counts of three or more from the spermatogenesis isolate (above the dashed line) were categorized as candidate spermatogenesis RRF-3 targets. Categorization from KIM *et al.* (2001) and REINKE *et al.* (2004) is based on mRNA expression measured by microarrays. Mountain 4 genes tend to have spermatogenesis enrichment. Increases in mRNA levels in *rrf-3* and *eri-1* mutants are based on mRNA microarray analysis from ASIKAINEN *et al.* (2007) and S. ASIKAINEN and G. WONG (personal communication). —, not included on the microarray; CND, change not detected.

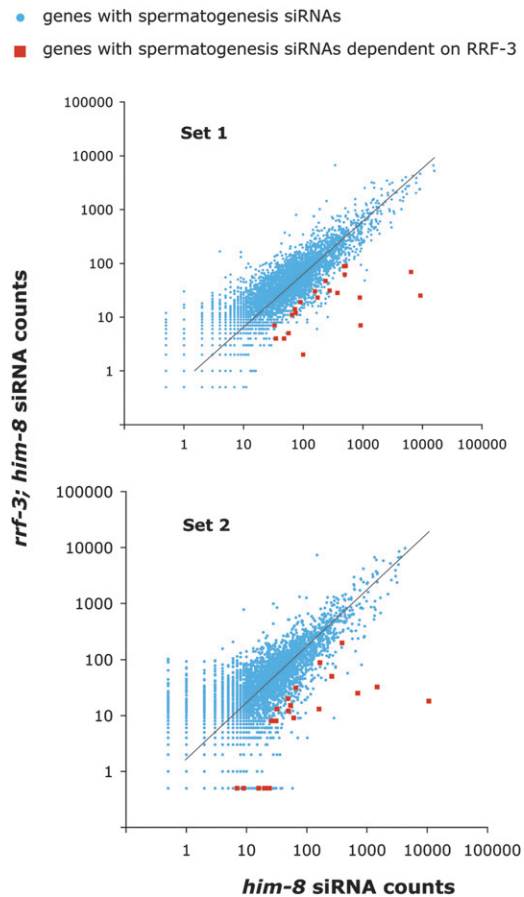


FIGURE 8.—Global RRF-3 effects on spermatogenesis siRNA accumulation. Scatter plots depict the siRNA alignment count per gene from *him-8(e1489)* control males (*x*-axis) and from *rrf-3(pk1426); him-8(e1489)* (*y*-axis). Blue dots correspond to the 4723 genes with spermatogenic cell siRNAs. Red dots correspond to the 21 genes with both spermatogenic siRNAs and dependency on RRF-3. Genes with siRNA alignment counts of zero were assigned a value of 0.5 to avoid exclusion from the logarithmically scaled plots. The trendlines indicate the expected siRNA alignment counts per gene if both samples were derived from the same population. On a linear scaled plot, the slopes deviate from 45° because of differences in sample sizes.

and/or transposable elements (http://www.sanger.ac.uk/Projects/C_elegans/REPEATS/elegans.lib). From this analysis we found that many transposons, especially Helitron (264 siRNAs aligned to a HELICOP1 sequence) and Tc1/mariner transposons (87 siRNAs aligned to a Tc1 sequence), were associated with high siRNA alignment counts from the spermatogenic cell sample. We did not find any transposons that required RRF-3 by the criteria of a threefold reduction in siRNA alignment count and a *P*-value of <0.005 between mutant and control from both sets of samples. Intriguingly, we found three cases in which siRNAs corresponding to a transposon were significantly more abundant in *rrf-3* mutants: CELE1, LINE2, and TURMOIL2. Of these, only TURMOIL2 had siRNAs present in the spermatogenic cell sample. The increased siRNAs from these transposons could reflect an activation

of RNAi-like processes as has previously been observed in exogenous RNAi and transgene silencing (Sijten *et al.* 2001; Simmer *et al.* 2002).

siRNAs produced by RRF-3 and ERI-1 function to downregulate mRNA levels during spermatogenesis: In the absence of RRF-3 or ERI-1, at least one putative target, *KO2E2.6*, has been shown to have increased mRNA levels (Duchaine *et al.* 2006). To test whether RRF-3 and ERI-1 generally act to downregulate their spermatogenesis targets, we compared the RRF-3 regulatory candidates with a global microarray analysis of RRF-3 and ERI-1 effects on mRNA levels in hermaphrodites undergoing spermatogenesis (Asikainen *et al.* 2007; S. ASIKAINEN and G. WONG, personal communication). We first note some limitations in the comparison with the microarray analysis: Three of the 21 genes that we identified as differentially regulated in males were not included in the microarrays used by ASIKAINEN *et al.* (2007). Furthermore, ASIKAINEN *et al.* (2007) reported data for whole L4 hermaphrodites, in which sperm or sperm precursors may have been a relatively rare component (so that substantial differences in spermatogenic mRNA abundance could have been masked by pools of unaffected somatic RNA). Similarly, spermatogenic cell-type-specific silencing could be hard to detect in the background of other sperm precursor cells still expressing the transcript at normal levels. Despite these limitations, it is of considerable interest to compare our siRNA data with the mRNA abundances determined by ASIKAINEN *et al.* (2007; Table 1). Of the 18 genes that were included in the microarray analysis and with RRF-3-dependent spermatogenesis siRNAs, 3 showed increased mRNA levels in both *rrf-3* and *eri* mutants, and an additional 5 showed increased mRNA levels in *eri-1* mutants alone (15.8-fold enrichment with a *P*-value of 8.8×10^{-4} for the *rrf-3* mutant; 10.6-fold enrichment with a *P*-value of 2.9×10^{-7} for the *eri-1* mutant; see MATERIALS AND METHODS).

DISCUSSION

Evidence for a developmental role for RRF-3 during spermatogenesis: Small RNA pathway functions are commonly categorized as defensive (*e.g.*, suppression of transposable elements and viruses) or regulatory (*e.g.*, downregulation of mRNA levels during development). Either function can be essential, as exemplified by the critical roles of microRNA developmental regulators (reviewed in FLYNT and LAI 2008) and by the roles of piRNAs in transposon control (reviewed in KLATTENHOFF and THEURKAUF 2008). These developmental/defense roles of small RNAs can overlap, as illustrated by a human cellular microRNA that targets a viral RNA (LECELLIER *et al.* 2005) and by the recent description of a *C. elegans* small RNA family (21U- or piRNAs) that apparently modulates both transpo-

sons and cellular transcripts during spermatogenesis (BATISTA *et al.* 2008; DAS *et al.* 2008; WANG and REINKE 2008). Although products of cellular RdRPs apparently differ from piRNAs in both structure and biosynthetic mode, some RdRPs can participate in responses to foreign nucleic acids, including quelling in *Neurospora crassa* (COGONI and MACINO 1999) and viral defense in *Arabidopsis* (MOURRAIN *et al.* 2000). On the basis of developmental phenotypes in mutant strains, other RdRP components have been hypothesized to carry out endogenous regulatory roles (SMARDON *et al.* 2000; SHIU and METZENBERG 2002).

Several characteristics of RRF-3 (the temperature-dependent character and the requirement for RRF-3 in a defined developmental pathway such as spermatogenesis) facilitate a detailed analysis of siRNAs associated with RRF-3 function and their potential regulatory roles. Using high-throughput sequencing as a tool for characterizing RNA populations, we found that antisense siRNAs corresponding to a variety of both transposable elements and cellular mRNAs are present in spermatogenic cells. Among the large and diverse set of cellular mRNAs reflected in the pool of siRNAs, we found a strong enrichment for those with expression during spermatogenesis (in particular, with mRNAs known to have elevated expression during spermatogenesis; KIM *et al.* 2001; REINKE *et al.* 2004). By comparing whole males either mutant or wild type for *rrf-3*, we have identified exemplary cellular mRNAs for which siRNA production during spermatogenesis depends on RRF-3. These cellular mRNAs show strong enrichment for previously identified genes whose mRNA levels are elevated in populations of whole animals in both *rrf-3* and *eri-1* mutants (ASIKAINEN *et al.* 2007).

RRF-3 and paternal contributions to embryogenesis:

In principle, paternal-effect lethality associated with RRF-3 and ERI-1 mutants could result either from a lack of sperm-provided factors essential for normal embryogenesis or from pathological effects of inappropriate sperm content. We favor the latter possibility for several reasons of parsimony. First, RNAi pathways are known to function broadly in downregulation of gene expression, such that loss-of-function mutations result in overexpression of spermatogenic factors. Second, the presence of ectopic microtubule structures that we observed in mutant sperm (and later defective microtubule structures in embryos) suggests failure to eliminate at least one structure (microtubules) during budding of spermatids. Whether due to sequestration defects or ectopic microtubule polymerization after budding, a plausible interpretation is that microtubules or associated factors in mutant sperm could have a pathological effect in embryos.

Production of functionally normal sperm requires a highly specialized cellular differentiation program to generate cells that are motile, fertilization competent, and capable of contributing centrioles (which will

nucleate the first mitotic spindles) and other polarity cues. Numerous genes whose expression is enriched or specific to spermatogenesis indicate that sperm production involves induction of gene expression programs (KIM *et al.* 2001; REINKE *et al.* 2004; JOHNSTON *et al.* 2008). As with virtually any biological process, it would be expected that biological functions will also need to be downregulated during sperm differentiation (LAMITINA and L'HERNAULT 2002; MUHLRAD and WARD 2002; KHALIL *et al.* 2004). In systems with interacting and potentially cooperating controls, loss of a single regulatory modality frequently leads to a conditional (rather than absolute) effect. For example, null mutations in certain regulators produce specific temperature-sensitive somatic phenotypes during larval development in *C. elegans* (GOLDEN and RIDDLE 1984; MELENDEZ and GREENWALD 2000). Spermatogenesis in *C. elegans* is particularly temperature-sensitive even in wild-type worms (which become sterile if spermatogenesis is attempted at 27° (SHAPIRA and TAN 2008). Null mutants of other *C. elegans* small RNA-related genes, including the Piwi-related gene *prg-1*, share an apparent null-mutant temperature-sensitive spermatogenesis character (BATISTA *et al.* 2008; DAS *et al.* 2008; WANG and REINKE 2008).

Models for negative regulation of gene expression by RRF-3: A “simple” model for RRF-3 function during spermatogenesis would entail RRF-3 association with a set of transcripts, specific synthesis of small RNA pools from these transcripts, subsequent downregulation of new synthesis for the corresponding protein products, and a contribution of this downregulation in providing balanced protein product levels to allow for an efficient developmental process (spermatogenesis) under diverse conditions.

Despite the attractiveness of such a model, we note that our data do not establish a direct connection between RRF-3, the production of siRNAs from specific mRNA transcripts, the observed RRF-3-dependent downregulation, and spermatogenic phenotypes resulting in the mutant background. Certainly, the observation of similar sets of template mRNAs, siRNA products, mRNA modulation, and spermatogenic/embryonic phenotypes in at least one other member (ERI-1) of the ERI protein supercomplex where RRF-3 is known to reside argues for concerted participation of this complex in a defined regulatory process in sperm. We note that small RNA biogenesis and regulatory mechanisms in *C. elegans* and other organisms are sufficiently complex and multimodal, so that assuming that the siRNAs identified here are the immediate products of RRF-3 may be an oversimplification.

From the observed defects in sperm form and function, it was somewhat surprising to observe only a small number of genes for which siRNA production requires RRF-3. Given a requirement for the alternative RNA-directed RNA polymerase EGO-1 during spermatogenesis

genesis (SMARDON *et al.* 2000), it seems plausible that two distinct classes of the *cis*-acting RNA signal (one for EGO-1 and one for RRF-3) are responsible for functional RdRP recruitment and subsequent genetic repression. Incomplete loss of RRF-3 target siRNAs in *rrf-3* mutants suggests redundancy with other RdRPs or with other mechanisms that trigger siRNA production. EGO-1, RRF-3, and the other *C. elegans* RdRPs thus may overlap in their recognition of target RNAs due to either overlapping signal specificity of RdRP recruitment or differential timing of RdRP expression relative to developmental events. We stress that our lists of regulated genes (at the siRNA and mRNA levels) are exemplary and not complete: in addition to the genes that missed our detection due to siRNA expression that is redundantly triggered, we would have failed to detect unannotated genes, genes where siRNA expression was limited to hermaphrodites, or genes where siRNAs were at a level too low or too transient to be detected in the analysis.

Despite the incompleteness of the identified regulated gene set, it is important to note that the majority of genes showed no difference in either mRNA or siRNA expression in *rrf-3* mutant animals. Thus the RRF-3 system appears somewhat exclusive in its choice of “client.” Misregulation of a small set of genes, or even of a single gene, could certainly have drastic effects on spermatogenesis. Single-gene requirements in *C. elegans* spermatogenesis have been extensively investigated in the literature, with hundreds of conditional and numerous nonconditional spermatogenesis mutants in several dozen genes (reviewed in L’HERNAULT 2009). While a single-gene process would be tempting to propose, multigenic requirements for developmental regulation have also been demonstrated in many small RNA-regulated systems; in the case of RRF-3 regulation, the existence of at least several dozen RRF-3-dependent siRNA templates suggests that the observed phenotypic syndrome could involve more than one target.

Our work, combined with other recent analyses, suggests the potential for at least four negative regulatory mechanisms that use small RNA effectors during spermatogenesis and that involve microRNAs (RO *et al.* 2007; MARCON *et al.* 2008), piRNAs (reviewed in KLATTENHOFF and THEURKAUF 2008), RRF-3-dependent siRNAs (PAVELEC *et al.* 2009), and RRF-3-independent siRNAs. Each of these four mechanisms appears poised to control a specific set of RNA targets in a manner that would depend on the expression patterns for specific mRNAs and relevant populations of small RNA effectors.

RdRPs as providers of inexpensive feedback regulation: For conventional feedback regulation (*e.g.*, employing a transcription factor), a biological system must be devised such that a specific repressive interaction between a gene product (or a metabolite that depends on the gene product) and the corresponding RNA or protein occurs. RdRP-based mechanisms provide a

much less costly mechanism to generate a self-regulated system. A key requirement for such a system is a negative regulator whose accumulation at any given time depends on the concentration of a product. An RdRP system would allow any gene to engage in feedback regulation by addition of an RdRP recruitment signal to its transcript. This would also provide the capacity to convert any “off-to-on” system into a temporal spike, since strong RdRP recruitment would result in a system in which an initial burst of gene expression could be self-silencing. Importantly for this potential contribution to gene regulation, the RdRP system could be present as a relatively ubiquitous component of cellular machinery, with any message to be autoregulated simply needing to make docking sites available for RdRP to acquire negative regulation following any burst of synthesis.

We thank Anton Gartner for anti-RAD-51, Josef Loidl for anti-REC-8, and Abby Dernburg for anti-HIM-8; Ayelet Lamm for flow cell preparation; Cheryl Smith, Ziming Weng, Phil Lacroute, Anton Valouev, and Arend Sidow for flow cell preparation, sequencing, and data processing; Weng-Onn Lui, Julia Pak, Poornima Parameswaran, and Jay Maniar for ideas on the preparation of small RNA libraries for sequencing; Virginia Walbot for comments on the manuscript; the Caenorhabditis Genetics Center for strains; and Suvi Asikainen, Gary Wong, Derek Pavelec, and Scott Kennedy for sharing data. This work was supported by National Institutes of Health (NIH) grant R01GM37706 to A.Z.F.; NIH grant R01GM53804 to A.M.V.; and a Vienna Science and Technology Fund WWTF grant LS05009 and an Austrian Science Fund FWF Elise Richter grant to V.J. J.I.G. was supported by the Stanford Department of Biological Sciences and by the Stanford Genome Training Program (NHGRI-T32-HG00044), and M.S. was supported by a Canadian Institutes of Health Research postdoctoral fellowship.

LITERATURE CITED

- ALPI, A., P. PASIERBEK, A. GARTNER and J. LOIDL, 2003 Genetic and cytological characterization of the recombination protein RAD-51 in *Caenorhabditis elegans*. *Chromosoma* **112**: 6–16.
- AMBROS, V., R. C. LEE, A. LAVANWAY, P. T. WILLIAMS and D. JEWELL, 2003 MicroRNAs and other tiny endogenous RNAs in *C. elegans*. *Curr. Biol.* **13**: 807–818.
- ASIKAINEN, S., M. STORVIK, M. LAKSO and G. WONG, 2007 Whole genome microarray analysis of *C. elegans* *rrf-3* and *eri-1* mutants. *FEBS Lett.* **581**: 5050–5054.
- BABIARZ, J. E., J. G. RUBY, Y. WANG, D. P. BARTEL and R. BLELLOCH, 2008 Mouse ES cells express endogenous shRNAs, siRNAs, and other microprocessor-independent, Dicer-dependent small RNAs. *Genes Dev.* **22**: 2773–2785.
- BARTON, M. K., T. B. SCHEDL and J. KIMBLE, 1987 Gain-of-function mutations of *fem-3*, a sex-determination gene in *Caenorhabditis elegans*. *Genetics* **115**: 107–119.
- BATISTA, P. J., J. G. RUBY, J. M. CLAYCOMB, R. CHIANG, N. FAHLGREN *et al.*, 2008 PRG-1 and 21U-RNAs interact to form the piRNA complex required for fertility in *C. elegans*. *Mol. Cell* **31**: 67–78.
- BRENNER, S., 1974 The genetics of *Caenorhabditis elegans*. *Genetics* **77**: 71–94.
- CHEN, Y., A. PANE and T. SCHUPBACH, 2007 Cutoff and aubergine mutations result in retrotransposon upregulation and checkpoint activation in *Drosophila*. *Curr. Biol.* **17**: 637–642.
- COGONI, C., and G. MACINO, 1999 Gene silencing in *Neurospora crassa* requires a protein homologous to RNA-dependent RNA polymerase. *Nature* **399**: 166–169.
- COLAIACOVO, M. P., A. J. MACQUEEN, E. MARTINEZ-PEREZ, K. McDONALD, A. ADAMO *et al.*, 2003 Synaptonemal complex assembly in *C. elegans* is dispensable for loading strand-exchange

- proteins but critical for proper completion of recombination. *Dev. Cell* **5**: 463–474.
- COX, D. N., A. CHAO, J. BAKER, L. CHANG, D. QIAO *et al.*, 1998 A novel class of evolutionarily conserved genes defined by piwi are essential for stem cell self-renewal. *Genes Dev.* **12**: 3715–3727.
- DAS, P. P., M. P. BAGIJN, L. D. GOLDSTEIN, J. R. WOOLFORD, N. J. LEHRBACH *et al.*, 2008 Piwi and piRNAs act upstream of an endogenous siRNA pathway to suppress Tc3 transposon mobility in the *Caenorhabditis elegans* germline. *Mol. Cell* **31**: 79–90.
- DERNBURG, A. F., K. McDONALD, G. MOULDER, R. BARSTEAD, M. DRESSER *et al.*, 1998 Meiotic recombination in *C. elegans* initiates by a conserved mechanism and is dispensable for homologous chromosome synapsis. *Cell* **94**: 387–398.
- DUCHAUINE, T. F., J. A. WOHLSCHEGEL, S. KENNEDY, Y. BEI, D. CONTE, JR. *et al.*, 2006 Functional proteomics reveals the biochemical niche of *C. elegans* DCR-1 in multiple small-RNA-mediated pathways. *Cell* **124**: 343–354.
- EDGLEY, M. L., and D. L. RIDDLE, 2001 LG II balancer chromosomes in *Caenorhabditis elegans*: mT1 (II/III) and the mIn1 set of dominantly and recessively marked inversions. *Mol. Genet. Genomics* **266**: 385–395.
- FLYNT, A. S., and E. C. LAI, 2008 Biological principles of microRNA-mediated regulation: shared themes amid diversity. *Nat. Rev. Genet.* **9**: 831–842.
- GHILDIYAL, M., H. SEITZ, M. D. HORWICH, C. LI, T. DU *et al.*, 2008 Endogenous siRNAs derived from transposons and mRNAs in *Drosophila* somatic cells. *Science* **320**: 1077–1081.
- GOLDEN, J. W., and D. L. RIDDLE, 1984 A pheromone-induced developmental switch in *Caenorhabditis elegans*: temperature-sensitive mutants reveal a wild-type temperature-dependent process. *Proc. Natl. Acad. Sci. USA* **81**: 819–823.
- GONCZY, P., S. PICHLER, M. KIRKHAM and A. A. HYMAN, 1999 Cytoplasmic dynein is required for distinct aspects of MTOC positioning, including centrosome separation, in the one cell stage *Caenorhabditis elegans* embryo. *J. Cell Biol.* **147**: 135–150.
- HODGKIN, J., H. R. HORVITZ and S. BRENNER, 1979 Nondisjunction mutants of the nematode *Caenorhabditis elegans*. *Genetics* **91**: 67–94.
- HUTVAGNER, G., and M. J. SIMARD, 2008 Argonaute proteins: key players in RNA silencing. *Nat. Rev. Mol. Cell Biol.* **9**: 22–32.
- JOHNSTON, D. S., W. W. WRIGHT, P. DICANDELORO, E. WILSON, G. S. KOPF *et al.*, 2008 Stage-specific gene expression is a fundamental characteristic of rat spermatogenic cells and Sertoli cells. *Proc. Natl. Acad. Sci. USA* **105**: 8315–8320.
- KEENEY, S., C. N. GIROUX and N. KLECKNER, 1997 Meiosis-specific DNA double-strand breaks are catalyzed by Spo11, a member of a widely conserved protein family. *Cell* **88**: 375–384.
- KENNEDY, S., D. WANG and G. RUVKUN, 2004 A conserved siRNA-degrading RNase negatively regulates RNA interference in *C. elegans*. *Nature* **427**: 645–649.
- KENT, W. J., 2002 BLAT: the BLAST-like alignment tool. *Genome Res.* **12**: 656–664.
- KHALIL, A. M., F. Z. BOYAR and D. J. DRISCOLL, 2004 Dynamic histone modifications mark sex chromosome inactivation and reactivation during mammalian spermatogenesis. *Proc. Natl. Acad. Sci. USA* **101**: 16583–16587.
- KIM, S. K., J. LUND, M. KIRALY, K. DUKE, M. JIANG *et al.*, 2001 A gene expression map for *Caenorhabditis elegans*. *Science* **293**: 2087–2092.
- KLASS, M. R., and D. HIRSH, 1981 Sperm isolation and biochemical analysis of major sperm protein from *Caenorhabditis elegans*. *Dev. Biol.* **84**: 299–312.
- KLATTENHOFF, C., and W. THEURKAUF, 2008 Biogenesis and germline functions of piRNAs. *Development* **135**: 3–9.
- KLATTENHOFF, C., D. P. BRATU, N. MCGINNIS-SCHULTZ, B. S. KOPPETSCH, H. A. COOK *et al.*, 2007 *Drosophila* rasiRNA pathway mutations disrupt embryonic axis specification through activation of an ATR/Chk2 DNA damage response. *Dev. Cell* **12**: 45–55.
- KNIGHT, S. W., and B. L. BASS, 2001 A role for the RNase III enzyme DCR-1 in RNA interference and germ line development in *Caenorhabditis elegans*. *Science* **293**: 2269–2271.
- LAMITINA, S. T., and S. W. L'HERNAULT, 2002 Dominant mutations in the *Caenorhabditis elegans* Myt1 ortholog wee-1.3 reveal a novel domain that controls M-phase entry during spermatogenesis. *Development* **129**: 5009–5018.
- LAMUNYON, C. W., and S. WARD, 1994 Assessing the viability of mutant and manipulated sperm by artificial insemination of *Caenorhabditis elegans*. *Genetics* **138**: 689–692.
- LAMUNYON, C. W., and S. WARD, 1995 Sperm precedence in a hermaphroditic nematode (*Caenorhabditis elegans*) is due to competitive superiority of male sperm. *Experientia* **51**(8): 817–823.
- LAU, N. C., L. P. LIM, E. G. WEINSTEIN and D. P. BARTEL, 2001 An abundant class of tiny RNAs with probable regulatory roles in *Caenorhabditis elegans*. *Science* **294**: 858–862.
- LECELLIER, C. H., P. DUNOYER, K. ARAR, J. LEHMANN-CHE, S. EYQUEM *et al.*, 2005 A cellular microRNA mediates antiviral defense in human cells. *Science* **308**: 557–560.
- LEE, R. C., C. M. HAMMELL and V. AMBROS, 2006 Interacting endogenous and exogenous RNAi pathways in *Caenorhabditis elegans*. *RNA* **12**: 589–597.
- L'HERNAULT, S. W., 2009 The genetics and cell biology of spermatogenesis in the nematode *C. elegans*. *Mol. Cell. Endocrinol.* **306**: 59–65.
- L'HERNAULT, S. W., and T. M. ROBERTS, 1995 Cell biology of nematode sperm. *Methods Cell Biol.* **48**: 273–301.
- MACHACA, K., L. J. DEFELICE and S. W. L'HERNAULT, 1996 A novel chloride channel localizes to *C. elegans* spermatids and chloride channel blockers induce spermatid differentiation. *Dev. Biol.* **176**: 1–16.
- MACQUEEN, A. J., M. P. COLAIACOVO, K. McDONALD and A. M. VILLENEUVE, 2002 Synapsis-dependent and -independent mechanisms stabilize homolog pairing during meiotic prophase in *C. elegans*. *Genes Dev.* **16**: 2428–2442.
- MADL, J. E., and R. K. HERMAN, 1979 Polyploids and sex determination in *Caenorhabditis elegans*. *Genetics* **93**: 393–402.
- MAINE, E. M., J. HAUTH, T. RATLIFF, V. E. VOUGHT, X. SHE *et al.*, 2005 EGO-1, a putative RNA-dependent RNA polymerase, is required for heterochromatin assembly on unpaired DNA during *C. elegans* meiosis. *Curr. Biol.* **15**: 1972–1978.
- MARCON, E., T. BABAK, G. CHUA, T. HUGHES and P. B. MOENS, 2008 miRNA and piRNA localization in the male mammalian meiotic nucleus. *Chromosome Res.* **16**: 243–260.
- MARTINEZ-PEREZ, E., and A. M. VILLENEUVE, 2005 HTP-1-dependent constraints coordinate homolog pairing and synapsis and promote chiasma formation during *C. elegans* meiosis. *Genes Dev.* **19**: 2727–2743.
- MARTINEZ-PEREZ, E., M. SCHVARZSTEIN, C. BARROSO, J. LIGHTFOOT, A. F. DERNBURG *et al.*, 2008 Crossovers trigger a remodeling of meiotic chromosome axis composition that is linked to two-step loss of sister chromatid cohesion. *Genes Dev.* **22**: 2886–2901.
- MELLENDEZ, A., and I. GREENWALD, 2000 *Caenorhabditis elegans* lin-13, a member of the LIN-35 Rb class of genes involved in vulval development, encodes a protein with zinc fingers and an LXCXE motif. *Genetics* **155**: 1127–1137.
- MILLER, M. A., 2006 Sperm and oocyte isolation methods for biochemical and proteomic analysis. *Methods Mol. Biol.* **351**: 193–201.
- MOURRAIN, P., C. BECLIN, T. ELMAYAN, F. FEUERBACH, C. GODON *et al.*, 2000 Arabidopsis SGS2 and SGS3 genes are required for post-transcriptional gene silencing and natural virus resistance. *Cell* **101**: 533–542.
- MUHLRAD, P. J., and S. WARD, 2002 Spermiogenesis initiation in *Caenorhabditis elegans* involves a casein kinase 1 encoded by the *spe-6* gene. *Genetics* **161**: 143–155.
- NIGON, V., 1951 Polyplôidie expérimentale chez un nematode libre. *Bull. Biol. Fr. Belg.* **85**: 187–225.
- OEGEMA, K., A. DESAI, S. RYBINA, M. KIRKHAM and A. A. HYMAN, 2001 Functional analysis of kinetochore assembly in *Caenorhabditis elegans*. *J. Cell Biol.* **153**: 1209–1226.
- OKKEMA, P. G., and J. KIMBLE, 1991 Molecular analysis of tra-2, a sex determining gene in *C. elegans*. *EMBO J.* **10**: 171–176.
- PAK, J., and A. FIRE, 2007 Distinct populations of primary and secondary effectors during RNAi in *C. elegans*. *Science* **315**: 241–244.
- PANE, A., K. WEHR and T. SCHUPBACH, 2007 Zucchini and squash encode two putative nucleases required for rasiRNA production in the *Drosophila* germline. *Dev. Cell* **12**: 851–862.
- PASIERBEK, P., M. JANTSCH, M. MELCHER, A. SCHLEIFFER, D. SCHWEIZER *et al.*, 2001 A *Caenorhabditis elegans* cohesion protein with functions in meiotic chromosome pairing and disjunction. *Genes Dev.* **15**: 1349–1360.

- PAVELEC, DEREK M., J. LACHOWIEC, T. F. DUCHAINE, H. E. SMITH and SCOTT KENNEDY, 2009 Requirement for ERI/DICER complex in endogenous RNA interference and sperm development in *Caenorhabditis elegans*. *Genetics* **183**: 1283–1295.
- PHILLIPS, C. M., C. WONG, N. BHALLA, P. M. CARLTON, P. WEISER *et al.*, 2005 HIM-8 binds to the X chromosome pairing center and mediates chromosome-specific meiotic synapsis. *Cell* **123**: 1051–1063.
- REINKE, V., I. S. GIL, S. WARD and K. KAZMER, 2004 Genome-wide germline-enriched and sex-biased expression profiles in *Caenorhabditis elegans*. *Development* **131**: 311–323.
- RO, S., C. PARK, K. M. SANDERS, J. R. MCCARREY and W. YAN, 2007 Cloning and expression profiling of testis-expressed microRNAs. *Dev. Biol.* **311**: 592–602.
- ROBERTS, T. M., F. M. PAVALKO and S. WARD, 1986 Membrane and cytoplasmic proteins are transported in the same organelle complex during nematode spermatogenesis. *J. Cell.* **102**: 1787–1796.
- RUBY, J. G., C. JAN, C. PLAYER, M. J. AXTELL, W. LEE *et al.*, 2006 Large-scale sequencing reveals 21U-RNAs and additional microRNAs and endogenous siRNAs in *C. elegans*. *Cell* **127**: 1193–1207.
- SCHEDL, T., and J. KIMBLE, 1988 *fog-2*, a germ-line-specific sex determination gene required for hermaphrodite spermatogenesis in *Caenorhabditis elegans*. *Genetics* **119**: 43–61.
- SCHNABEL, H., and R. SCHNABEL, 1990 An organ-specific differentiation gene, *pha-1*, from *Caenorhabditis elegans*. *Science* **250**: 686–688.
- SHAPIRA, M., and M. W. TAN, 2008 Genetic analysis of *Caenorhabditis elegans* innate immunity. *Methods Mol. Biol.* **415**: 429–442.
- SHIU, P. K., and R. L. METZENBERG, 2002 Meiotic silencing by unpaired DNA: properties, regulation and suppression. *Genetics* **161**: 1483–1495.
- SIJEN, T., J. FLEENOR, F. SIMMER, K. L. THIJSSSEN, S. PARRISH *et al.*, 2001 On the role of RNA amplification in dsRNA-triggered gene silencing. *Cell* **107**: 465–476.
- SIJEN, T., F. A. STEINER, K. L. THIJSSSEN and R. H. PLASTERK, 2007 Secondary siRNAs result from unprimed RNA synthesis and form a distinct class. *Science* **315**: 244–247.
- SIMMER, F., M. TIJSTERMAN, S. PARRISH, S. P. KUSHIKA, M. L. NONET *et al.*, 2002 Loss of the putative RNA-directed RNA polymerase RRF-3 makes *C. elegans* hypersensitive to RNAi. *Curr. Biol.* **12**: 1317–1319.
- SLOTKIN, R. K., M. VAUGHN, F. BORGES, M. TANURDZIC, J. D. BECKER *et al.*, 2009 Epigenetic reprogramming and small RNA silencing of transposable elements in pollen. *Cell* **136**: 461–472.
- SMARDON, A., J. M. SPOERKE, S. C. STACEY, M. E. KLEIN, N. MACKIN *et al.*, 2000 EGO-1 is related to RNA-directed RNA polymerase and functions in germ-line development and RNA interference in *C. elegans*. *Curr. Biol.* **10**: 169–178.
- TABARA, H., M. SARKISSIAN, W. G. KELLY, J. FLEENOR, A. GRISHOK *et al.*, 1999 The *rde-1* gene, RNA interference, and transposon silencing in *C. elegans*. *Cell* **99**: 123–132.
- TOPS, B. B., H. TABARA, T. SIJEN, F. SIMMER, C. C. MELLO *et al.*, 2005 RDE-2 interacts with MUT-7 to mediate RNA interference in *Caenorhabditis elegans*. *Nucleic Acids Res.* **33**: 347–355.
- WANG, G., and V. REINKE, 2008 A *C. elegans* Piwi, PRG-1, regulates 21U-RNAs during spermatogenesis. *Curr. Biol.* **18**: 861–867.
- WARD, S., 1986 *The Asymmetric Localization of Gene Products During the Development of Caenorhabditis elegans Spermatozoa*. A. R. Liss, New York.
- WARD, S., T. M. ROBERTS, S. STROME, F. M. PAVALKO and E. HOGAN, 1986 Monoclonal antibodies that recognize a polypeptide antigenic determinant shared by multiple *Caenorhabditis elegans* sperm-specific proteins. *J. Cell Biol.* **102**: 1778–1786.
- YIGIT, E., P. J. BATISTA, Y. BEI, K. M. PANG, C. C. CHEN *et al.*, 2006 Analysis of the *C. elegans* Argonaute family reveals that distinct Argonautes act sequentially during RNAi. *Cell* **127**: 747–757.

Communicating editor: K. KEMPHUES

GENETICS

Supporting Information

<http://www.genetics.org/cgi/content/full/genetics.109.109686/DC1>

***A Caenorhabditis elegans* RNA-Directed RNA Polymerase in Sperm Development and Endogenous RNA Interference**

**Jonathan I. Gent, Mara Schvarzstein, Anne M. Villeneuve, Sam Guoping Gu,
Verena Jantsch, Andrew Z. Fire and Antoine Baudrimont**

Copyright © 2009 by the Genetics Society of America
DOI: 10.1534/genetics.109.109686

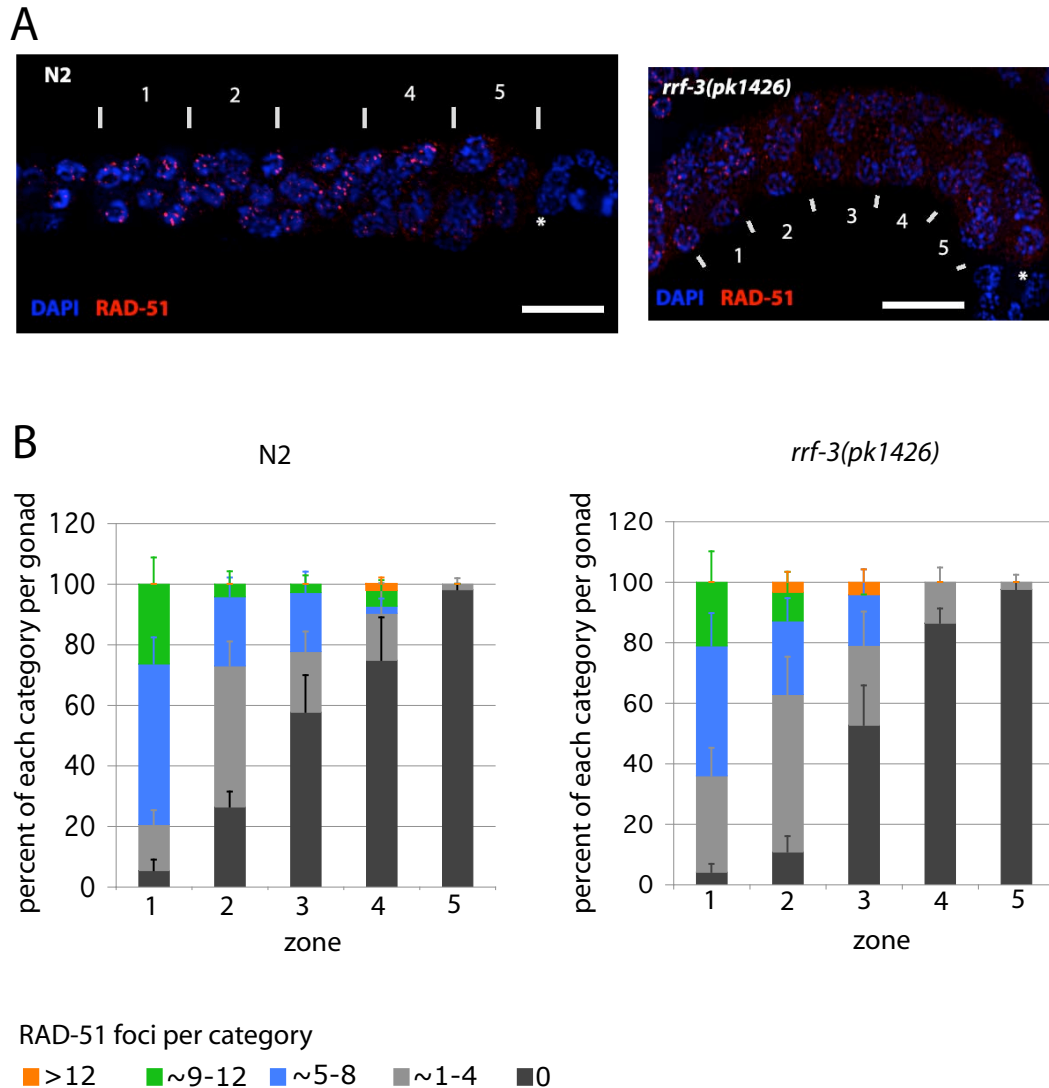


FIGURE S1.—Meiotic chromosome organization—quantification of RAD-51 foci in wildtype and *rrf-3* mutant hermaphrodite gonads undergoing spermatogenesis at 25°C. (A) Partitioning of gonads into zones for scoring. Gonads from L4 larvae were stained with DAPI (blue) and anti-RAD-51 antibody (red). The first 30 nuclei to enter meiosis (the most proximal ones, which give rise to sperm) were identified and the region they occupied divided into five zones of equal length, zone 5 being most proximal. The number of RAD-51 foci in individual nuclei in each zone was counted. Asterisks denote the proximal ends. Scale bars are 10 μ m. (B) Similar patterns in N2 and *rrf-3(pk1426)* RAD-51 foci counts. Zones 1 through 5 of each gonad were categorized according to the number of RAD-51 foci. Six gonads of each genotype were scored. Error bars denote standard errors of the means.

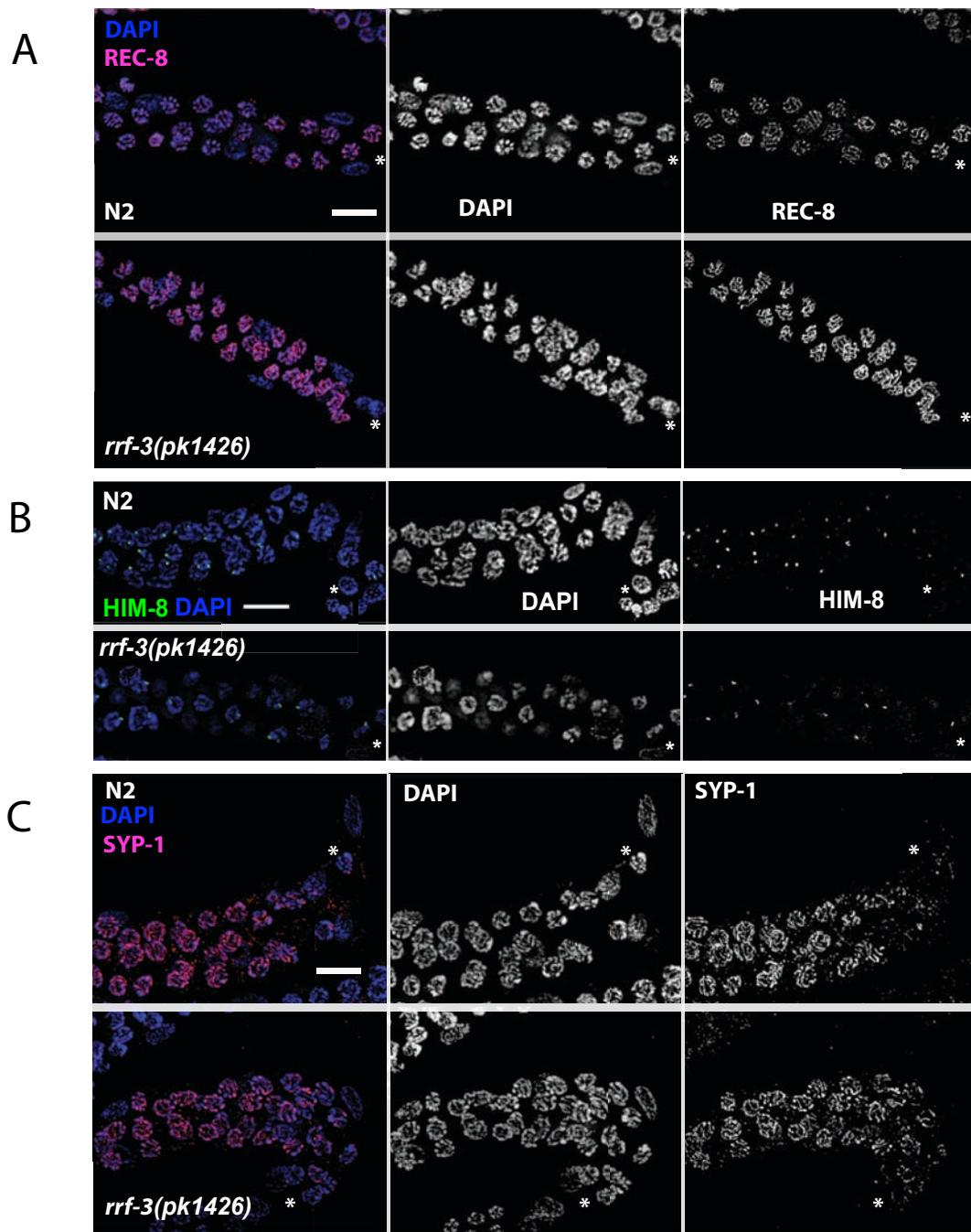


FIGURE S2.—Meiotic chromosome organization—similar patterns in *rrf-3* mutant and wildtype for anti-REC-8 (A) anti-HIM-8 antibody (B) or anti-SYP-1 antibody (C) staining of spermatogenic prophase I nuclei at 25°C. Spermatogenic nuclei in L4 larvae were identified based on their being the first cells to enter meiosis and proximal localization in the gonad (proximal ends marked by asterisks). The scale bars are 10 μ m. (A) In both wildtype and mutant, REC-8 (magenta) is localized in continuous tracks at the interface between parallel aligned DAPI-stained chromosomes (blue). (B) Both wildtype and mutant nuclei have either a single focus or two closely spaced foci of HIM-8 (green) indicating pairing of X-chromosomes (WT: 100%, n=50; *rrf-3*: 100%, n=91). (C) In both wildtype and mutant, SYP-1 (magenta) is localized in continuous tracks at the interface between parallel aligned DAPI-stained chromosomes (blue).

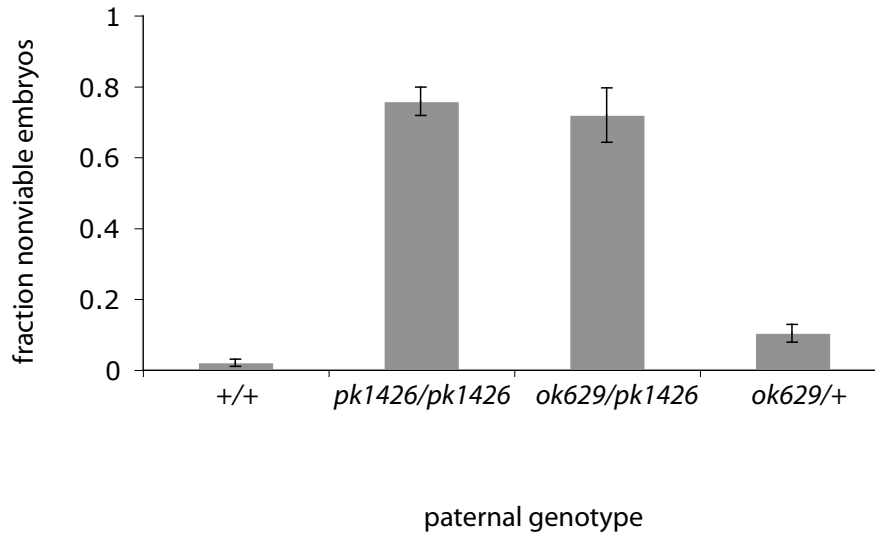


FIGURE S3.—*pk1426/ok629* trans-heterozygote males sire nonviable embryos. Matings were set up with *tra2(q122)* females and *ok629/pk1426* heterozygote males at 25°C. The proportion of dead embryos was estimated by counting newly laid embryos and the resulting survivors. *ok629* homozygous males were not tested due to defective male tail development and inability to mate (not shown). *pk1426* has a weak effect, if any, on embryogenesis when delivered through wildtype heterozygous males (Figure 3C). Error bars denote standard errors of the means.

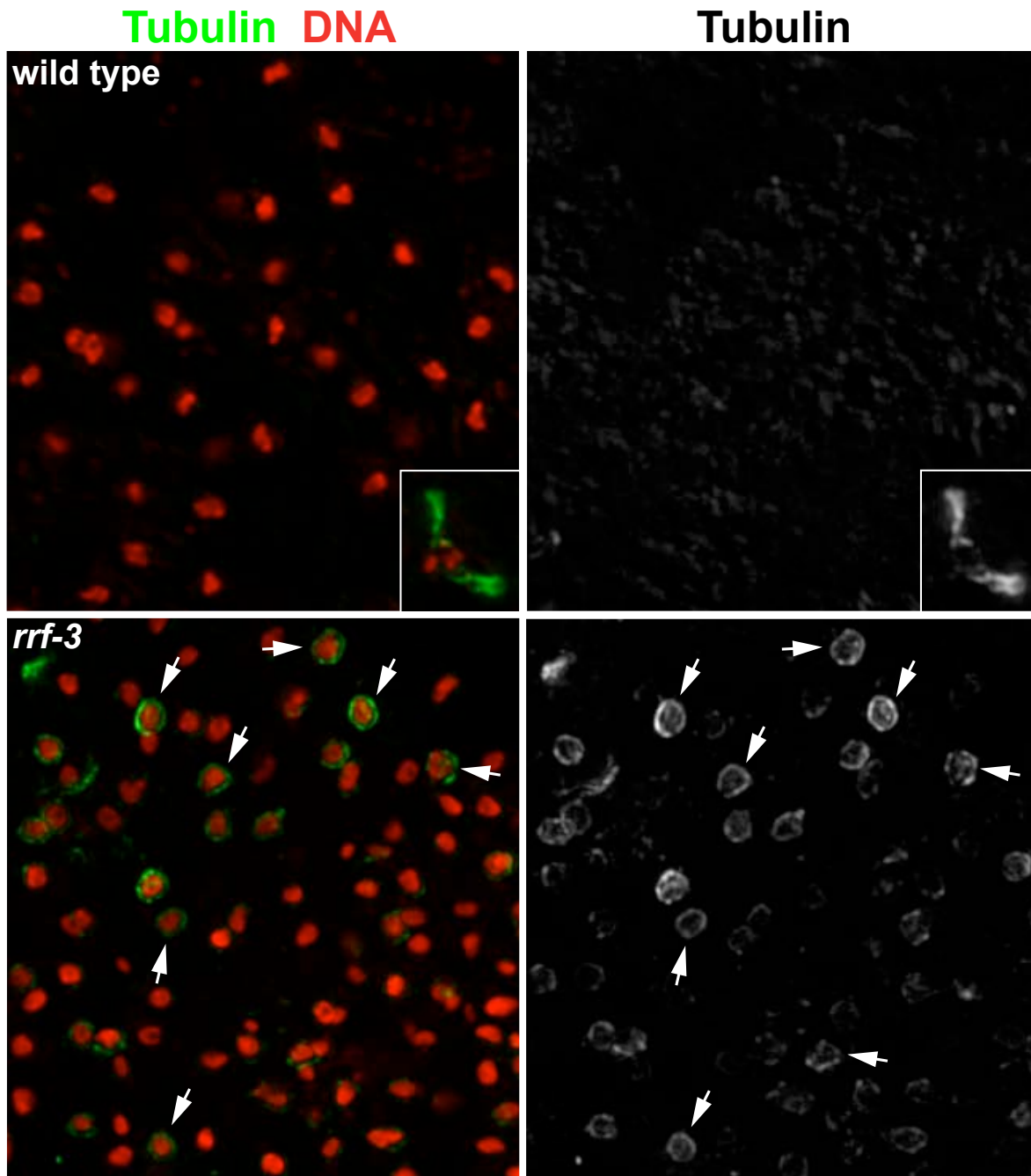


FIGURE S4.—Microtubule accumulation around spermatid nuclei of *rrf-3* mutant males. Spermatids from either a wildtype male gonad (top two panels) or an *rrf-3* mutant male gonad (bottom two panels) stained with Hoechst to label chromosomes (Red) and anti-tubulin antibody to label microtubules (Green). Males were grown at 25°C. The insets in the top two panels show a spermatocyte from the same gonad that is undergoing the first meiotic division; this serves as an internal control demonstrating the effectiveness of tubulin immunostaining in the wildtype sample. Arrows highlight a fraction of the tubulin wreaths observed in *rrf-3* mutant spermatids. Scale bar is 5 μm .

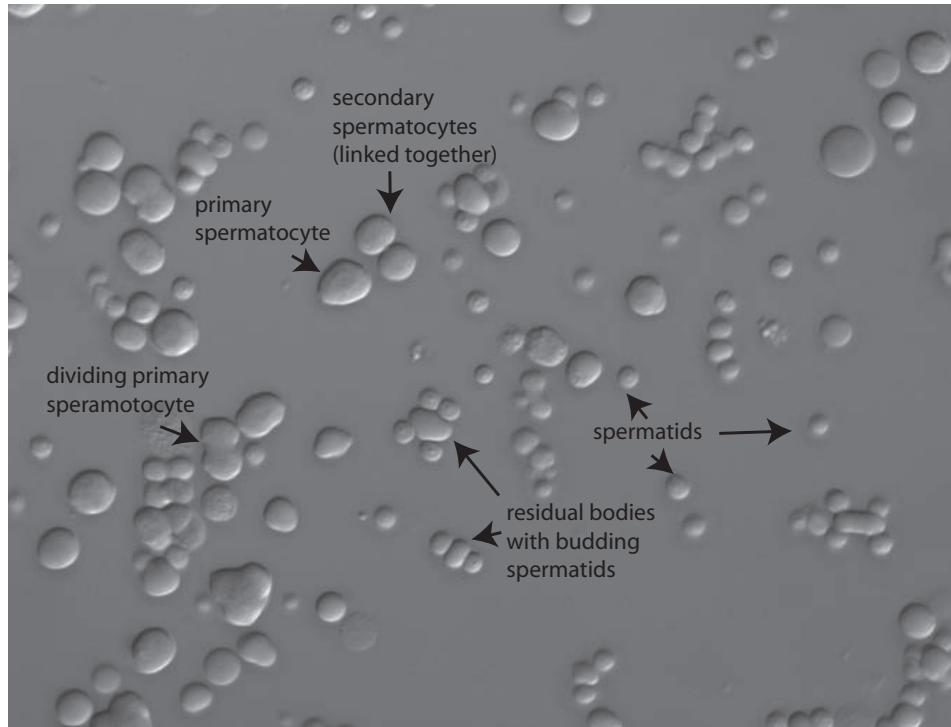


FIGURE S5.—A mix of cell stages in the isolated spermatogenic cell sample. A small portion of the isolated spermatogenic cells in M9 buffer were immediately put on a slide after the rest had been flash frozen into liquid N₂. The isolated cells contain a mixture of primary spermatocytes, secondary spermatocytes, residual bodies, mature spermatids, and various intermediates, as indicated by labels and arrows.

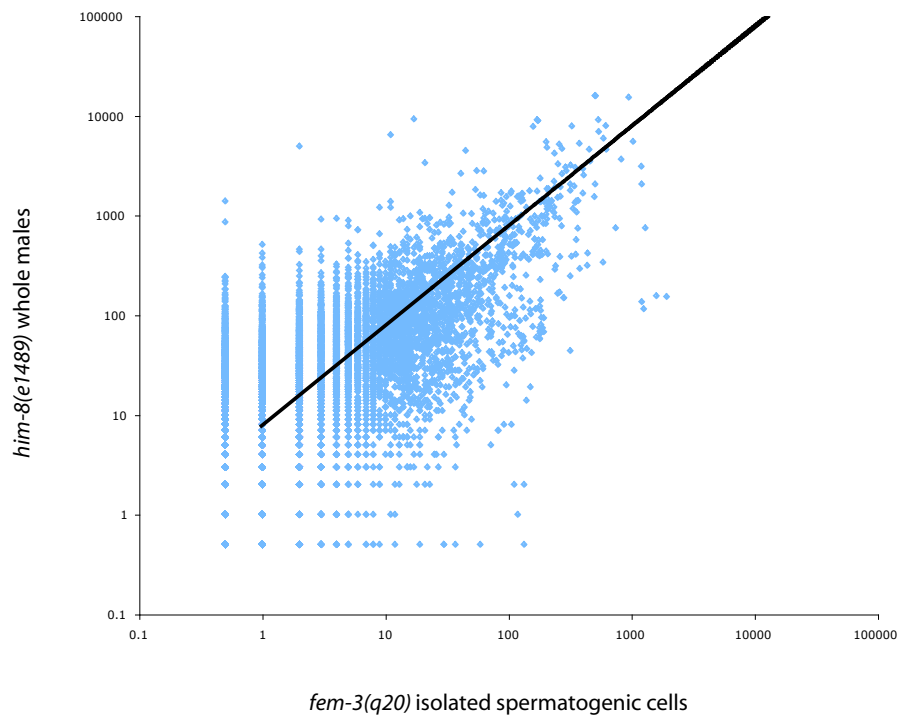


FIGURE S6.—Comparison of siRNA expression profiles from *him-8(e1489)* whole males and from *fem-3(q20)* isolated spermatogenic cells. Scatter plots depict siRNA alignment count per gene from *him-8(e1489)* whole males (Y-axis) and *fem-3(q20)* isolated spermatogenic cells (X-axis). Genes with siRNA alignment counts of zero were assigned a value of 0.5 to avoid exclusion from the logarithmically scaled plots. The trendlines indicate the expected siRNA alignment counts per gene if both samples had been derived from the same population. On a linear scaled plot, the slopes deviate from 45° because of differences in sample sizes.

FILE S1**siRNA sequencing sample descriptions**

File S1 is available for download as an Excel file at <http://www.genetics.org/cgi/content/full/genetics.109.108134/DC1>.

“Sequence reads” refers to the 19 to 28 nt sequences that were parsed from the 36 nt Illumina Genome Analyzer output sequences (containing 5’ barcodes and 3’ adapter sequences). The sequence reads were aligned to both the *C. elegans* genome and to a cDNA dataset to obtain both numbers of alignments and numbers of sequence reads that produced the alignments. Alignments were generated using BLAT with parameters set to default, except stepSize was set to 5 and tileSize to 10. Repetitive alignments (derived from sequence reads with multiple equally good alignments) were subtracted from the complete set of alignments to obtain the numbers of uniquely aligning sequences. Since a sequence read could align uniquely to the cDNA dataset but align repetitively to the genome, unique cDNA alignments were identified by first aligning to the genome, then to the cDNA dataset.

TABLE S1
Read counts and alignment counts

	isolated spermatogenic cells	whole males			
		set 1		set 2	
		rrf-3; him-8	him-8	rrf-3; him-8	him-8
sequence reads with identifiable barcodes and 3' adapters	375821	1756562	1709935	1492364	755627
sequence reads with alignments to genome	291234	1446458	1392664	875154	498799
genomic alignments	930132	3668399	3207360	2135279	1201832
unique genome alignments	218682	1152152	1141417	692909	364763
sequence reads with alignments to cDNA dataset	100380	484827	739144	480423	278821
cDNA alignments	124241	599454	939733	602471	347875
unique cDNA alignments	91840	447051	687451	442101	255343
volume of frozen <i>C. elegans</i> tissue used for RNA extraction	~5 μ L	~30 μ L	~30 μ L	~30 μ L	~30 μ L
mass of small RNA-enriched RNA used for library preparation	<1 μ g	~2.5 μ g	~14 μ g	~2 μ g	~4 μ g
total PCR cycles in amplification	22	24	22	28	26
barcode	AGCG	TATG	GTTA	GTTA	TATG

**Chapter 4. Meiotic Chromosome
Homology Search Involves
Modifications of the Nuclear
Envelope Protein Matefin/SUN-1**

Meiotic Chromosome Homology Search Involves Modifications of the Nuclear Envelope Protein Matefin/SUN-1

Alexandra M. Penkner,^{1,*} Alexandra Fridkin,^{2,*} Jiradet Gloggnitzer,¹ Antoine Baudrimont,¹ Thomas Machacek,¹ Alexander Woglar,¹ Edina Csaszar,³ Pawel Pasierbek,⁴ Gustav Ammerer,³ Yosef Gruenbaum,² and Verena Jantsch^{1,*}

¹Department of Chromosome Biology, Max F. Perutz Laboratories, University of Vienna, 1030-Vienna, Austria

²Department of Genetics, Hebrew University of Jerusalem, 91904 Jerusalem, Israel

³Mass Spectrometry Unit, Max F. Perutz Laboratories, University of Vienna, 1030-Vienna, Austria

⁴Research Institute of Molecular Pathology, 1030-Vienna, Austria

*Correspondence: alexandra.penkner@univie.ac.at (A.M.P.), moloko@cc.huji.ac.il (A.F.), verena.jantsch@univie.ac.at (V.J.)

DOI 10.1016/j.cell.2009.10.045

SUMMARY

Genome haploidization during meiosis depends on recognition and association of parental homologous chromosomes. The *C. elegans* SUN/KASH domain proteins Matefin/SUN-1 and ZYG-12 have a conserved role in this process. They bridge the nuclear envelope, connecting the cytoplasm and the nucleoplasm to transmit forces that allow chromosome movement and homolog pairing and prevent nonhomologous synapsis. Here, we show that Matefin/SUN-1 forms rapidly moving aggregates at putative chromosomal attachment sites in the meiotic transition zone (TZ). We analyzed requirements for aggregate formation and identified multiple phosphotarget residues in the nucleoplasmic domain of Matefin/SUN-1. These CHK-2 dependent phosphorylations occur in leptotene/zygotene, diminish during pachytene and are involved in pairing. Mimicking phosphorylation causes an extended TZ and univalents at diakinesis. Our data suggest that the properties of the nuclear envelope are altered during the time window when homologs are sorted and Matefin/SUN-1 aggregates form, thereby controlling the movement, homologous pairing and interhomolog recombination of chromosomes.

INTRODUCTION

Homologous chromosomes are segregated to opposite cell poles at the first meiotic division to accomplish genome haploidization. To assure their proper alignment on the metaphase spindle, homologs have to identify each other to allow the generation of a physical connection between them. How homolog recognition and correct pairing is established is a question under intense investigation (for review, see Petronczki et al., 2003; Pawlowski and Cande, 2005; Bhalla and Dernburg, 2008).

Integral nuclear envelope (NE) proteins play a conserved role in homolog pairing in eukaryotes (for review, see Fridkin et al., 2009; Alsheimer, 2009; Starr, 2009). Inner and outer nuclear membrane proteins (SUN/KASH proteins) bridge the NE by the interaction of their conserved C-terminal domains within the perinuclear space. While the N terminus of the SUN domain protein faces the nucleoplasm, the N terminus of the KASH domain protein protrudes into the cytoplasm, thus allowing the connection of nuclear components to cytoplasmic structures, such as the cytoskeleton (Tzur et al., 2006).

Chromosome ends attachment to the NE is dependent on SUN domain-bearing inner NE proteins as shown for yeast and mammals. SUN domain proteins aggregate at the site of telomere attachment to the NE, and their absence causes a randomized localization of telomeres within the nucleus (Conrad et al., 2007, 2008; Chikashige et al., 2006; Ding et al., 2007). In rodents, SUN domain proteins are engaged in the formation of attachment plaques, electron-dense plates observed at the site where conically thickened chromosome ends attach to the nucleoplasmic side of the NE (Schmitt et al., 2007). At these sites, the nuclear membrane is spanned by fibrils that are connected to cytoplasmic structures (Alsheimer, 2009; Scherthan, 2007).

During meiotic prophase I, chromosomes display pronounced movements. In *S. cerevisiae*, the motility of chromosome ends during prophase I is driven by actin-based motors, whereas in *S. pombe*, tubulin motors likely drive chromosome ends into the bouquet and the chromosomes in a horseshoe configuration (Trelles-Sticken et al., 2005; Scherthan et al., 2007; Koszul et al., 2008; Ding et al., 1998; Yamamoto et al., 1999; Chikashige et al., 2006). In yeast and mammals, chromosomes also transiently adopt a polarized configuration termed the “chromosomal bouquet.” The timing of telomere clustering coincides with chromosome pairing, synapsis, and recombination (for review, see Scherthan, 2007; Harper et al., 2004). Interference with SUN domain proteins or their interactors abrogates bouquet formation (Conrad et al., 2007; Ding et al., 2007; Chikashige et al., 2006; Tang et al., 2006).

Once homologs have paired, a proteinaceous structure, the synaptonemal complex (SC), assembles between them. Stable,

close juxtaposition of homologs is a prerequisite for the repair of deliberately induced DNA double-strand breaks (DSBs) to generate crossovers by homologous recombination. In budding yeast, the timely repair of meiotic DSBs depends on chromosome movement during very early steps in meiotic recombination. This movement supports the removal of nonspecific chromosomal interactions and entanglements, thus ensuring homolog juxtaposition along the entire length of the chromosome. Additionally, these chromosome movements promote later steps during recombination, possibly by affecting chromatin structure (Koszul et al., 2008; Conrad et al., 2008; Kosaka et al., 2008; Wanat et al., 2008).

The *C. elegans* inner NE protein Matefin/SUN-1 is expressed in the germline in adult hermaphrodites and in embryos (Fridkin et al., 2004). A missense mutation within the conserved SUN domain strongly reduces the retention of the KASH protein ZYG-12 at the outer membrane of the NE and completely abrogates homolog alignment. Instead, nonhomologous synapsis is prematurely established (Penkner et al., 2007).

In *C. elegans*, only the pairing center (PC)-carrying chromosome end attaches to the NE upon entry into meiosis (Goldstein and Slaton, 1982; Phillips et al., 2005; Phillips and Dernburg, 2006). The PC or homolog recognition region (HRR) comprises a *cis*-acting chromosomal region responsible for the pairing and synapsis of homologs (MacQueen et al., 2005). PC regions have to interact with one of four zinc-finger proteins termed ZIM-1, ZIM-2, ZIM-3, and HIM-8 (Phillips et al., 2005; Phillips and Dernburg, 2006) and are sufficient to mediate pairing and synapsis when ectopically inserted into a different chromosome (Phillips et al., 2009). Independent of recombination, the PCs establish the first contacts between homologous chromosomes in the transition zone (TZ) corresponding to the leptotene/zygotene stage in *C. elegans* (MacQueen et al., 2005; Phillips et al., 2005; Phillips and Dernburg, 2006; Dernburg et al., 1998). Clustering of chromosomes within a subvolume of the nucleus strongly correlates with an ongoing homology search (Couteau et al., 2004; MacQueen and Villeneuve, 2001). In pachytene, when chromosomes are synapsed, chromosomes disperse and adopt a homogeneous arrangement at the nuclear periphery. At this stage DSBs are repaired by homologous recombination.

Here, we describe a dramatic change in properties of the NE protein Matefin/SUN-1, especially during the time window of ongoing homologous pairing and chromosome movement. Matefin/SUN-1 forms dynamic local aggregates at the site of the chromosome end attachment to the NE. Chromosome end movement in the TZ requires a functional SUN domain. An intact SUN domain correlates with size changes of Matefin/SUN-1 aggregates and chromatin clustering and is essential for homologous pairing. At the same time, the nuclear N terminus of Matefin/SUN-1 is phosphorylated at multiple serines and the presence of the modification correlates with the presence of polarized chromatin. Phosphorylations of Matefin/SUN-1 impact faithful bivalent formation and suggest a connection to the regulation of Matefin/SUN-1 aggregate formation/resolution. Furthermore, we have examined triggers and factors responsible for Matefin/SUN-1 phosphorylation during leptotene/zygotene.

RESULTS

Matefin/SUN-1 Redistributes during the Time Window of Homologous Pairing

A C-terminally GFP-tagged Matefin/SUN-1 transgene was generated to allow high-resolution cytological analysis and biochemical purification. The transgene is fully functional as it rescues the highly reduced brood size and the embryonic lethality of *mtf-1/sun-1(ok1282)* knockout worms (Table S1 available online). The expression and localization patterns of SUN-1::GFP fully overlap with those of the endogenous protein (Figure 1B and data not shown; hereafter, we refer to Matefin/SUN-1 as SUN-1). SUN-1::GFP localizes to the NE of germline nuclei in hermaphrodites (Figure 1A) (Fridkin et al., 2004; Penkner et al., 2007) and males (data not shown). SUN-1 colocalizes with ZYG-12ABC::GFP in mitosis (Malone et al., 2003) (data not shown) and during meiotic prophase I (Figure 1B). This and the fact that we could coprecipitate both proteins (Figure 1E) support the assumption that SUN-1 and ZYG-12 interact in vivo. Furthermore, the western blot demonstrates that SUN-1 forms dimers/multimers in vivo.

The progressive developmental stages of meiotic prophase I can be found in a spatial gradient from distal to proximal in the *C. elegans* gonad. Mitotic precursor cells display a uniform rim-like GFP signal enclosing the chromatin and highlighting the centrosome as evidenced by the colocalization with the centrosomal marker SPD-5 (Hamill et al., 2002) (Figures 1A and 1D). Once germline nuclei enter the TZ, SUN-1 redistributes and forms aggregates of variable size and number (see also Sato et al., 2009). In contrast to mitosis, SUN-1 aggregates in the TZ do not mark the centrosome (Figure 1D) (Penkner et al., 2007).

In addition to the local enrichment of SUN-1::GFP, a weak protein signal is detectable along the remaining NE. The majority of aggregates are observed in the TZ. SUN-1 aggregates disassemble concomitantly with the redispersal of chromosomes in mid-prophase (Figure 1A). In nuclei in later prophase I, SUN-1::GFP distributes uniformly. We conclude that SUN-1/ZYG-12 protein complexes undergo extensive reorganization within the nuclear periphery during prophase I.

The localization pattern of SUN-1 and ZYG-12::GFP in the TZ is reminiscent of the distribution of all four PC-binding proteins (Phillips and Dernburg, 2006). In the TZ, the signal of the PC-proteins HIM-8 (X chromosome) and ZIM-3 (chromosomes I and IV) overlaps with SUN-1 aggregates (Figure 1C, ii and iv), demonstrating that PC-containing chromosome ends localize to the nuclear periphery at the sites of SUN-1 aggregation. SUN-1 aggregates likely represent an equivalent to chromosomal attachment plaques to the NE.

The Formation of SUN-1 Aggregates Requires Establishment of Chromosome Axes, CHK-2 Kinase Activity, and Chromosome Movement

We next analyzed genes that are likely to play a role in the establishment and/or kinetics of SUN-1 aggregates. SUN-1::GFP and HIM-8 were coimmunostained in various mutant gonads subdivided into six zones of equal length. We counted the number and size of aggregates per nucleus for each zone and analyzed their colocalization with HIM-8 (Figures 2A and S1). Spherical

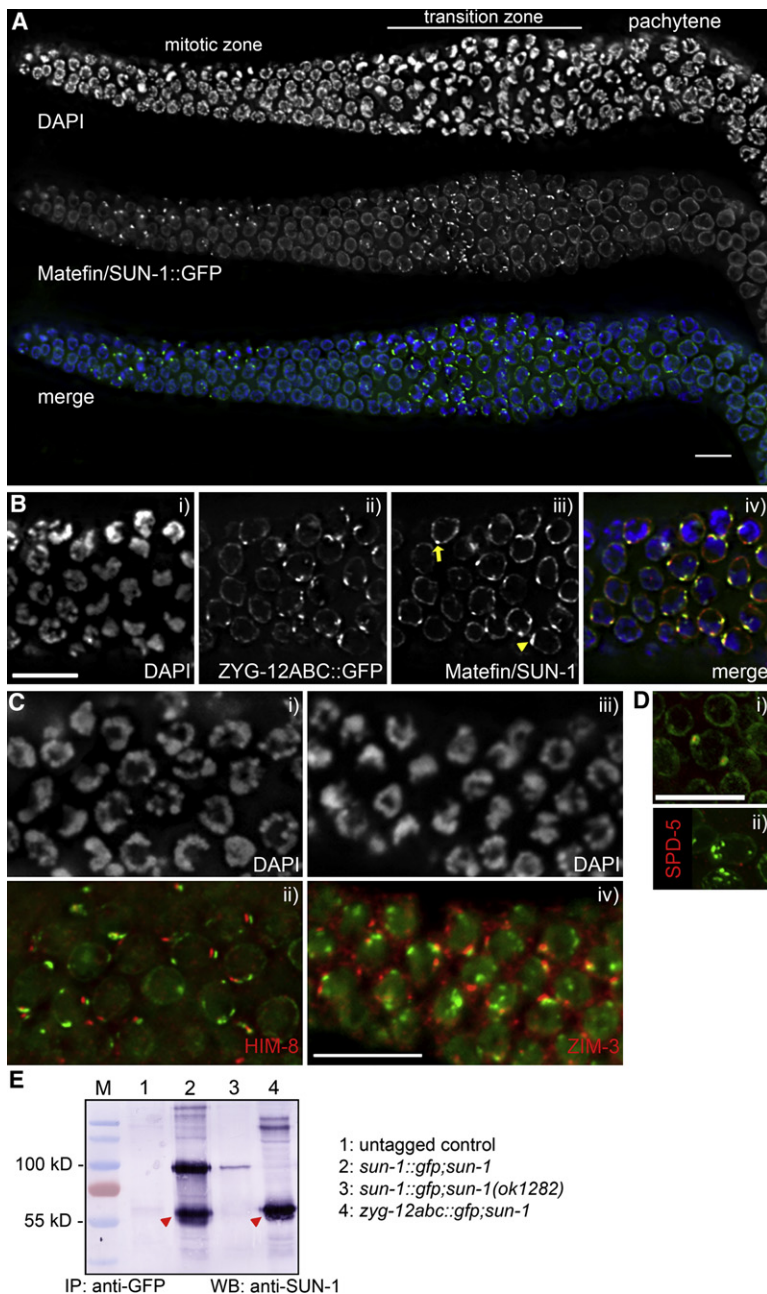


Figure 1. SUN-1 Forms Aggregates at the Nuclear Envelope during the Time of Ongoing Homolog Pairing

(A) A *mtf-1/sun-1::gfp;mtf-1/sun-1(ok1282)* hermaphrodite gonad expressing SUN-1::GFP (middle, green in merge) was stained for DNA with DAPI (top, blue in merge).

(B) SUN-1 staining (iii, red in merge) of hermaphrodite gonads expressing ZYG-12ABC::GFP (ii, green in merge). i, DAPI; iv, merge. The yellow arrowhead marks the position of a patch, while the yellow arrow highlights a focus.

(C) DAPI staining (i, iii) and antibody staining (ii, iv). PC-binding proteins HIM-8 or ZIM-3 (red) are shown in combination with SUN-1::GFP (green). The green channel is shifted to the right to allow better visualization of green and red signals.

(D) Centrosome marked by SPD-5 staining (red) in mitotic (i) and meiotic (ii, transition zone) nuclei expressing SUN-1::GFP (green). Scale bars represent 10 μ m.

(E) Western blot to show the in vivo interaction of ZYG-12ABC::GFP and endogenous SUN-1 (54 kD, red arrowheads). Coimmunoprecipitations were performed with anti-GFP antibodies. SUN-1 was detected with anti-SUN-1 antibodies. Genotypes are on the right.

both foci and patches, more than half of the nuclei with aggregates did not form foci (Figure 2A). Combined, zones 2 and 3 (the TZ) nuclei had an average of 1.9 patches ($n = 137$, $SD = 1.3$) and 1.0 focus ($SD = 1.4$) (Table S2).

While most patches disassembled within zone 4 (early pachytene), the patch colocalizing with HIM-8 remained into zone 5 (mid-pachytene) (Figure S1), suggesting that X chromosome aggregates persist longer than autosomal ones.

SYP-2 comprises a central element component of the SC. Besides a defect in the assembly of the SC, *syp-2(ok307)* is defective in the timely redistribution of chromatin, as seen by a prolongation of the TZ (Colaiácovo et al., 2003). In *syp-2(ok307)*, SUN-1 aggregates extend into zone 5. Foci are even present until late pachytene (zone 6). Maximum patch formation is observed from zones 2–4. While patch formation is slightly reduced as compared to that of the wild-type (an average of 1.4 patches is seen in zones 2 and 3 [$SD = 0.9$, $n = 122$]), SUN-1 foci are significantly more abundant in *syp-2(ok307)* ($x = 3.4$, $SD = 2.2$ in zones 2 and 3; Student's *t* test, $p = 6.33E-22$) (Table S2).

Foci are already seen upon entry into meiosis (zone 1) and reach a maximum in zone 4, concomitant with the start of disassembly of patches. Interestingly, while wild-type nuclei always display foci in addition to patches, *syp-2* nuclei in zones 2–4 can display foci without having patches.

him-3(gk149) lacks the chromosome axis component HIM-3, which is essential for homologous pairing, synapsis, and spatial chromatin rearrangement (Couteau et al., 2004). In *him-3*, SUN-1 foci form, but no more than one patch was observed in zone 2. The reduced patch formation is reflected by an average of 0.5 patches in zones 2 and 3 ($n = 129$, $SD = 0.5$; Student's *t* test, $p = 3.14E-24$), while an average of 1.8 foci ($SD = 1.4$) documents

SUN-1::GFP aggregates with a diameter $< 1.1 \mu$ m were classified as foci (yellow arrow in Figure 2B). Aggregates elongated in one dimension ($\geq 1.1 \mu$ m) were termed patches (yellow arrowhead in Figure 2B).

In hermaphrodite gonads expressing the transgenic SUN-1::GFP and lacking endogenous SUN-1 (referred to as wild-type), zones 2 to 4, including the TZ and early pachytene, showed both foci and patches (Figure 2A). Maximum aggregate formation was observed in zone 3, with 75% of nuclei displaying mostly two to three and up to four patches. In zone 3, in addition to patches, 30% of the nuclei formed foci, usually one to two. In contrast to the zone 2, where almost all nuclei displayed

an increase in focus formation (Student's t test; $p = 2.89E-06$) (Table S2). SUN-1 foci are present from zone 2 until zone 5, with the maximum number of nuclei displaying foci in zone 3 (90%). These data demonstrate that HIM-3 is required for efficient aggregate formation.

The serine/threonine kinase mutant *chk-2(me64)* lacks a TZ. It is deficient in homologous alignment and DSB formation (MacQueen and Villeneuve, 2001). SUN-1 aggregates were not observed in *chk-2(me64)*.

A point mutation within the SUN domain of SUN-1 (*mtf-1/sun-1(ff18)*) causes reduced ZYG-12 retention at the NE and a failure in homolog alignment and chromatin polarization (Penkner et al., 2007). A GFP transgene engineered with this mutation, SUN-1(G311V)::GFP, does not form patches. Instead, numerous foci ($x = 9.6 \pm 1.6$ aggregates; ranging from 7 to 12 foci; $n = 17$ nuclei) are present in early meiotic nuclei (Figure 2B) that colocalize with PC-binding proteins such as HIM-8 and ZIM-3 (Figure 2B and data not shown). They mark sites of chromosome end attachment to the NE. Time-lapse microscopy of SUN-1::GFP aggregates showed displacement tracks distributed over a subarea of the NE covering the underlying polarized chromatin. In striking contrast, SUN-1(G311V)::GFP aggregates were only mildly shifted, suggesting that chromosome ends barely moved (Figure 2C and Movies S1–S3; detailed analysis of chromosome movement will be published elsewhere).

Taken together, our data demonstrate a correlation between chromatin polarization and SUN-1 aggregate formation. Patches were only observed at the NE of nuclei with clustered chromatin, consistent with the observations that they require CHK-2 activity and that they disassemble concomitantly with chromatin rearrangement in pachytene. The data also suggest that chromosome ends are moved in the TZ by a mechanism that requires a functional SUN domain of SUN-1. Chromosome clustering is a consequence of the movement of chromosome ends and not a consequence of relocating the nucleolus.

In both wild-type and mutant situations, unpaired HIM-8 foci overlapped with SUN-1 foci. We therefore hypothesize that these foci mark the NE attachment sites of single chromosome ends. Consistently, patches correspond to areas where multiple chromosome ends meet. Patches are not formed in the absence of chromosome end movement.

The N Terminus of SUN-1 Is Modified in Leptotene/Zygotene

Antibodies recognizing an N-terminal peptide of SUN-1 (Fridkin et al., 2004) disclosed an unexpected staining pattern in wild-type hermaphrodite gonads (compare SUN-1 levels in Figures 3A and 3B). While germline nuclei in the mitotic zone and later prophase I showed a clear reactivity with these antibodies, the signal intensity was strikingly weaker in nuclei in leptotene/zygotene (TZ). Asynchronous, interspersed nuclei, which display a uniform distribution of chromatin, also exhibit enhanced SUN-1 signals compared to nuclei that surround the TZ (Figure 3B, red stars).

The reduced staining of the nuclear periphery could be correlated with polarization of the chromatin characteristic for TZ nuclei, over a prolonged zone like in *syp-2(ok307)*, conversely reduced to a few nuclei [*him-3(gk149)*] or was completely absent

[*chk-2(me64)*], (Figure 3C). We hypothesized that the N-terminal epitope/s recognized by the antibodies is/are transiently and reversibly masked during the time of homolog pairing.

The N Terminus of SUN-1 Is Phosphorylated at Multiple Serines

To determine potential posttranslational modifications of SUN-1, we performed mass spectrometry analysis on immunoprecipitated SUN-1::GFP from strains producing embryos or devoid of embryos. Multiple phosphorylated residues in SUN-1's N terminus were identified (protein coverage of ~90%; Figures 4B and S2) No differential phosphorylation sites could be uncovered from extracts devoid of embryos (Figure S3). In total, six phosphorylated serines (Ser8, Ser12, Ser24, Ser43, Ser58, and Ser62) and one phosphorylated serine or threonine (Ser35 or Thr36) showed reproducible mass spectrometry results (Figure 4B). Difficulties arose from the discrimination between putative phosphorylations of Ser12 or Ser16. Ser12, however, is considered to be the most probable candidate for a phosphorylation site (see below and Figures S2 and S3). Moreover, Ser35 and Thr36 are equally likely to be phosphorylated.

Antibodies directed against the phosphoepitope of Ser8 (S8-Pi) were raised and their specificity verified [dot blot experiments and lack of immunofluorescence of the SUN-1(S8A)::GFP line, data not shown]. In the mitotic zone, S8-Pi antibodies stained the NE and centrosomes. The rim-like staining at the nuclear periphery was observed from prometaphase onward, concomitant with the beginning of chromatin condensation (Figure 4C). Interestingly, the phosphorylation signal became stronger as the nuclei proceeded through mitosis. A strong signal was also detected in diakinesis nuclei.

In meiosis, staining of S8-Pi was first detected in the TZ, highlighting SUN-1 protein localized in foci and patches, as well as over the rest of the NE (Figure 4C). S8-Pi was most prevalent until early pachytene, when the aggregates disappeared. The signal became continuously weaker and eventually disappeared in later pachytene. Prolonged S8-Pi staining was observed in *syp-2(ok307)*, which develops an extended TZ. The peak of staining was seen in nuclei with clustered chromatin (Figure S4A). SUN-1 Ser12 and Ser24 exhibit a comparable phosphorylation pattern in wild-type and *syp-2(ok307)* hermaphrodite gonads. Centrosomal SUN-1 is detectable in mitosis, and the antibodies highlight the SUN-1 population located in aggregates during early meiosis (Figures S4B and S4C).

The phosphorylations of SUN-1 during the time window of ongoing homology search, when chromatin is polarized and SUN-1::GFP aggregates are formed, and the dephosphorylations concomitant with the redistribution of paired chromosomes support a potential role for SUN-1 phosphorylation in homologous pairing.

The CHK-2 Kinase Is Required for SUN-1 Phosphorylation in Meiosis

We analyzed the regulation of Matefin Ser8, Ser12, and Ser24 phosphorylation. Early meiotic *chk-2(me64)* nuclei showed no S8-Pi, S12-Pi, and S24-Pi staining above background level, whereas mitotic NE or centrosome staining remained as in wild-type nuclei (Figures 4D, S4B, and S4C). These results

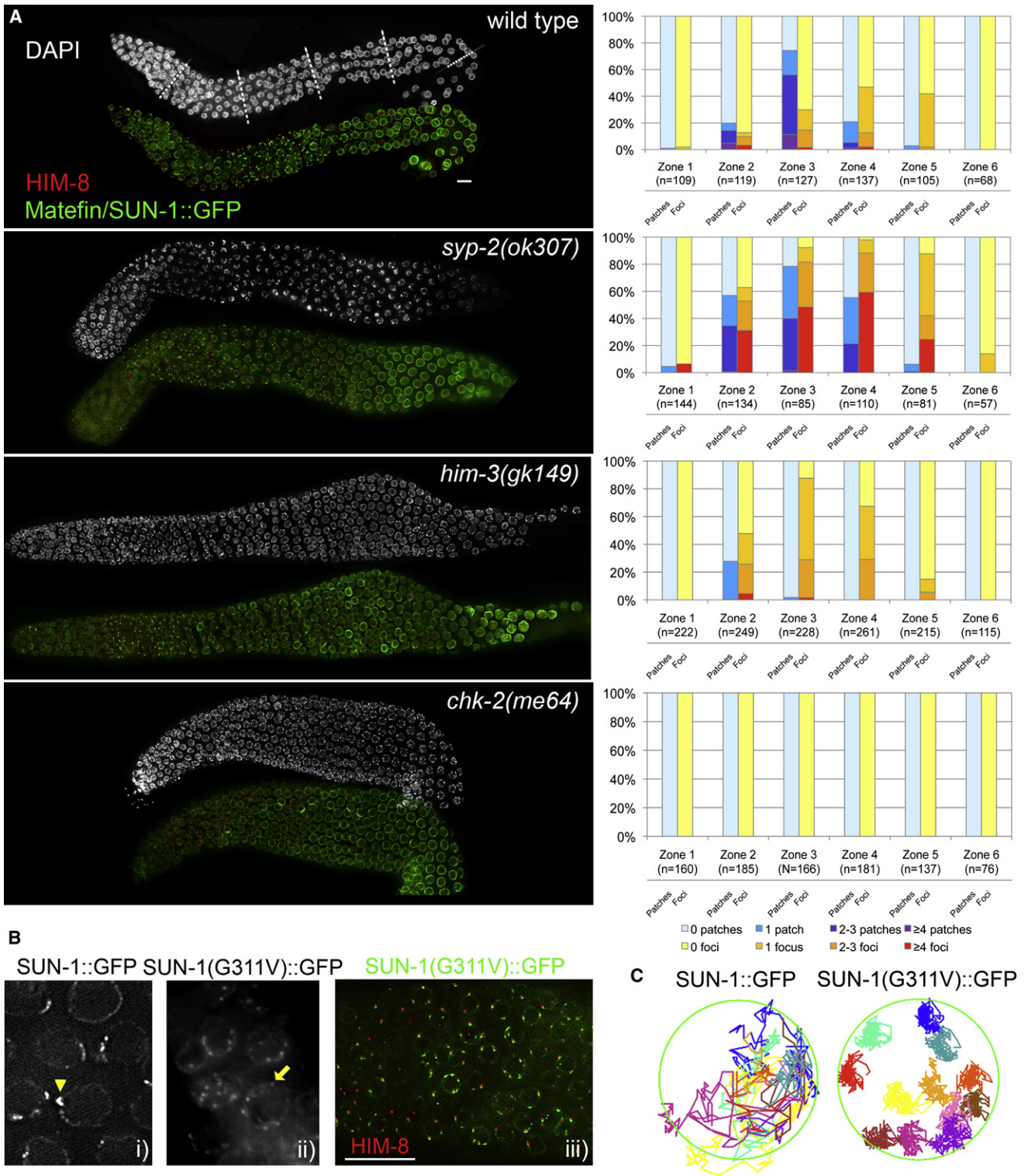


Figure 2. The Formation of SUN-1 Aggregates Requires Chromosome Axes, the Kinase CHK-2, and Chromosome Movement
 (A) Analysis of SUN-1::GFP aggregates in various mutant backgrounds. White, DAPI staining; green, SUN-1::GFP; red, HIM-8. Wild-type: *mtf-1/sun-1::gfp;mtf-1/sun-1(ok1282)*. *syp-2(ok307)*: *syp-2(ok307);mtf-1/sun-1::gfp;mtf-1/sun-1(ok1282)*. *him-3(gk149)*: *him-3(gk149);mtf-1/sun-1::gfp;mtf-1/sun-1(ok1282)*. *chk-2(me64)*: *chk-2(me64);mtf-1/sun-1::gfp;mtf-1/sun-1(ok1282)*. Dotted lines in the wild-type DAPI-stained gonad indicate subdivision into six zones. Quantification of aggregate forms (foci and patches) and numbers are shown in the right panel.

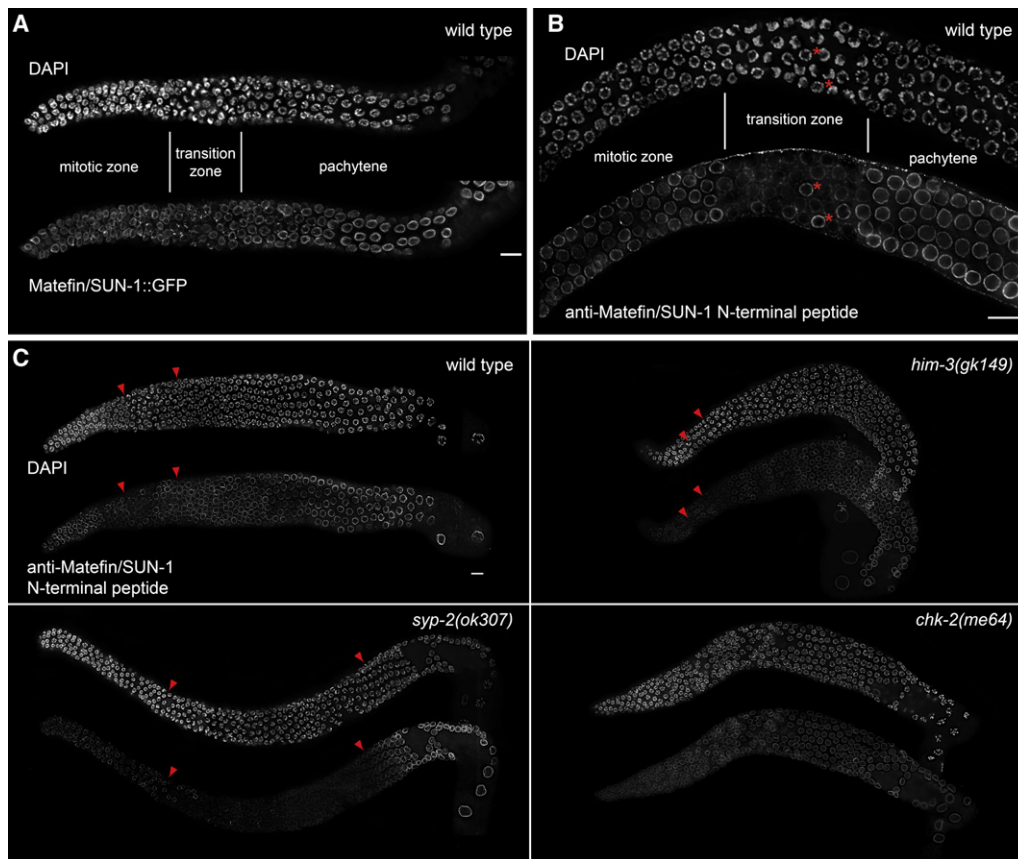


Figure 3. The N Terminus of SUN-1 Is Not Recognized by N Terminus-Specific Matefin Antibodies in the Transition Zone

(A) A wild-type hermaphrodite gonad expressing SUN-1::GFP.

(B) Labeling of SUN-1 in wild-type (N2) hermaphrodite gonads with antibodies recognizing an N-terminal peptide (number 3663). Red stars mark the asynchronous nuclei interspersed in the transition zone.

(C) Analysis of wild-type (N2), *syp-2(ok307)*, *him-3(gk149)*, and *chk-2(me64)* mutants representing varying development of transition zone. The SUN-1 staining is weak at the nuclear periphery of nuclei displaying the typical polarized chromatin configuration of transition zone nuclei. Red arrowheads mark the beginning and the end of the TZ [in wild-type and *syp-2(ok307)*] and TZ-nuclei in *him-3(gk149)*.

Scale bars represent 10 μ m.

suggest that CHK-2 is required for the early meiotic phosphorylation of Ser8, Ser12, and Ser24, but not for phosphorylation in mitosis or diakinesis.

Activation of CHK-2, however, is not or not solely dependent on the ATM/ATR orthologs of *C. elegans* (Chen and Poon, 2008; Perona et al., 2008; Stergiou et al., 2007; Garcia-Muse and Boulton, 2005), since *atm-1(gk186)*, *atl-1(tm853)*, or double *atm-1(gk186);atl-1(tm853)* mutants did not display a reduction in S8-Pi staining (Figure 4F and data not shown).

Since *chk-2(me64)* is defective in both homologous chromosome alignment and DSBs formation, we investigated *htp-1*

(*gk174*) (Figure 4G) and *him-3(gk149)* (data not shown), both defective in homologous alignment (Couteau and Zetka, 2005; Martinez-Perez and Villeneuve, 2005; Couteau et al., 2004), to determine which process affects Ser8 phosphorylation. We also analyzed S8-Pi staining in *spo-11(me44)* (Figure 4E) and *mre-11(ok179)* (data not shown), which are deficient in DSB initiation but competent for homologous pairing (Dernburg et al., 1998; Chin and Villeneuve, 2001). In all mutant backgrounds, SUN-1 was phosphorylated at Ser8 (Figure 4 and data not shown), demonstrating that the absence of DSBs or defective homologous alignment alone do not interfere with the

(B) Comparison of SUN-1::GFP (i) and SUN-1(G311V)::GFP (ii) aggregates at the NE of nuclei proximal to the mitotic zone. The yellow arrowhead marks the position of a patch, while the yellow arrow highlights a focus. iii, containing of SUN-1(G311V)::GFP foci (green) and the PC-binding protein HIM-8 (red; channel shifted upward).

(C) Displacement tracks of SUN-1::GFP and SUN-1(G311V)::GFP aggregates in a representative nucleus in the transition zone. Various colors correspond to individual aggregates analyzed. The yellow SUN-1::GFP displacement track documents a protuberance of the NE. SUN-1 aggregates were analyzed in live specimen.

Scale bars represent 10 μ m.

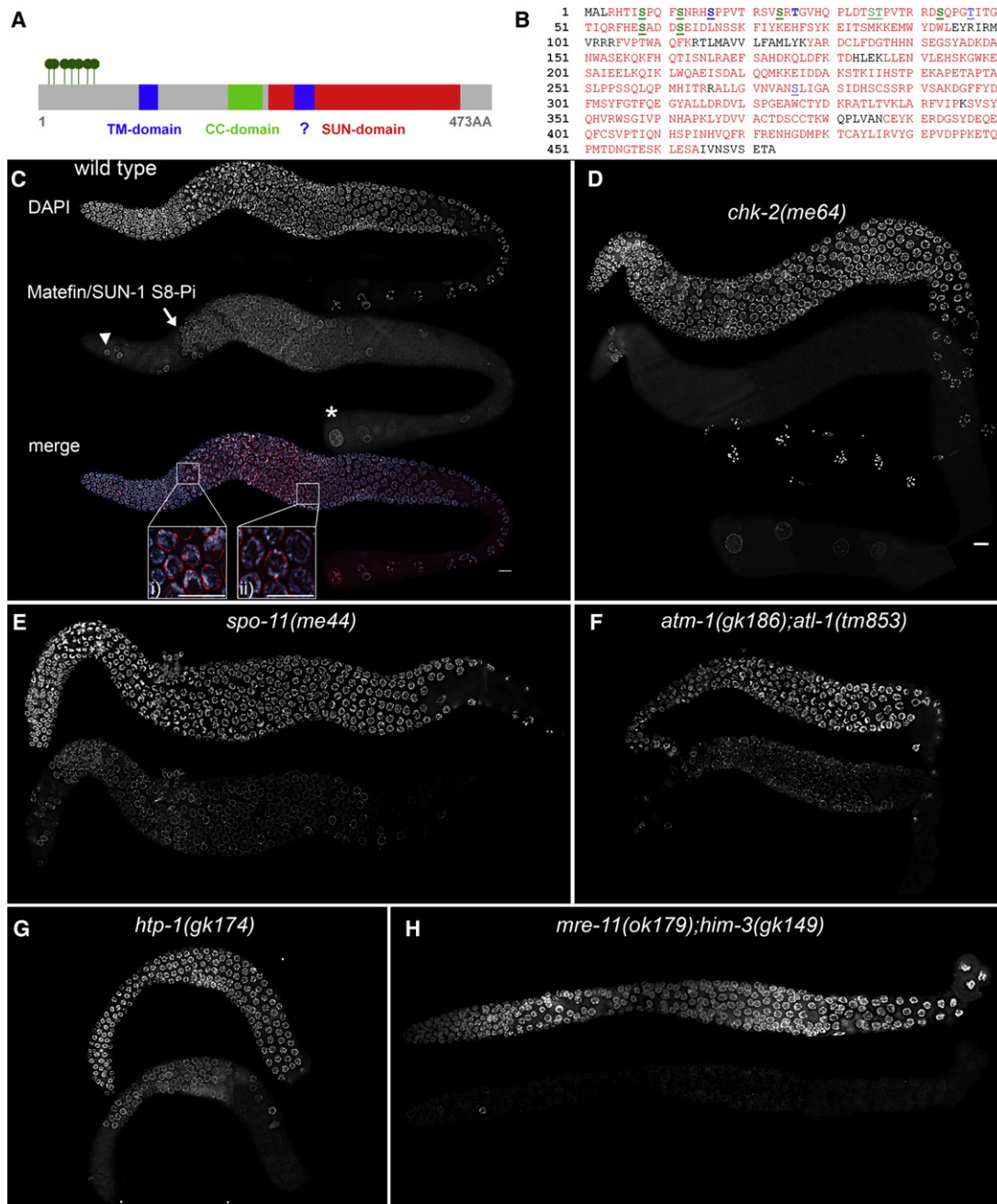


Figure 4. SUN-1 Is Phosphorylated at Its N Terminus

(A) Schematic representation of the SUN-1 protein. The position of the six phosphorylated serines and one serine or threonine at the N-terminal domain are marked (dark green). Also indicated are the positions of the putative transmembrane domains (TM and ?), the putative coiled-coil domain (CC) and the SUN domain.

(B) A single letter sequence of SUN-1. Residues covered by mass spectrometry are in red. Phosphorylated serine/threonine residues are in green. Phosphorylated residues in a mixture of embryonically and germline-expressed SUN-1 are shown with bold letters, and phosphorylations in the germline are underlined. Blue letters designate not-certified phosphorylations.

(C) Wild-type hermaphrodite gonad costained with DAPI (top and blue in merge) and with antibodies that recognize the phosphoepitope of serine8, SUN-1 S8-Pi (middle and red in merge). Insets display magnified nuclei of transition zone (i) and mid-pachytene (ii). The arrowhead marks a mitotic nucleus. The arrow indicates the beginning of TZ, and the star highlights a diakinesis nucleus.

(D–H) Mutant hermaphrodite gonads: *chk-2(me64)* (D), *spo-11(me44)* (E), *atm-1(gk186);atl-1(tm853)* (F), *htp-1(gk174)* (G), and *mre-11(ok179);him-3(gk149)* (H). Note that there is only background S8-Pi staining of transition zone and early pachytene nuclei in *chk-2(me64)* and *mre-11(ok179);him-3(gk149)* mutant backgrounds. Scale bars represent 10 μ m.

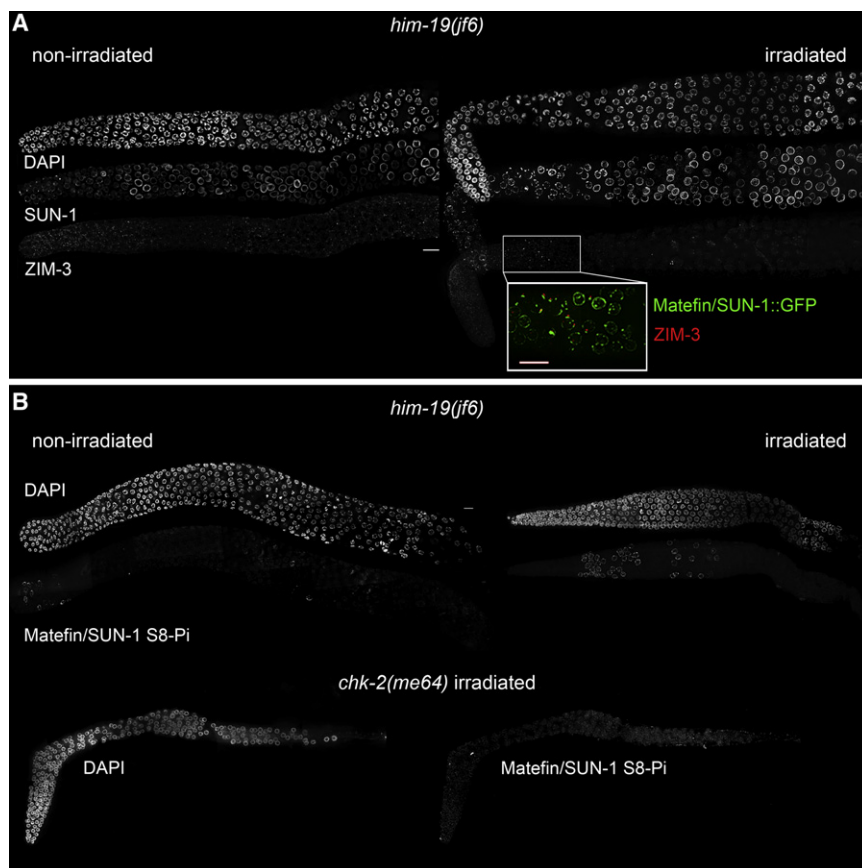


Figure 5. DNA Damage Can Induce SUN-1 Aggregation and Phosphorylation on Serine8

(A) SUN-1::GFP aggregates and ZIM-3 loading in germline nuclei proximal to the mitotic zone are induced by ionizing radiation of 2-day-old *him-19(jf6)* hermaphrodites. SUN-1::GFP (green in merge) and ZIM-3 (red in merge) colocalize (red channel is shifted upwards).

(B) SUN-1 S8-Pi staining in unirradiated (left) and irradiated (right) 2-day-old *him-19(jf6)* hermaphrodites. SUN-1 Ser8 does not become phosphorylated after ionizing radiation in *chk-2(me64)* mutants.

Scale bars represent 10 μ m.

dynamic movement along the nuclear surface (A.B. and V.J., unpublished data) and appeared to be colocalized with reloaded ZIM proteins, as revealed by ZIM-3 immunolocalization (Figure 5A, inset).

Consistent with the severe defect in chromatin polarization, phosphorylation of SUN-1 at Ser8 was rarely detected in unirradiated aged *him-19(jf6)* hermaphrodite gonads (Figure 5B, left panel). The phospho-specific immunostaining of SUN-1 was restored in irradiated *him-19(jf6)* nuclei progressing through early meiotic prophase I, but not in gamma-irradiated *chk-2(me64)* hermaphrodites (Figure 5B, right panel and lower panel).

phosphorylation of Ser8. However, in 46.2% ($n = 13$ gonads) of *mre-11(ok179);him-3(gk149)* double-mutant gonads the meiotic phosphorylation of Ser8 was undetectable (Figure 4H). These data suggest that elimination of both DSB initiation and an intact chromosomal axis prevents CHK-2 from influencing SUN-1 phosphorylation.

DNA Damage Induces the Phosphorylation of SUN-1 at Ser8

him-19 is an early meiotic regulator necessary for homologous pairing, chromatin clustering, synapsis, and recombination. The phenotype only becomes cytologically apparent in 2-day-old hermaphrodites (L. Tang and V.J., unpublished data). Two-day-old adult *him-19(jf6)* animals are most probably defective in the initiation of DSBs, as judged by the absence of repair intermediates marked by RAD-51. Importantly, gamma radiation-induced DSBs restored the clustering of chromosomes in *him-19(jf6)* nuclei proximal to the mitotic zone.

In accordance with a pairing defect and an absent TZ, SUN-1 aggregates could barely be detected in aged *him-19(jf6)* hermaphrodites (Figure 5A, left panel, and Figure S5). Because chromosome clustering could be induced by gamma radiation, we assayed whether polarization coincides with the restoration of SUN-1 aggregates. After irradiation, meiotic nuclei in the TZ region adopted the polarized chromatin configuration with SUN-1 patches and foci (Figure 5A, right panel). These displayed

We conclude that induction of artificial DSBs in the *him-19(jf6)* background restores the characteristics of TZ nuclei, including chromatin reorganization and phosphorylation of the SUN-1 N terminus, probably by activation of the CHK-2 kinase.

Mutation of SUN-1 Phospho-Sites Elicits Meiotic Defects

We substituted each of the phosphoserines either for alanine (nonphosphorylatable) or for glutamic acid (to mimic constitutively phosphorylated SUN-1). Only a subset of the substitutions could be recovered as viable transgenic lines, possibly because of disruption of other essential functions of SUN-1 (Fridkin et al., 2004).

Animals expressing SUN-1(S12E)::GFP with no endogenous SUN-1 (referred to as S12E) displayed a reduced brood size, embryonic lethality, and a Him phenotype (Table S1). SUN-1(S12E)::GFP hermaphrodites display a lack of chiasmata, with an average of 8.6 DAPI-positive structures at diakinesis, ranging from six to 12 ($n = 54$; Figure 6A, ii and iii) compared to six in the wild-type ($n = 57$). SUN-1(S12E)::GFP-expressing hermaphrodites display an extended TZ with tightly clustered chromatin (Figure 6A). Accordingly, SUN-1(S12E) aggregates are detected at the NE and colocalize with PC-binding proteins such as HIM-8 and ZIM-3 in the elongated TZ (Figures 6A and 6B). Those “artificial” aggregates are movement competent, as shown in Movies S4 and S5.

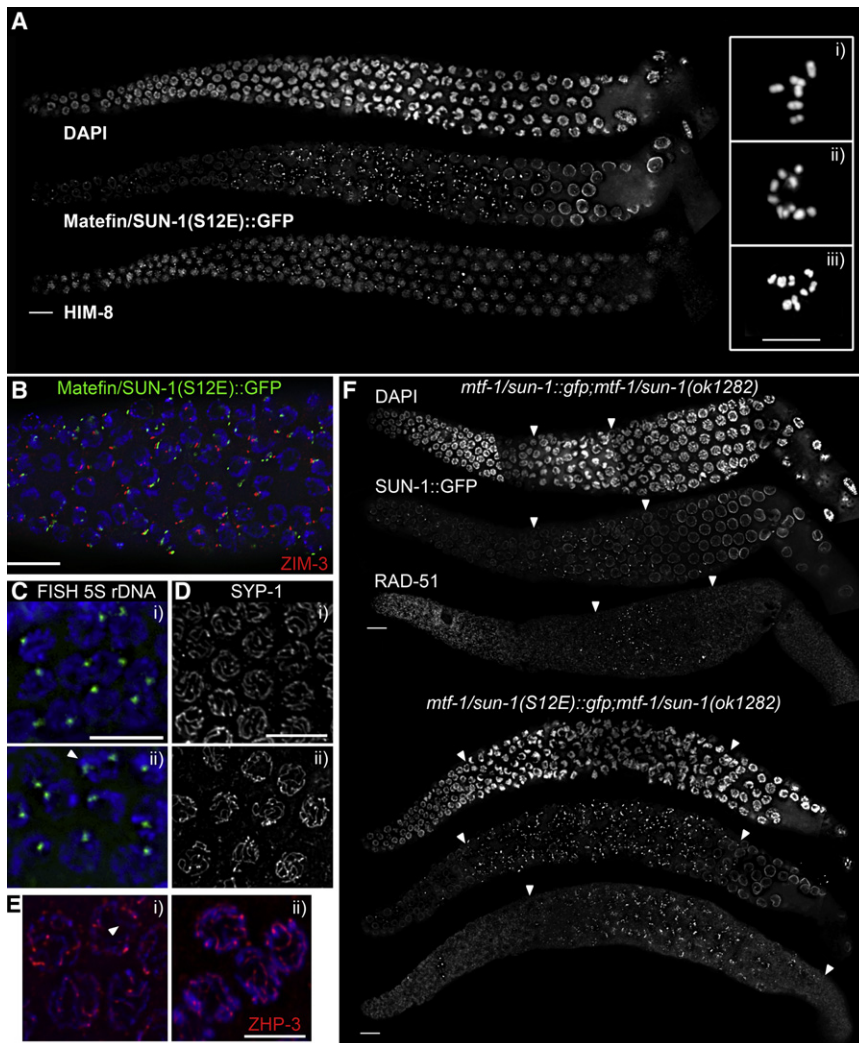


Figure 6. Dephosphorylation of SUN-1 Serine12 Promotes Timely Exit from the Transition Zone and Proper DNA Repair

(A) Chromatin clustering, SUN-1(S12E)::GFP aggregation, and HIM-8 localization in hermaphrodite gonads expressing solely SUN-1(S12E)::GFP. i, diakinesis in *mtf-1/sun-1::gfp;mtf-1/sun-1(ok1282)* (wild-type); ii and iii, diakinesis in *mtf-1/sun-1(S12E)::gfp;mtf-1/sun-1(ok1282)*.

(B) Costaining of SUN-1(S12E)::GFP (green) aggregates and ZIM-3 (red, channel shifted to the left). Blue, DAPI staining.

(C) Paired FISH signals (green) marking LG V right arm in a region corresponding to mid-pachytene of wild-type (i) and mutant (ii) gonads. White arrowhead marks a nucleus with unpaired FISH signals in the mutant.

(D) SYP-1 assembly in the wild-type situation (i) and in *mtf-1/sun-1(S12E)::gfp;mtf-1/sun-1(ok1282)* (ii) gonads (pachytene region shown).

(E) ZHP-3 (red) disassembly in diplotene of wild-type and mutant hermaphrodites. Blue, DAPI staining. Arrowhead highlights ZHP-3-free chromosome region.

(F) RAD-51 staining in SUN-1(S12E)::GFP-expressing transgenic worms and in hermaphrodites expressing the wild-type protein. Arrowheads border the zones of tight chromatin clustering (DAPI staining), SUN-1::GFP and SUN-1(S12E)::GFP aggregation, and RAD-51 staining. Scale bars represent 10 μ m.

Defects in the timely exit from the TZ are characteristic of mutants affecting the assembly of the SC (MacQueen et al., 2002; Colaiácovo et al., 2003; Smolikov et al., 2007a). In SUN-1(S12E), SYP-1 was loaded normally and elongated into linear structures (Figure 6D). Almost full-pairing levels were reached for chromosomes X and V, (Figures 6A, 6C, and S6A). Interestingly, in late S12E pachytene nuclei (zone 6), the percentage of paired homologs decreased, indicating that the pairing is not completely stabilized (Figure S6A). Therefore, a pairing defect is not the primary reason for the decrease in bivalent formation.

Extending the zone of polarized chromatin can be the consequence of a defect in the timely repair of DSBs and can be suppressed by the absence of SPO-11 (Carlton et al., 2006). In order to monitor recombination, we visualized the repair protein RAD-51 (Alpi et al., 2003; Colaiácovo et al., 2003). In SUN-1::GFP-expressing worms, RAD-51 is detected from the late TZ to mid-pachytene. In contrast, in SUN-1(S12E), RAD-51 foci are present from the mid-TZ until diplotene and in greater numbers (Figures 6F and S6B). Persistence of RAD-51 into late pachytene and its subsequent disappearance in diplotene,

combined with the failure to observe chiasmata on all chromosomes, is indicative of DSB repair from the sister chromatid. This conclusion is supported by the fact that ZHP-3, whose asymmetric disassembly at the end of pachytene is dependent on crossover establishment (Bhalla et al., 2008) (Figure 6E, i), did not disappear as in the wild-type but rather remained in SUN-1(S12E)::GFP-expressing animals as elongated structures decorating the whole chromosome in late pachytene and in diplotene (Figure 6E, ii).

As the tight chromatin clustering of SUN-1(S12E)::GFP transgenic worms is still observed in the *spo-11(me44)* background (Figure S6C), we conclude that the dephosphorylation of SUN-1 S12 directly regulates the timely redispersion of chromosomes upon exit from the TZ. Moreover, we suggest that the timely exit from the TZ regulates proper DNA repair to generate crossovers.

Worms expressing SUN-1(S62E)::GFP with no endogenous SUN-1 displayed a prolonged early pachytene zone characterized by the relaxed clustering of chromatin (Carlton et al., 2006) (Figure S6D). The brood size and embryonic viability was reduced accompanied by an increase in DAPI-positive structures at diakinesis ($x = 6.9$, $n = 38$ diakinesis) and a Him phenotype (Table S1). The S62E line reproduces the extended clustering phenotype seen with S12E, therefore strongly supporting the specificity of this phenotype.

We also analyzed the single-alanine substitution of Ser8. These lines showed reduced embryonic viability and a Him phenotype accompanied by an increase of DAPI-positive bodies at diakinesis (Table S1). Seventeen and a half percent of diakinesis nuclei display more than six DAPI signals, ranging from seven to 12 ($n = 120$ diakinesis).

Hermaphrodites expressing transgenic SUN-1(S12A,S16A)::GFP display defects in meiotic prophase I entailing univalent formation, described in detail below (Figure 7 and Table S1). The single S16A substitution line, however, did not display a cytologically detectable meiotic phenotype (Figure S7A and data not shown). Consistently, six signals at diakinesis ($n = 101$ diakinesis of 30 hermaphrodites; inset in Figure S6A) were seen. Therefore, we concluded that the meiotic prophase I phenotype seen in SUN-1(S12A,S16A) represents the loss of Ser12Pi.

In SUN-1(S12A,S16A)::GFP, an average of 11.7 DAPI signals ($SD = 0.6$; $n = 22$ diakinesis, ten gonads) were counted at diakinesis, documenting failed bivalent formation. Consistently, RAD-51 is present longer (from the mid-TZ until diplotene) and in greater numbers as compared to wild-type transgenes (Figure 7A), indicating a defect in DSB repair. SUN-1(S12A,S16A)::GFP aggregates are formed upon entry into meiosis, and they colocalize with the PC-binding protein HIM-8 (Figure 7A and data not shown). However, fewer large aggregates (patches) can be detected (Figures 7A and S7C), correlating with the lack of pronounced chromatin clustering. Despite HIM-8 localization at aggregates, X chromosome pairing is defective (Figure 7B). However, the SC central component SYP-1 is timely and extensively loaded in the mutant worms (Figure 7C), suggesting the presence of nonhomologous synapsis.

Nonhomologous synapsis is also observed in the movement-defective SUN-domain mutated *jf18* allele caused by the loss of ZYG-12 from the outer NE. Immunostaining for ZYG-12 in SUN-1(S12A,S16A)::GFP-expressing lines showed that ZYG-12 is retained at the outer NE (Figure S7B). This is consistent with time-lapse analysis of movement competent SUN-1(S12A,S16A)::GFP aggregates (see Movies S6 and S7).

To address how this substitution elicits nonhomologous synapsis, we analyzed the size distribution of the SUN-1 aggregates. A reduced number of patches can be seen in the mutant line in comparison to the wild-type SUN-1 and SUN-1(S16A) (Figure S7C). Importantly, the size of single chromosome SUN-1(S12A,S16A)::GFP attachment foci is comparable to the wild-type. Despite the lack of transgenic lines with Ser to Ala exchanges for all the phospho-target sites, the SUN-1(S12A,S16A)::GFP-expressing transgenic line suggests that the modification is required for proper homolog pairing. The reduction of large SUN-1 patches proposes a defect in the homology check.

DISCUSSION

The Induction of SUN-1 Aggregates in Early Meiosis

Our data reveal a strong correlation between SUN-1 aggregate formation and PC protein binding to one chromosome end. The foci and patches of SUN-1 form upon entry into the TZ, concomitantly with the attachment of PC-containing chromo-

some ends at the NE. PC-binding proteins colocalize with SUN-1 aggregates and ZIM-1 and ZIM-3 could be coprecipitated with SUN-1 (see the model in Figure 7; data not shown). While the autosome-associated ZIM-proteins are detectable in the TZ up to early pachytene, HIM-8, the PC-binding protein of the X chromosome, is present until later stages of meiotic prophase, where it colocalizes with the only persisting SUN-1 aggregate.

In chromosome axis mutants, such as HIM-3 and HTP-1, SUN-1 aggregates are strongly reduced. Moreover, in aged *him-19(jf6)* hermaphrodite gonads, the restoration of SUN-1 aggregates by artificially induced DSBs correlates with the reassociation of ZIM-3 with the chromosomes. Full chromosomal association of PC-binding proteins, except for HIM-8, depends on CHK-2 activity (Phillips and Dernburg, 2006), whereas in *chk-2(me64)* SUN-1 aggregates are completely absent. These observations could be explained by a model in which PC-binding proteins, perhaps in a phosphorylated form, are involved in the induction of SUN-1 aggregates at the beginning of the TZ. The aggregates are induced as soon as *chk-2*-dependent modified PC-binding proteins associate with chromosome ends and attach to the inner NE (Figure 7). Consistently, Sato et al. (2009) show that in the *him-8* missense allele *me4* (S85F), HIM-8 still localizes to chromosome ends and the NE, but colocalizing SUN-1 aggregates cannot be detected. S85 might be a potential CHK-2 target site.

Alternatively, the *chk-2*-dependent phosphorylation of SUN-1 indirectly influences the recruitment of the ZIM proteins to chromosomal ends. Deciphering the regulatory mechanisms leading to CHK-2 activation is a challenge for future studies.

The Function of SUN-1 Aggregates

The local enrichment of the SUN-1/ZYG-12 NE bridge provides a powerful connective interface for mechanically stable attachment of chromosome ends to the nuclear periphery. Small SUN-1 foci appear earlier and mature into larger SUN-1 patches as nuclei progress through the TZ and into pachytene.

Several lines of evidence suggest that SUN-1 foci with a diameter $< 1.1 \mu\text{m}$ are the primary aggregates formed upon attachment of chromosome ends to the NE, while larger aggregates or patches constitute sites where different chromosome ends coalesce to assess homology and initiate synapsis. First, the SUN-1(G311V)::GFP line only forms movement impaired foci. Second, SUN-1 patches could only be observed in nuclei with clustered chromatin (an indicator of chromosome movement). Third, in *him-19(jf6)* large aggregates could only be observed in nuclei where the clustering of chromatin is restored concomitantly with movement. Finally, in mutants deficient for homologous alignment or synapsis, only a few patches but an increased number of SUN-1 foci could be seen. If the homologous partner is not available, as in *htp-1*, chromosome ends remain mobile and patches would be broken into smaller foci (Figure 7). The presence of an increased number of SUN-1 foci would, therefore, be consistent with an ongoing homology search, where chromosomes move randomly over one hemisphere of the nucleus, meet, and coalesce. Chromosome movement not only assists in the homology search process as a “mixing force,” but additionally acts as a “repelling force,” preventing nonhomologous synapsis.

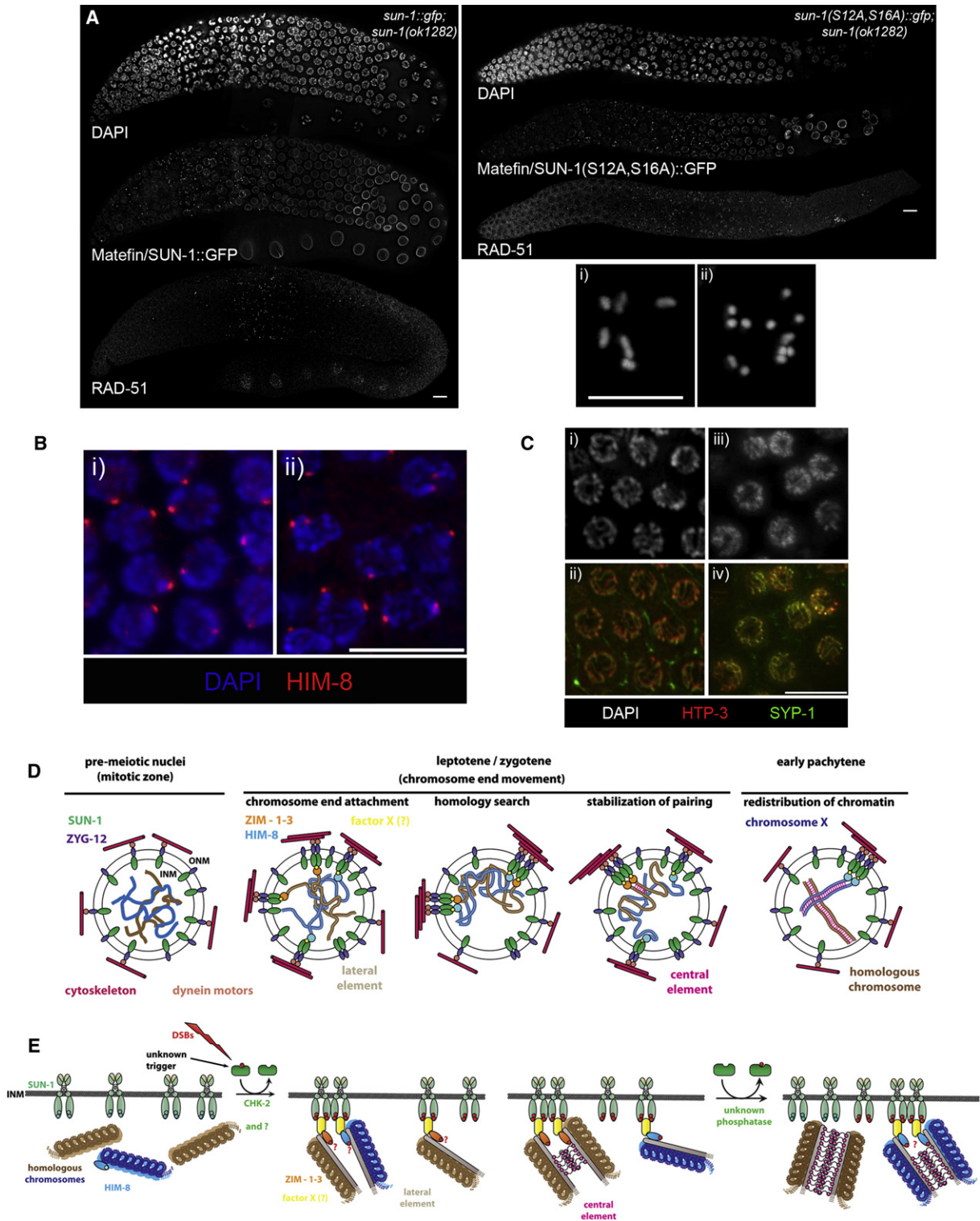


Figure 7. Unphosphorylatable Serine12 Elicits a Meiotic Pairing Defect

(A) Chromatin clustering, SUN-1::GFP aggregation, and RAD-51 staining in hermaphrodite gonads expressing solely SUN-1(S12A,S16A)::GFP or wild-type SUN-1::GFP. i, diakinesis in *mtf-1/sun-1::gfp; mtf-1/sun-1(ok1282)* (wild-type); ii, diakinesis in *mtf-1/sun-1(S12A,S16A)::gfp; mtf-1/sun-1(ok1282)*.

(B) HIM-8 localization in hermaphrodite gonads solely expressing SUN-1(S12A,S16A)::GFP. Blue, DAPI staining; red, HIM-8 staining. Paired HIM-8 signals in wild-type pachytene (i) and unpaired HIM-8 signals in *mtf-1/sun-1(S12A,S16A)::gfp; mtf-1/sun-1(ok1282)* pachytene region (ii) are shown.

Interestingly, the special allele *me42* of the SC component SYP-3 results in a C-terminal truncation and leads to a premature exit from the TZ. *syp-3(me42)* is synapsis defective and appears to employ an alternative meiotic repair pathway (Smolikov et al., 2007a, 2007b). This suggests that a specific synapsis and/or recombination intermediate activates the phosphatase to act on SUN-1. We hypothesize that chromosomes continue to move as a united parental chromosomal pairs once synapsed followed by the concerted resolution of aggregates mediated by the so far unknown phosphatase. This is supported by the fact that the average number of four patches remains constant throughout the TZ.

Phosphorylation of the SUN-1 N Terminus and Functional Implications

Six N-terminally located serines and one serine or threonine are phosphorylated in germline-expressed SUN-1. Our cytological analysis of phosphorylations has revealed a cell cycle-specific phosphorylation in mitosis, peaking toward anaphase, and a meiotic phosphorylation pattern overlapping with the time window of homologous pairing and reappearing later on in diakinesis nuclei.

In meiotic prophase I, phosphorylated serines of SUN-1 overlap with clustered chromatin and the presence of SUN-1 aggregates in the TZ. As nuclei enter early pachytene, S8-Pi staining becomes progressively weaker, eventually disappearing concomitantly with homogenous redispersion of the chromatin throughout the nucleus. This suggests that S8-Pi is first dephosphorylated in SUN-1 aggregates and that the dephosphorylated protein redistributes throughout the NE, resulting in gradually weaker signals as nuclei progress through meiotic prophase I.

In meiosis, the phosphorylation might influence the binding affinity of chromatin-binding proteins or the nuclear lamina to the NE. We found that in an unphosphorylatable SUN-1 mutant chromosomes nonhomologously synapse despite retaining aggregate mobility. The phosphorylation of SUN-1 could promote the interaction to the PC proteins directly or indirectly (PC proteins can be found in a SUN-1 protein complex by mass spectrometry analysis, data not shown). The PC proteins were proposed to have a prominent role in licensing synapsis (Sato et al., 2009). The weakening of this connection could account for the reduced amount of large SUN-1 patches representing the ongoing homology check. We therefore conclude

that the phosphorylation is required for the induction of functional chromosomal attachment plaques. Stable association of chromosome ends at the nuclear periphery is a prerequisite for pronounced chromosome movement. Furthermore, we hypothesize that the phosphorylations of the SUN-1 N terminus impact the mobility of chromosomal attachment plaques by influencing its capability to self-oligomerize or support the mobility of the protein within the inner nuclear membrane, while dephosphorylation of SUN-1 regulates the dissolution of aggregates.

Dramatic phenotypes were observed in the phosphomimic S12E mutation, suggesting that timely dephosphorylation of SUN-1 is required for aggregate dissociation and chromatin redistribution. Consistently, the TZ prolongation phenotype was also observed in S8E and S62E mutants. The data also suggest that the dephosphorylation is necessary for ongoing DSB repair. Possibly, the movement out from the TZ clustering allows for the polymerization of the SC central element along the length of the entire chromosome, a prerequisite for crossover formation. Also in yeast, chromosome movement influences recombinational repair by resolving chromosome entanglements, ectopic contacts, and/or restructuring chromosomes (Koszul et al., 2008; Wanat et al., 2008; Kosaka et al., 2008).

The trigger for the induction of SUN-1 Ser8, 12, and 24 phosphorylation is less clear. We favor the idea that CHK-2 is directly involved in the phosphorylation of the SUN-1 N terminus. It is possible that CHK-2 recruited by PC-binding proteins phosphorylates the inner nuclear membrane protein, as soon as chromosome ends attach to the NE. The induction of DSBs is apparently involved in S8-Pi induction, as demonstrated by the restoration of the phosphorylation pattern upon irradiation of *him-19(jf6)* aged hermaphrodites. In *C. elegans*, full homolog pairing and synapsis are independent of SPO-11 (Dernburg et al., 1998). Consistently, we found that the elimination of DSBs is not sufficient to prevent phosphorylation of SUN-1, arguing for redundant pathways that lead to CHK-2 activation to induce SUN-1 phosphorylation.

Concomitantly with chromosome recruitment of PC proteins, chromosomes are moved over the surface of the nucleus searching proper and repelling improper interactions (see also Sato et al., 2009). Our study strongly supports a model in which the modification of SUN-1, a core component of the movement apparatus, adds the temporal frame to the searching process.

(C) SYP-1 (green) and HTP-3 (red) assembly in wild-type (ii) and in *mtf-1/sun-1(S12A,S16A)::gfp;mtf-1/sun-1(ok1282)* (iv) pachytene regions. Gray, DAPI staining in wild-type (i) and in *mtf-1/sun-1(S12A,S16A)::gfp;mtf-1/sun-1(ok1282)* (iii).

Scale bars represent 10 μ m.

(D and E) A model of SUN-1-mediated homologous chromosome pairing.

(D) Overview of chromosome pairing. Homologous chromosomes depicted as blue (chromosome X) and brown (an autosome) lines.

(E) Chromosome attachment and SUN-1 modifications.

Green ellipses, SUN-1. For simplicity, only the inner nuclear membrane (INM) with associated proteins is drawn. Upon entry into meiosis, PC-binding proteins (blue and orange ellipses), most likely CHK-2-dependent phosphorylated (small red circles), associate with the respective chromosome ends. PC-containing chromosome ends attach to SUN-1 at the NE. The N terminus of Matefin/SUN-1 is phosphorylated (Ser8 and Ser12 are marked) in a CHK-2-dependent manner activated by DSBs or a so far unknown trigger. SUN-1/ZYG-12 (violet ellipses in D) form aggregates at chromosomal attachment sites to establish a proteinaceous bridge across the NE. Chromosome ends are, thereby, connected through motors (brick in D) to the cytoskeleton (dark pink bars in D) to provide a link between the motile forces in the cytoplasm and chromosome ends in the nuclear interior. When chromosome ends meet, small SUN-1 aggregates coalesce to form larger patches that likely represent sites of ongoing homology check. If the homologous partner is not available, chromosome ends are moved further. As homology is successfully assessed, the SC (magenta lines and circles) polymerizes. Autosomal PC-binding proteins are lost from chromosome ends and the respective SUN-1 aggregates dissolve in early pachytene after dephosphorylation. HIM-8 remains bound to the X chromosome until mid-pachytene.

EXPERIMENTAL PROCEDURES

Cytological Preparation of Gonads and Immunostaining

Hermaphrodite gonads were dissected and fixed as described in [Martinez-Perez and Villeneuve \(2005\)](#). For immunostaining, gonads were blocked in 3% BSA/1 × PBS for 20 min. Antibodies were diluted in 1 × PBS/0.01% sodium azide as follows: anti-SUN-1 (antibody against an N-terminal peptide, this study) 1:700, anti-SUN-1 (antibody against an N-terminal peptide, [Fridkin et al. \(2004\)](#)) 1:700, anti-SUN-1 Ser8-Pi (this study) 1:700, anti-GFP (Roche Diagnostics, #11814460001) 1:300, anti-HIM-8 ([Phillips et al., 2005](#)) 1:500, anti-ZIM-3 (this study) 1:100, anti-RAD-51 ([Alpi et al., 2003](#)) 1:300, anti-SYP-1 ([MacQueen et al., 2002](#)) 1:200, anti-SPD-5 ([Pelletier et al., 2004](#)) 1:2000, and anti-ZYG-12 ([Malone et al., 2003](#)) 1:400.

Fluorescence In Situ Hybridization

5S ribosomal DNA (rDNA) was used as a probe for the right arm of chromosome V. 5S rDNA was labeled by PCR with digoxigenin-11-dUTP ([Pasierbek et al., 2001](#)). Digoxigenin-labeled probes were detected with FITC-conjugated anti-digoxigenin antibodies (1:100).

Microscopy and Evaluation

Evaluation of cytological phenotypes was performed in animals kept at 20°C, 18–24 hr after L4. A Zeiss Axioskop epifluorescence microscope was used in combination with a cooled CCD camera (Photometrics, Tucson, AZ). 3D stacks of images were taken (MetaVue software, Universal Imaging, Downingtown, PA), deconvolved (AutoDeblur software, AutoQuant Imaging, Troy, NY) and projected (Helicon Focus software, <http://helicon.com.ua/heliconfocus/>). Artificial coloring and merging were done with Adobe Photoshop 7.0 (Adobe Systems).

Live Imaging of SUN-1::GFP Constructs

Worms were mounted in 10 mM levamisole in M9 buffer on 2% agarose, covered with a coverslip, and sealed with melted Vaseline. Images were acquired at room temperature every 5 s for 15 min as stacks of optical sections with 1 μm intervals with a Deltavision deconvolution microscopy system (Applied Precision, Issaquah, WA). The following conditions were used: FITC fluorescence filter, 10% ND, bin 1 × 1, exposure time 200 ms, objective 60× (CoolSNAP HQ digital camera from photometrics).

Maximum-intensity projections with Softworx software (Applied Precision) were created and the collection of files saved as stack files with Metamorph Offline (Molecular Devices, Downingtown, PA). Nonspecific signals of the stack pictures were removed with Autoquant X2 (AutoQuant Imaging), and the slices realigned with the first slice used as a reference. With Metamorph Offline, the position of the dots was followed manually. The position of the dots was plotted with Gnuplot software (<http://www.gnuplot.info/>).

Aggregate movements were recorded with a Deltavision microscope scanning through the gonad every 5 s. After projection, the image sequences were saved as movies (Quicktime) with a rate of six frames per second. Therefore, aggregates move 30 times faster than in real time.

Irradiation Assay

Hermaphrodites were exposed to 5000 rads of γ -radiation from a ^{137}Cs source. Cytological analysis was performed 120 min after irradiation.

Immunoprecipitation and Silver Staining of SUN-1::GFP

Worms were harvested in 1 × homogenization buffer, frozen in liquid nitrogen, thawed on ice, and sonicated twice on ice (5–7 × 30 s bursts at an amplitude of 28%). Protein lysates were added to anti-GFP (Roche Diagnostics, #11814460001) coupled Dynabeads Pan Mouse IgG (DynaL Biotech, #110.41) and incubated overnight at 4°C.

Precipitated proteins were washed four times in 1 × PBS and eluted at 60°C for 10 min in SDS-sample buffer. Samples were loaded onto SDS-PAGE gels (Bio-Rad Laboratories) and silver stained ([Shevchenko et al., 1996](#)).

Mass Spectrometry Analysis

See the [Supplemental Data](#).

SUPPLEMENTAL DATA

Supplemental Data include Supplemental Experimental Procedures, seven figures, two tables, and seven movies and can be found with this article online at [http://www.cell.com/supplemental/S0092-8674\(09\)01371-3](http://www.cell.com/supplemental/S0092-8674(09)01371-3).

ACKNOWLEDGMENTS

We thank Christian Pflügl, Ella Kaplan, Sonja Kolar, and Sophie Wöhrer for technical assistance. We are grateful to Chris Malone, Tony Hyman, Abby Dernburg, Anton Gartner, Anne Villeneuve, Monique Zetka, and the Caenorhabditis Genetics Center for strains, plasmids, and antibodies. We are indebted to Abby Dernburg for sharing unpublished results. We are grateful to Peter Carlton, Cécile Brocard, and Simon Boulton for helpful suggestions. We thank Iain Wilson, Maria Siomos, Yudith Yanowitz, and Josef Loidl for discussion. This work was supported by grants from the FWF (P-21107 and SFB-F3402), the WWTF (LS05009), the University of Vienna (I031-B), as well as an Elise-Richter grant to V.J., a DOC scholarship to A.W., an Israel Science Foundation grant to Y.G., and a Clore scholarship to A.F.

Received: June 5, 2009

Revised: October 16, 2009

Accepted: October 30, 2009

Published online: November 12, 2009

REFERENCES

- Alpi, A., Pasierbek, P., Gartner, A., and Loidl, J. (2003). Genetic and cytological characterization of the recombination protein RAD-51 in *Caenorhabditis elegans*. *Chromosoma* 112, 6–16.
- Alsheimer, M. (2009). The dance floor of meiosis: evolutionary conservation of nuclear envelope attachment and dynamics of meiotic telomeres. *Genome Dyn.* 5, 81–93.
- Bhalla, N., and Dernburg, A.F. (2008). Prelude to a division. *Annu. Rev. Cell Dev. Biol.* 24, 397–424.
- Bhalla, N., Wynne, D.J., Jantsch, V., and Dernburg, A.F. (2008). ZHP-3 acts at crossovers to couple meiotic recombination with synaptonemal complex disassembly and bivalent formation in *C. elegans*. *PLoS Genet.* 4, e1000235.
- Carlton, P.M., Farruggio, A.P., and Dernburg, A.F. (2006). A link between meiotic prophase progression and crossover control. *PLoS Genet.* 2, e12.
- Chen, Y., and Poon, R.Y.C. (2008). The multiple checkpoint functions of CHK1 and CHK2 in maintenance of genome stability. *Front Biosci.* 13, 5016–5029.
- Chikashige, Y., Tsutsumi, C., Yamane, M., Okamasa, K., Haraguchi, T., and Hiraoka, Y. (2006). Meiotic proteins bqt1 and bqt2 tether telomeres to form the bouquet arrangement of chromosomes. *Cell* 125, 59–69.
- Chin, G.M., and Villeneuve, A.M. (2001). *C. elegans* mre-11 is required for meiotic recombination and DNA repair but is dispensable for the meiotic G(2) DNA damage checkpoint. *Genes Dev.* 15, 522–534.
- Colaiácovo, M.P., MacQueen, A.J., Martinez-Perez, E., McDonald, K., Adamo, A., Volpe, A.L., and Villeneuve, A.M. (2003). Synaptonemal complex assembly in *C. elegans* is dispensable for loading strand-exchange proteins but critical for proper completion of recombination. *Dev. Cell* 5, 463–474.
- Conrad, M.N., Lee, C.-Y., Wilkerson, J.L., and Dresser, M.E. (2007). MPS3 mediates meiotic bouquet formation in *Saccharomyces cerevisiae*. *Proc. Natl. Acad. Sci. USA* 104, 8863–8868.
- Conrad, M.N., Lee, C.-Y., Chao, G., Shinohara, M., Kosaka, H., Shinohara, A., Conchello, J.-A., and Dresser, M.E. (2008). Rapid telomere movement in meiotic prophase is promoted by NDJ1, MPS3, and CSM4 and is modulated by recombination. *Cell* 133, 1175–1187.
- Couteau, F., and Zetka, M. (2005). HTP-1 coordinates synaptonemal complex assembly with homolog alignment during meiosis in *C. elegans*. *Genes Dev.* 19, 2744–2756.

- Couteau, F., Nabeshima, K., Villeneuve, A., and Zetka, M. (2004). A component of *C. elegans* meiotic chromosome axes at the interface of homolog alignment, synapsis, nuclear reorganization, and recombination. *Curr. Biol.* *14*, 585–592.
- Dernburg, A.F., McDonald, K., Moulder, G., Barstead, R., Dresser, M., and Villeneuve, A.M. (1998). Meiotic recombination in *C. elegans* initiates by a conserved mechanism and is dispensable for homologous chromosome synapsis. *Cell* *94*, 387–398.
- Ding, D.Q., Chikashige, Y., Haraguchi, T., and Hiraoka, Y. (1998). Oscillatory nuclear movement in fission yeast meiotic prophase is driven by astral microtubules, as revealed by continuous observation of chromosomes and microtubules in living cells. *J. Cell Sci.* *111*, 701–712.
- Ding, X., Xu, R., Yu, J., Xu, T., Zhuang, Y., and Han, M. (2007). SUN1 is required for telomere attachment to nuclear envelope and gametogenesis in mice. *Dev. Cell* *12*, 863–872.
- Fridkin, A., Mills, E., Margalit, A., Neufeld, E., Lee, K.K., Feinstein, N., Cohen, M., Wilson, K.L., and Gruenbaum, Y. (2004). Matefin, a *Caenorhabditis elegans* germ line-specific SUN-domain nuclear membrane protein, is essential for early embryonic and germ cell development. *Proc. Natl. Acad. Sci. USA* *101*, 6987–6992.
- Fridkin, A., Penkner, A., Jantsch, V., and Gruenbaum, Y. (2009). SUN-domain and KASH-domain proteins during development, meiosis and disease. *Cell. Mol. Life Sci.* *66*, 1518–1533.
- Garcia-Muse, T., and Boulton, S.J. (2005). Distinct modes of ATR activation after replication stress and DNA double-strand breaks in *Caenorhabditis elegans*. *EMBO J.* *24*, 4345–4355.
- Goldstein, P., and Slaton, D.E. (1982). The synaptonemal complexes of *Caenorhabditis elegans*: comparison of wild-type and mutant strains and pachytene karyotype analysis of wild-type. *Chromosoma* *84*, 585–597.
- Hamil, D.R., Severson, A.F., Carter, J.C., and Bowerman, B. (2002). Centrosome maturation and mitotic spindle assembly in *C. elegans* require SPD-5, a protein with multiple coiled-coil domains. *Dev. Cell* *3*, 673–684.
- Harper, L., Golubovskaya, I., and Cande, W.Z. (2004). A bouquet of chromosomes. *J. Cell Sci.* *117*, 4025–4032.
- Kosaka, H., Shinohara, M., and Shinohara, A. (2008). Csm4-dependent telomere movement on nuclear envelope promotes meiotic recombination. *PLoS Genet.* *4*, e1000196.
- Kozul, R., Kim, K.P., Prentiss, M., Kleckner, N., and Kameoka, S. (2008). Meiotic chromosomes move by linkage to dynamic actin cables with transduction of force through the nuclear envelope. *Cell* *133*, 1188–1201.
- MacQueen, A.J., and Villeneuve, A.M. (2001). Nuclear reorganization and homologous chromosome pairing during meiotic prophase require *C. elegans* *chk-2*. *Genes Dev.* *15*, 1674–1687.
- MacQueen, A.J., Colaiácovo, M.P., McDonald, K., and Villeneuve, A.M. (2002). Synapsis-dependent and -independent mechanisms stabilize homolog pairing during meiotic prophase in *C. elegans*. *Genes Dev.* *16*, 2428–2442.
- MacQueen, A.J., Phillips, C.M., Bhalla, N., Weiser, P., Villeneuve, A.M., and Dernburg, A.F. (2005). Chromosome sites play dual roles to establish homologous synapsis during meiosis in *C. elegans*. *Cell* *123*, 1037–1050.
- Malone, C.J., Misner, L., Bot, N.L., Tsai, M.-C., Campbell, J.M., Ahinger, J., and White, J.G. (2003). The *C. elegans* hook protein, ZYG-12, mediates the essential attachment between the centrosome and nucleus. *Cell* *115*, 825–836.
- Martinez-Perez, E., and Villeneuve, A.M. (2005). HTP-1-dependent constraints coordinate homolog pairing and synapsis and promote chiasma formation during *C. elegans* meiosis. *Genes Dev.* *19*, 2727–2743.
- Pasierbek, P., Jantsch, M., Melcher, M., Schleiffer, A., Schweizer, D., and Loidl, J. (2001). A *Caenorhabditis elegans* cohesion protein with functions in meiotic chromosome pairing and disjunction. *Genes Dev.* *15*, 1349–1360.
- Pawlowski, W.P., and Cande, W.Z. (2005). Coordinating the events of the meiotic prophase. *Trends Cell Biol.* *15*, 674–681.
- Pelletier, L., Oziü, N., Hannak, E., Cowan, C., Habermann, B., Ruer, M., Müller-Reichert, T., and Hyman, A.A. (2004). The *Caenorhabditis elegans* centrosomal protein SPD-2 is required for both pericentriolar material recruitment and centriole duplication. *Curr. Biol.* *14*, 863–873.
- Penkner, A., Tang, L., Novatchkova, M., Ladurner, M., Fridkin, A., Gruenbaum, Y., Schweizer, D., Loidl, J., and Jantsch, V. (2007). The nuclear envelope protein Matefin/SUN-1 is required for homologous pairing in *C. elegans* meiosis. *Dev. Cell* *12*, 873–885.
- Perona, R., Moncho-Amor, V., Machado-Pinilla, R., Belda-Iniesta, C., and Pérez, I.S. (2008). Role of CHK2 in cancer development. *Clin. Transl. Oncol.* *10*, 538–542.
- Petronczki, M., Siomos, M.F., and Nasmyth, K. (2003). Un ménage à quatre: the molecular biology of chromosome segregation in meiosis. *Cell* *112*, 423–440.
- Phillips, C.M., and Dernburg, A.F. (2006). A family of zinc-finger proteins is required for chromosome-specific pairing and synapsis during meiosis in *C. elegans*. *Dev. Cell* *11*, 817–829.
- Phillips, C.M., Wong, C., Bhalla, N., Carlton, P.M., Weiser, P., Meneely, P.M., and Dernburg, A.F. (2005). HIM-8 binds to the X chromosome pairing center and mediates chromosome-specific meiotic synapsis. *Cell* *123*, 1051–1063.
- Phillips, C.M., Meng, X., Zhang, L., Chretien, J.H., Urnov, F.D., and Dernburg, A.F. (2009). Identification of chromosome sequence motifs that mediate meiotic pairing and synapsis in *C. elegans*. *Nat. Cell Biol.* *11*, 934–942.
- Sato, A., Isaac, B., Phillips, C.M., Rillo, R., Carlton, P.M., Wynne, D.J., Roshni, A., Kasad, R.A., and Dernburg, A.F. (2009). Cytoskeletal forces span the nuclear envelope to coordinate meiotic chromosome pairing and synapsis. *Cell* *139*, this issue, 907–919.
- Scherthan, H. (2007). Telomere attachment and clustering during meiosis. *Cell. Mol. Life Sci.* *64*, 117–124.
- Scherthan, H., Wang, H., Adelfalk, C., White, E.J., Cowan, C., Cande, W.Z., and Kaback, D.B. (2007). Chromosome mobility during meiotic prophase in *Saccharomyces cerevisiae*. *Proc. Natl. Acad. Sci. USA* *104*, 16934–16939.
- Schmitt, J., Benavente, R., Hodzic, D., Höög, C., Stewart, C.L., and Alsheimer, M. (2007). Transmembrane protein Sun2 is involved in tethering mammalian meiotic telomeres to the nuclear envelope. *Proc. Natl. Acad. Sci. USA* *104*, 7426–7431.
- Shevchenko, A., Wilm, M., Vorm, O., and Mann, M. (1996). Mass spectrometric sequencing of proteins silver-stained polyacrylamide gels. *Anal. Chem.* *68*, 850–858.
- Smolnikov, S., Eizinger, A., Schild-Prufert, K., Hurlburt, A., McDonald, K., Engebrecht, J., Villeneuve, A.M., and Colaiácovo, M.P. (2007a). SYP-3 restricts synaptonemal complex assembly to bridge paired chromosome axes during meiosis in *Caenorhabditis elegans*. *Genetics* *176*, 2015–2025.
- Smolnikov, S., Eizinger, A., Hurlburt, A., Rogers, E., Villeneuve, A.M., and Colaiácovo, M.P. (2007b). Synapsis-defective mutants reveal a correlation between chromosome conformation and the mode of double-strand break repair during *Caenorhabditis elegans* meiosis. *Genetics* *176*, 2027–2033.
- Starr, D.A. (2009). A nuclear-envelope bridge positions nuclei and moves chromosomes. *J. Cell Sci.* *122*, 577–586.
- Stergiou, L., Doukometzidis, K., Sandoel, A., and Hengartner, M.O. (2007). The nucleotide excision repair pathway is required for UV-C-induced apoptosis in *Caenorhabditis elegans*. *Cell Death Differ.* *14*, 1129–1138.
- Tang, X., Jin, Y., and Cande, W.Z. (2006). Bqt2p is essential for initiating telomere clustering upon pheromone sensing in fission yeast. *J. Cell Biol.* *173*, 845–851.
- Trelles-Sticken, E., Adelfalk, C., Loidl, J., and Scherthan, H. (2005). Meiotic telomere clustering requires actin for its formation and cohesin for its resolution. *J. Cell Biol.* *170*, 213–223.
- Tzur, Y.B., Wilson, K.L., and Gruenbaum, Y. (2006). SUN-domain proteins: 'Velcro' that links the nucleoskeleton to the cytoskeleton. *Nat. Rev. Mol. Cell Biol.* *7*, 782–788.
- Wanat, J.J., Kim, K.P., Kozul, R., Zanders, S., Weiner, B., Kleckner, N., and Alani, E. (2008). Csm4, in collaboration with Ndj1, mediates telomere-led chromosome dynamics and recombination during yeast meiosis. *PLoS Genet.* *4*, e1000188.
- Yamamoto, A., West, R.R., McIntosh, J.R., and Hiraoka, Y. (1999). A cytoplasmic dynein heavy chain is required for oscillatory nuclear movement of meiotic prophase and efficient meiotic recombination in fission yeast. *J. Cell Biol.* *145*, 1233–1249.

Cell, Volume 139

Supplemental Data

Meiotic Chromosome Homology Search

Involves Modifications of the Nuclear

Envelope Protein Matefin/SUN-1

Alexandra M. Penkner, Alexandra Fridkin, Jiradet Gloggnitzer, Antoine Baudrimont, Thomas Machacek, Alexander Woglar, Edina Csaszar, Pawel Pasierbek, Gustav Ammerer, Yosef Gruenbaum, Verena Jantsch

Supplemental Experimental Procedures

Nematode strains, strain construction and culture conditions

All *C. elegans* strains were cultured using standard techniques (Brenner, 1974). *C. elegans* strains used: N2 Bristol, RB1276 *mtf-1/sun-1(ok1282)*, WH223 *ojls9 [zyg-12ABC::GFP unc-119(ed3)]; unc-119(ed3)* (Malone et al., 2003), AV276 *syp-2(ok307)* (Colaiacovo et al., 2003), VC418 *him-3(gk149)* (Couteau et al., 2004), *chk-2(me64)* (MacQueen and Villeneuve, 2001), BA821 *spe-26(hc138)* (Van Voorhies, 1992), AV393 *htp-1(gk174)* (Martinez-Perez and Villeneuve, 2005), AV157 *spo-11(me44)* (Hayashi et al., 2007), VC381 *atm-1(gk186)* (Stergiou et al., 2007), DW101 *atl-1(tm853)* (Garcia-Muse and Boulton, 2005), UV21 *him-19(jf6)* (Tang and Jantsch, unpublished). Nematode strains were provided by the *Caenorhabditis Genetics Center*, which is funded by the NIH National Center for Research Resources (NCRR).

Matefin/SUN-1::GFP-expressing transgenic worm strains were generated by microparticle bombardment (Praitis et al., 2001). The *mtf-1/sun-1*-coding locus including 2.8 kb of its 5' sequence and 780 bp of its 3' regulatory sequence was inserted into the pEGFP-1 vector of BD Biosciences Clontech (#6086-1) and co-bombarded with plasmid pDP#mm051 carrying the *unc-119* locus into the *C. elegans* mutant *unc-119(ed3)*. Mutated forms of Matefin/SUN-1::GFP were generated by site-directed mutagenesis. Mutated Matefin/SUN-1::GFP proteins were analyzed in the homozygous *mtf-1/sun-1(ok1282)* deletion background.

Immunoprecipitation and silver staining of Matefin/SUN-1::GFP

1x homogenization buffer: 15 mM Hepes pH7.6, 10 mM KCl, 250 mM NaCl, 1.5 mM MgCl₂, 0.1 mM EDTA, 0.5 mM EGTA, 0.2% Triton*100, 1 mM DTT, 44 mM sucrose, 0.1 mM AEBSF, 5 mM benzamidine, 1:200 aprotinin, 50 mM NaF, 0.1 mM Na₃VO₄, 60 mM β-glycerophosphate, Roche® Complete Mini protease inhibitor cocktail tablets (#11836170001).

SDS-sample buffer: 55 mM Tris/HCl pH6.8, 6 M Urea, 2% (w/v) SDS, 0.1 mM EDTA, 5% (v/v) β-mercaptoethanol, 6% glycerol, 0.025% bromophenol blue.

Mass spectrometry analysis

Enzymatic digest, LC-MS/MS analysis and data analysis

Silver stained gel bands were used for nano-electrospray LC-MS/MS analysis. The gel bands were cut, chopped and washed several times with high quality water. Proteins were reduced by dithiothreitol (DTT) and alkylated by iodoacetamide, trypsin digested overnight at 37°C and stopped by acidifying to 1% with formic acid. We used an HPLC UltiMate™ system equipped with a PepMap C18 purification column (300 µm x 5 mm) and a 75 µm x 150 mm analytical column of the same material. 0.1% TFA was used on the Switchos module for the binding of the peptides and a linear gradient of acetonitrile and 0.1% formic acid in water was used for the elution. LC-MS/MS analyses were carried out with the UltiMate™ system interfaced to an LTQ (Thermo; San Jose, CA, USA) linear ion trap mass spectrometer. The nanospray source of Proxeon (Odense, Denmark) was used with the distal coated silica capillaries of New Objective (Woburn, MA, USA). The electrospray voltage was set to 1500 V. Peptide spectra were recorded over the mass range of m/z 450-1600, MS/MS spectra were recorded in information dependent data acquisition and the default charge state was set to 3; the mass range for MS/MS measurements was calculated according to the masses of the parent ions. One full spectrum was recorded followed by 4 MS/MS spectra for the most intense ions, automatic gain control was applied and the collision energy was set to the arbitrary value of 35. Neutral loss dependent MS/MS/MS experiments were carried out to enhance the fragmentation of phosphopeptides. It was used as collision gas. The instrument was operated in data-dependent modus; fragmented ions were set onto an exclusion list for 20 sec.

Raw spectra were interpreted by Mascot 2.2.04 (Matrix Science Ltd, London, UK) using Mascot Daemon 2.2.2. and Bioworks 3.3 (Thermo; San Jose, CA, USA). Peptide tolerance was set to +/-2 Da, MS/MS tolerance was set to +/-0.8 Da. Carbamidomethylcysteine was set as static modification, oxidation of M, phosphorylation of STY residues and water loss of ST residues were set as variable modifications for both search programs.

The database used for Mascot search was the nr protein database of NIH (NCBI Resources, NIH, Bethesda, MD, USA); taxonomy was *C. elegans*. In order to reduce the search time, the Bioworks search was carried out with a homemade database prepared by the extraction (Bioworks) of all *C. elegans* entries out of the NIH nr database. Ion score cut off was set to 30 for Mascot.

Xcorr versus charge state was set as the filter for Bioworks with the following values: 1.5, 2.00, 2.50, 3.00 for singly, doubly, triply and quadruply charged ions, respectively. Peptide spectra indicated to contain phosphorylated residues were validated manually in both cases.

Live imaging of Matefin/SUN-1::GFP constructs

M9 buffer: 0.6% (w/v) Na₂HPO₄ x(H₂O)₇, 0.3% (w/v) KH₂PO₄, 0.5% (w/v) NaCl, 0.02% (w/v) MgSO₄ x(H₂O)₇

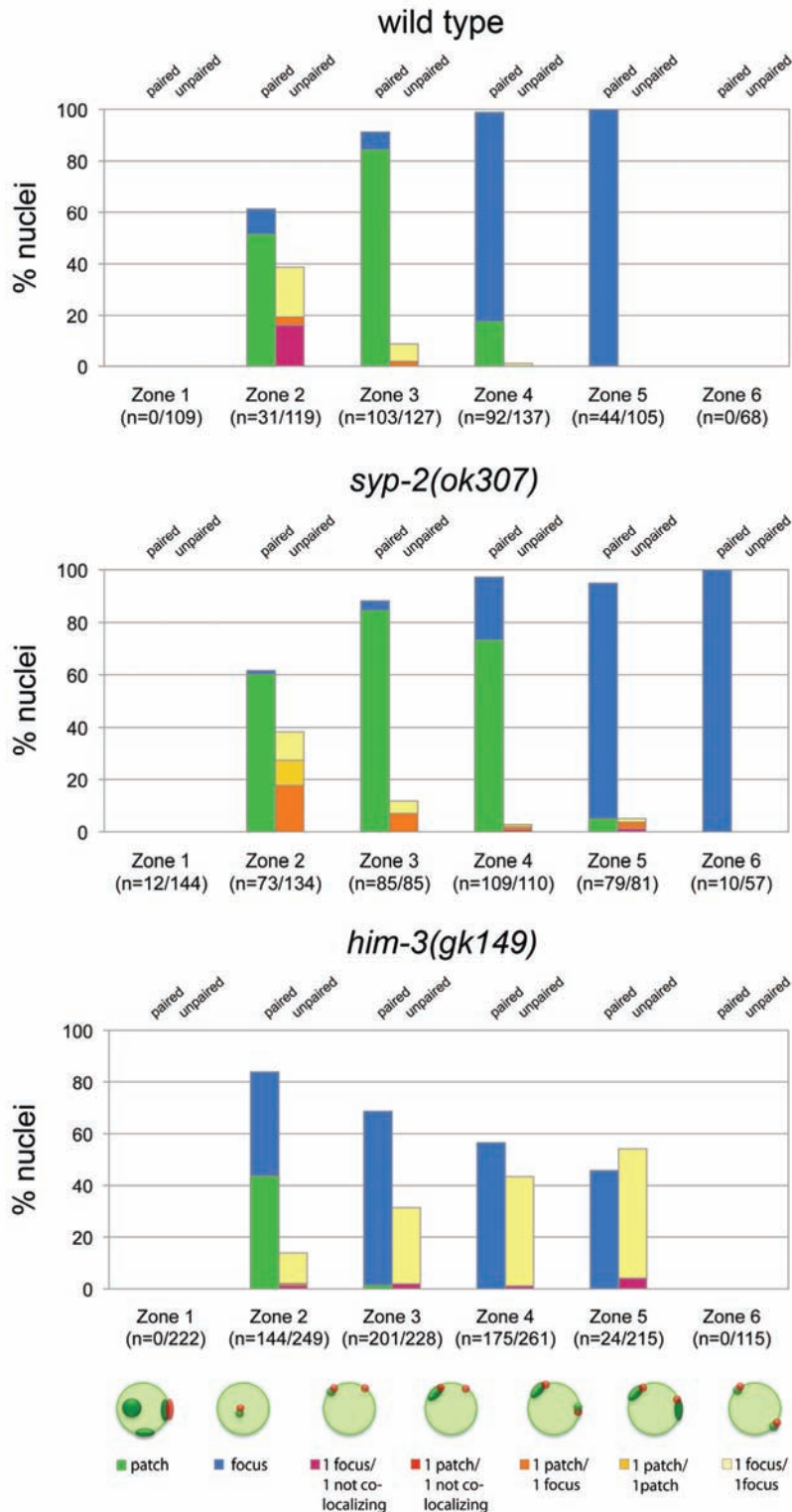


Figure S1. Analysis of the co-localization of Matefin/SUN-1 aggregates and the X chromosome-specific pairing center-binding protein HIM-8 in nuclei displaying aggregates as well as HIM-8 foci. Diagrams of wild type (*mtf-1/sun-1::gfp;mtf-1/sun-1(ok1282)*), *syp-2(ok307)* (*syp-2(ok307);mtf-1/sun-1::gfp;mtf-1/sun-1(ok1282)*) and *him-*

3(*gk149*) (*him-3(gk149);mtf-1/sun-1::gfp;mtf-1/sun-1(ok1282)*) are shown. The number of nuclei analyzed per total number of nuclei is given for each zone.

Figure S2. Mass spectrometry analysis of Matefin/SUN-1::GFP purified from *mtf-1/sun-1::gfp;mtf-1/sun-1(ok1282)* hermaphrodites.

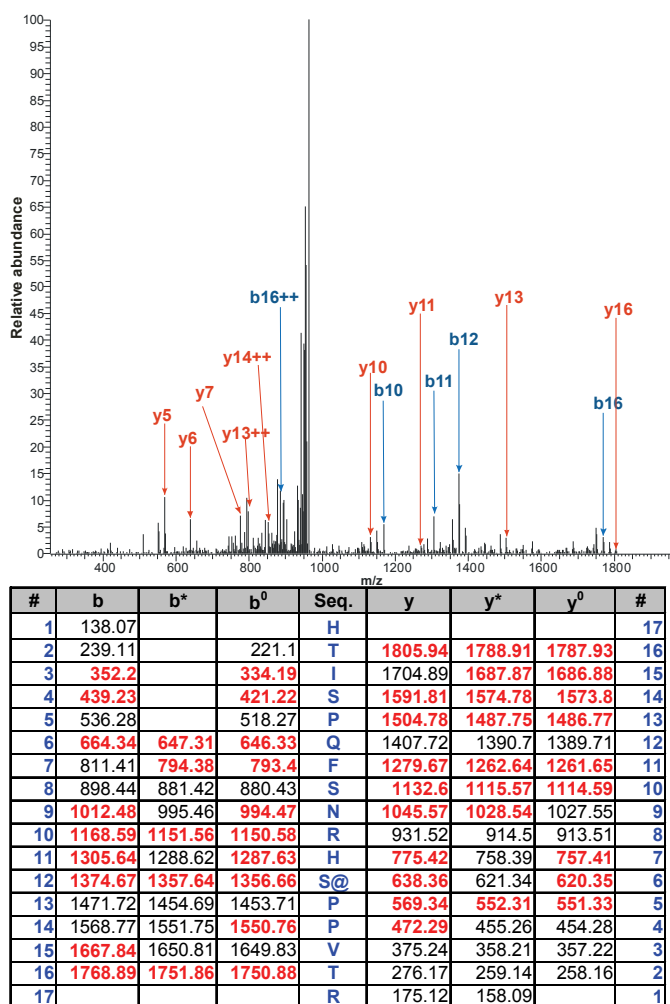


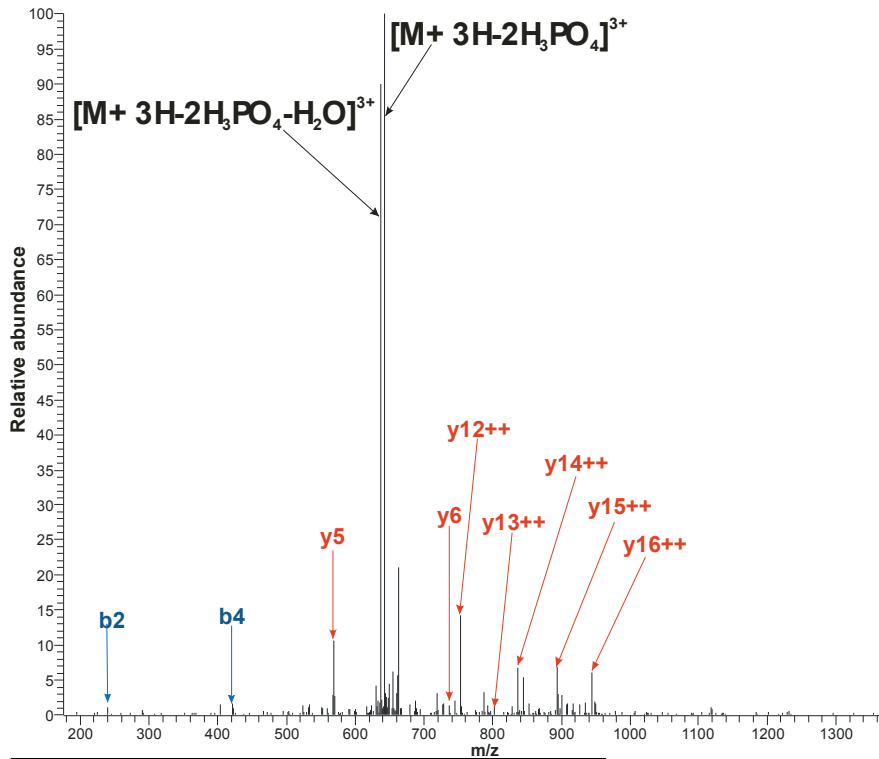
Figure S2.1 Positive ionization low energy CID fragmentation spectrum of the singly phosphorylated peptide HTISPQFSNRHSPPVTR originating from the Matefin/SUN-1::GFP; *mtf-1/sun-1(ok1282)* sample

MS³ spectrum of the doubly charged peptide. The position of the dehydro-alanine generated by the loss of phosphoric acid from the phosphorylated serine residue was labeled with “@”. Identified b and y fragment ions detected in the measurement are colored in the fragmentation table and labeled blue and red, respectively in the spectrum. Identified satellite ions originating from the loss of water (b⁰ or y⁰ ions) or ammonia (b* or y* ions) are also labeled in the table. Although the peptide was doubly charged, it contains several basic residues which account for the doubly charged fragment ions.

#	b	b ⁺	Seq.	y	y ⁺	#	#	b	b ⁺	Seq.	y	y ⁺	#	#	b	b ⁺	Seq.	y	y ⁺	#
1	138.07	69.54	H			17	1	138.07	69.54	H			17	1	138.07	69.54	H			17
2	239.11	120.06	T	1805.94	903.47	16	2	239.11	120.06	T	1805.94	903.47	16	2	239.11	120.06	T	1805.94	903.47	16
3	352.2	176.6	I	1704.89	852.95	15	3	352.2	176.6	I	1704.89	852.95	15	3	352.2	176.6	I	1704.89	852.95	15
4	439.23	220.12	S	1591.81	796.41	14	4	421.22	211.11	S@	1591.81	796.41	14	4	439.23	220.12	S	1591.81	796.41	14
5	536.28	268.64	P	1504.78	752.89	13	5	518.27	259.64	P	1522.79	761.9	13	5	536.28	268.64	P	1504.78	752.89	13
6	664.34	332.67	Q	1407.72	704.37	12	6	646.33	323.67	Q	1425.73	713.37	12	6	664.34	332.67	Q	1407.72	704.37	12
7	811.41	406.21	F	1279.67	640.34	11	7	793.4	397.2	F	1297.68	649.34	11	7	811.41	406.21	F	1279.67	640.34	11
8	898.44	449.72	S	1132.6	566.8	10	8	880.43	440.72	S	1150.61	575.81	10	8	898.44	449.72	S@	1132.6	566.8	10
9	1012.48	506.75	N	1045.57	523.29	9	9	994.47	497.74	N	1063.58	532.29	9	9	1012.48	506.75	N	1045.57	523.29	9
10	1168.59	584.8	R	931.52	466.26	8	10	1150.58	575.79	R	949.53	475.27	8	10	1168.59	584.8	R	931.52	466.26	8
11	1305.64	653.33	H	775.42	388.21	7	11	1287.63	644.32	H	793.43	397.22	7	11	1305.64	653.33	H	775.42	388.21	7
12	1374.67	687.84	S@	638.36	319.68	6	12	1374.67	687.84	S	656.37	328.69	6	12	1374.67	687.84	S@	638.36	319.68	6
13	1471.72	736.36	P	569.34	285.17	5	13	1471.72	736.36	P	569.34	285.17	5	13	1471.72	736.36	P	569.34	285.17	5
14	1568.77	784.89	P	472.29	236.65	4	14	1568.77	784.89	P	472.29	236.65	4	14	1568.77	784.89	P	472.29	236.65	4
15	1667.84	834.42	V	375.24	188.12	3	15	1667.84	834.42	V	375.24	188.12	3	15	1667.84	834.42	V	375.24	188.12	3
16	1768.89	884.95	T	276.17	138.59	2	16	1768.89	884.95	T	276.17	138.59	2	16	1768.89	884.95	T	276.17	138.59	2
17			R	175.12	88.06	1	17			R	175.12	88.06	1	17			R	175.12	88.06	1

Figure S2.2 Assignment of the phosphorylation site in the peptide HTISPQFSNRHSPVTR

Fragment ion coverages for three possible phosphorylation sites. Identified b and y fragment ions detected in the MS³ measurement are colored red in the fragmentation table. The position of the dehydro-alanine was labeled with “@”. Although this peptide was fragmented several times, the unambiguous identification of the modification site was not possible. The phosphorylation was identified by both applied search engines (Mascot and Sequest), but three possible positions were proposed with nearly identical score values. Manual assignment of the fragment ions did not make the differentiation possible either. We concluded, that this spectrum was a mixture of different singly phosphorylated species, which eluted and were fragmented simultaneously. This peptide version with one missed cleavage site was only present in the phosphorylated version. The unphosphorylated peptide was always cleaved C-terminal to R14 by trypsin. This fact supports the phosphorylation on S12. The doubly phosphorylated version of the peptide was also detected (Figure S2.3).



#	b	b ⁺⁺	Seq.	y	y ⁺⁺	#	#	b	b ⁺⁺	Seq.	y	y ⁺⁺	#
1	138.07	69.54	H	-	-	17	1	138.07	69.54	H	-	-	17
2	239.11	120.06	T	1885.92	943.46	16	2	239.11	120.06	T	1983.88	992.45	16
3	352.2	176.6	I	1784.87	892.94	15	3	352.2	176.6	I	1882.84	941.92	15
4	421.23	211.12	S@	1671.79	836.4	14	4	519.2	260.1	S#	1769.75	885.38	14
5	518.28	259.64	P	1602.75	801.88	13	5	616.25	308.63	P	1602.75	801.88	13
6	646.34	323.67	Q	1505.7	753.35	12	6	744.31	372.66	Q	1505.7	753.35	12
7	793.41	397.21	F	1377.64	689.32	11	7	891.38	446.19	F	1377.64	689.32	11
8	880.44	440.72	S	1230.57	615.79	10	8	978.41	489.71	S	1230.57	615.79	10
9	994.48	497.75	N	1143.54	572.27	9	9	1092.45	546.73	N	1143.54	572.27	9
10	1150.59	575.8	R	1029.5	515.25	8	10	1248.55	624.78	R	1029.5	515.25	8
11	1287.64	644.33	H	873.4	437.2	7	11	1385.61	693.31	H	873.4	437.2	7
12	1454.64	727.83	S#	736.34	368.67	6	12	1552.61	776.81	S#	736.34	368.67	6
13	1551.7	776.35	P	569.34	285.17	5	13	1649.66	825.33	P	569.34	285.17	5
14	1648.75	824.88	P	472.29	236.65	4	14	1746.71	873.86	P	472.29	236.65	4
15	1747.82	874.41	V	375.24	188.12	3	15	1845.78	923.4	V	375.24	188.12	3
16	1848.86	924.94	T	276.17	138.59	2	16	1946.83	973.92	T	276.17	138.59	2
17	-	-	R	175.12	88.06	1	17	-	-	R	175.12	88.06	1

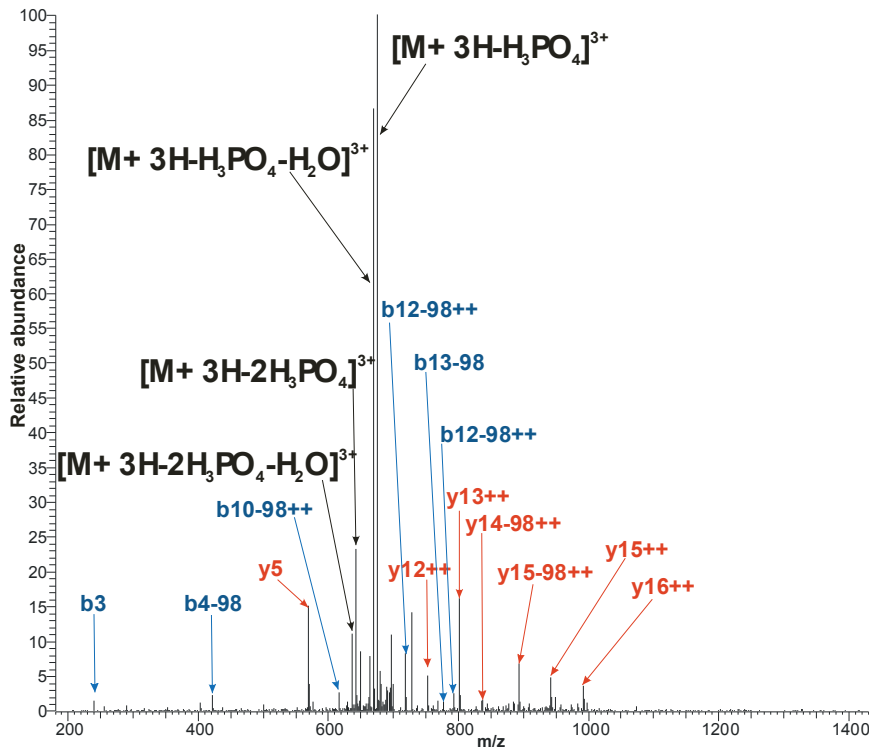
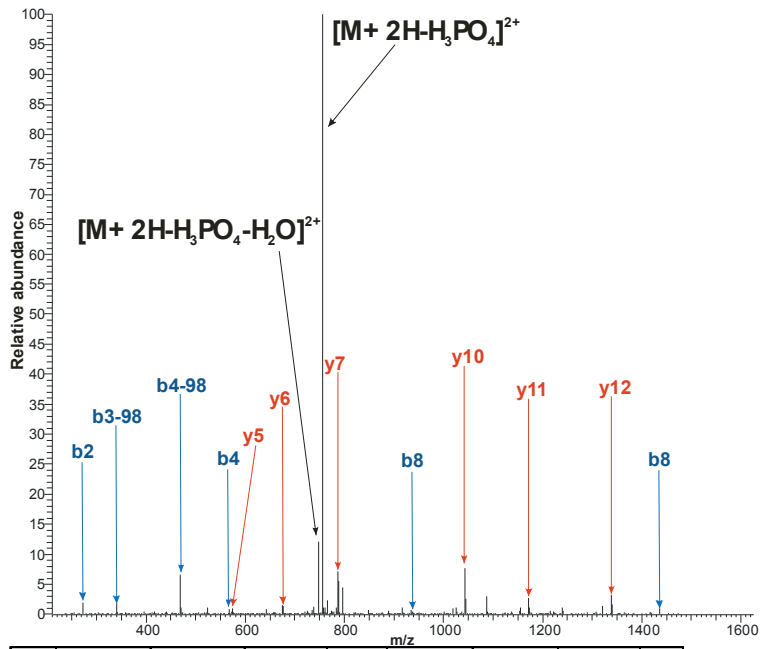


Figure S2.3 Positive ionization low energy CID fragmentation spectrum of the doubly phosphorylated peptide HTISPQFSNRHSPPVTR originating from the Matefin/SUN-1::GFP; *mtf-1/sun-1(ok1282)* sample

MS² (a) and MS³ (b) spectrum of the triply charged peptide. The position of the phosphorylated residue was labeled with “#”, the position of dehydro-alanine in the MS³ spectrum was labeled with “@”. Identified b and y fragment ions detected in the measurement are colored in the fragmentation table and labeled blue and red, respectively, in the spectrum. Identified satellite ions originating from the loss of water (b₀ or y₀ ions) or ammonia (b* or y* ions) are also labeled in the table. Although the fragmentation was poor, important characteristic ions (neutral losses, water loss, intensive fragmentation at prolines) could be easily recognized.



#	b	b*	b ⁰	Seq.	y	y*	y ⁰	#
1	157.11	140.08		R				14
2	272.14	255.11	254.12	D	1453.67	1436.64	1435.66	13
3	439.13	422.11	421.12	S#	1338.64	1321.61	1320.63	12
4	567.19	550.17	549.18	Q	1171.64	1154.62	1153.63	11
5	664.25	647.22	646.23	P	1043.58	1026.56	1025.57	10
6	721.27	704.24	703.26	G	946.53	929.51	928.52	9
7	822.31	805.29	804.3	T	889.51	872.48	871.5	8
8	935.4	918.37	917.39	I	788.46	771.44	770.45	7
9	1036.45	1019.42	1018.44	T	675.38	658.35	657.37	6
10	1093.47	1076.44	1075.46	G	574.33	557.3	556.32	5
11	1194.52	1177.49	1176.5	T	517.31	500.28	499.3	4
12	1307.6	1290.57	1289.59	I	416.26	399.24		3
13	1435.66	1418.63	1417.65	Q	303.18	286.15		2
14				R	175.12	158.09		1

#	b	b*	b ⁰	Seq.	y	y*	y ⁰	#
1	157.11	140.08		R				14
2	272.14	255.11	254.12	D	1355.69	1338.66	1337.68	13
3	341.16	324.13	323.15	S@	1240.66	1223.64	1222.65	12
4	469.22	452.19	451.2	Q	1171.64	1154.62	1153.63	11
5	566.27	549.24	548.26	P	1043.58	1026.56	1025.57	10
6	623.29	606.26	605.28	G	946.53	929.51	928.52	9
7	724.34	707.31	706.33	T	889.51	872.48	871.5	8
8	837.42	820.39	819.41	I	788.46	771.44	770.45	7
9	938.47	921.44	920.46	T	675.38	658.35	657.37	6
10	995.49	978.46	977.48	G	574.33	557.3	556.32	5
11	1096.54	1079.5	1078.53	T	517.31	500.28	499.3	4
12	1209.62	1192.6	1191.61	I	416.26	399.24		3
13	1337.68	1320.7	1319.67	Q	303.18	286.15		2
14				R	175.12	158.09		1

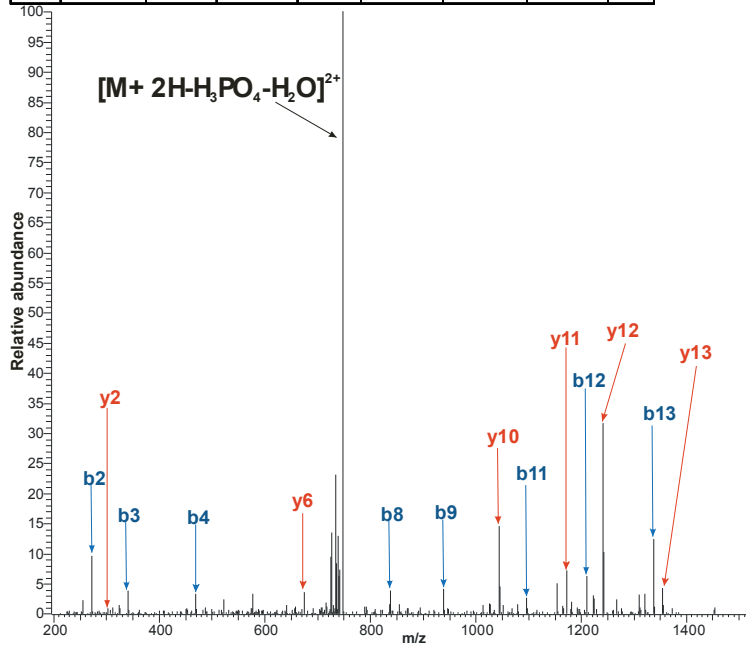
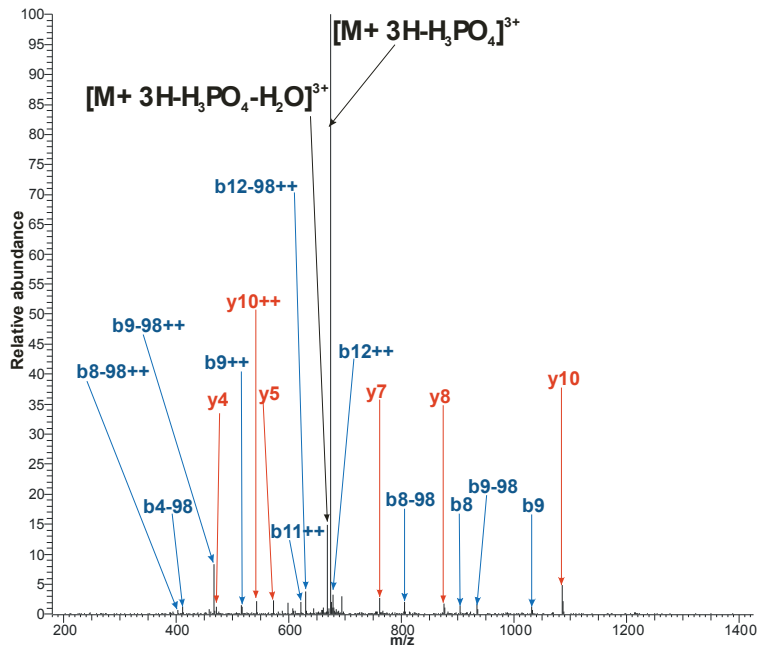


Figure S2.4 Positive ionization low energy CID fragmentation spectrum of the singly phosphorylated peptide RDSQPGTITGTIQR originating from the Matefin/SUN-1::GFP; *mtf-1/sun-1(ok1282)* sample

MS² (a) and MS³ (b) spectrum of the doubly charged peptide. The position of the phosphorylated residue was labeled with “#”, the position of the dehydro-alanine in the MS³ spectrum was labeled with “@”. Identified b and y fragment ions detected in the measurement are colored in the fragmentation table and labeled blue and red, respectively, in the spectrum. Identified satellite ions originating from the loss of water (b⁰ or y⁰ ions) or ammonia (b* or y* ions) are also labeled in the table.

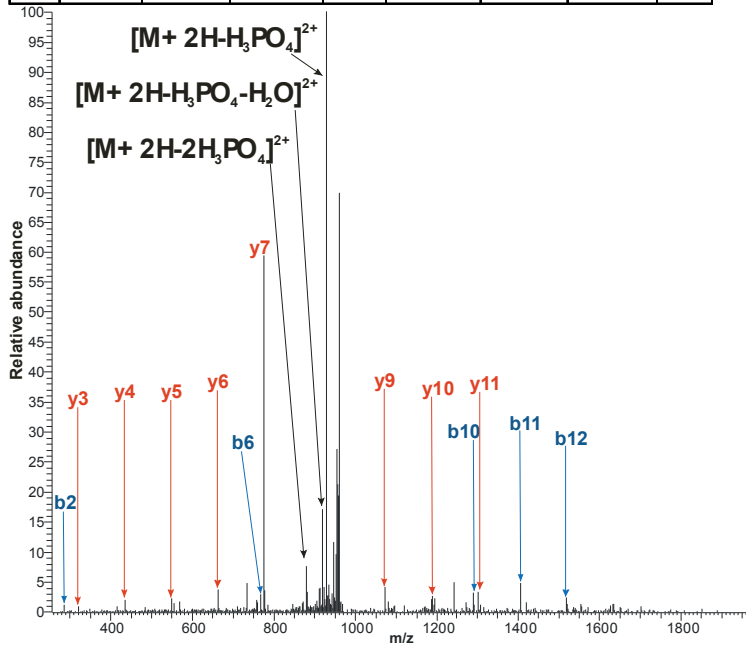


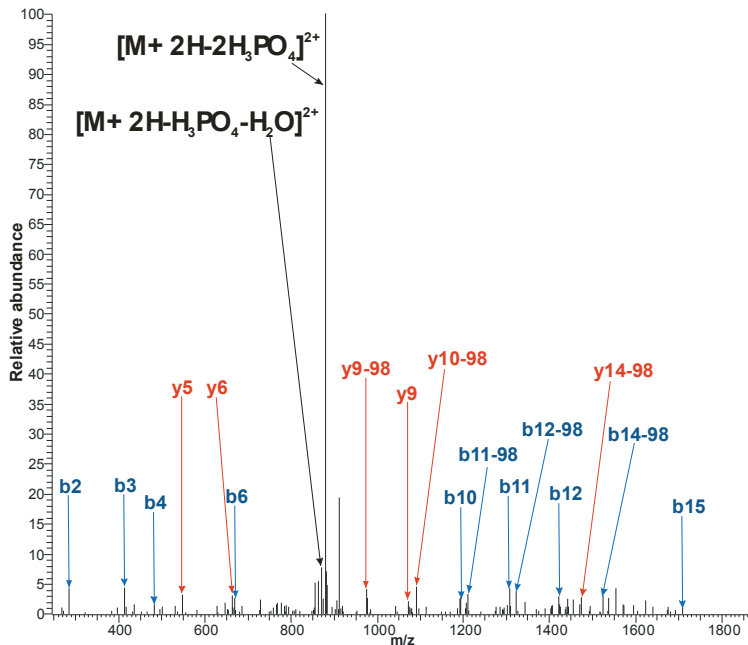
#	b	b ⁺⁺	b [*]	b ⁺⁺⁺	b ⁰	b ⁰⁺⁺	Seq.	y	y ⁺⁺	y [*]	y ⁺⁺⁺	y ⁰	y ⁰⁺⁺	#
1	88.0393	44.52329			70.02874	35.51801	S							19
2	187.1077	94.0575			169.0972	85.05221	V	1933.025	967.0161	1915.998	958.5029	1915.014	958.0109	18
3	256.1292	128.5682			238.1186	119.5629	S#	1833.957	917.4819	1816.93	908.9687	1815.946	908.4767	17
4	412.2303	206.6188	395.2037	198.1055	394.2197	197.6135	R	1764.935	882.9712	1747.909	874.4579	1746.925	873.9659	16
5	513.278	257.1426	496.2514	248.6294	495.2674	248.1373	T	1608.834	804.9206	1591.807	796.4074	1590.823	795.9154	15
6	570.2994	285.6534	553.2729	277.1401	552.2889	276.6481	G	1507.786	754.3968	1490.76	745.8835	1489.776	745.3915	14
7	669.3678	335.1876	652.3413	326.6743	651.3573	326.1823	V	1450.765	725.8861	1433.738	717.3728	1432.754	716.8808	13
8	806.4268	403.717	789.4002	395.2037	788.4162	394.7117	H	1351.696	676.3519	1334.67	667.8386	1333.686	667.3466	12
9	934.4853	467.7463	917.4588	459.233	916.4748	458.741	Q	1214.638	607.8224	1197.611	599.3091	1196.627	598.8171	11
10	1031.538	516.2727	1014.512	507.7594	1013.528	507.2674	P	1086.579	543.7931	1069.552	535.2799	1068.568	534.7878	10
11	1144.622	572.8147	1127.596	564.3014	1126.612	563.8094	L	989.5262	495.2667	972.4997	486.7535	971.5156	486.2615	9
12	1259.649	630.3282	1242.623	621.8149	1241.639	621.3229	D	876.4421	438.7247	859.4156	430.2114	858.4316	429.7194	8
13	1360.697	680.852	1343.67	672.3388	1342.686	671.8468	T	761.4152	381.2112	744.3887	372.698	743.4046	372.206	7
14	1447.729	724.368	1430.702	715.8548	1429.718	715.3628	S	660.3675	330.6874	643.341	322.1741	642.357	321.6821	6
15	1548.776	774.8919	1531.75	766.3786	1530.766	765.8866	T	573.3355	287.1714	556.3089	278.6581	555.3249	278.1661	5
16	1645.829	823.4183	1628.803	814.905	1627.819	814.413	P	472.2878	236.6475	455.2613	228.1343	454.2772	227.6423	4
17	1744.898	872.9525	1727.871	864.4392	1726.887	863.9472	V	375.2351	188.1212	358.2085	179.6079	357.2245	179.1159	3
18	1845.945	923.4763	1828.919	914.963	1827.935	914.471	T	276.1666	138.587	259.1401	130.0737	258.1561	129.5817	2
19							R	175.119	88.06311	158.0924	79.54984			

Figure S2.5 Positive ionization low energy CID spectrum of the singly phosphorylated peptide SVSRTGVHQPLDSTPVRT originating from the Matefin/SUN-1::GFP; *mtf-1/sun-1(ok1282)* sample

MS² spectrum of the triply charged peptide. The position of the phosphorylated residue was labeled with "#". Identified b and y fragment ions are labeled in the fragmentation table and colored (b* or y* ions) are also labeled in the table. According to the information provided by the fragmentation it was not possible to unambiguously localize the phosphorylation site to S22 or S24. Because of the presence of a missed cleavage site at R25 we assumed, that the phosphorylation was probably on S24. This missed cleavage site was only detected in the phosphorylated peptide.

#	b	b*	b ⁰	Seq.	y	y*	y ⁰	#
1	148.08			F				16
2	285.13			H	1806.65	1789.62	1788.64	15
3	414.18		396.17	E	1669.59	1652.56	1651.58	14
4	581.18		563.16	S#	1540.55	1523.52	1522.53	13
5	652.21		634.2	A	1373.55	1356.52	1355.54	12
6	767.24		749.23	D	1302.51	1285.48	1284.5	11
7	882.27		864.26	D	1187.48	1170.46	1169.47	10
8	1049.26		1031.25	S#	1072.46	1055.43	1054.45	9
9	1178.31		1160.3	E	905.46	888.43	887.45	8
10	1291.39		1273.38	I	776.41	759.39	758.4	7
11	1406.42		1388.41	D	663.33	646.3	645.32	6
12	1519.5		1501.49	L	548.3	531.28	530.29	5
13	1633.55	1616.52	1615.53	N	435.22	418.19	417.21	4
14	1720.58	1703.55	1702.57	S	321.18	304.15	303.17	3
15	1807.61	1790.58	1789.6	S	234.14	217.12	216.13	2
16				K	147.11	130.09		1



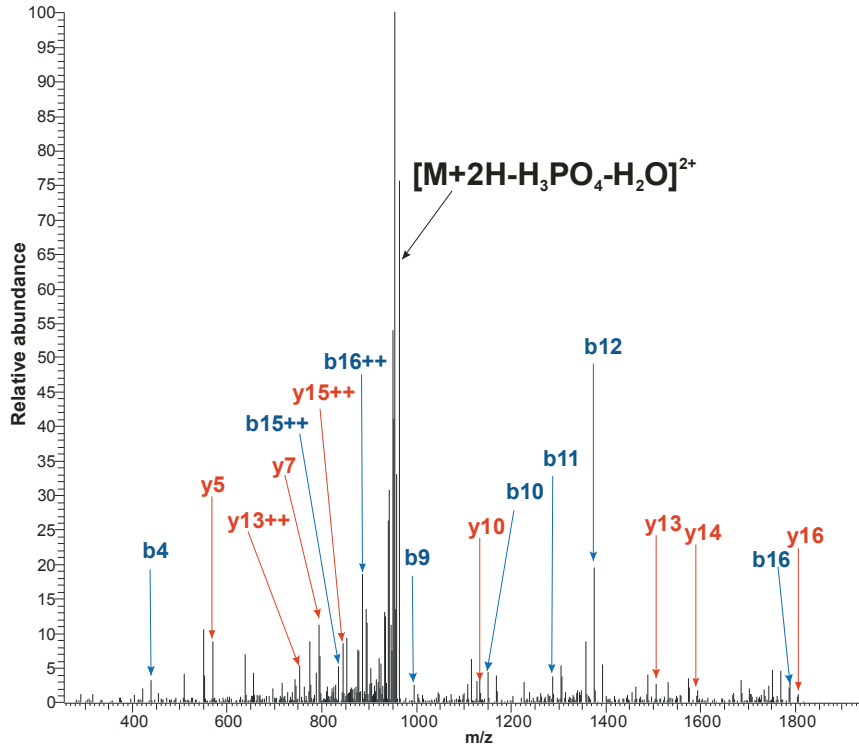


#	b	b*	b ⁰	Seq.	y	y*	y ⁰	#
1	148.08			F				16
2	285.13			H	1708.67	1691.64	1690.66	15
3	414.18		396.17	E	1571.61	1554.58	1553.6	14
4	483.2		465.19	S@	1442.57	1425.54	1424.56	13
5	554.24		536.23	A	1373.55	1356.52	1355.54	12
6	669.26		651.25	D	1302.51	1285.48	1284.5	11
7	784.29		766.28	D	1187.48	1170.46	1169.47	10
8	951.29		933.28	S#	1072.46	1055.43	1054.45	9
9	1080.33		1062.32	E	905.46	888.43	887.45	8
10	1193.41		1175.4	I	776.41	759.39	758.4	7
11	1308.44		1290.43	D	663.33	646.3	645.32	6
12	1421.53		1403.52	L	548.3	531.28	530.29	5
13	1535.57	1518.54	1517.56	N	435.22	418.19	417.21	4
14	1622.6	1605.57	1604.59	S	321.18	304.15	303.17	3
15	1709.63	1692.61	1691.62	S	234.14	217.12	216.13	2
16				K	147.11	130.09		1

Figure S2.6 Positive ionization low energy CID spectrum of the doubly phosphorylated peptide FHESADDSEIDLNSSK originating from the Matefin/SUN-1::GFP; *mtf-1/sun-1(ok1282)* sample

MS² (a) and MS³ (b) spectrum of the doubly charged peptide. The positions of the phosphorylated residue and dehydro-alanine were labeled by “#” and “@”. Identified b and y fragment ions are colored blue and red, respectively, in the spectrum and labeled in the fragmentation tables (a,b) Identified satellite ions originating from the loss of water (b⁰ or y⁰ ions) or ammonia (b* or y* ions) are also labeled in the fragmentation tables. Only the doubly phosphorylated peptide was detected.

Figure S3. Mass spectrometry analysis of Matefin/SUN-1::GFP purified from *mtf-1/sun-1::gfp;spe-26(hc138)* hermaphrodites.



#	b	b++	b*	b*++	b0	b0++	Seq.	y	y++	y*	y*++	y0	y0++	#
1	138.07	69.54					H							17
2	239.11	120.06			221.1	111.06	T	1805.94	903.47	1788.91	894.96	1787.93	894.47	16
3	352.2	176.6			334.19	167.6	I	1704.89	852.95	1687.87	844.44	1686.88	843.94	15
4	439.23	220.12			421.22	211.11	S	1591.81	796.41	1574.78	787.89	1573.8	787.4	14
5	536.28	268.64			518.27	259.64	P	1504.78	752.89	1487.75	744.38	1486.77	743.89	13
6	664.34	332.67	647.31	324.16	646.33	323.67	Q	1407.72	704.37	1390.7	695.85	1389.71	695.36	12
7	811.41	406.21	794.38	397.7	793.4	397.2	F	1279.67	640.34	1262.64	631.82	1261.65	631.33	11
8	880.43	440.72	863.4	432.21	862.42	431.71	S@	1132.6	566.8	1115.57	558.29	1114.59	557.8	10
9	994.47	497.74	977.45	489.23	976.46	488.74	N	1063.58	532.29	1046.55	523.78	1045.56	523.29	9
10	1150.58	575.79	1133.55	567.28	1132.56	566.79	R	949.53	475.27	932.51	466.76	931.52	466.26	8
11	1287.63	644.32	1270.61	635.81	1269.62	635.32	H	793.43	397.22	776.4	388.71	775.42	388.21	7
12	1374.67	687.84	1357.64	679.32	1356.66	678.83	S	656.37	328.69	639.35	320.18	638.36	319.68	6
13	1471.72	736.36	1454.69	727.85	1453.71	727.36	P	569.34	285.17	552.31	276.66	551.33	276.17	5
14	1568.77	784.89	1551.75	776.38	1550.76	775.88	P	472.29	236.65	455.26	228.13	454.28	227.64	4
15	1667.84	834.42	1650.81	825.91	1649.83	825.42	V	375.24	188.12	358.21	179.61	357.22	179.12	3
16	1768.89	884.95	1751.86	876.43	1750.88	875.94	T	276.17	138.59	259.14	130.07	258.16	129.58	2
17							R	175.12	88.06	158.09	79.55			1

Figure S3.1 Positive ionization low energy CID fragmentation spectrum of the singly phosphorylated peptide HTISPQFSNRHSPVTR originating from the Matefin/SUN-1::GFP; *mtf-1/sun-1(ok1282);spe-26(hc138)* sample

MS3 spectrum of the triply charged peptide. The position of the dehydro-alanine generated by the loss of phosphoric acid from the phosphorylated serine residue was labeled with “@”. Identified b and y fragment ions detected in the MS3 measurement are labeled in the fragmentation table and colored blue and red, respectively, in the spectrum. Identified satellite ions originating from the loss of water (b0 or y0 ions) or ammonia (b* or y* ions) are also labeled in the table. Even the intensive fragmentation of the ion in the MS³ measurement did not make the unambiguous localization of the phosphorylation site possible. Fragment ions indicating the phosphorylation of residues S8, S12 and S16 were detected, which indicated that in this spectrum, a mixture of isobaric, singly phosphorylated peptide species were fragmented. The interpretation of

MS³ spectra by Mascot and Sequest resulted in very similar fragment ion coverages (Figure S2.2) and score values for all three phosphorylation sites. The phosphorylated peptide contains a missed cleavage site at R14. This indicates the phosphorylation of the S16 residue. The shorter version of the peptide (HTISPQFSNR) was only detected unphosphorylated.

The doubly phosphorylated version of the peptide was also detected and the phosphorylation sites were localized either on S8 and S12 or on S8 and S16. This verified the assumption that the spectrum of the singly phosphorylated peptide was derived from a mixture.

#	b	b++	Seq.	y	y++	#	#	b	b++	Seq.	y	y++	#	#	b	b++	Seq.	y	y++	#
1	138.07	69.54	H			17	1	138.07	69.54	H			17	1	138.07	69.54	H			17
2	239.11	120.06	T	1805.94	903.47	16	2	239.11	120.06	T	1805.94	903.47	16	2	239.11	120.06	T	1805.94	903.47	16
3	352.2	176.6	I	1704.89	852.95	15	3	352.2	176.6	I	1704.89	852.95	15	3	352.2	176.6	I	1704.89	852.95	15
4	439.23	220.12	S	1591.81	796.41	14	4	439.23	220.12	S	1591.81	796.41	14	4	421.22	211.11	S@	1591.81	796.41	14
5	536.28	268.64	P	1504.78	752.89	13	5	536.28	268.64	P	1504.78	752.89	13	5	518.27	259.64	P	1522.79	761.9	13
6	664.34	332.67	Q	1407.72	704.37	12	6	664.34	332.67	Q	1407.72	704.37	12	6	646.33	323.67	Q	1425.73	713.37	12
7	811.41	406.21	F	1279.67	640.34	11	7	811.41	406.21	F	1279.67	640.34	11	7	793.4	397.2	F	1297.68	649.34	11
8	880.43	440.72	S@	1132.6	566.8	10	8	898.44	449.72	S	1132.6	566.8	10	8	880.43	440.72	S	1150.61	575.81	10
9	994.47	497.74	N	1063.58	532.29	9	9	1012.48	506.75	N	1045.57	523.29	9	9	994.47	497.74	N	1063.58	532.29	9
10	1150.58	575.79	R	949.53	475.27	8	10	1168.59	584.8	R	931.52	466.26	8	10	1150.58	575.79	R	949.53	475.27	8
11	1287.63	644.32	H	793.43	397.22	7	11	1305.64	653.33	H	775.42	388.21	7	11	1287.63	644.32	H	793.43	397.22	7
12	1374.67	687.84	S	656.37	328.69	6	12	1374.67	687.84	S@	638.36	319.68	6	12	1374.67	687.84	S	656.37	328.69	6
13	1471.72	736.36	P	569.34	285.17	5	13	1471.72	736.36	P	569.34	285.17	5	13	1471.72	736.36	P	569.34	285.17	5
14	1568.77	784.89	P	472.29	236.65	4	14	1568.77	784.89	P	472.29	236.65	4	14	1568.77	784.89	P	472.29	236.65	4
15	1667.84	834.42	V	375.24	188.12	3	15	1667.84	834.42	V	375.24	188.12	3	15	1667.84	834.42	V	375.24	188.12	3
16	1768.89	884.95	T	276.17	138.59	2	16	1768.89	884.95	T	276.17	138.59	2	16	1768.89	884.95	T	276.17	138.59	2
17			R	175.12	88.06	1	17			R	175.12	88.06	1	17			R	175.12	88.06	1

Figure S3.2 Fragment ion coverages in the MS³ spectrum of the singly phosphorylated peptide HTISPQFSNRHSPPVTR

The possible positions of the dehydro-alanine generated by the loss of phosphoric acid from the phosphorylated serine residue was labeled with “@”. Identified b and y fragment ions are colored red in the fragmentation table.

#	b	b*	b0	Seq.	y	y*	y0	#
1	157.11	140.08		R				14
2	272.14	255.11	254.12	D	1355.69	1338.66	1337.68	13
3	341.16	324.13	323.15	S@	1240.66	1223.64	1222.65	12
4	469.22	452.19	451.2	Q	1171.64	1154.62	1153.63	11
5	566.27	549.24	548.26	P	1043.58	1026.56	1025.57	10
6	623.29	606.26	605.28	G	946.53	929.51	928.52	9
7	724.34	707.31	706.33	T	889.51	872.48	871.5	8
8	837.42	820.39	819.41	I	788.46	771.44	770.45	7
9	938.47	921.44	920.46	T	675.38	658.35	657.37	6
10	995.49	978.46	977.48	G	574.33	557.3	556.32	5
11	1096.54	1079.51	1078.53	T	517.31	500.28	499.3	4
12	1209.62	1192.6	1191.61	I	416.26	399.24		3
13	1337.68	1320.65	1319.67	Q	303.18	286.15		2
14				R	175.12	158.09		1

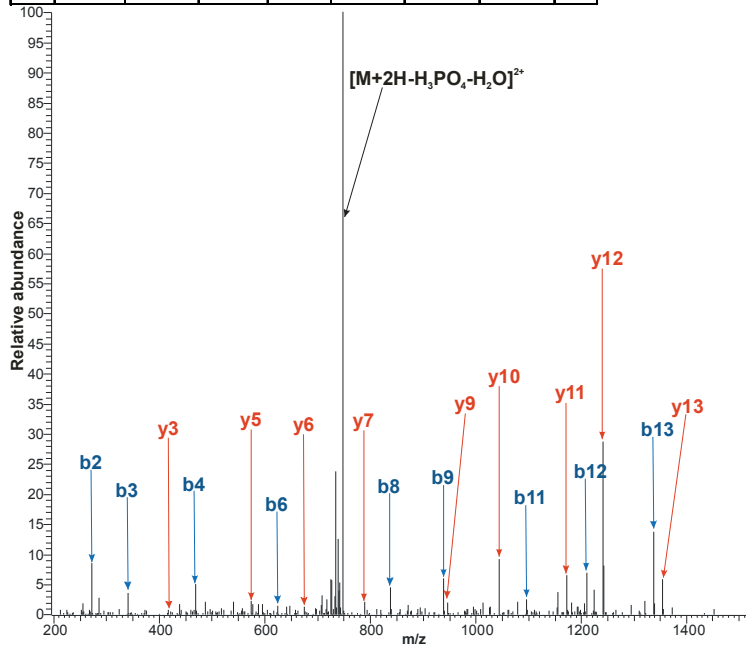
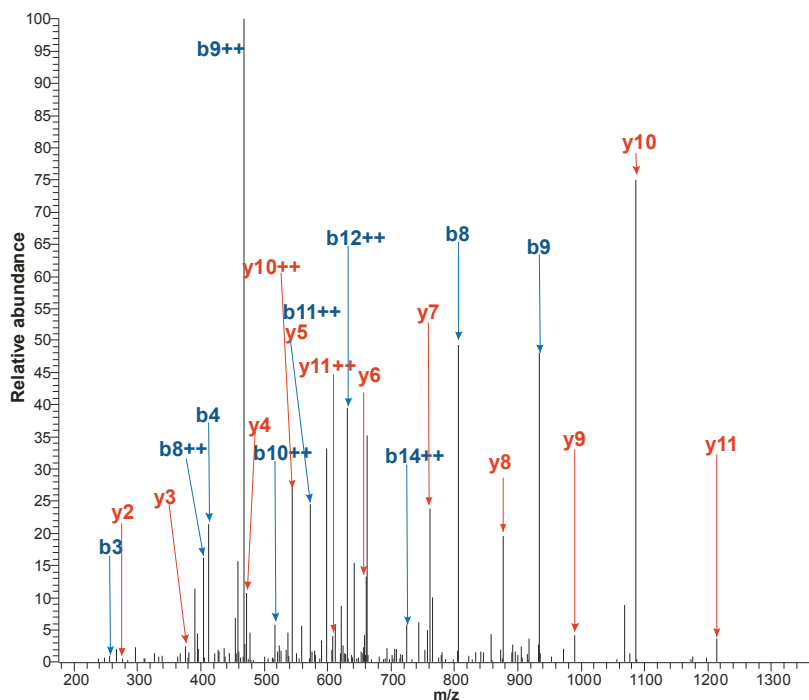


Figure S3.3 Positive ionization low energy CID spectrum of the singly phosphorylated peptide RDSQPQTITGTIQR originating from the Matefin/SUN-1::GFP; *mtf-1/sun-1(ok1282);spe-26(hc138)* sample

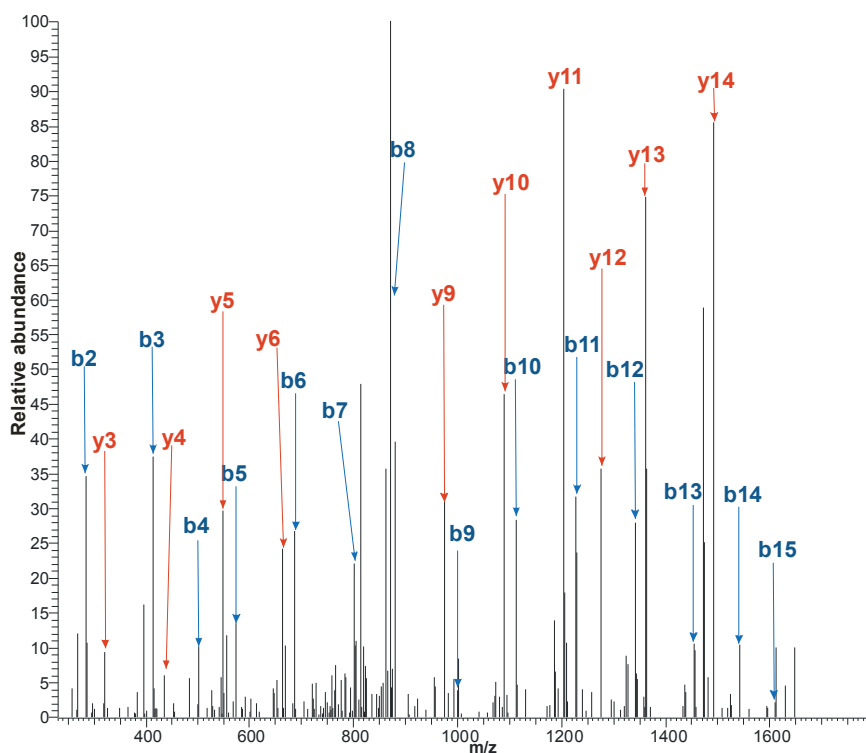
MS³ spectrum of the doubly charged peptide. The position of the dehydro-alanine generated by the loss of phosphoric acid from the phosphorylated serine residue was labeled with “@”. Identified b and y fragment ions are labeled in the fragmentation table and colored blue and red, respectively, in the spectrum. Identified satellite ions originating from the loss of water (b0 or y0 ions) or ammonia (b* or y* ions) are also labeled in the table. The localization of the phosphorylated residue was unambiguous and the presence of the missed cleavage at residue R41 verifies the modification of S43.



#	b	b++	b*	b***	b0	b0++	Seq.	y	y++	y*	y***	y0	y0++	#
1	88.04	44.52			70.03	35.52	S							19
2	187.11	94.06			169.1	85.05	V	1933.03	967.02	1916	958.5	1915.01	958.01	18
3	256.13	128.57			238.12	119.56	S@	1833.96	917.48	1816.93	908.97	1815.95	908.48	17
4	412.23	206.62	395.2	198.11	394.22	197.61	R	1764.94	882.97	1747.91	874.46	1746.92	873.97	16
5	513.28	257.14	496.25	248.63	495.27	248.14	T	1608.83	804.92	1591.81	796.41	1590.82	795.92	15
6	570.3	285.65	553.27	277.14	552.29	276.65	G	1507.79	754.4	1490.76	745.88	1489.78	745.39	14
7	669.37	335.19	652.34	326.67	651.36	326.18	V	1450.76	725.89	1433.74	717.37	1432.75	716.88	13
8	806.43	403.72	789.4	395.2	788.42	394.71	H	1351.7	676.35	1334.67	667.84	1333.69	667.35	12
9	934.49	467.75	917.46	459.23	916.47	458.74	Q	1214.64	607.82	1197.61	599.31	1196.63	598.82	11
10	1031.54	516.27	1014.51	507.76	1013.53	507.27	P	1086.58	543.79	1069.55	535.28	1068.57	534.79	10
11	1144.62	572.81	1127.6	564.3	1126.61	563.81	L	989.53	495.27	972.5	486.75	971.52	486.26	9
12	1259.65	630.33	1242.62	621.81	1241.64	621.32	D	876.44	438.72	859.42	430.21	858.43	429.72	8
13	1360.7	680.85	1343.67	672.34	1342.69	671.85	T	761.42	381.21	744.39	372.7	743.4	372.21	7
14	1447.73	724.37	1430.7	715.85	1429.72	715.36	S	660.37	330.69	643.34	322.17	642.36	321.68	6
15	1548.78	774.89	1531.75	766.38	1530.77	765.89	T	573.34	287.17	556.31	278.66	555.32	278.17	5
16	1645.83	823.42	1628.8	814.91	1627.82	814.41	P	472.29	236.65	455.26	228.13	454.28	227.64	4
17	1744.9	872.95	1727.87	864.44	1726.89	863.95	V	375.24	188.12	358.21	179.61	357.22	179.12	3
18	1845.95	923.48	1828.92	914.96	1827.93	914.47	T	276.17	138.59	259.14	130.07	258.16	129.58	2
19							R	175.12	88.06	158.09	79.55			

Figure S3.4 Positive ionization low energy CID spectrum of the singly phosphorylated peptide SVSRTGVHQLDTPVTR originating from the Matefin/SUN-1::GFP; *mtf-1/sun-1(ok1282);spe-26(hc138)* sample

MS³ spectrum of the triply charged peptide. The position of the dehydro-alanine generated by the loss of phosphoric acid from the phosphorylated serine residue was labeled with “@”. Identified b and y fragment ions are labeled in the fragmentation table and colored blue and red, respectively, in the spectrum. Identified satellite ions originating from the loss of water (b0 or y0 ions) or ammonia (b* or y* ions) are also labeled in the table. According to the information provided by the fragmentation, it was not possible to ambiguously localize the phosphorylation site to S22 or S24. Because of the presence of a missed cleavage site at R25 we assumed, that the phosphorylation is probably on S24. This missed cleavage site was only detected in the phosphorylated peptide.



#	b	b*	b0	Seq.	y	y*	y0	#	#	b	b*	b0	Seq.	y	y*	y0	#
1	148.08			F				16	1	148.08			F	y			16
2	285.13			H	1628.7	1611.68	1610.69	15	2	285.13			H	1628.7	1611.68	1610.69	15
3	414.18		396.17	E	1491.64	1474.62	1473.63	14	3	414.18		396.17	E	1491.64	1474.62	1473.63	14
4	501.21		483.2	S	1362.6	1345.58	1344.59	13	4	483.2		465.19	S@	1362.6	1345.58	1344.59	13
5	572.25		554.24	A	1275.57	1258.54	1257.56	12	5	554.24		536.23	A	1293.58	1276.55	1275.57	12
6	687.27		669.26	D	1204.53	1187.51	1186.52	11	6	669.26		651.25	D	1222.54	1205.52	1204.53	11
7	802.3		784.29	D	1089.51	1072.48	1071.5	10	7	784.29		766.28	D	1107.52	1090.49	1089.51	10
8	871.32		853.31	S@	974.48	957.45	956.47	9	8	871.32		853.31	S	992.49	975.46	974.48	9
9	1000.36		982.35	E	905.46	888.43	887.45	8	9	1000.36		982.35	E	905.46	888.43	887.45	8
10	1113.45		1095.44	I	776.41	759.39	758.4	7	10	1113.45		1095.44	I	776.41	759.39	758.4	7
11	1228.48		1210.46	D	663.33	646.3	645.32	6	11	1228.48		1210.46	D	663.33	646.3	645.32	6
12	1341.56		1323.55	L	548.3	531.28	530.29	5	12	1341.56		1323.55	L	548.3	531.28	530.29	5
13	1455.6	1438.58	1437.59	N	435.22	418.19	417.21	4	13	1455.6	1438.58	1437.59	N	435.22	418.19	417.21	4
14	1542.63	1525.61	1524.62	S	321.18	304.15	303.17	3	14	1542.63	1525.61	1524.62	S	321.18	304.15	303.17	3
15	1629.67	1612.64	1611.66	S	234.14	217.12	216.13	2	15	1629.67	1612.64	1611.66	S	234.14	217.12	216.13	2
16				K	147.11	130.09		1	16				K	147.11	130.09		1

Figure S3.5 Positive ionization low energy CID spectrum of the singly phosphorylated peptide FHESADDSEIDLNSSK originating from the Matefin/SUN-1::GFP; *mtf-1/sun-1(ok1282);spe-26(hc138)* sample

MS³ spectrum of the doubly charged peptide. The position of the dehydro-alanine generated by the loss of phosphoric acid from the phosphorylated serine residue was labeled with "@". Identified b and y fragment ions are colored blue and red in the spectrum, respectively, and labeled in the fragmentation tables (a,b). Identified fragment ions are labeled in the spectrum according to table "a". Identified satellite ions originating from the loss of water (b0 or y0 ions) or ammonia (b* or y* ions) are also labeled in the fragmentation tables. This peptide contains a second serine residue (S58). The presence of the fragment ions b4-b7 in the MS3 spectrum verifies the phosphorylation of S62. There are also some fragment ions, which support the phosphorylation of S58, but they are less significant in the spectrum. Indeed, according to the mass spectrometry

data, it cannot be ruled out, that the spectrum was generated from a mixture of both peptide species and this residue was phosphorylated as well. The doubly phosphorylated peptide was not detected.

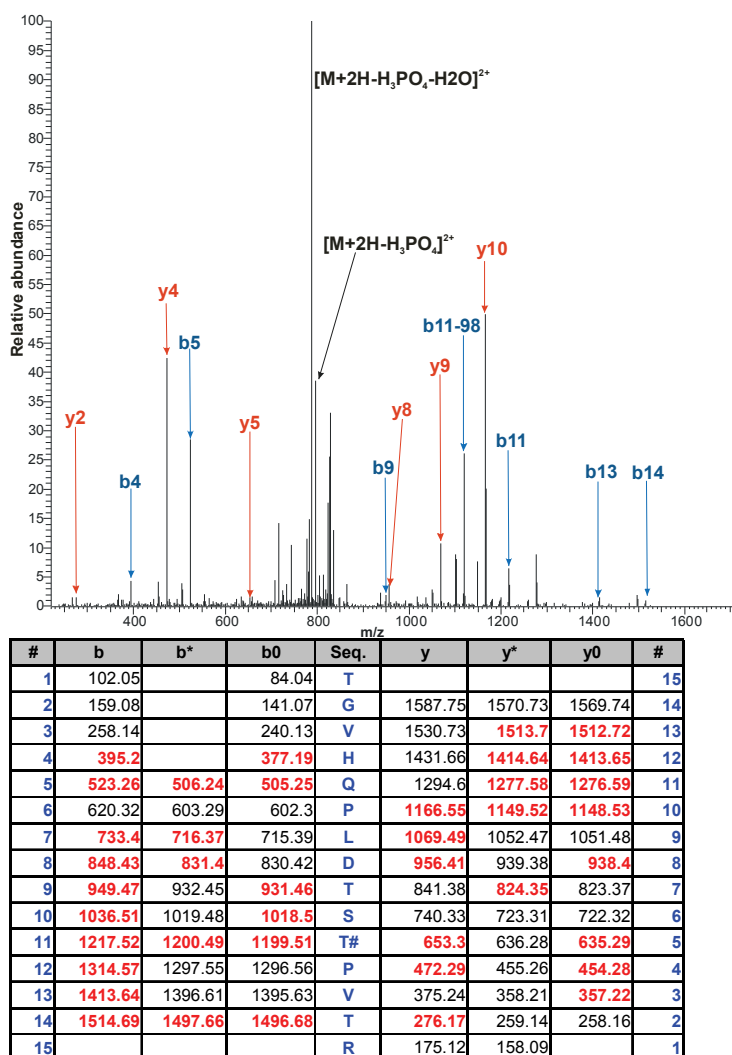
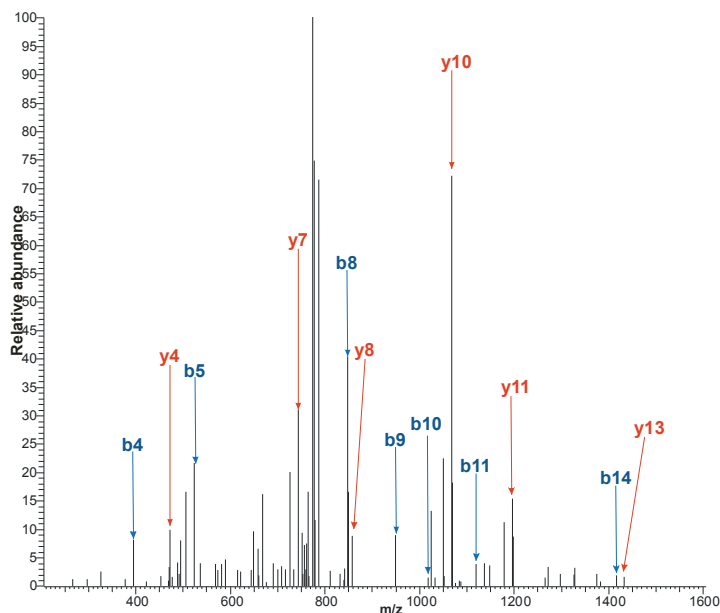


Figure S3.6 Positive ionization low energy CID spectrum of the singly phosphorylated peptide TGVHQPLDTSTPVTR originating from the Matefin/SUN-1::GFP; *mtf-1/sun-1(ok1282);spe-26(hc138)* sample

MS² spectrum of the doubly charged peptide. The characteristic neutral loss was labeled in the spectrum. The position of the phosphothreonine is indicated with “#” in the fragment ion table. Identified b and y fragment ions are labeled in the fragmentation table and colored blue and red, respectively, in the spectrum. Identified satellite ions originating from the loss of water (b0 or y0 ions) or ammonia (b* or y* ions) are also labeled in the table. The peak generated by the loss of phosphoric acid was not under the three most intensive ions, thus no MS³ measurement was triggered, but the fragmentation of the peptide made it possible to localize the modification site to T36.



#	b	b*	b0	Seq.	y	y*	y0	#
1	102.05		84.04	T				15
2	159.08		141.07	G	1489.78	1472.75	1471.77	14
3	258.14		240.13	V	1432.75	1415.73	1414.74	13
4	395.2		377.19	H	1333.69	1316.66	1315.68	12
5	523.26	506.24	505.25	Q	1196.63	1179.6	1178.62	11
6	620.32	603.29	602.3	P	1068.57	1051.54	1050.56	10
7	733.4	716.37	715.39	L	971.52	954.49	953.51	9
8	848.43	831.4	830.42	D	858.43	841.41	840.42	8
9	949.47	932.45	931.46	T	743.4	726.38	725.39	7
10	1018.5	1001.47	1000.48	S@	642.36	625.33	624.35	6
11	1119.54	1102.52	1101.53	T	573.34	556.31	555.32	5
12	1216.6	1199.57	1198.59	P	472.29	455.26	454.28	4
13	1315.66	1298.64	1297.65	V	375.24	358.21	357.22	3
14	1416.71	1399.69	1398.7	T	276.17	259.14	258.16	2
15				R	175.12	158.09		1

Figure S3.7 Positive ionization low energy CID spectrum of the singly phosphorylated peptide TGVHQPLDTSTPVTR originating from the Matefin/SUN-1::GFP; *mtf-1/sun-1(ok1282);spe-26(hc138)* sample

MS³ spectrum of the doubly charged peptide. The position of the dehydro-alanine was labeled with "@". Identified b and y fragment ions are labeled red in the fragmentation table and colored blue and red, respectively, in the spectrum. Identified satellite ions originating from the loss of water (b0 or y0 ions) or ammonia (b* or y* ions) are also labeled in the table. The peptides in Figure 1.6 and 1.7 have the same mass, but slightly different elution times. The peptide, which was identified as being phosphorylated at the S35 residue had a retention time of 26.93 min; the peptide phosphorylated at T35 eluted at 25.14 min. This fact and the different fragmentation characteristics of the two peptides may confirm the existence of the two different phosphorylated residues.

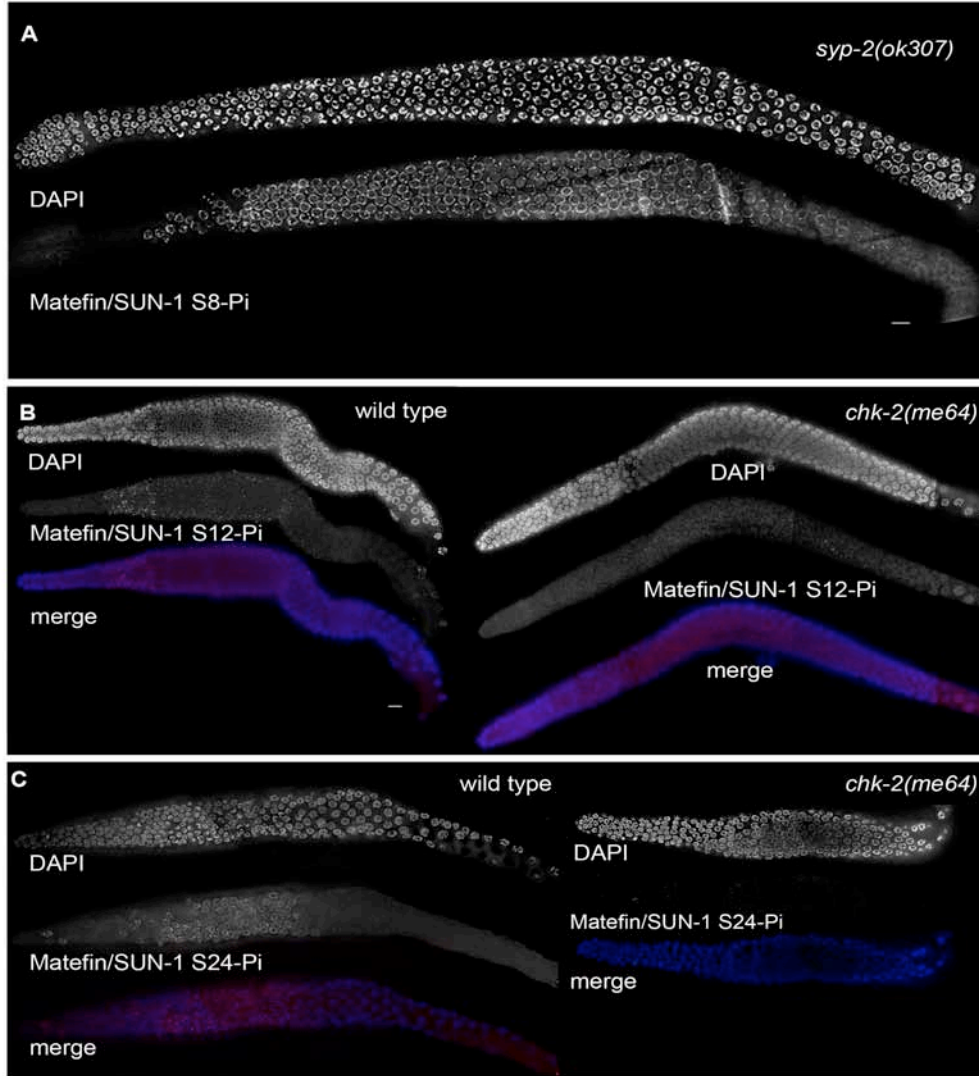


Figure S4. (A) Matefin/SUN-1 S8-Pi staining in *syp-2(ok307)* mutant gonads. The persistence of the immunostaining correlates with the prolongation of the transition zone. (B) Wild-type and *chk-2(me64)* hermaphrodite gonads co-stained with DAPI (top and blue in merge) and with antibodies against Matefin/SUN-1 S12-Pi (middle and red in merge). (C) Wild-type and *chk-2(me64)* hermaphrodite gonads co-stained with DAPI (top and blue in merge) and with antibodies against Matefin/SUN-1 S24-Pi (middle and red in merge). Scale bars: 10 μ m.

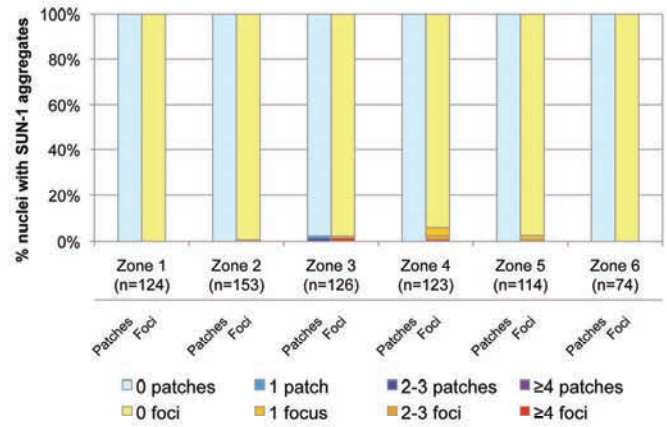
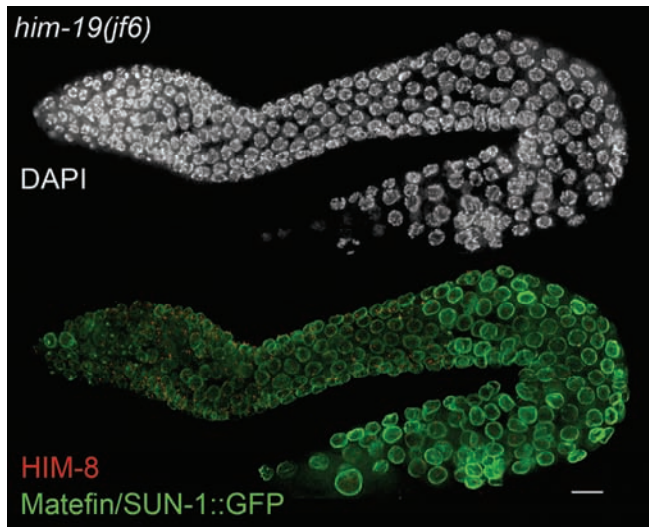


Figure S5. Analysis of Matefin/SUN-1::GFP aggregate formation in *him-19(jf6)* mutants. White: DAPI staining, green: Matefin/SUN-1::GFP, red: HIM-8. Scale bars: 10 μ m.

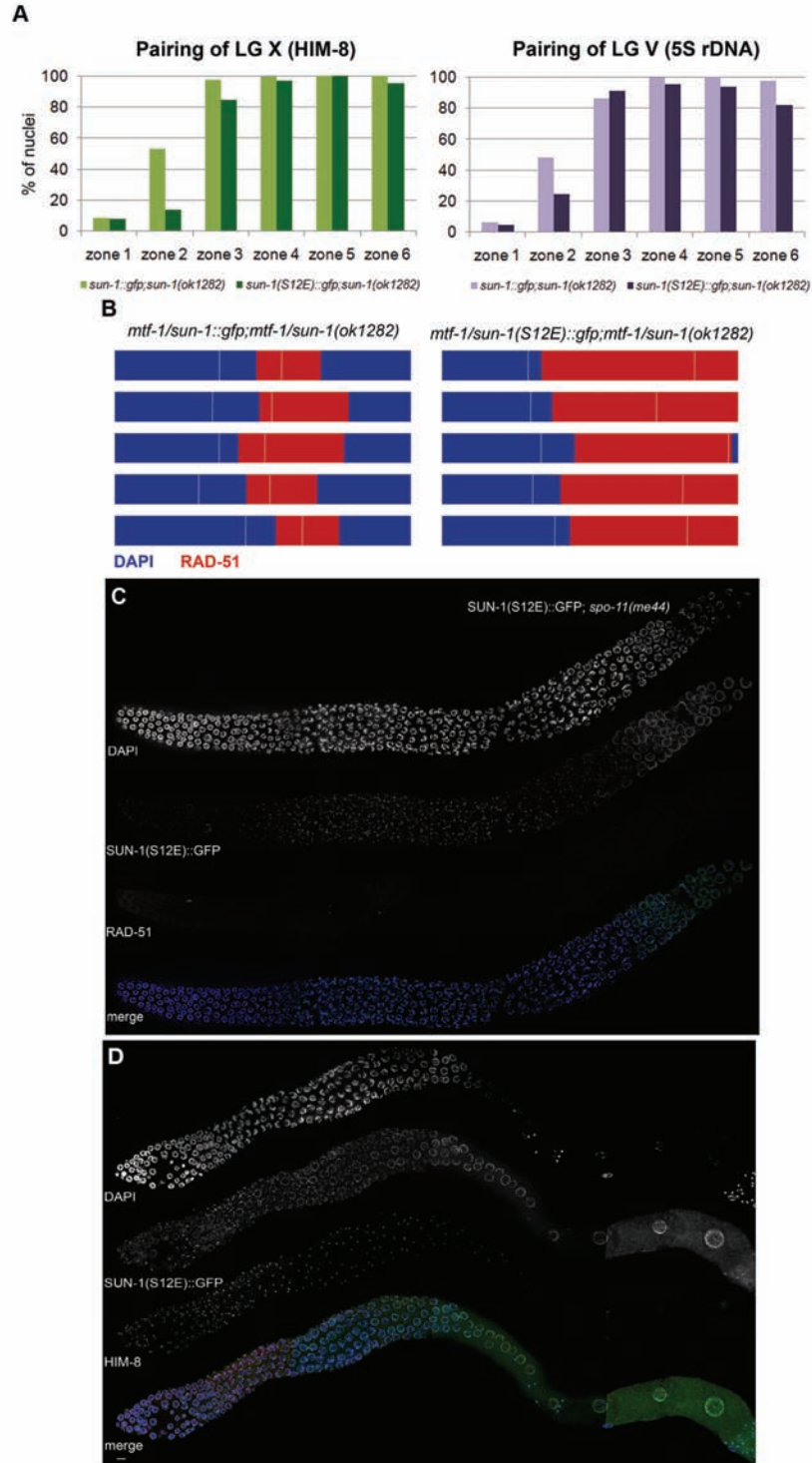


Figure S6. (A) Pairing of the X chromosome within the germline of *mtf-1/sun-1::gfp;mtf-1/sun-1(ok1282)* and *mtf-1/sun-1(S12E)::gfp;mtf-1/sun-1(ok1282)* worms as assessed by immunostaining of the pairing center-binding protein HIM-8. zone 1: n=80/77 nuclei, zone 2: n=149/108, zone 3: n=178/167, zone 4: n=157/174, zone 5: n=120/117, zone 6: n=54/43 (5 gonads counted for each genotype). Pairing of chromosome V within the germline of *mtf-1/sun-1::gfp;mtf-1/sun-1(ok1282)* and *mtf-1/sun-1(S12E)::gfp;mtf-1/sun-1(ok1282)* worms as assessed by FISH of the 5S rDNA locus. zone 1: n=129/108

nuclei, zone 2: n=193/128, zone 3: n=173/162, zone 4: n=155/166, zone 5: n=113/126, zone 6: n=72/105 (5 gonads counted for each genotype). (B) RAD-51-positive zones (in red) of 5 individual gonads of *mtf-1/sun-1::gfp*; *mtf-1/sun-1(ok1282)* and *mtf-1/sun-1(S12E)::gfp;mtf-1/sun-1(ok1282)* hermaphrodites. White vertical lines mark the beginning and the end of the zone displaying clustered chromatin. (C) Matefin/SUN-1(S12E)::GFP aggregates and RAD-51 staining in *mtf-1/sun-1(S12E)::gfp;mtf-1/sun-1(ok1282);spo-11(me44)* hermaphrodite gonads; compare to figure 6 for stainings of wild type and the S12E substitution. (D) Highlighting of chromatin clustering, Matefin/SUN-1(S62E)::GFP aggregation and HIM-8 localization in hermaphrodite gonads expressing solely Matefin/SUN-1(S62E)::GFP. blue: DAPI staining, green: Matefin/SUN-1(S62E)::GFP, red: HIM-8.
Scale bars: 10 μ m.

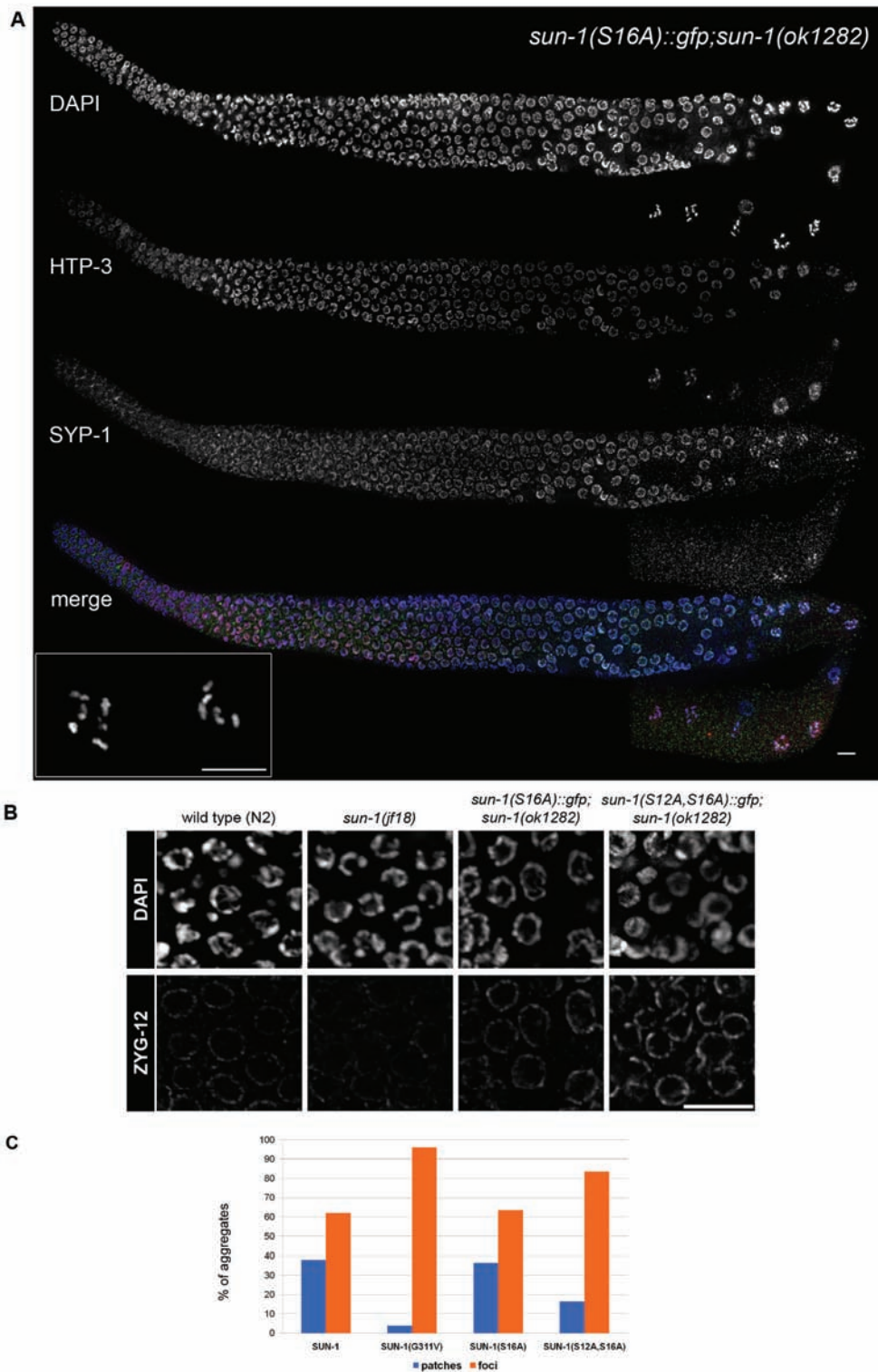


Figure S7. (A) Highlighting of the SC components HTP-3 (red in merge), SYP-1 (green in merge) and DAPI staining (blue in merge) in *sun-1(S16A)::gfp;sun-1(ok1282)* hermaphrodite gonads. inset: DAPI staining of diakinesis nuclei. (B) ZYG-12 staining (lower panel) of nuclei in the pachytene region of hermaphrodite gonads of wild type,

sun-1(jf18), *sun-1(S16A)::gfp;sun-1(ok1282)* and *sun-1(S12A,S16A)::gfp;sun-1(ok1282)*. DAPI staining: upper panel. (C) Distribution of patches and foci formed by Matefin/SUN-1::GFP (n=250 aggregates), Matefin/SUN-1(G311V)::GFP (n=130 aggregates), Matefin/SUN-1(S16A)::GFP (n=315 aggregates) and Matefin/SUN-1(S12A,S16A)::GFP (n=206 aggregates).

Table S1.

Genotype	Viability	n (eggs/ hermaphrodites)	Brood size	Males in surviving offspring
<i>sun-1(ok1282)</i>	0±0%	6/7	0.86±0.9	n.d.
<i>sun-1::gfp;sun-1(ok1282)</i>	98.2±1.4%	653/5	130.6±17.5	0%
<i>sun-1(S12E)::gfp;sun-1(ok1282)</i>	25.1±11.1%	1542/9	171.3±35.9	4.7%
<i>sun-1(S62E)::gfp;sun-1(ok1282)</i>	73.6±22.3%	482/14	34.4±15.9	4.7%
<i>sun-1(S8A)::gfp;sun-1(ok1282)</i>	24.6±7.2%	736/n.d.	n.d.	4.5%
<i>sun-1(S16A)::gfp;sun-1(ok1282)</i>	89±25%	2593/15	172.9±49.7	n.d.
<i>sun-1(S12A,S16A)::gfp;sun-1(ok1282)</i>	3.9±3.4%	597/13	45.9±20.4	n.d.

Summary of viability, broodsize and Him counts for various SUN-1 wild-type and serine mutated transgenic lines.

Table S2.

Genotype	Scored zone	n (nuclei)	Mean number	
			patches (p-value)	foci (p-value)
wild type	2+3	137	1.9±1.3	1.0±1.4
<i>syp-2(ok307)</i>	2+3	122	1.4±0.9 (p=1.2E-3)	3.4±2.2 (p=6.3E-22)
<i>him-3(gk149)</i>	2	129	0.5±0.5 (p=3.1E-24)	1.8±1.4 (p=2.9E-6)
<i>chk-2(me64)</i>	-	-	-	-
<i>him-19(jf6)</i>	-	-	-	-

Analysis of Matefin/SUN-1::GFP aggregates in various mutant backgrounds (wild type: *mtf-1/sun-1::gfp;mtf-1/sun-1(ok1282)*. *syp-2(ok307)*: *syp-2(ok307);mtf-1/sun-1::gfp;mtf-1/sun-1(ok1282)*. *him-3(gk149)*: *him-3(gk149);mtf-1/sun-1::gfp;mtf-1/sun-1(ok1282)*. *chk-2(me64)*: *chk-2(me64);mtf-1/sun-1::gfp;mtf-1/sun-1(ok1282)*. *him-19(jf6)*: *him-19(jf6);mtf-1/sun-1::gfp;mtf-1/sun-1(ok1282)*). The mean of Matefin/SUN-1::GFP patches and foci is listed. Four independent gonads were scored per genotype. Values were compared using a two-tailed Student's t-test with a significance level below p=0.05.

Supplemental References

Brenner, S. (1974). The genetics of *Caenorhabditis elegans*. *Genetics* 77, 71-94.

Colaiácovo, M. P.; MacQueen, A. J.; Martinez-Perez, E.; McDonald, K.; Adamo, A.; Volpe, A. L. & Villeneuve, A. M. (2003). Synaptonemal complex assembly in *C. elegans* is dispensable for loading strand-exchange proteins but critical for proper completion of recombination. *Dev Cell* 5, 463-474.

Couteau, F.; Nabeshima, K.; Villeneuve, A. & Zetka, M. (2004). A component of *C. elegans* meiotic chromosome axes at the interface of homolog alignment, synapsis, nuclear reorganization, and recombination. *Curr Biol* 14, 585-592.

Garcia-Muse, T. & Boulton, S. J. (2005). Distinct modes of ATR activation after replication stress and DNA double-strand breaks in *Caenorhabditis elegans*. *EMBO J* 24, 4345-4355.

Hayashi, M.; Chin, G. M. & Villeneuve, A. M. (2007). *C. elegans* germ cells switch between distinct modes of double-strand break repair during meiotic prophase progression. *PLoS Genet* 3, e191.

MacQueen, A. J. & Villeneuve, A. M. (2001). Nuclear reorganization and homologous chromosome pairing during meiotic prophase require *C. elegans* chk-2. *Genes Dev* 15, 1674-1687.

Malone, C. J.; Misner, L.; Bot, N. L.; Tsai, M.-C.; Campbell, J. M.; Ahringer, J. & White, J. G. (2003). The *C. elegans* hook protein, ZYG-12, mediates the essential attachment between the centrosome and nucleus. *Cell* 115, 825-836.

Martinez-Perez, E. & Villeneuve, A. M. (2005). HTP-1-dependent constraints coordinate homolog pairing and synapsis and promote chiasma formation during *C. elegans* meiosis. *Genes Dev* 19, 2727-2743.

Praitis, V.; Casey, E.; Collar, D. & Austin, J. (2001). Creation of low-copy integrated transgenic lines in *Caenorhabditis elegans*. *Genetics* 157, 1217-1226.

Stergiou, L.; Doukoumetzidis, K.; Sendoel, A. & Hengartner, M. O. (2007). The nucleotide excision repair pathway is required for UV-C-induced apoptosis in *Caenorhabditis elegans*. *Cell Death Differ* 14, 1129-1138.

Tang L., Machacek T., Mamnun Y.M., Gloggnitzer J., Penkner A., Konrat R., Jantsch M., Loidl J., and Jantsch V. (2009) Mutations in *C. elegans* HIM-19 show meiotic defects that worsen with age (*submitted*)

Voorhies, W. A. V. (1992). Production of sperm reduces nematode lifespan. *Nature* 360, 456-458.

Chapter 5. Leptotene/Zygotene Chromosome Movement Via the SUN/KASH Protein Bridge in *C. elegans*

PloS Genetics, in press.

Leptotene/Zygotene Chromosome Movement via the SUN/KASH Protein Bridge in *C. elegans*

Antoine Baudrimont¹, Alexandra Penkner¹, Alexander Woglar¹, Thomas Machacek¹, Christina Wegrostek¹, Jiradet Gloggnitzer^{1, 2}, Alexandra Fridkin³, Franz Klein¹, Yosef Gruenbaum³, Pawel Pasierbek^{4, 5}, Verena Jantsch¹

¹Department of Chromosome Biology, Max F. Perutz Laboratories, University of Vienna, Vienna, Austria; ²current address: Gregor Mendel Institute of Molecular Plant Biology, Austrian Academy of Sciences, Vienna, Austria; ³Department of Genetics, Hebrew University, Jerusalem, Israel; ⁴Institute of Molecular Biotechnology of the Austrian Academy of Sciences, Vienna, Austria; ⁵Institute of Molecular Pathology, Vienna, Austria

corresponding author: verena.jantsch@univie.ac.at

Abstract

The *C. elegans* inner nuclear envelope protein matefin/SUN-1 plays a conserved, pivotal role in the process of genome haploidization. CHK-2-dependent phosphorylation of SUN-1 regulates homologous chromosome pairing and interhomolog recombination in *C. elegans*. Using time-lapse microscopy, we characterized the movement of matefin/SUN-1::GFP aggregates (the equivalent of chromosomal attachment plaques) and showed that the dynamics of matefin/SUN-1 aggregates remained unchanged throughout leptotene/zygotene, despite the progression of pairing. Movement of SUN-1 aggregates correlated with chromatin polarization. We also analyzed the requirements for the formation of movement-competent matefin/SUN-1 aggregates in the context of chromosome structure, and found that chromosome axes were required to produce wild-type numbers of attachment plaques. Abrogation of synapsis led to a deceleration of SUN-1 aggregate movement. Analysis of matefin/SUN-1 in a double-strand break deficient mutant revealed that repair intermediates influenced matefin/SUN-1 aggregate dynamics. Investigation of movement in meiotic regulator mutants substantiated that proper orchestration of the meiotic program and effective repair of DNA double-strand breaks were necessary for the wild-type behavior of matefin/SUN-1 aggregates.

Author summary

During meiosis, homologous chromosomes from each parent must pair, synapse, and recombine before being assorted to the gametes. In *C. elegans*, to find the correct pairing partner, telomere-led chromosome movement occurs in a restricted subvolume of the nucleus. This feature is comparable to the widely conserved meiotic bouquet, a configuration where telomeres cluster in a limited area at the nuclear periphery. Chromosomes are moved by cytoskeletal forces transmitted via the SUN/KASH bridge across the nuclear envelope, and abrogation of movement leads to precocious nonhomologous synapsis. Using live cell imaging, we followed the movement of matefin/SUN-1 aggregates, which highlight chromosome ends. Instead of single chromosome ends looking for their homologous partners, we observed that duplets/multiplets and single chromosome ends were brought together into “patches” by the ongoing movement during the leptotene/zygotene stages of meiosis. Chromosome ends then shuffled through these patches in search of the correct partner. This study was a comprehensive analysis of matefin/SUN-1 aggregate dynamics in wild type, known *C. elegans* pairing mutants, and the recombination mutant *spo-11*, and examined the contributions of these aggregates to leptotene/zygotene chromosome movement.

Introduction

During the first meiotic division, homologous parental chromosomes must accomplish numerous tasks that eventually result in their connection via homologous recombination. They must recognize one another, align, synapse via the tripartite proteinaceous synaptonemal complex (SC), and repair programmed double-strand breaks (DSBs); a subset of DSBs are repaired using the homologous partner as a template [1]. During this period, the chromosomes are connected to the nuclear envelope at one or both ends [2]. The highly conserved protein interaction module of SUN/KASH domain proteins has emerged as a core element for the attachment of chromosomal ends to the nuclear envelope, and for telomere-led chromosomal movement. The mechanism for moving chromosomes during early prophase I inside the nucleus via the SUN/KASH bridge, which provides a connection to various cytoskeletal forces in the cytoplasm, appears to be a general, evolutionarily conserved phenomenon (for reviews see [3-5]). Studies in *Saccharomyces cerevisiae* [6,7], *Schizosaccharomyces pombe* [8], and maize [9] discovered differences among organisms with regard to which factors are employed to build the connection of the chromosome ends to the SUN-domain proteins in the inner nuclear envelope, and which cytoskeletal forces drive the movement. For example, in *S. cerevisiae*, telomere-led chromosome movement has been observed during meiotic prophase I, from leptotene to pachytene [6,7,10]. Interference with prophase chromosome movement in *S. cerevisiae* results in delayed pairing and DSB processing, aberrant crossover formation, and loss of crossover interference [6,7,11-16].

In many organisms, formation of the synaptonemal complex requires the formation of programmed meiotic DSBs; however, in *C. elegans*, synapsis is independent of DSBs [17]. In *C. elegans*, the SC is comprised of the lateral element components HTP-1 to 3 and HIM-3, and the central region components SYP-1 to SYP-4 [18,19]. HTP-1, in addition to being part of the lateral element, also plays a role in licensing synapsis [20,21].

Another characteristic of *C. elegans* is that the pairing of homologues involves homolog recognition regions (HRRs), also called pairing center (PC) regions, which are enriched in heterochromatic repeats localized at one end

of each chromosome. HRRs were shown to be required to initiate the subsequent key features of meiosis I, recombination and disjunction [22-24]. The PC proteins ZIM-1 to ZIM-3 and HIM-8 bind to HRRs, and specifically localize to either one or two chromosomes [25-27]. When extrachromosomal arrays of the heterochromatic repeats found in HRRs are introduced into *C. elegans* germline cells, they recruit PC proteins and the arrays localize to the nuclear periphery [27].

In *C. elegans*, the protein matefin/SUN-1 (referred to as SUN-1 from this point forward) and its interacting partner ZYG-12 bridge the nuclear membranes and play a central role in the pairing of homologous chromosomes and the licensing of synapsis [28,29]. The PC proteins colocalize with SUN-1, and are thought to connect chromosome ends to SUN-1 [28,29]. A point mutation in the SUN domain of *C. elegans* SUN-1 revealed that prophase movement is required for chromosomes to find each other and to prevent nonhomologous synapsis [29,30]. Recently, it was found that in worms, microtubules and dynein motors act through the nuclear envelope bridge formed by matefin/SUN-1 and ZYG-12, and that these components are at the core of licensing synapsis only for properly aligned bivalents [29].

Progression of meiosis is tightly regulated in *C. elegans*, and involves the checkpoint protein kinase CHK-2 at the meiotic entry. CHK-2 is responsible for the polarization of the chromatin, which is characteristic of the transition zone (TZ) [31], and is involved in induction of DSBs and proper SC polymerization, as well as the phosphorylation of SUN-1 [28]. PROM-1, an F-box-containing protein, controls progression of early meiosis; its depletion leads to an extended meiotic entry zone followed by nonhomologous synapsis [32]. The newly identified meiotic regulator HIM-19 is involved in chromatin polarization, formation of DSBs, and elongation of the SC. It encodes a protein with an RNA helicase domain, as determined by metastructure analysis [33]. In *cra-1* mutants, central-region components of the SC first fail to localize extensively to chromosomes; later, they instead polymerize along chromosomal axes, leading to unconnected bivalents. The tetratricopeptide repeat domain-bearing protein CRA-1 uncouples the polymerization of the central region components of the SC from the repair of DSBs [34].

In this study, we used live imaging microscopy to show that chromosome ends, highlighted as SUN-1 aggregates, were highly dynamic and contributed to chromosome movement in the leptotene/zygotene stages of *C. elegans* prophase I; they came together, coalesced and redispersed. Disruption of the SUN/KASH interaction in *mtf-1/sun-1(jf18)* mutants resulted in an absence of motion of the SUN-1 aggregates. We also analyzed the SUN-1-GFP aggregates in different mutant backgrounds affecting phosphorylation of SUN-1 and structural components of the lateral and central region of the SC, the DSB inducing enzyme SPO-11 and a group of genes that play a regulatory role during prophase I in *C. elegans*. Abrogation of synapsis led to a deceleration of SUN-1 aggregate movement. Aggregate behavior was influenced by recombination. Quantification of SUN-1 aggregates in meiotic regulators suggested that mere chromosome collisions driven by movement of nuclear envelope–attached chromosomes were insufficient for successful homologous pairing.

Results

Erratic movement of SUN-1 aggregates at one pole of the nucleus

C. elegans gonads recapitulate the progression of nuclei through meiotic prophase I in a spatial manner [35]. The mitotic zone is followed by the TZ, with its characteristically polarized chromatin (corresponding to leptotene/zygotene). In the next stage (pachytene), chromatin is redistributed and forms parallel tracks of DNA. Later, chromosomes condense (diplotene) and connected bivalents become apparent at diakinesis. SUN-1 forms foci and patches (the equivalent of the chromosomal attachment plaque seen in vertebrates) in the TZ [28-30].

We followed the movement of a functional SUN-1::GFP transgene integrated into the corresponding deletion background *sun-1(ok1282)* using in vivo imaging microscopy [28]. By additionally applying Hoechst 33342, we recorded both the motion of chromatin and the movement of SUN-1::GFP (Figure 1A, Video S1). SUN-1::GFP formed both large and small aggregates that moved in an erratic manner on one half of the nuclear periphery. Small and large aggregates met, fused and dispersed during the leptotene/zygotene stage of prophase I. Small aggregates, termed foci, likely define single chromosome end attachments, whereas large aggregates, termed patches, likely define multiple chromosome ends that are locally enriched. Indeed, only a single patch was visible at $t = 425$ s (Figure 1A), whereas at an earlier timepoint ($t = 140$ s), one patch and five foci were observed. Later ($t = 555$ s), we observed three foci and one patch. The coalescence of foci and patches were often very transient: in less than 130 s, we observed three foci driven out from the patch. Once two foci or one focus and a patch fused, they dispersed within a short time.

SUN-1::GFP aggregates, via cytoplasmic forces, also triggered protrusion of the chromatin, deforming the nuclear membranes. At $t = 140$ s, the chromatin was pulled outward by the SUN-1::GFP patch, which moved at the periphery of the nucleus (Figure 1A, white arrow; $t = 140$ s).

SUN-1 aggregates are highly dynamic

General features of SUN-1 aggregates

Because of unreliable Hoechst staining, as reported by [7], only SUN-1::GFP dynamics were recorded during this study. To study the dynamics of SUN-1 aggregates, we manually followed their movement and characterized features such as the number of aggregates, distribution of the projected speed, the distance traveled, number of fusion/splitting events, and coalescence time. No distinction was made between patches and foci when tracking their movement; therefore, both SUN-1 patches and foci are referred to as aggregates.

Throughout the entire TZ, there were a minimum of 2.4 ± 1.1 (standard deviation [SD], $n = 27$ nuclei) aggregates and a maximum of 6.1 ± 2.8 (SD, $n = 27$ nuclei) aggregates. During the recorded time, on average, 3.9 ± 1.4 (SD, $n = 27$ nuclei) aggregates (Table 1) per frame moved in an erratic manner over the surface of the nuclear membrane of single wild-type nuclei throughout the TZ (Video S2). The movement of SUN-1 aggregates was restricted to one hemisphere of the nucleus (Figure 1Di, 1Ei, and 1Fi; Video S1). The resulting displacement tracks of SUN-1 aggregates overlapped. In most cases, the projected movement of SUN-1 aggregates on the surface of the nucleus resembled the polarized conformation of the chromatin characteristic of leptotene/zygotene (Figure 1Dii, 1Eii, and 1Fii). In rare cases, the movement of the attachment plaques was observed from the top of the nuclei (Figure 1Bi). We reconstructed the 3D movement by considering that aggregates traveled only on one hemisphere of a spherical nucleus. (Figure 1Bi-iv). This reconstructed movement displayed undirected movement of chromosome ends. In addition, SUN-1::GFP aggregates moved outward toward the boundary of the nuclei (Figure 1Bii), (Figure 1A, $t = 140$ s), leading to bulging of the nuclear membrane. Aggregates usually moved randomly over short distances, but occasionally they traveled longer distances (Figure 1B).

We also defined background motion in the filmed germ cells. To assess background motion, we measured the movement of SUN-1::GFP aggregates in animals killed with sodium azide. The values for the projected speed defined the background projected speed between 0 and 40 nm/s (Figure S1A).

The projected speed of SUN-1::GFP aggregates did not display a normal distribution, but rather a “Maxwellian-shaped” distribution (Figure 1Ci; see Figure S1B for an explanation of the term). Overall, more than half of the SUN-1 aggregates inside a nucleus (66%) moved within a range of 40–160 nm/s; approximately 10% of the aggregates showed a higher projected speed of up to 260 nm/s (long tails), and 24% were in the range of the background projected speed ($n = 27$ nuclei, taken from two movies, illustrated by the orange and blue colors in the figures).

To analyze the distance traveled, we extrapolated that the aggregates were moving on the periphery of a circle (projected nucleus), and measured the angle formed by the most extreme points of the tracks (Figure S2). Arcs do not express the absolute distance traveled; instead, they measure the area covered on the circle (a measurement of how vigorously aggregates move). We followed the arc for each track inside a nucleus, and also recorded the overall minimum and maximum values for the observed arcs (Figure 1Cii). Note that 180° is placed on the left of the x-axis, because angles were computed in a trigonometric circle. When the aggregate moved more than 180° /half plane, the radius of the circle increased, and the line representing this “arc” is dashed. Arc values for SUN-1 aggregates were not centered, but were evenly distributed between 13° and 163° (Figure 1Cii).

Because SUN-1 aggregates appeared to transiently coalesce (Figure 1A), we counted the number of fusion or splitting events of the aggregates during the first 15 min of the recordings (Figure 2A). The two most representative classes for the number of fusion/splitting events were 1–5 and 6–10 fusion/splitting events during the 15 min measuring period. A representative number of nuclei displayed between 11–15 fusion/splitting events, with an observed maximum of 25 exchanges. To assess how often exchanges take place, we looked at the time period between two fusion/splitting events. The “coalescence time” between aggregates was <1 min before splitting/fusing in 71% of cases, 1–3 min in 22% of cases, and >3 min in 7% of cases (Figure 2B).

Wild-type SUN-1 aggregates were particularly dynamic: they were movement-competent (traveled a distance of up to 160°) and able to reach

high projected speeds (>160 nm/s). They fused and dispersed with high frequency (up to 15 fusion/splitting events during a 15 min interval of filming) during the leptotene/zygotene stage.

SUN-1 aggregate dynamics are independent of the position of the nucleus inside the TZ

To analyze whether SUN-1 aggregate behavior changes as the homology search progresses, we compared the aggregates in different parts of the TZ: distal (first row of cells of the TZ), proximal (last row of cells of the TZ), and central (row of cells clearly in the middle of the TZ). The appearance of tracks of SUN-1 aggregates was similar in each case. First, they exhibited the crescent form characteristic of the leptotene/zygotene stage (Figure 1Dii, 1Eii, and 1Fii). Second, no distinctions among the nuclei (from different positions in the TZ) could be made when looking at the distribution of the projected speeds. Aggregates in the three nuclei shown displayed the two classes of projected speed distribution: with or without long tails (Figure 1Diii, 1Eiii, 1Fiii). Aggregate numbers increased and decreased during the recorded time, independent of their position inside the TZ (Figure 1Div, 1Eiv, and 1Fiv). The distance traveled did not show a distinct pattern corresponding to the position in the TZ (Figure S3). No differences were found in the number of aggregates exchanged or the periodicity of these exchanges (data not shown). Therefore, we concluded that SUN-1 aggregates showed identical behavior, irrespective of their position in the TZ and the progress of homologous chromosome pairing.

Leptotene/zygotene characteristic chromatin polarization requires connection of the chromosome ends to the cytoskeleton via a functional SUN/KASH bridge

A point mutation in the SUN domain of SUN-1 results in the absence of a defined TZ, and disturbs the interaction of SUN-1 with ZYG-12 [30]. In the cytoplasm, ZYG-12 interacts with the cytoskeleton via a dynein motor [29,36]. We performed a time-lapse analysis of the mutated SUN-1(G311V)::GFP transgenic line in the *sun-1(ok1282)* deletion background and found that, on

average, 7.8 ± 2.3 (SD) aggregates inside a nucleus exhibited restrained movement (Table 1, Figure 3A and 3B, and Video S3). The distribution of the projected speed of these aggregates was a sharp bell, with 95% of the aggregates moving within a range of 10–100 nm/s (Figure 3C); the projected speed was significantly reduced compared to wild-type aggregates (Mann-Whitney test, $p < 0.001$). The displacement tracks indicated weak local oscillatory movement (Figure 3B), and the distances traveled were significantly reduced. The arcs varied between 27° and 59° (Figure 3D). No exchange of SUN-1 aggregates was seen (Figure 2A). A functional SUN/KASH bridge mediating the connection to the cytoskeleton was, thus, necessary for the movement of SUN-1 aggregates and correlated with the absence of polarized chromatin.

Loading of SC components is required for the formation of functional SUN-1 aggregates

The SC is a “zipper-like” structure that stabilizes the close pairing of parental chromosomes. This complex is composed of lateral elements on chromosome axes bridged by central region components [18]. We explored the behavior of SUN-1 aggregates in the SC mutants *him-3(gk149)*, *htp-1(gk174)*, *syp-2(ok307)*, and *syp-3(me42)*. HIM-3 is a major constituent of the lateral element, and HTP-1, in addition to being part of the lateral element, licenses synapsis [20,21]. The central region components of the SC, SYP-1, SYP-2, SYP-3 and SYP-4 zip up paired homologues [37,38,19]. An allele of the central region component SYP-3 revealed that SYP-3 plays a role in meiotic repair pathway decisions, in addition to its role in SC formation [39].

The *him-3(gk149)* null allele displays loss of the polarized conformation of chromatin in the TZ of the gonad and lacks presynaptic alignment [40]. Depleting HIM-3 resulted in 1.1 ± 0.3 (SD, $n = 53$) SUN-1 aggregates moving inside a nucleus (Table 1), and, on rare occasions, up to two aggregates (Figures 4Ai and 4Aii) unable to fuse (Figure 2A, Video S4). The projected speed distribution of the aggregates was “Gaussian-shaped,” with 95% of the aggregates moving within a range of 10–100 nm/s (Figure 4Aiii); this was significantly reduced compared to wild type (Mann-Whitney test, $p < 0.001$).

Depletion of HIM-3 also reduced the distance traveled by the SUN-1 aggregates: arc values only varied between 23° and 91° (Figure 4Aiv). HIM-8 is one of the four PC proteins, and binds specifically to the X chromosome [25]. In *him-3(gk149)*, HIM-8 always colocalizes with SUN-1::GFP, as shown by immunostaining [28]. Thus, the single SUN-1 aggregate moving with a reduced projected speed corresponds to the X chromosome and HIM-3 is, therefore, required for the formation of autosomal chromosome attachment plaques ([28] and this study). To test whether the formation of SUN-1 aggregates was impaired in *him-3(gk149)* due to mislocalization of the PC proteins, we stained *him-3(gk149)* with the PC protein ZIM-3 (marker for chromosomes I and IV). In *him-3(gk149)* mutant worms, the PC protein ZIM-3 did not colocalize with SUN-1 aggregates, although chromatin-associated signals were observed (Figure S4, text S2). Therefore, we hypothesize that defective lateral elements of the SC impeded functional attachment plaque formation.

htp-1 mutants precociously synapse with the wrong partner despite proper loading of HIM-3 [20,21]. In *htp-1(gk174)*, the average number of aggregates was reduced (Mann-Whitney test, $p < 0.05$). The maximum number of aggregates was comparable to the average number of SUN-1 aggregates in wild-type worms (Table 1). The displacement tracks of SUN-1::GFP in this background recapitulated the polarization of the chromatin characteristic of the TZ (Figures 4Bi and 4Bii; Video S5). The projected speed distribution within a nucleus was comparable to that in *him-3(gk149)*. For most SUN-1 aggregates (>95%), the projected speed varied between 10 and 100 nm/s (Figure 4Biii). The distance traveled was significantly reduced compared to *him-3(gk149)* (Mann-Whitney test, $p < 0.001$): arc values ranged from 20° to 62° (Figure 4Biv). The precocious synapsis in *htp-1(gk174)* mutant worms likely inhibits the mobility of SUN-1 aggregates (see below). This interpretation was reinforced by a significant decrease in the number of fusion/splitting events (Figure 2A and Table S1) and a significant increase in the time without exchange (Figure 2B and Table S2). Indeed, SUN-1 aggregates coalesced for longer than 1 min in 60% of cases. Although ZIM-3 loading was defective in *him-3(gk149)*, it was unaffected in *htp-1(gk174)*, with

2–4 ZIM-3 signals overlapping with SUN-1 aggregates (Figure S4). We conclude that *htp-1(gk174)* mutant worms readily formed single chromosomal attachment plaques.

The SC central region component mutant *syp-2(ok307)* has an extended TZ, characteristic of SC mutants [38]. We compared the dynamics of SUN-1 aggregates in distal (first half of the TZ, Video S6) and proximal (second half of the TZ, Video S7) positions in the prolonged TZ. In the distal part, on average, 2.8 ± 1 (SD, $n = 30$) SUN-1 aggregates showed reduced movement (Figure 4Ci and 4Cii); in addition, the maximum number of SUN-1 aggregates was reduced (3.5 ± 1.1 ; SD, $n = 30$) compared to wild type (Table 1; Mann-Whitney test, $p < 0.05$). Although the projected speed distribution of 95% of SUN-1 aggregates was 10–100 nm/s (Figure 4Ciii), comparable to *him-3(gk149)*, the distribution was more Maxwellian-shaped. The distance traveled by SUN-1::GFP aggregates was reduced (from 16° up to 90° , with the exception of one track that went up to 163° ; Figure 4Civ) compared to wild type. Depletion of SYP-2 also reduced the number of SUN-1::GFP fusion/splitting events in the distal part of the TZ (Figure 2A and Table S1), with mostly 1–5 fusion/splitting events occurring within 15 min. The time of coalescence between SUN-1 aggregates was increased. Indeed, only 50% of SUN-1 aggregates coalesced for less than 1 min, while 22% of them coalesced for more than 3 min (Figure 2B and Table S2).

syp-2(ok307) SUN-1::GFP aggregates in the proximal part of the TZ traveled longer distances. The arcs were between 20° and 150° (Figure 4Civ'), which is in accordance with a broader projected speed distribution. The projected speed distribution for 95% of the aggregates ranged between 15 and 140 nm/s (Figure 4Ciii'), and adopted a more Maxwellian-shaped distribution than in the early TZ, with the distribution shifted towards the higher speed. In the proximal part of the TZ, the displacement tracks were more reminiscent of the crescent shape of the chromatin than in the distal part of the TZ (compare Figures 4Ci and 4Ci'). In the proximal part of the TZ, the maximum number of SUN-1 aggregates went up to 4.2 ± 1.2 (SD, $n = 45$) (Table 1); nevertheless, their average number remained decreased compared to wild type (Mann-Whitney test, $p < 0.05$). The number of SUN-1::GFP

fusion/splitting events also differed from those seen in wild-type worms; there were less than ten exchanges within 15 min (Figure 2A and Table S1). The periodicity of the exchanges was similar to wild type (Figure 2B and Table S2). Disruption of synapsis resulted in a lack of long tails in the speed distribution and a decrease in the number of SUN-1 aggregates exchanged in both the distal and proximal parts of the TZ.

The *syp-3* allele *me42* is special because it has a shortened TZ and appears to use a different repair pathway for the repair of meiotic DSBs [39]. In contrast to SC-deficient mutants, in *me42*, the central region component SYP-1 was found to be polymerized on univalents. The displacement tracks of SUN-1::GFP in *syp-3(me42)* followed a half-moon shape (Figure 4Di and 4D ii; Video S8). The number of SUN-1 aggregates was significantly decreased compared to wild-type values (Table 1; Mann-Whitney test, $p < 0.001$). The distribution of the projected speed was more Maxwellian-shaped and comparable to the distribution of SUN-1::GFP aggregates in the distal part of the *syp-2(ok307)* mutants (Figure 4Diii). The distance traveled was greater than in *syp-2(ok307)* mutant worms, and covered angles from 37° to 100° (Figure 4Div). The number of SUN-1::GFP fusion/splitting events was comparable to those in wild-type worms (Figure 2A and Table S1), but the frequency of the exchanges was significantly decreased (Figure 2B and Table S2).

To test the idea that restricted aggregate behavior in *htp-1(gk174)* was due to nonhomologous synapsis, we depleted SYP-1 in *htp-1(gk174)* mutants. Surprisingly, in *htp-1(gk174); syp-1(RNAi)* SUN-1 aggregates were extended and not restricted to the first cell row where chromatin is strongly polarized (Figure S5). SUN-1 aggregates were still detectable in nuclei with more loosely clustered chromatin. We divided the zone with aggregates into distal (Video S9) and proximal (Video S10) for analysis. In the distal part of *htp-1(gk174); syp-1(RNAi)* the average number of SUN-1 aggregates (3.5 ± 0.6 , SD, $n = 23$, Table 1) was close to wild type, but their maximum number was significantly reduced (Mann-Whitney test, $p < 0.05$). Displacement tracks adopted a circular form, in contrast to the crescent shape seen in wild type (Figure 5A and 5B, 11 out of 23 nuclei), where movement pushes the

nucleolus to one side of the nucleus. Here the tracks are found at the periphery, with chromatin likely rotating around the nucleolus. SYP-1 depletion in *htp-1(gk174)* significantly increased the projected speed of SUN-1 aggregates when compared to *htp-1(gk174)*, nevertheless the percentage of long tails (4%) was significantly below wild-type values (Figure 5C, Mann-Whitney test, $p < 0.05$). The distance traveled was also significantly increased in *htp-1(gk174); syp-1(RNAi)*, with arc values reaching 156° (compare Figure 4Biv and Figure 5D, Mann-Whitney test, $p < 0.05$). Depletion of SYP-1 in *htp-1(gk174)* resulted in an increase of exchanged aggregates (Figure 2A, Table S1) and restored the periodicity of these exchanges to the wild type value (Figure 2B, Table S2).

In the proximal region of *htp-1(gk174); syp-1(RNAi)* gonads the number of SUN-1 aggregates was significantly reduced compared to the distal part (Mann-Whitney test, $p < 0.05$) with an average of 2.8 ± 0.6 (SD, $n=24$, Table 1). Of the 23 nuclei analyzed, 16 nuclei displayed circular displacement tracks (Figure 5A' and 5B'). The distribution of the projected speed was significantly increased compared to the distal part (6% long tails, Figure 5C', Mann-Whitney test, $p < 0.05$), but still below wild-type values (Mann-Whitney test, $p < 0.05$). SUN-1 aggregates traveled longer distances in the proximal part than in the distal (Figure 5D', Mann-Whitney test, $p < 0.05$), but the distances traveled, the exchanges, and the frequencies were still below wild-type values (Mann-Whitney test, $p < 0.05$). (Figure 2A and 2B, Tables S1 and S2).

Our analysis of the behavior of SUN-1 aggregates in mutants defective in SC formation confirmed that intact lateral elements of the SC were necessary for the formation of functional SUN-1 aggregates. We showed that SC components played a role in the exchange of SUN-1 aggregates. HTP-1 has an inhibitory influence on the exchange of aggregates as we observed reduced exchanges in *htp-1(gk174)* and *syp-2(ok307)* single mutants, whereas exchanges were increased to wild type values in *htp-1(gk174); syp-1(RNAi)*. Strikingly, defects in SC polymerization reduced the projected speed of aggregates, whereas decreasing synapsis in the *htp-1* mutant increased the projected speed of SUN-1 aggregates. The persistent

aggregates in the *syp-1 htp-1* double mutant formed circular displacement tracks concomitant with only loosely clustered chromatin.

Modulation of SUN-1 aggregate properties by meiotic regulators CHK-2, HIM-19, PROM-1, and CRA-1

To date, known early meiotic regulators with a role in chromosome pairing in *C. elegans* include CHK-2, HIM-19, PROM-1, and CRA-1. Depletion of CHK-2 results in a lack of SUN-1 aggregates in *chk-2* [28]; therefore, no live imaging can be shown. HIM-19 is a newly identified meiotic regulator. In *him-19(jf6)* mutants, meiotic defects are aggravated with age. In 2-day-old (2-d-old) *him-19(jf6)* mutant worms, the TZ is not defined, DSB formation is likely defective, and elongation of the SC is restricted and nonhomologous [33]. PROM-1 is involved in the progression of meiosis I, and its depletion elicits nonhomologous synapsis. *prom-1(ok1140)* mutant worms lack a defined TZ and instead display dispersed nuclei with a polarized conformation after a prolonged meiotic entry zone [32]. CRA-1 regulates SC formation. Unlike *chk-2*, *prom-1*, and *him-19*, *cra-1* mutant worms display an extended TZ. In addition, *cra-1(tm2144)* mutant worms are defective in the formation of the SC central region [34].

In dispersed nuclei with a TZ-like appearance in *prom-1(ok1140)* mutant worms, SUN-1::GFP aggregates were movement competent (Video S11), and their tracking reconstructed the crescent shape of the chromatin (Figure 6Ai and 6Aii). The number of SUN-1 aggregates in *prom-1(ok1140)* was reduced compared to wild type (Mann-Whitney test, $p < 0.05$), despite a similar average number of aggregates (Table 1). In this background, SUN-1 aggregates displayed a Maxwellian-shaped projected speed distribution and lacked long tails (Figure 6Aiii; Mann-Whitney test, $p < 0.05$ compared to wild type), although the distance traveled by SUN-1::GFP aggregates was unaffected (from 19° up to 143°; Figure 6Aiv; Mann-Whitney test, $p > 0.05$). Depletion of PROM-1 also reduced the number of exchanged aggregates (Figure 2A). Indeed, in a significant number of nuclei, SUN-1 aggregates were unable to fuse or split, and the number of nuclei showing 6–10 fusion/splitting

events was considerably reduced (Table S1). The time period without exchange was significantly increased in *prom-1(ok1140)* compared to wild type: 47% of SUN-1::GFP aggregates were found to coalesce for less than 1 min and 23% for more than 3 min (Figure 2B and Table S2).

In *prom-1(ok1140)*, it is likely that the delayed orchestration of the meiotic program led to a reduction in the speed of SUN-1 aggregates without affecting the distance traveled. In addition, the number and frequency of exchanges were reduced in *prom-1(ok1140)* mutants.

The formation of SUN-1 aggregates in 2-d-old *him-19(jf6)* mutants was restricted to the few dispersed nuclei with a polarized chromatin conformation, but could be augmented by γ -irradiation (Figure 6B and [28]). In aged *him-19(jf6)* worms, a few SUN-1::GFP aggregates were movement competent (Video S12), and their displacement tracks resembled a crescent shape (Figure 6Bi and 6Bii). Both the average number of SUN-1 aggregates (2.8 ± 0.8 ; SD, $n=8$) and the maximum number of aggregates was decreased (4.0 ± 1.3 ; SD, $n = 8$) (Table 1; Mann-Whitney test, $p < 0.05$). In addition, the projected speed distribution of SUN-1::GFP aggregates was reduced compared to wild type (Mann-Whitney test, $p < 0.05$): it was similar to the speed of SUN-1::GFP aggregates in *htp-1(gk174)*, with 95% of the aggregates moving from 10 to 130 nm/s (Figure 6Biii). The distance covered was also reduced, as demonstrated by arc values ranging from 9° up to 137° (Figure 6Biv; Mann-Whitney test, $p < 0.05$). In *him-19(jf6)* mutants, the number of SUN-1 fusion/splitting events was wild type (Figure 2A and Table S1), whereas the time without exchange increased, with 38% of SUN-1 aggregates coalescing for less than 1 min and 21% for more than 3 min (Figure 2B and Table S2).

Two hours after γ -irradiation, the average number of SUN-1 aggregates reached wild-type levels in 2-d-old *him-19(jf6)* worms (Table 1); however, the number of SUN-1 aggregates was significantly reduced (Mann-Whitney test, $p < 0.05$). The displacement tracks of SUN-1::GFP in 2-d-old irradiated *him-19(jf6)* worms recapitulated the polarized conformation of the chromatin (Figure 6Bi' and ii'; Video S13). The distribution of the projected speed of SUN-1::GFP aggregates was shifted towards the higher speed after

irradiation and became more Maxwellian-shaped. Nevertheless, long tails were absent from the distribution (Figure 6Biii'). The projected speed of SUN-1 aggregates was reduced in aged irradiated *him-19(jf6)* compared to wild type (Mann-Whitney test, $p < 0.05$). In contrast, irradiation-induced SUN-1::GFP aggregates in *him-19(jf6)* moved similar to those in wild-type worms in terms of the distance traveled (Figure 6Biv'; Mann-Whitney test, $p > 0.05$), whereas the number of exchanges was significantly reduced. The class of 1–5 fusion/splitting events represented more than 50% of nuclei, and the exchange was abrogated for a representative number of nuclei (Figure 2A and Table S1). The frequency of these exchanges was reduced compared to wild type (Figure 2B and Table S2), and there was no significant increase compared to nonirradiated *him-19(jf6)* worms.

We conclude that γ -irradiation restored the formation of SUN-1 aggregates to wild-type levels with respect to their numbers and distances traveled, whereas the dynamics of SUN-1 aggregates remained impaired both in terms of the distribution of the projected speed and the number and frequency of exchanges.

To ensure that γ -irradiation had no side effects, we irradiated 2-d-old worms solely expressing SUN-1::GFP and performed the same analysis. The appearance of the displacement tracks of SUN-1::GFP aggregates was circular in 12 of the 24 nuclei analyzed whereas the other ones recapitulated the crescent shape of the chromatin (Figure 6Ci and 6Cii; Video S14). The distribution of the projected speed of SUN-1::GFP aggregates was shifted markedly towards lower values, with only 3% long tails (>160 nm/s) (Figure 6Ciii; Mann-Whitney test, $p < 0.05$). Nonetheless, after γ -irradiation, SUN-1::GFP aggregates move faster in wild-type worms than in irradiated *him-19(jf6)* (Mann-Whitney test, $p < 0.05$). In addition, the maximum number of SUN-1 aggregates was reduced (Table 1; Mann-Whitney test, $p < 0.05$) compared to nonirradiated wild type. γ -irradiation also reduced the distance traveled by SUN-1 aggregates; arc values ranged between 19° and 128° (Figure 6Civ; Mann-Whitney test, $p < 0.05$). γ -irradiation had no impact on the number of SUN-1::GFP fusion/splitting events (Figure 2A and Table S1). However, it significantly increased the time without exchanges (Figure 2B and

Table S2). FISH analysis with a probe specific for chromosome V revealed that pairing was affected after γ -irradiation (Figure S6A and S6B). To ascertain whether the decrease in the speed distribution might be due to an SC defect, we stained for SYP-1 in nonirradiated and irradiated wild-type worms. No gross irregularities in SYP-1 polymerization were evident 2 h after γ -irradiation (Figure S6C, text S2).

γ -irradiation clearly had an impact on the dynamics of SUN-1 aggregates in wild-type gonads. Nonetheless, the behavior of restored SUN-1 aggregates in irradiated *him-19(jf6)* mutants adopted a more wild-type-like behavior compared to the sparse aggregates in non-irradiated *him-19(jf6)* gonads.

In *cra-1(tm2144)* mutants, SUN-1 aggregates were movement competent (Video S15), and their displacement tracks adopted a rather circular form (19 out of 22), like in *htp-1(gk174); syp-1(RNAi)* (Figure 6Di and 6Dii). Likewise, in *cra-1(tm2144)* chromatin loosely clustered following a short stretch of nuclei with strong chromatin polarization (Figure S5). The number of SUN-1 aggregates was similar to that of wild type (Table 1; Mann-Whitney test, $p > 0.05$). However, the distribution of the projected speeds of SUN-1 aggregates increased towards higher speeds (12% long tails) (Figure 6Diii; (Mann-Whitney test, $p < 0.05$). This was also the case for the distance traveled, with arcs ranging from 15° up to 173° (Figure 6Div; Mann-Whitney test, $p < 0.05$). Except for the class of 1–5 fusion/splitting events, which was significantly reduced compared to wild type, the number of SUN-1 fusion/splitting events was similar to that of wild type in the *cra-1(tm2144)* background (Figure 2A and Table S1). The frequency of SUN-1 aggregate exchanges was unaffected in *cra-1(tm2144)* (Figure 2B and Table S2).

In *cra-1(tm2144)*, the kinetics of SUN-1 aggregates were increased (speed and distance traveled) compared to wild type, whereas the number and frequency of fusion/splitting events was unaffected.

Impairment of meiotic regulators showed that DSBs could be involved in the formation of functional SUN-1 aggregates, and that γ -irradiation nonetheless had some impact on SUN-1 aggregate movement. Improper orchestration of the meiotic program disturbed SUN-1 aggregate dynamics.

DSBs are required for wild-type SUN-1 aggregate behavior

In order to test whether recombination impacts SUN-1 aggregate dynamics, we followed SUN-1 movement in the *spo-11(me44)* mutant (Video S16).

The average number of SUN-1 aggregates was significantly reduced (3.0 ± 0.6 , SD, $n=18$, Table 1) compared to wild type. Surprisingly, the appearance of SUN-1 displacement tracks was circular in 9 out of the 18 nuclei analyzed (Figure 7Ai and 7Aii). The distribution of the projected speed of SUN-1 aggregates in *spo-11(me44)* showed only 5% long tails (Figure 7Aiii), and was reduced in terms of speed and distance traveled (Mann-Whitney test, $p < 0.05$) (Figure 7Aiv). In *spo-11(me44)*, the number and frequency of exchanges (Figure 2A and 2B, Tables S1 and S2) were wild type.

Next we tested whether introduction of artificial DSBs by γ -irradiation in *spo-11(me44)* (Video S17) could restore the properties of SUN-1 aggregates to wild-type values. The average number of SUN-1 aggregates (3.6 ± 0.6 , SD, $n=23$, Table 1) in *spo-11(me44)* mutants increased to wild-type levels after irradiation. The displacement tracks were circular in 11 of the 23 nuclei analyzed (Figure 7Bi and 7Bii). The distribution of the projected speed of SUN-1 aggregates displayed 3% of long tails, like wild type 2 hours after irradiation, but SUN-1 aggregates tended to move faster (Mann-Whitney test, $p < 0.05$). γ -irradiation had no impact on the distance traveled (Figure 7Biv, Mann-Whitney test, $p > 0.05$). The frequency of exchanges was significantly reduced when compared to wild type (Figure 2B, Table S2), but no effect could be detected in the number of SUN-1 aggregates exchanged (Figure 2A, Table S1). The properties of SUN-1 aggregates in *spo-11(me44)* after irradiation were close to wild-type values after irradiation.

Intrigued by the fact that less SUN-1 aggregates can be found in *spo-11(me44)*, we compared the ratio of foci and patches in the gonad of both irradiated and non-irradiated wild type and *spo-11(me44)* worms. We found a significant increase in the number of foci in *spo-11(me44)* compared to wild type (Figure 7C, Fisher's exact test, $p < 0.05$). The ratio of foci to patches was significantly reduced after irradiation (Figure 7C, Fisher's exact test, $p < 0.05$) with an increase in the fraction of patches for wild type and *spo-11(me44)*.

All together, these results confirm that formation of DSBs is necessary for the generation of wild-type numbers of SUN-1 aggregates and patches. The appearance of circular tracks in *spo-11(me44)* confirms loose chromatin clustering in *spo-11(me44)* (not shown).

Discussion

During early meiotic prophase, SUN-1 forms movement-competent aggregates that can be categorized into two classes: foci and patches. Foci most likely represent single chromosome end attachments, whereas patches harbor multiple chromosome ends in a local cluster, reminiscent of the chromosomal bouquet [28]. These aggregates fuse and disperse, with an average number of four aggregates during leptotene/zygotene, and cover distances on the order of half a circle after projecting movement into two dimensions. The movement of SUN-1 aggregates anchored in the inner nuclear membrane is able to induce outward directed protrusion of the chromatin and, thus, of the nuclear envelope, as in budding yeast [7] and maize [9].

Formation of functional SUN-1 aggregates

Wild-type numbers of SUN-1 aggregates require HIM-3, a component of the lateral elements of the SC. The sole movement-competent aggregate in the *him-3(gk149)* mutant colocalizes with the X chromosome [28]. The “autosomal SUN-1 aggregates” are, therefore, missing. Lateral elements of the SC are possibly required for their formation; alternatively, they may affect their stability. The fact that formation of attachment plaques at the nuclear periphery is independent of the lateral element of the SC in rat testis [41] provides support for the latter explanation. The reduced mobility of the SUN-1 aggregate in *him-3(gk149)* could be explained by the ability of the lateral element of the SC to rigidify the chromosomes, thereby supporting resolution of chromatin entanglements that otherwise might slow down movement.

Formation of functional SUN-1 aggregates also requires a functional SUN-domain, enabling the movement of SUN-1 aggregates. We showed that disruption of the SUN/KASH bridge abrogated the movement of SUN-1 aggregates, leading to nonhomologous synapsis in SUN-1(G311V)::GFP. The movement of SUN-1 aggregates, thus, exerted an inhibitory action on synapsis with the wrong partners. In addition, SUN/KASH-mediated movement exerted a positive effect on synapsis by mixing chromosomes in the nucleus, thereby positively reinforcing homologous synapsis. The

movement of SUN-1 aggregates also elicited the polarized appearance of the chromatin, which required more than one aggregate to be moving, as exemplified in *him-3(gk149)*, where chromatin did not cluster.

Do SUN-1 patches solely reflect chromosome end shuffling as the driving force for pairing?

Chromosome ends move along the inner surface of the nuclear envelope and come together in areas where patches of SUN-1 are seen. At the same time, SC polymerization is present, implying that once parental partner chromosomes have met, they engage in synapsis [37]. At this point, successful synapsis did not lead to dissolution of the aggregate. There was no difference in terms of the number of SUN-1 aggregates during the progression of leptotene/zygotene (as assessed by dividing this stage into three substages); instead, the average number of SUN-1 aggregates fluctuated at around four.

We propose that duplets/multiplets of chromosome ends are linked to SUN-1 patches. These duplets/multiplets of chromosome ends attached to SUN-1 patches continue to move and meet other SUN-1 patches or foci. While the newly met SUN-1 aggregates coalesce, homology is assessed; how homology is assessed is still an open question. Chromosome ends are then shuffled through patches of SUN-1, and when the right partner is met, synapsis can take place. The shuffling of chromosome ends through the patches continues until all of the chromosomes have found their homolog. This process is dynamic, as most SUN-1 aggregates coalesce for less than 1 min. The shuffling of the chromosome ends during SUN-1 aggregate coalescence is, thus, one of the driving forces for homology search (Figure 8A and 8B). This allows homologous chromosome ends to meet and nonhomologous chromosomes to separate.

Chromosome ends coalescing in SUN-1 patches might not solely reflect shuffling chromosome ends but also interactions caused by recombination repair intermediates. Indeed, in *spo-11* fewer patches are formed than in wild type and introduction of DSBs significantly increases the formation of patches. These two processes (assessing homology) and

ongoing repair of DSBs (up to the strand invasion step) might be the source of the long tails observed in the speed distribution of SUN-1 aggregates (see below). In addition interlocked chromosomes could contribute to the long tails.

Formation of high-speed SUN-1 aggregates

During the leptotene/zygotene stage, SUN-1 aggregates in *C. elegans* moved more slowly and did not accelerate abruptly, similar to what was reported for telomere ends in budding yeast and maize [6,7,9]. Nonetheless, SUN-1 aggregates reached relatively high speeds (>160 nm/s), as demonstrated by the long tails in the distribution of the projected speed of SUN-1 aggregates.

Two nonexclusive explanations could account for the formation of the long tails in the projected speed distribution of SUN-1 aggregates: first, “a model of tension” [29], where assessment of homology (Figure 8A and 8B), a nascent repair intermediate (Figure 8C) or chromosome entanglements (Figure 8D) leads to the formation of tension between chromosome ends. These interactions are counteracted by cytoplasmic forces (generation of tension). When cytoplasmic forces overcome these interactions, the two chromosome ends are disjoined (loss of accumulated tension), leading to an increase in the speed distribution of SUN-1 aggregates. Absence of DSBs significantly reduces the formation of long tails. Indeed other factors, such as chromosome interlocks, could contribute to the formation of the tension. Recently, the repair protein *mlh-1* in *S. macrospora* had been assigned a critical role in resolution of interlocks [42]. When SYP-1 is depleted in *htp-1*, long tails reappear in the speed distribution despite their absence in *htp-1*, and fewer DSBs are made, as previously observed in *htp-1;syp-2* [21]. This suggests that entanglements can also contribute to the generation of tensions.

A second explanation for the formation of high speed could be that a patch containing paired homologues could move faster than a patch of nonpaired homologues. In the mutant SUN-1(S12E), pairing is fairly effective in the proximal part of the TZ [28]. The distribution of the projected speed of SUN-1 aggregates in this area was significantly shifted towards higher speeds (16% of long tails), supporting the idea that patches containing paired

homologues could move faster (see text S1 and Figures S7, 8 and 9). This is in contradiction with our finding that SUN-1 dynamics remained unchanged during the leptotene/zygotene stage despite processing of pairing. In fact, paired homologues in patches cannot account for the shift towards higher speeds, because we showed that patches (paired or unpaired homologues) and foci (most likely single chromosome ends) were both able to reach high speeds (Text S1). Patches are only faster than foci in the middle segment of the speed distribution. Addressing this paradox will require live imaging of the tagged end of a single chromosome.

Exit of the polarized conformation

It has been shown that an unpaired chromosome keeps chromatin loosely clustered once stable strand invasion is established [43]. Similarly, we found that in *htp-1; syp-1*, chromatin was also loosely clustered concomitant with circular displacement tracks. Circular displacement tracks are likewise found in *cra-1* where partial synapsis is coupled with accumulation of DSB intermediates [34]. The fact that in *htp-1; syp-2* DSBs do not accumulate [21] could be an explanation why circular tracks were less frequent than in *cra-1*. Previously, we proposed that exit from polarized chromatin requires a certain recombination intermediate and/or full synapsis [28]. Loose chromatin clustering in *spo-11*, together with circular displacement tracks, could be explained by the absence of the particular recombination intermediate required to dissolve chromosomal attachment plaques.

Chromosome end-led prophase movement alone is not sufficient for successful pairing

The absence of SUN-1 aggregates in *chk-2(me64)* confirms that this gene plays an indispensable role in pairing [28]. The triggers to activate CHK-2 are unknown, but DSBs could be one such trigger, as shown by the analyses of SUN-1 aggregates in aged *him-19(jf6)* irradiated worms [28]. In the present study, γ -irradiation significantly rescued some aspects of the behavior of SUN-1 aggregates in aged *him-19(jf6)*.

Despite their different roles during meiosis, *htp-1* and *prom-1* mutants display nonhomologous synapsis [20,21,32]. Deletion of either of these two proteins results in different phenotypes (precocious synapsis or delayed progression of meiosis). These mutants highlight the necessity of coordinating sub-events right after meiotic entry for the generation of functional SUN-1 aggregates. In both mutants, the speed distributions of SUN-1 aggregates lacked long tails; perhaps when chromosomes nonhomologously synapse, the tension-generating process cannot take place (assessment of pairing). The maximum number of aggregates was five in both cases, because when aggregates coalesce into a patch, chromosome ends could not be shuffled, because synapsis had already taken place. The two mutants were also similar in terms of the number of fusion/splitting events and of periodicity of coalescence time. The analysis of these two mutants strongly suggests that effective pairing of homologues requires more than just chromosome end movement. Other prophase I events are also necessary for successful pairing.

In this study, we showed that instead of single chromosome ends looking for their homologous partner, duplets or multiplets and single chromosome ends were brought together in groups (patches) during the leptotene/zygotene stage by SUN-1 aggregate movement. Chromosome ends shuffled through these patches in search of the correct partner. Simultaneous *in vivo* imaging of specific chromosome ends and SUN-1 aggregates should be the next step to substantiate our finding. Second, these patches might represent ongoing repair of DSBs. Deciphering the regulation of synapsis initiation while chromosome ends are being shuffled in a tightly regulated process is one of the challenges for the future.

Materials and methods

Nematode strains, strain construction and culture conditions

All *C. elegans* strains were cultured using standard techniques [44]. The following *C. elegans* strains were used: N2 Bristol, *sun-1(ok1282)*; *sun-1::GFP* [28], *sun-1(ok1282)/nT1[let-?qls51]*; *sun-1::GFP(G311V)* [28], *chk-2(me64)/unc-51(e369) rol-9(sc148)*; *sun-1::GFP* [28], *syp-2(ok307)/nT1[qls51]*; *sun-1::GFP* [28], *him-3(gk149)/nT1[let-?qls51]*; *sun-1::GFP* [28], *htp-1(gk174)/nT1[let-?qls51]*; *sun-1::GFP* [28] *him-19(jf6)*; *sun-1::GFP* [33], *syp-3(me42)/hT2[bli-4(e937)let-?(q782)qls48]*; *sun-1::GFP*, *prom-1(ok1140)*; *sun-1::GFP*, *cra-1(tm2144) /hT2(GFP)*; *sun-1::GFP*, *spo-11(me44) /nT1[unc-?(n754) let-? qls50]*; *sun-1::GFP* .

Nematode strains were provided by the *Caenorhabditis Genetics Center*, which is funded by the NIH National Center for Research Resources (NCRR). *him-19(jf6)*; *sun-1::GFP* and *sun-1(ok1282)*; *sun-1::GFP* worms were γ - irradiated with a dose of 50 Gy for 10 sec using a ^{137}Cs source and the time lapse microscopy was recorded 2 hrs after irradiation. *syp-1(RNAi)* was done as described in [46].

Time lapse microscopy

For time lapse acquisitions, adult hermaphrodites preselected at the L4 stage 16 hrs before were mounted in a drop of 10 mM Levamisol on a 2% agarose pad and covered with a coverslip. For *him-19(jf6)*, worms were preselected 2 days before irradiation. The coverslip was sealed with melted Vaseline. Images were acquired at room temperature every 5 sec over a 15 min time period as stacks of optical sections at 1 μm intervals using a Deltavision deconvolution microscopy system (Applied Precision, Inc, 1040 12th Avenue, Northwest Issaquah, Washington 98027, USA) under the following conditions: FITC channel, 32%ND, bin 1x1, exposure time 200 msec, objective 60x. To assay the effect of Levamisole on the worms, worms were mounted as described above in a drop of Levamisole or M9 and then the hatch rate of the filmed worms evaluated under the two conditions. No significant decrease of

the hatch rate was observed (Levamisol hatch rate: 93% (>500 eggs laid), M9 hatch rate: 96% (>200 eggs laid), Fisher's exact test: $p > 0.05$).

Maximum intensity projection was done using Softworx software (Applied Precision, Inc, 1040 12th Avenue, Northwest Issaquah, Washington 98027, USA) and the collection of files saved. The collection of pictures was opened with Metamorph Offline (Molecular Devices, 402 Boot Rd., Downingtown, PA 19335, USA) and saved as stack files. To support the plotting process, the background of the stack pictures was removed using Autoquant X2 (AutoQuant Imaging, Troy, NY, USA) and the slices realigned using the first slice as a reference.

Image analysis

With the help of Metamorph Offline, the positions of SUN-1 aggregates were manually followed. When two aggregates split, instead of starting to record two new tracks, tracking of the larger aggregate was continued. Then movement of the second aggregate was recorded. Subsequently positions of SUN-1 aggregates were plotted using Gnuplot software (Thomas Williams, Colin Kelley et al. 2004, <http://www.gnuplot.info>). Frequency and number of fusion/splitting events were computed using the number of aggregates as a function of time. Automated plotting of the movement of SUN-1 aggregates was done using Image J (NIH, <http://rsbweb.nih.gov/ij/>) and the plug-in MTrack2 (author: Nico Stuurman, <http://valelab.ucsf.edu/people/p-stuurman.htm>) (see Figure S9).

Computations and statistics

The speed of the object between two successive data points was calculated as the distance covered divided by the time required to cover the distance. Arcs were computed as described in Figure S3. Three-dimensional reconstruction of SUN-1 aggregate movement was done using the relationship $x^2 + y^2 + z^2 = r^2$, where x , y , z are the coordinates of a point situated on a sphere of radius r . The z -coordinates were computed from the x - and y -coordinates of the nuclei viewed from the top as follows: $z = \sqrt{(r^2 - x^2 - y^2)}$, and when $x^2 + y^2 > r^2$, the previous z -coordinate was used. Statistical analysis was

done using the software R (R Development Core Team, <http://www.R-project.org>).

Acknowledgements

We thank Christian Pflügl for technical support. We are grateful to Peter Carlton, Arndt von Haeseler, Maria Siomos and Josef Loidl for suggestions. We thank Anne Villeneuve, Monique Zetka, Monica Colaiacovo, Enrique Martinez-Perez and the *Caenorhabditis Genetics Center*, which is funded by the NIH National Center for Research Resources (NCRR) for strains and reagents.

References

1. Petronczki M, Siomos M, Nasmyth K (2003) Un menage a quatre: the molecular biology of chromosome segregation in meiosis. *Cell* 112: 423-440.
2. Scherthan H (2001) A bouquet makes ends meet. *Nat Rev Mol Cell Biol* 2: 621-627.
3. Chikashige Y, Haraguchi T, Hiraoka Y (2007) Another way to move chromosomes. *Chromosoma* 116: 497-505.
4. Fridkin A, Penkner A, Jantsch V, Gruenbaum Y (2008) SUN-domain and KASH-domain proteins during development, meiosis and disease. *Cell Mol Life Sci* 66: 1518-1533.
5. Hiraoka Y, Dernburg AF (2009) The SUN rises on meiotic chromosome dynamics. *Dev Cell* 17: 598-605.
6. Conrad MN, Lee CY, Chao G, Shinohara M, Kosaka H, et al. (2008) Rapid telomere movement in meiotic prophase is promoted by NDJ1, MPS3, and CSM4 and is modulated by recombination. *Cell* 133: 1175-1187.
7. Koszul R, Kim KP, Prentiss M, Kleckner N, Kameoka S (2008) Meiotic chromosomes move by linkage to dynamic actin cables with transduction of force through the nuclear envelope. *Cell* 133: 1188-1201.
8. Chikashige Y, Tsutsumi C, Yamane M, Okamasa K, Haraguchi T, et al. (2006) Meiotic proteins bqt1 and bqt2 tether telomeres to form the bouquet arrangement of chromosomes. *Cell* 125: 59-69.
9. Sheehan M, Pawlowski W (2009) Live imaging of rapid chromosome movements in meiotic prophase I in maize. *Proc Natl Acad Sci USA* 106: 20989–20994.
10. Scherthan H, Wang H, Adelfalk C, White EJ, Cowan C, et al. (2007) Chromosome mobility during meiotic prophase in *Saccharomyces cerevisiae*. *Proc Natl Acad Sci U S A* 104: 16934-16939.
11. Trelles-Sticken E, Dresser ME, Scherthan H (2000) Meiotic telomere protein Ndj1p is required for meiosis-specific telomere distribution,

- bouquet formation and efficient homologue pairing. *J Cell Biol* 151: 95-106.
12. Wanat JJ, Kim KP, Koszul R, Zanders S, Weiner B, et al. (2008) Csm4, in collaboration with Ndj1, mediates telomere-led chromosome dynamics and recombination during yeast meiosis. *PLoS Genet* 4: e1000188.
 13. Kosaka H, Shinohara M, Shinohara A (2008) Csm4-dependent telomere movement on nuclear envelope promotes meiotic recombination. *PLoS Genet* 4: e1000196.
 14. Conrad MN, Lee CY, Wilkerson JL, Dresser ME (2007) MPS3 mediates meiotic bouquet formation in *Saccharomyces cerevisiae*. *Proc Natl Acad Sci U S A* 104: 8863-8868.
 15. Conrad MN, Dominguez AM, Dresser ME (1997) Ndj1p, a meiotic telomere protein required for normal chromosome synapsis and segregation in yeast. *Science* 276: 1252-1255.
 16. Wu HY, Burgess SM (2006) Two distinct surveillance mechanisms monitor meiotic chromosome metabolism in budding yeast. *Curr Biol* 16: 2473-2479.
 17. Dernburg AF, McDonald K, Moulder G, Barstead R, Dresser M, et al. (1998) Meiotic recombination in *C. elegans* initiates by a conserved mechanism and is dispensable for homologous chromosome synapsis. *Cell* 94: 387-398.
 18. Colaiacovo MP (2006) The many facets of SC function during *C. elegans* meiosis. *Chromosoma* 115: 195-211.
 19. Smolikov S, Schild-Prüfert K, Colaiácovo MP (2009) A yeast two-hybrid screen for SYP-3 interactors identifies SYP-4, a component required for synaptonemal complex assembly and chiasma formation in *Caenorhabditis elegans* meiosis. *PLoS Genet* 5: e1000669.
 20. Couteau F, Zetka M (2005) HTP-1 coordinates synaptonemal complex assembly with homolog alignment during meiosis in *C. elegans*. *Genes Dev* 19: 2744-2756.
 21. Martinez-Perez E, Villeneuve AM (2005) HTP-1-dependent constraints coordinate homolog pairing and synapsis and promote chiasma formation during *C. elegans* meiosis. *Genes Dev* 19: 2727-2743.

22. McKim KS, Howell AM, Rose AM (1988) The effects of translocations on recombination frequency in *Caenorhabditis elegans*. *Genetics* 120: 987-1001.
23. Rosenbluth RE, Baillie DL (1981) The genetic analysis of a reciprocal translocation, eT1(III; V), in *Caenorhabditis elegans*. *Genetics* 99: 415-428.
24. MacQueen AJ, Phillips CM, Bhalla N, Weiser P, Villeneuve AM, et al. (2005) Chromosome sites play dual roles to establish homologous synapsis during meiosis in *C. elegans*. *Cell* 123: 1037-1050.
25. Phillips CM, Wong C, Bhalla N, Carlton PM, Weiser P, et al. (2005) HIM-8 binds to the X chromosome pairing center and mediates chromosome-specific meiotic synapsis. *Cell* 123: 1051-1063.
26. Phillips CM, Dernburg AF (2006) A Family of Zinc-Finger Proteins Is Required for Chromosome-Specific Pairing and Synapsis during Meiosis in *C. elegans*. *Dev Cell* 11: 817-829.
27. Phillips C, Meng X, Zhang L, Chretien J, Urnov F, et al. (2009) Identification of chromosome sequence motifs that mediate meiotic pairing and synapsis in *C. elegans*. *Nat Cell Biol* 11: 934 - 942.
28. Penkner A, Fridkin A, Gloggnitzer J, Baudrimont A, Machacek T, et al. (2009) Meiotic Chromosome Homology Search Involves Modifications of the Nuclear Envelope Protein Matefin/SUN-1. *Cell* 139: 920-933.
29. Sato A, Isaac B, Phillips C, Rillo R, Carlton P, et al. (2009) Cytoskeletal Forces Span the Nuclear Envelope to Coordinate Meiotic Chromosome Pairing and Synapsis. *Cell* 139: 907-919.
30. Penkner A, Tang L, Novatchkova M, Ladurner M, Fridkin A, et al. (2007) The nuclear envelope protein Matefin/SUN-1 is required for homologous pairing in *C. elegans* meiosis. *Dev Cell* 12: 873-885.
31. MacQueen A, Villeneuve A (2001) Nuclear reorganization and homologous chromosome pairing during meiotic prophase require *C. elegans* chk-2. *Genes Dev* 15: 1674-1687.
32. Jantsch V, Tang L, Pasierbek P, Penkner A, Nayak S, et al. (2007) *Caenorhabditis elegans* prom-1 is required for meiotic prophase

- progression and homologous chromosome pairing. *Mol Biol Cell* 18: 4911-4920.
33. Tang L, Machacek T, Mamnun YM, Penkner A, Gloggnitzer J, et al. (2010) Mutations in *C. elegans* him-19 show meiotic defects that worsen with age. *MBC* 21: 885-896.
 34. Smolikov S, Schild-Prüfert K, Colaiácovo MP (2008) CRA-1 uncovers a double-strand break-dependent pathway promoting the assembly of central region proteins on chromosome axes during *C. elegans* meiosis. *PLoS Genet* 4: e1000088.
 35. Hubbard EJA, Greenstein D (2005) Introduction to the germ line. *WormBook* : the online review of *C. elegans* biology: 1-4.
 36. Malone CJ, Misner L, Le Bot N, Tsai MC, Campbell JM, et al. (2003) The *C. elegans* hook protein, ZYG-12, mediates the essential attachment between the centrosome and nucleus. *Cell* 115: 825-836.
 37. MacQueen AJ, Colaiácovo MP, McDonald K, Villeneuve AM (2002) Synapsis-dependent and -independent mechanisms stabilize homolog pairing during meiotic prophase in *C. elegans*. *Genes Dev* 16: 2428-2442.
 38. Colaiácovo MP, MacQueen AJ, Martinez-Perez E, McDonald K, Adamo A, et al. (2003) Synaptonemal complex assembly in *C. elegans* is dispensable for loading strand-exchange proteins but critical for proper completion of recombination. *Dev Cell* 5: 463-474.
 39. Smolikov S, Eizinger A, Hurlburt A, Rogers E, Villeneuve AM, et al. (2007) Synapsis-defective mutants reveal a correlation between chromosome conformation and the mode of double-strand break repair during *Caenorhabditis elegans* meiosis. *Genetics* 176: 2027-2033.
 40. Couteau F, Nabeshima K, Villeneuve A, Zetka M (2004) A component of *C. elegans* meiotic chromosome axes at the interface of homolog alignment, synapsis, nuclear reorganization, and recombination. *Curr Biol* 14: 585-592.
 41. Schmitt J, Benavente R, Hodzic D, Hoog C, Stewart CL, et al. (2007) Transmembrane protein Sun2 is involved in tethering mammalian

- meiotic telomeres to the nuclear envelope. Proc Natl Acad Sci U S A 104: 7426-7431.
42. Storlazzi A, Gargano S, Ruprich-Robert G, Falque M, David M, et al. (2010) Recombination proteins mediate meiotic spatial chromosome organization and pairing. Cell 141: 94-106.
 43. Carlton PM, Farruggio AP, Dernburg AF (2006) A link between meiotic prophase progression and crossover control. PLoS Genet 2: e12.
 44. Brenner S (1974) The genetics of *Caenorhabditis elegans*. Genetics 77: 71-94.
 45. Hayashi M, Chin GM, Villeneuve AM (2007) *C. elegans* Germ Cells Switch between Distinct Modes of Double-Strand Break Repair During Meiotic Prophase Progression. PLoS Genet 3: e191.
 46. Jantsch V, Pasierbek P, Mueller MM, Schweizer D, Jantsch M, et al. (2004) Targeted gene knockout reveals a role in meiotic recombination for ZHP-3, a Zip3-related protein in *Caenorhabditis elegans*. Mol Cell Biol 24: 7998-8006.

Figure and table legends

Figure 1. Dynamics of SUN-1 aggregates.

(A) Frames from a movie showing the movement of SUN-1::GFP (green); chromatin stained with Hoechst 33342 (blue). White arrowhead highlights protrusion of chromatin. (B) Three-dimensional reconstruction of SUN-1::GFP displacement track dynamics. View from top (i), 30° z-axis rotation and 60° x-axis rotation (ii), and view from right side (iii) and left side (iv). (C) (i) Each line represents the distribution of the projected speed of all SUN-1 aggregates inside a nucleus from individual movies (yellow and orange: tracks from first movie, seven nuclei shown; light and dark blue: tracks from second movie, seven nuclei shown). (ii) Arcs show distance traveled for each SUN-1 track inside a nucleus. Yellow and orange: tracks from first movie, seven nuclei shown; light and dark blue: tracks from second movie, seven nuclei shown). Nuclei in the distal (D), central (E), and proximal (F) TZ, with projection of the cumulative movement of SUN-1::GFP (i), displacement tracks with different colors for each track (ii), distribution of speed for each track, using the same color code as for displacement tracks (iii), and number of SUN-1 aggregates as a function of time (iv). See Table 1 for number of nuclei analyzed. Scale bar: 2 μm .

Figure 2. Dynamics of fusion/splitting events of SUN-1 aggregates for all genotypes studied (15 min recording).

(A) Number of SUN-1 fusion/splitting events grouped into classes. (B) Quantification of the coalescence time (t) grouped into classes ($t < 1$ min, $1 \text{ min} \leq t < 3$ min, and $t \geq 3$ min).

Figure 3. Disruption of the SUN/KASH bridge abrogates SUN-1 aggregate movement.

Restrained movement in SUN-1(G311V)::GFP (A), displacement tracks (B), distribution of the projected speed of all SUN-1 aggregates inside a nucleus (C), and arcs representing the traveled distance for each track inside a nucleus (D). Blue lines represent values from the first movie, orange lines

from the second. Eight out of the eight nuclei analyzed are shown. See Table 1 for number of nuclei analyzed. Scale bar: 2 μ m.

Figure 4. Impact of SC components on the dynamics of SUN-1 aggregates.

him-3(gk149) (A), *htp-1(gk174)* (B), *syp-2(ok307)* (C), and *syp-3(me42)* (D), with projection of cumulative movement (i), displacement tracks (ii), and distribution of the projected speed (iii). Arcs represent traveled distance (iv). Blue lines represent values from the first movie, orange lines from the second. (C) *syp-2(ok307)* (i), (ii), (iii), and (iv) from the distal part of the extended TZ and i', ii', iii', and iv' from the proximal part. See Table 1 for number of nuclei analyzed. Scale bar: 2 μ m.

Figure 5. Restrained movement of SUN-1 aggregates in *htp-1(gk174)* is due to precocious synapsis.

Projection of the cumulative movement of SUN-1::GFP in *htp-1(gk174); syp-1(RNAi)* (A, A'), displacement tracks (B, B'), distribution of the projected speed (C, C'), and arcs (D, D'). Blue lines represent values from the first movie; orange lines values from the second. (A, B, C, D) from distal TZ, (A', B', C', D') from proximal zone where SUN-1 aggregates move. See Table 1 for number of nuclei analyzed. Scale bar: 2 μ m.

Figure 6. Influence of meiotic regulators on dynamics of SUN-1 aggregates.

prom-1(ok1140) (A), *him-19(jf6)* (B), irradiated wild type (C), and *cra-1(tm2144)* (D), showing projection of the cumulative movement of SUN-1::GFP aggregates (i), displacement tracks (ii), distribution of the projected speed (iii), and arcs representing travelled distances (iv). Blue lines represent values from the first movie, orange lines from the second. See Table 1 for number of nuclei analyzed. Scale bar: 2 μ m.

Figure 7. Effect of DSB formation on SUN-1 aggregate dynamics.

spo-11(me44) (A), 2-d-old *spo-11(me44)* (B) 2 hours after irradiation with projection of cumulative movement (i), displacement tracks (ii), and distribution of the projected speed (iii). Arcs represent traveled distance (iv). Blue lines represent values from the first movie, orange lines from the second. See Table 1 for number of nuclei analyzed. (C) Distribution of SUN-1 foci and patches formed in wild type, *spo-11(me44)*, 2-d-old wild type 2 hours after irradiation and 2-d-old *spo-11(me44)* 2 hours after irradiation. >400 SUN-1 aggregates counted per genotype. Scale bar: 2 μ m.

Figure 8. Establishment of synapsis and formation of high speed via shuffling of chromosome ends through SUN-1 patches.

Chromosome axes (green lines) support binding of PC proteins (red or violet shapes) that connect chromosome ends (red, blue, and violet loops) to SUN-1 (brown ellipses), directly or indirectly, (unknown factor, blue circle). ZYG-12 (pink ellipses) and SUN-1 bridge chromosomes to cytoplasmic forces (orange arrow) to move chromosome ends. (A) SUN-1 patch containing two nonhomologous chromosome ends (red and blue loops) fuses with SUN-1 focus carrying a single chromosome end, a homolog (red loops). After fusion, chromosome ends will be shuffled inside the newly formed SUN-1 patch. When the homologous chromosome is found, synapsis overcomes the cytoplasmic forces and synapsis can be established. (B) The same scenario is depicted, except that ends of nonhomologous chromosomes are in the SUN-1 aggregate (violet loops). After fusion, chromosome ends will be shuffled. However, as the cytoplasmic forces overcome the attempt to synapse, one SUN-1 focus will be driven out of the patch. This tension-generated splitting event is one of the factors leading to the formation of high speed in the distribution of SUN-1 aggregates. Our data support other factors as sources for the high speed aggregates: recombination intermediates (C) and chromosomes entanglements (D).

Table 1. Numbers of aggregates in the region proximal to the mitotic zone for the different genotypes.

number of aggregates	SUN-1::GFP			SUN-1(G311V)::GFP	
	entire TZ	distal part of TZ	central part of TZ	proximal part of TZ	
average	3.9±1.4	3.5±1.1	4.6±1.1	3.9±1.6	7.8±2.3
minimum	2.4±1.1	2.1±0.7	2.3±1.6	2.1±0.9	7.8±2.3
maximum	6.1±2.8	5.7±2.0	7.5±2.5	5.4±3.0	7.8±2.3
n	27	10	4	9	8

number of aggregates	<i>him-3(gk149); SUN-1::GFP</i>	<i>htp-1(gk174); SUN-1::GFP</i>	<i>syp-2(ok307); SUN-1::GFP</i>		<i>syp-3(me42); SUN-1::GFP</i>
			distal part	proximal part	entire TZ
average	1.1±0.3	3.1±08	2.8±1.0	3.3±0.9	3.0±0.9
minimum	1.1±0.3	2.6±1.0	1.7±1	2.0±1.0	1.7±0.6
maximum	1.1±0.3	3.9±1.0	3.5±1.1	4.2±1.2	4.3±1.4
n	82	14	30	45	14

	<i>htp-1(gk149); syp-1(RNAi);</i> SUN-1::GFP		<i>spo-11(me44);</i> SUN-1::GFP	<i>spo-11(me44); SUN-1:</i> :GFP irradiated	
number of aggregates	distal part of TZ	proximal part of TZ	entire TZ	entire TZ	
average	3.5±0.6	2.8±0.6	3.0±0.6	3.6±0.6	
minimum	2.4±0.8	2.2±0.6	1.9±0.6	2.3±0.6	
maximum	4.5±0.9	3.3±0.8	4.1±0.9	4.7±0.9	
n	23	24	18	23	

	<i>prom-1(ok1140);</i> SUN-1::GFP	<i>him-19(jf6);</i> SUN-1::GFP	<i>him-19(jf6); SUN-</i> 1::GFP irradiated	SUN-1::GFP irradiated	<i>cra-1(tm2144);</i> SUN-1::GFP	
number of aggregates	dispersed nuclei	dispersed nuclei	entire TZ	entire TZ	entire TZ	
average	3.4±0.9	2.8±0.8	3.9±1.5	3.7±0.9	3.7±0.7	
minimum	2.7±0.9	1.9±0.6	3.2±1.7	2.8±1.0	2.3±0.8	
maximum	3.8±1.1	4.0±1.3	4.7±1.5	4.6±1.1	5.4±1.0	
n	37	8	34	24	22	

Table 1. The variations indicated correspond to the standard deviation. It should be noted that the number of nuclei analyzed for SUN-1::GFP in the distal, central, and proximal parts of the TZ do not add up to the number of nuclei for the entire TZ, because nuclei that were localized in the middle of these zones (distal and central or central and proximal) were not assigned to any specific part.

n, number of nuclei.

Text S1.**Effect of phosphorylation state of SUN-1(S12) on SUN-1 aggregate dynamics**

Recently, we showed that the nuclear N terminus of SUN-1 is subjected to multiple phosphorylations at the onset of leptotene/zygotene, when chromosome movement is observed. Phospho-mimicking substitutions of the phosphorylation sites revealed that they are involved in the regulation of aggregate dissolution and meiotic progression [1]. We subjected a transgenic line bearing the mutated phospho-target site S12E to time-lapse analysis.

In the gonads of hermaphrodite worms solely expressing SUN-1(S12E)::GFP, which mimics constitutive phosphorylation of S12, the zone of nuclei displaying a clustered conformation of chromatin was extended compared to wild type [1]. The aggregates covered a surface area resembling the crescent shape of the chromatin (Figure S7A, S7B, S7A', and S7B'). Because the clustering of the chromatin was prolonged in this line, we compared nuclei in the distal part (first half of the TZ, Video S18) to nuclei in the proximal part of the TZ (second half of the TZ, Video S19).

In the distal part of the TZ, we detected wild-type characteristics with respect to the number of aggregates (Figure S8A; Mann-Whitney test, $p > 0.05$), displacement tracks (Figure S7A and S7B), distances traveled (Figure S7D; Mann-Whitney test, $p > 0.05$), number of fusion/splitting events, and coalescence time (Figure S8B, S8C, S8D, S8E). In contrast, the distribution of the projected speed of SUN-1(S12E)::GFP was significantly reduced compared to the wild type (Figure S7C; Mann-Whitney test $p < 0.05$): the distribution between 40 and 160 nm/s was shifted towards the lower values and the ability of SUN-1(S12E)::GFP aggregates to reach a high projected speed (>160 nm/s) was reduced (4% long tails versus 10% long tails in the wild type). In contrast, in the proximal part of the prolonged TZ, SUN-1(S12E)::GFP aggregates showed a significant increase, both in their projected speed (16% long tails, Figure S7C'; Mann-Whitney test, $p < 0.05$) and the distance traveled, which reached values of 180° (Figure S7D'; Mann-

Whitney test, $p < 0.05$). The average number of aggregates increased (Mann-Whitney test, $p < 0.05$). The number (Figure S8B and S8D) and periodicity (Figure S8C and S8E) of the fusion/splitting events remained in the wild-type range.

Phosphorylation of SUN-1 therefore affected the speed distribution and the distance traveled by the SUN1 aggregates. Pairing was effective, but DSBs repair was impaired in the SUN-1(S12E) mutant worms (Penkner et al., 2009). In other words, in the proximal part of the TZ, SUN-1 aggregates most likely represented paired homologues, which appeared to travel faster (16% long tails) than homologues in the process of pairing (distal part of the TZ; 4% long tails).

SUN-1 patches tend to move faster than foci.

SUN-1 aggregates are classified into foci and patches, and patches most likely represent many chromosome ends simultaneously assessing homology [1]. We followed the movement of SUN-1::GFP aggregates while keeping track of their size (Figure S9). This allowed us to address the question of whether the size of the aggregates has an influence on their instantaneous projected speed. A focus had a defined size of up to $2.15 \mu\text{m}^2$ and patches a size $>2.15 \mu\text{m}^2$. We calculated the projected speed of foci and patches. No correlation between the size of the aggregates and their instantaneous projected speed was found (correlation factor for foci: -0.017 and for patches: -0.0169). The size of SUN-1 foci or patches, thus, had no influence on their respective speed.

However, there was a difference between foci and patches in their projected speed distribution. Both classes of aggregates were able to reach projected speeds higher than 160 nm/s (3% for the foci and 4% for the patches; Figure S9B), but their distribution was different (Mann-Whitney test, $p < 0.05$). Indeed, the cumulative distribution function (CDF) of the foci and the patches showed that foci tended to move more slowly than patches. From 16 to 120 nm/s , the CDF of the foci began to increase significantly compared to the CDF of SUN-1 patches (blue curve, Figure S9B). We conclude that

although there was no direct link between the size of the aggregates and their projected speed, SUN-1 patches tended to move faster than SUN-1 foci.

1. Penkner A, Fridkin A, Gloggnitzer J, Baudrimont A, Machacek T, et al. (2009) Meiotic Chromosome Homology Search Involves Modifications of the Nuclear Envelope Protein Matefin/SUN-1. *Cell* 139: 920-933.

Text S2. Supplemental methods.

Cytological preparation of gonads and immunostaining

Hermaphrodite gonads were dissected and fixed as described in [2] for SUN-1 and ZIM-3 staining. Gonads were blocked in 1× PBS 3% BSA for 20 min after being fixed for one min in methanol (−20°C) and washed three times in 1× PBS 0.01% Tween-20. Antibodies were diluted in 1× PBS 0.01% sodium azide as follows: anti-GFP (catalog number 11814460001, Roche Diagnostics,), 1:300 and anti-ZIM-3 [1], 1:100.

For SYP-1 staining, gonads were fixed as described in [3]. After dissection of gonads, samples were frozen in liquid nitrogen and then fixed for five min in methanol (−20°C). Twenty microliters of 3.7% formaldehyde was applied, and the samples were left at room temperature for 20 min. After washing three times in 1× PBS 0.01% Tween-20, antibodies raised against SYP-1 were applied at a dilution of 1:200 in 1× PBS 0.01% sodium azide.

1. Penkner A, Fridkin A, Gloggnitzer J, Baudrimont A, Machacek T, et al. (2009) Meiotic Chromosome Homology Search Involves Modifications of the Nuclear Envelope Protein Matefin/SUN-1. *Cell* 139: 920-933.
2. Martinez-Perez E, Villeneuve AM (2005) HTP-1-dependent constraints coordinate homolog pairing and synapsis and promote chiasma formation during *C. elegans* meiosis. *Genes Dev* 19: 2727-2743.
3. MacQueen AJ, Colaiacovo MP, McDonald K, Villeneuve AM (2002) Synapsis-dependent and -independent mechanisms stabilize homolog pairing during meiotic prophase in *C. elegans*. *Genes Dev* 16: 2428-2442.

Fluorescence in situ hybridization

5S ribosomal DNA (rDNA) was used as a probe for the right arm of chromosome V. 5S rDNA was labeled by PCR with digoxigenin-11-dUTP [4]. Digoxigenin-labeled probes were detected with FITC-conjugated anti-digoxigenin antibodies (1:100).

4. Pasierbek P, Jantsch M, Melcher M, Schleiffer A, Schweizer D, et al. (2001) A *Caenorhabditis elegans* cohesion protein with functions in meiotic chromosome pairing and disjunction. *Genes Dev* 15: 1349-1360.

Microscopy and evaluation

Evaluation of cytological phenotypes on fixed samples was performed on worms kept at 20°C for 18–24 h after preselecting them at the L4 stage. A Zeiss Axioskop epifluorescence microscope was used in combination with a cooled CCD camera (Photometrics) to take 3D stacks of images (MetaVue software; Universal Imaging, Downingtown, PA, USA). Stack pictures were deconvolved (AutoDeblur software; AutoQuant Imaging, Troy, NY, USA) and then projected (Helicon Focus software; <http://helicon.com.ua/heliconfocus/>). Artificial coloring and merging were done with Adobe Photoshop CS3 (Adobe Systems).

Supplemental figure and table legends

Figure S1. Background movement during time-lapse microscopy and definition of Maxwellian-shaped distribution.

(A) Worms were killed in sodium azide and analyzed. Each line corresponds to the distribution of the projected speed of SUN-1::GFP aggregates in wild-type (blue), *him-3(gk149)* (yellow), and *htp-1(gk174)* (red) backgrounds. The corresponding cumulative projections of moving SUN-1::GFP aggregates are shown. (B) Left, a normal distribution, which is symmetric around the mean value. Right, a Maxwellian distribution with tails in the distribution (in red).

Figure S2. Lack of patterns for the traveled distance of SUN-1::GFP aggregates in nuclei located at different positions in the TZ.

Box plot of the arc values for subregions in TZ (distal, central, and proximal parts of TZ). Red box plot, first movie; blue box plot, second movie. Green line represents the median value in the distribution of the arc; extremities of the whiskers are minima and maxima; bottom of the box, first quartile; top of the box, last quartile of the distribution of the arcs.

Figure S3. Arc computation.

Distances a and b were calculated from the most extreme positions of the tracks (orange in A [SUN-1::GFP], red in A' [SUN-1(G311V)::GFP]). Distance c was calculated using the Pythagoras theorem (B, B'). c was circumscribed on a circle with the radius of the average size of a nucleus. Angle β (pink) was calculated using the cosine law (C, C'). When distance c was greater than radius r (D), the value of r was increased so that c could be circumscribed and the line for this arc is shown as a dotted line (e.g., Figure 4D). Description of the tracks by expressing the sum of their total length is misleading, because this does not reflect how far the tracks reach. For example, small oscillations, as in SUN-1(G311V), add up to large distances traveled, although the aggregates have not moved far. Arcs have the advantage of allowing for comparisons between different genotypes (compare C and C').

Figure S4. Lateral elements are required for proper loading of PC proteins.

Localization of the PC protein ZIM-3 in *him-3(gk149)* and *htp-1(gk174)*. Immunostaining of ZIM-3 (red) and SUN-1::GFP (green); DAPI (blue).

Figure S5. SUN-1 aggregates are present in nuclei with loose clustering of the chromatin.

Immunostaining of SUN-1 in wild type, *htp-1(gk174)*, *syp-1(RNAi)* and *cra-1(tm2144)*. White arrows indicate nuclei with loose clustering of the chromatin.

Figure S6. An excess of DSBs affected pairing but not SC polymerization.

Dissected gonads of aged irradiated and nonirradiated worms were divided into seven zones of equal length (A), and the pairing of homologues was assessed by FISH with a probe for 5S rDNA (on chromosome V). (B) Pairing in nonirradiated 3-d-old wild-type gonads (dark blue) and three-day-old wild-type gonads 24 h after irradiation (light blue). The histogram shows at least two gonads with or without irradiation. Asterisks highlight the differences that are significant (Fisher's exact test, $p < 0.05$). (C) SYP-1 polymerization in wild-type worms without irradiation (upper part) and γ -irradiated wild-type worms 2 h after irradiation (lower part).

Figure S7. Effect of SUN-1 phosphorylation on aggregate dynamics.

Projection of the cumulative movement of SUN-1(S12E)::GFP (A, A'), displacement tracks (B, B'), distribution of the projected speed (C, C'), and arcs (D, D'). Blue lines represent values from the first movie; orange lines values from the second. (A, B, C, D) from distal TZ, (A', B', C', D') from proximal TZ. See Table 1 for number of nuclei analyzed. Scale bar: 2 μ m.

Figure S8. Dynamics of SUN-1(S12E)::GFP aggregates.

A. Numbers of aggregates in the region proximal to the mitotic zone. The variations indicated correspond to the standard deviation. B. Number of SUN-1 fusion/splitting events grouped into classes. C. Quantification of the coalescence time (t) grouped into classes ($t < 1$ min, $1 \text{ min} \leq t < 3$ min, and $t \geq 3$ min). D. Fisher's exact test to assess the difference between wild type and SUN-1(S12E)::GFP for the values 'number of fusion/splitting events'. E. Fisher's exact to assess the difference between wild type and SUN-1(S12E)::GFP for the values 'time-window of SUN-1 aggregate coalescence'.

Figure S9. Correlation between speed and size of SUN-1 aggregates.

(A) A deconvolved image was converted to a binary image using a threshold and then initial segmentation restored using a watershed transform (i).

Aggregates $<2.15 \mu\text{m}^2$ were defined as foci, aggregates $>2.15 \mu\text{m}^2$ as patches. Output image (yellow) overlaid with the starting picture (i, right panel). Collection of background-subtracted movies treated in same manner (ii). Correlation factor = -0.017 for size of foci and their speed. Correlation factor = -0.016 for size of patches and their speed. No correlation was found in either case. (B) CDF of the foci (red) and patches (green). Differences in distribution of the projected speed of SUN-1 foci and patches are highlighted by the subtraction of the CDF of the foci to the CDF of the patches (blue). SUN-1 patches in the range of 15–120 nm/s moved faster than SUN-1 foci.

Supplemental movies

Video S1

Time lapse series of SUN-1::GFP with counterstaining of the chromatin using Hoechst 33342. The first inset shows the merging of SUN-1::GFP (green) and the chromatin (blue). The second inset shows the chromatin and the third inset SUN-1::GFP. Scale bar: 2 μ m.

Video S2

Time lapse series of SUN-1::GFP in the *sun-1(ok1282)* background. The three insets show three enlarged independent nuclei. Scale bar: 2 μ m.

Video S3

Time lapse series of SUN-1(G311V)::GFP in the *sun-1(ok1282)* background. The three insets show three enlarged independent nuclei. Scale bar: 2 μ m.

Video S4

Time lapse series of SUN-1::GFP in the *him-3(gk149)* background. The three insets show three enlarged independent nuclei. Scale bar: 2 μ m.

Video S5

Time lapse series of SUN-1::GFP in the *htp-1(gk174)* background. The three insets show three enlarged independent nuclei. Scale bar: 2 μ m.

Video S6

Time lapse series of SUN-1::GFP in the *syp-2(ok307)* background; distal part of the TZ. The three insets show three enlarged independent nuclei. Scale bar: 2 μ m.

Video S7

Time lapse series of SUN-1::GFP in the *syp-2(ok307)* background; proximal part of the TZ. The three insets show three enlarged independent nuclei. Scale bar: 2 μ m.

Video S8

Time lapse series of SUN-1::GFP in the *syp-3(me42)* background. The three insets show three enlarged independent nuclei. Scale bar: 2 μ m.

Video S9

Time lapse series of SUN-1::GFP in the *htp-1(gk174), syp-1(RNAi)* background in the distal part of the zone with SUN-1 aggregates. The three insets show three enlarged independent nuclei. Scale bar: 2 μ m.

Video S10

Time lapse series of SUN-1::GFP in the *htp-1(gk174), syp-1(RNAi)* background in the proximal part of the zone with SUN-1 aggregates. The three insets show three enlarged independent nuclei. Scale bar: 2 μ m.

Video S11

Time lapse series of SUN-1::GFP in the *prom-1(ok1140)* background. The three insets show three enlarged independent nuclei. Scale bar: 2 μ m.

Video S12

Time lapse series of SUN-1::GFP in the *him-19(jf6)* background; non-irradiated 2-day-old hermaphrodites. Scale bar: 2 μ m.

Video S13

Time lapse series of SUN-1::GFP in the *him-19(jf6)* background; irradiated 2-day-old hermaphrodites. The three insets show three enlarged independent nuclei. Scale bar: 2 μ m.

Video S14

Time lapse series of SUN-1::GFP in the *sun-1(ok1282)* background; irradiated 2-day-old hermaphrodites. The three insets show three enlarged independent nuclei. Scale bar: 2 μ m.

Video S15

Time lapse series of SUN-1::GFP in the *cra-1(tm2144)* background. The three insets show three enlarged independent nuclei. Scale bar: 2 μ m.

Video S16

Time lapse series of SUN-1::GFP in the *spo-11(me44)* background. The three insets show three enlarged independent nuclei. Scale bar: 2 μ m.

Video S17

Time lapse series of SUN-1::GFP in the *spo-11(me44)* background; irradiated 2-day-old hermaphrodites. The three insets show three enlarged independent nuclei. Scale bar: 2 μ m.

Video S18

Time lapse series of SUN-1(S12E)::GFP in the *sun-1(ok1282)* background in the distal part of the prolonged TZ. The three insets show three enlarged independent nuclei. Scale bar: 2 μ m.

Video S19

Time lapse series of SUN-1(S12E)::GFP in the *sun-1(ok1282)* background in the proximal part of the prolonged TZ. The three insets show three enlarged independent nuclei. Scale bar: 2 μ m.

Table S1. Fisher's exact test to assess the difference between wild type and all other genotypes tested for the values 'number of fusion/splitting events'.

Number of fusion/splitting events	SUN-1(G311V)::GFP	<i>him-3(gk149);</i> SUN-1::GFP	<i>htp-1(gk174);</i> SUN-1::GFP	<i>syp-2(ok307);</i> SUN-1::GFP	<i>syp-2(ok307);</i> SUN-1::GFP	<i>syp-3(me42);</i> SUN-1::GFP
	entire TZ	entire TZ	entire TZ	distal part	proximal part	entire TZ
0	4,249E-08	2,2E-16	0,04538	0,5023	0,1504	1
1~5	0,0815	0,0002905	0,03162	0,0002281	0,09493	0,3256
6~10	0,07339	0,0000769	0,158	0,04098	0,7998	1
11~15	0,2994	0,001248	0,06921	0,004357	0,008902	0,3898
16~20	1	0,3506	1	0,4286	0,3699	1
21~25	1	0,3506	1	0,4286	0,3699	1
26~30	1	1	1	1	1	1

Number of fusion/splitting events	<i>htp-1(gk149); syp-1(RNAi);</i> SUN-1::GFP		<i>spo-11(me44);</i> SUN-1::GFP	<i>spo-11(me44);</i> SUN-1::GFP irradiated
	distal part of TZ	proximal part of TZ	entire TZ	distal part of TZ
0	1	0.04252	1	1
1~5	0.563	0.00473	0.1563	0.1119
6~10	1	0.02153	0.1376	1
11~15	0.2609	0.02391	1	0.2284
16~20	1	1	1	0.3223

Results / Chapter 5 / SUN/KASH protein bridge / Supplemental Tables

	21~25	0.5881	1	1	1	
	26~30	1	1	1	1	
	<i>him-19(jf6); SUN-1::GFP</i>	<i>him-19(jf6); irradiated</i>	SUN-1::GFP irradiated	<i>prom-1(ok1140); SUN-1::GFP</i>	<i>cra-1(tm2144); SUN-1::GFP</i>	
Number of fusion/splitting events	entire TZ	entire TZ	entire TZ	entire TZ	entire TZ	entire TZ
0	1	0.02804	0.4130	0,0001014	1	
1~5	0.2667	0.03699	1	0,02854	0.01529	
6~10	0.7115	0.03269	0.767	0,2023	0.3575	
11~15	0.3026	0.1239	1	0,02292	0.1267	
16~20	1	0.45	1	1	0.1597	
21~25	1	0.45	1	1	0.5809	
26~30	1	1	1	1	1	

Significant p-values ($p < 0.05$) are highlighted in bold.

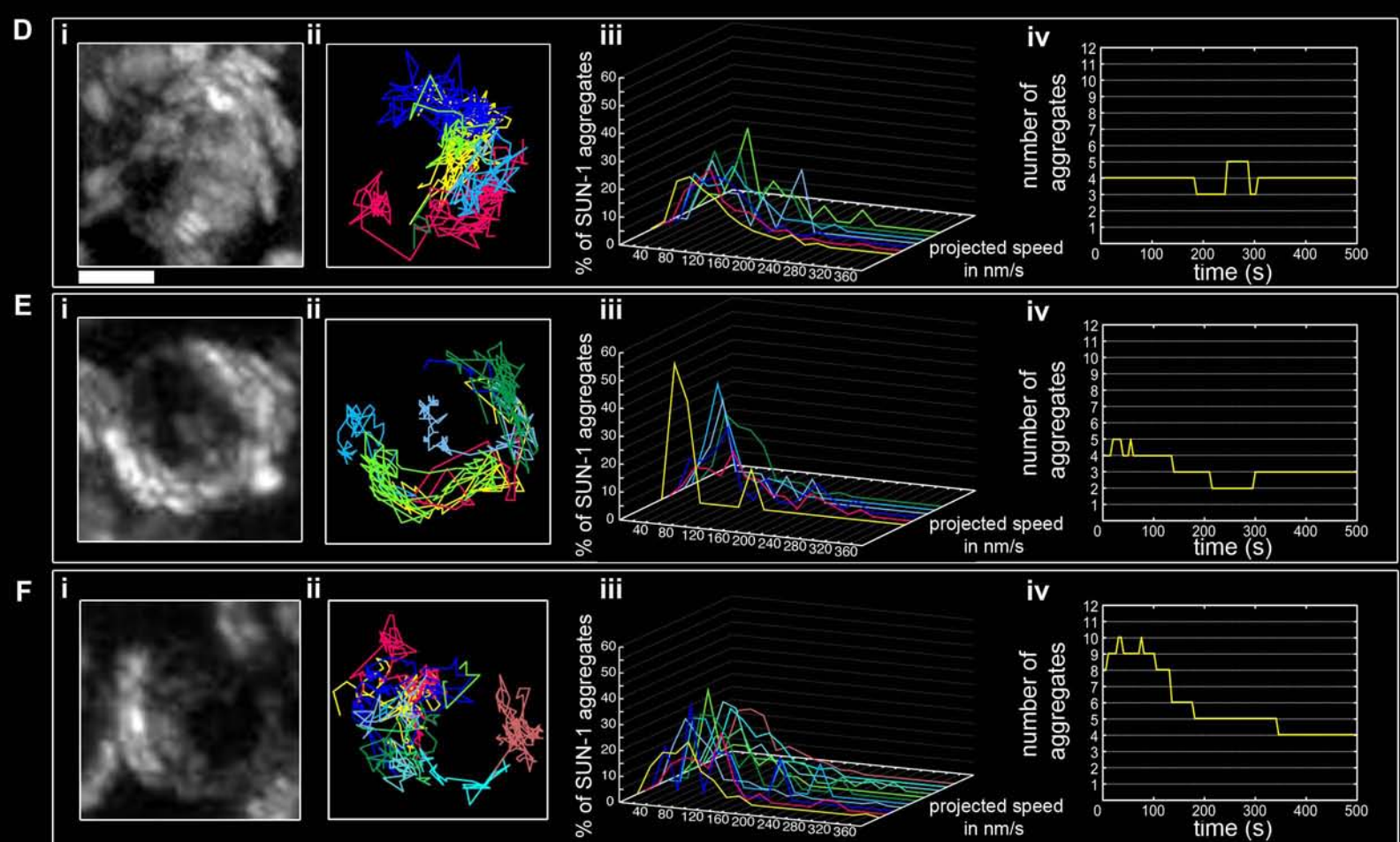
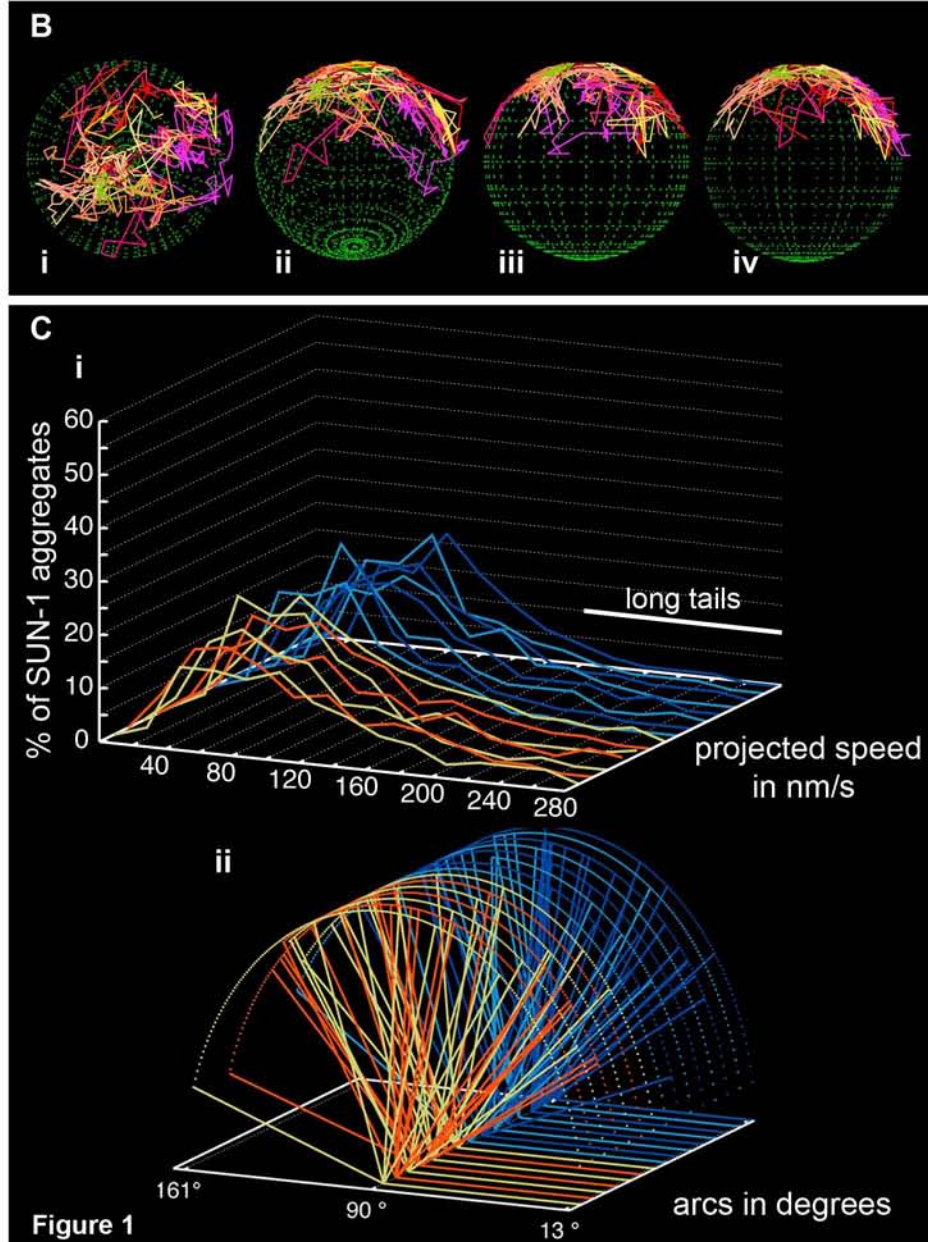
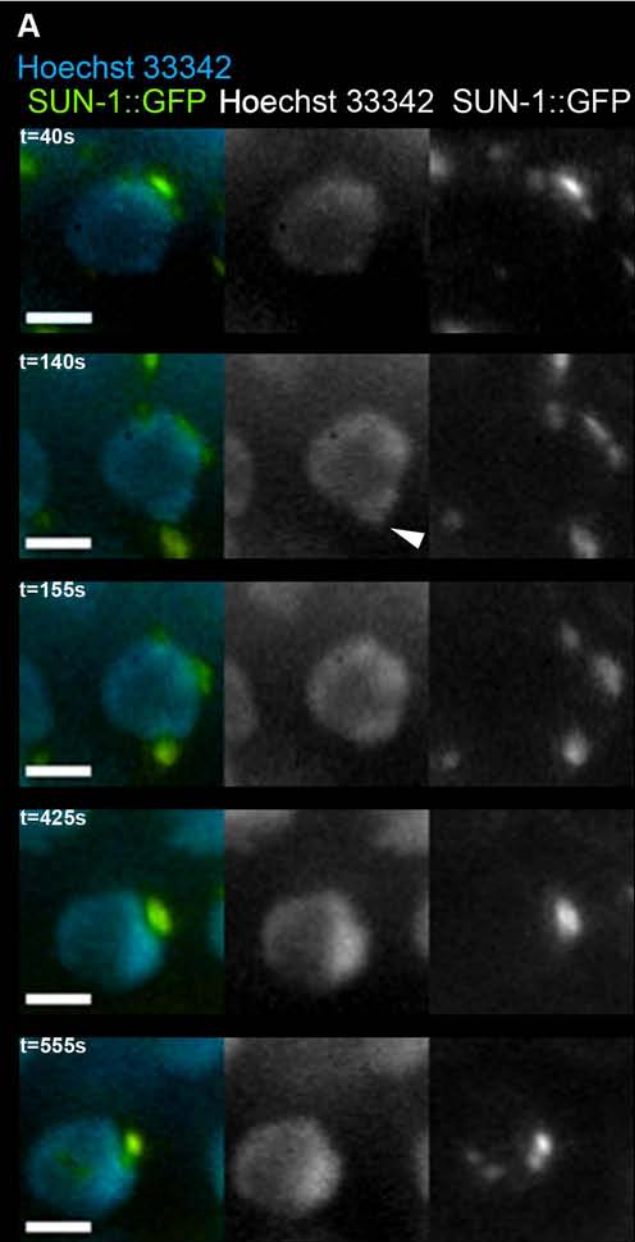
Table S2. Fisher's exact to assess the difference between wild type and all other genotypes tested for the values' time-window of SUN-1 aggregate coalescence'.

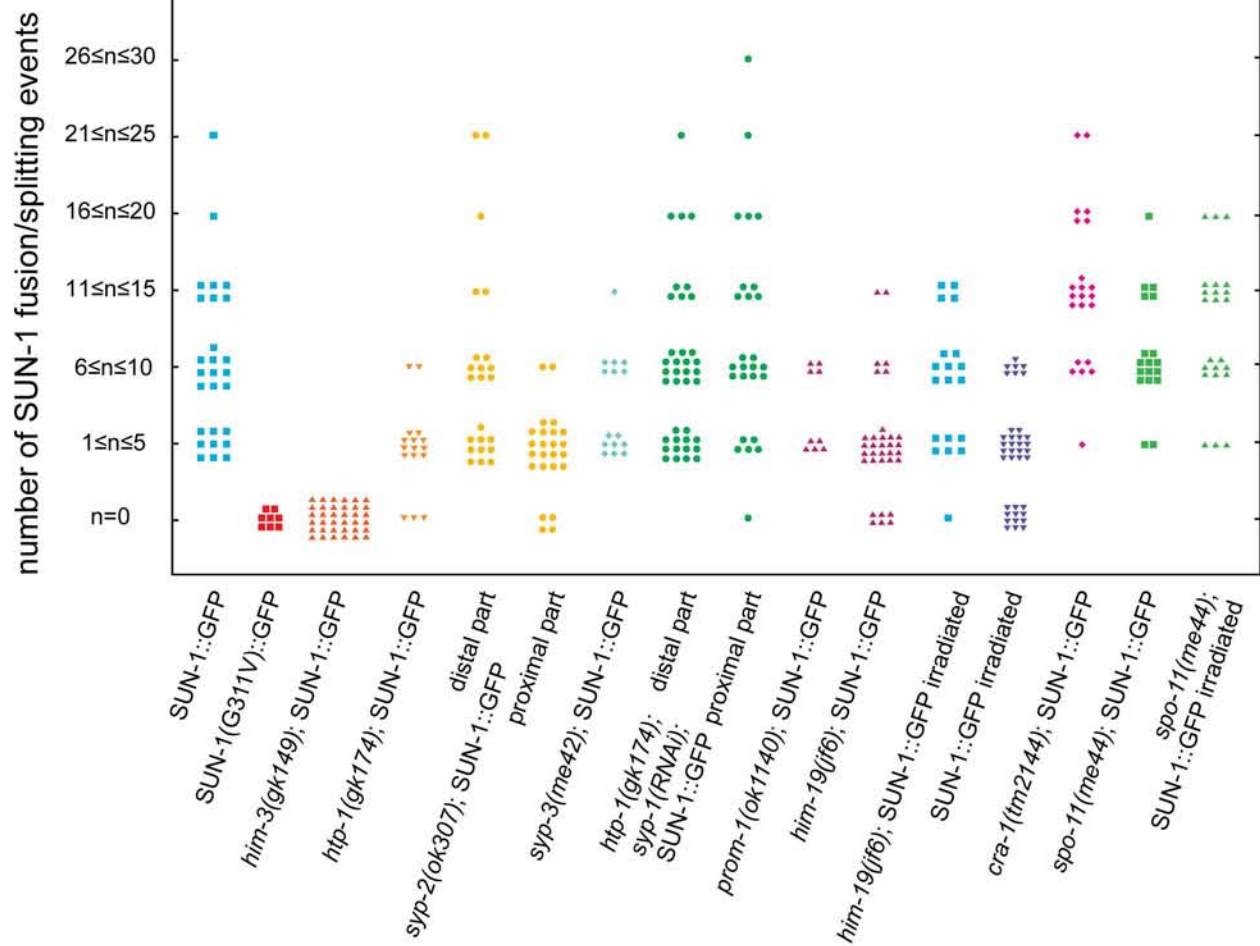
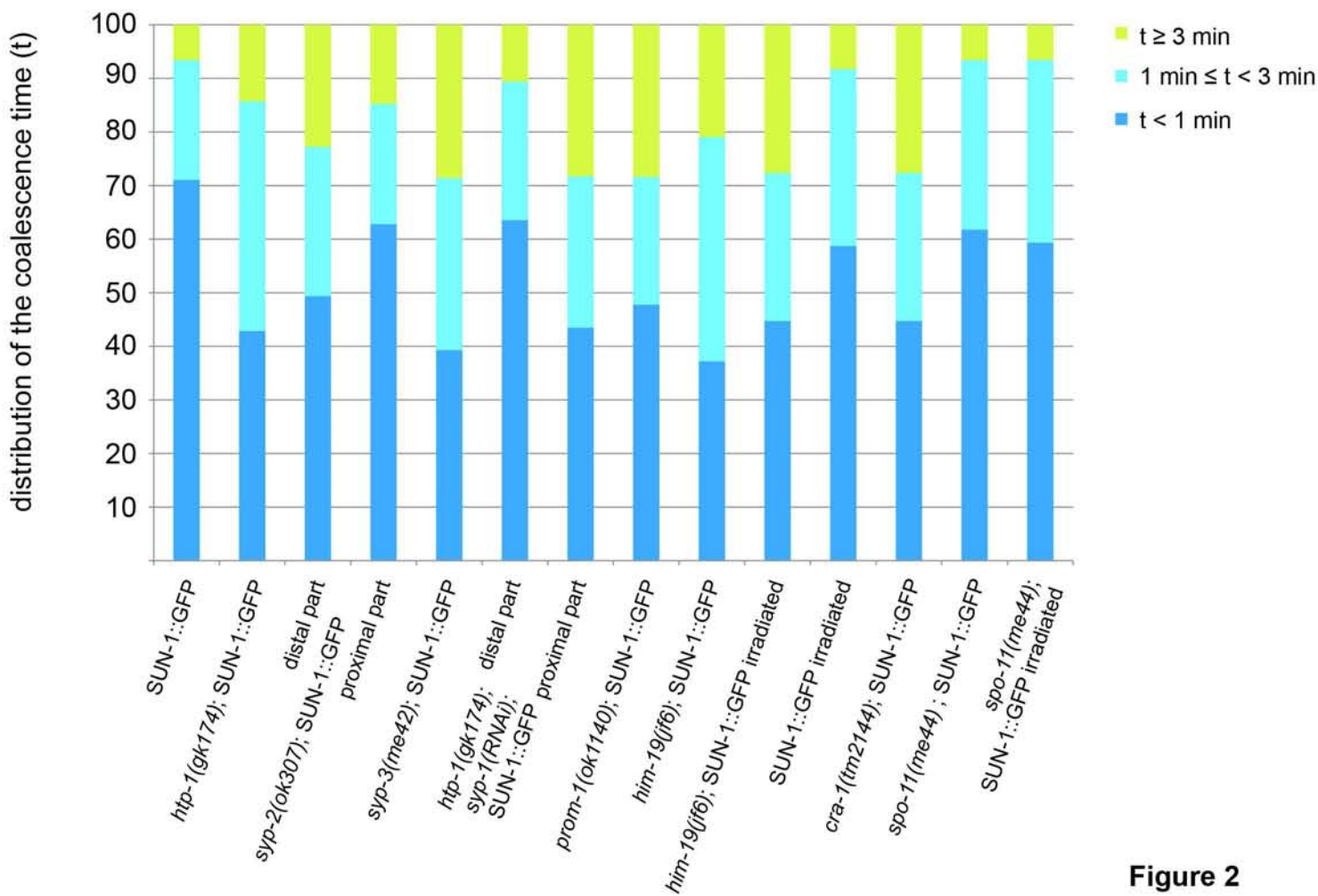
Time window without exchange (t)	<i>htp-1(gk174);</i> SUN-1::GFP	<i>syp-2(ok307);</i> SUN-1::GFP	<i>syp-2(ok307);</i> SUN-1::GFP	<i>syp-3(me42);</i> SUN-1::GFP
	entire TZ	distal part	proximal part	entire TZ
t<1 min	0.01260	4.24e-05	0.1457	2.906e-05
1 min≤t<3 min	0.1172	0.27	1	0.03373
t≥3 min	1	0.05597	0.1617	0.0002778

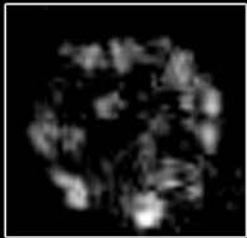
Time window without exchange (t)	<i>htp-1(gk149); syp-1(RNAi);</i> SUN-1::GFP	<i>spo-11(me44);</i> SUN-1::GFP	<i>spo-11(me44);</i> SUN-1: :GFP irradiated	
	distal part of TZ	proximal part of TZ	entire TZ	distal part of TZ
t<1 min	1	0.04252	0.09603	0.01331
1 min≤t<3 min	0.563	0.00473	0.633	0.02071
t≥3 min	1	0.02153	0.2104	0.0777

	<i>him-19(jf6); SUN-1::GFP</i>	<i>him-19(jf6); SUN- 1::GFP irradiated</i>	SUN-1::GFP irradiated	<i>prom-1(ok1140); SUN-1::GFP</i>	<i>cra-1(tm2144); SUN-1::GFP</i>
Time window without exchange (t)	entire TZ	entire TZ	entire TZ	entire TZ	entire TZ
t<1 min	6.884e-05	7.537e-05	0.04290	0.0009864	0.2205
1 min≤t<3 min	0.006124	0.394	0.000807	0.08724	0.1417
t≥3 min	0.2577	0.008372	1	5.776e-05	0.443

Significant p-values ($p < 0.05$) are highlighted in bold.



A**B****Figure 2**

A

SUN-1(G311V)::GFP

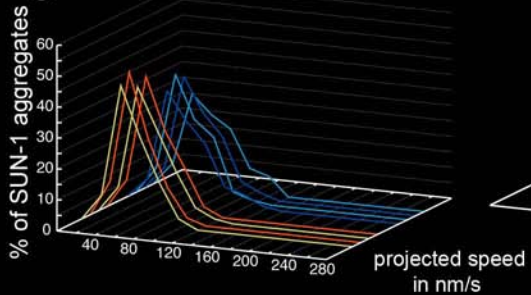
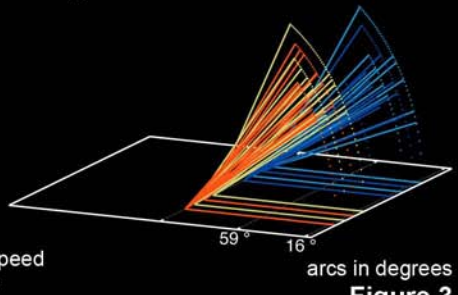
B**C****D**

Figure 3

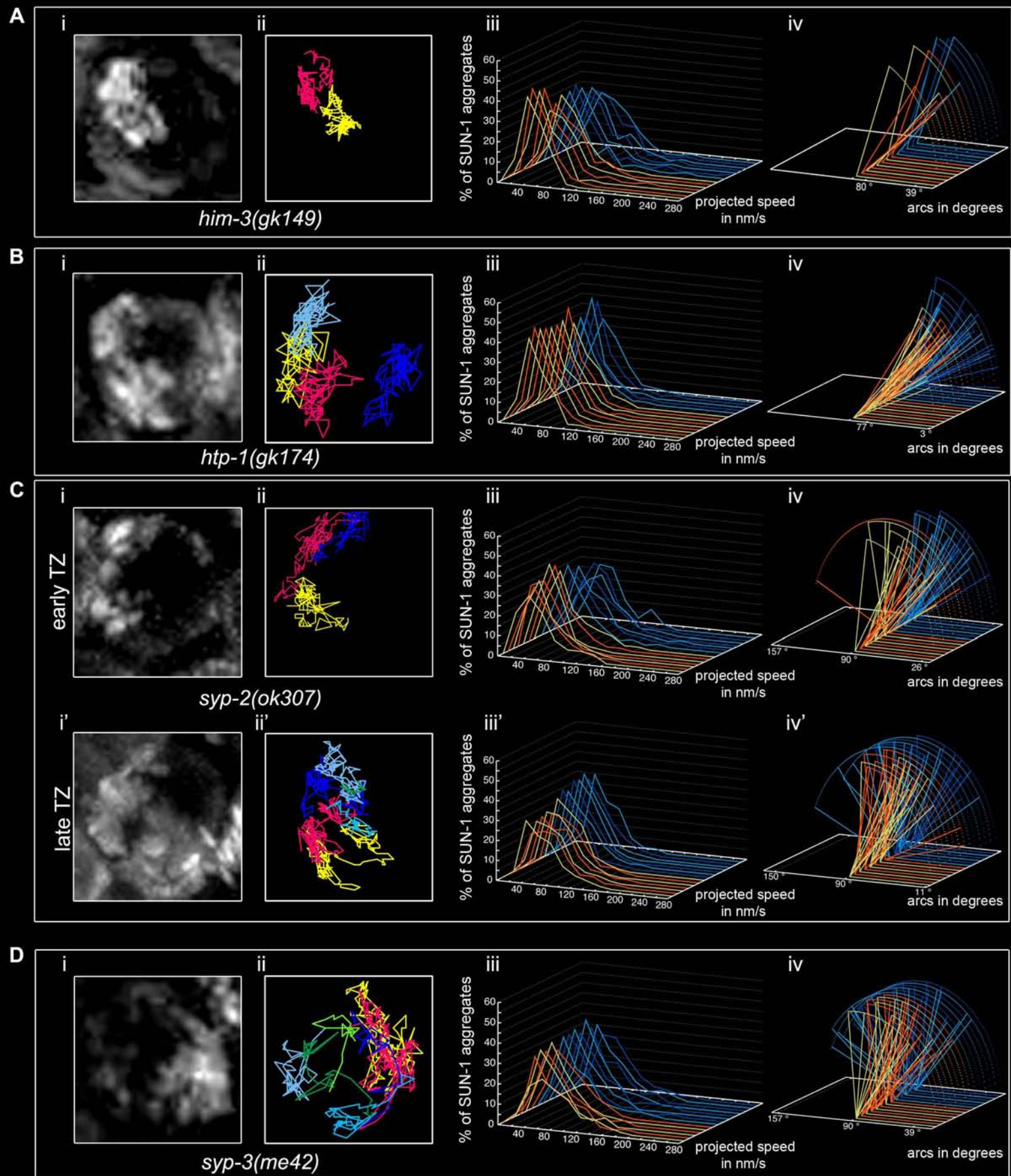


Figure 4

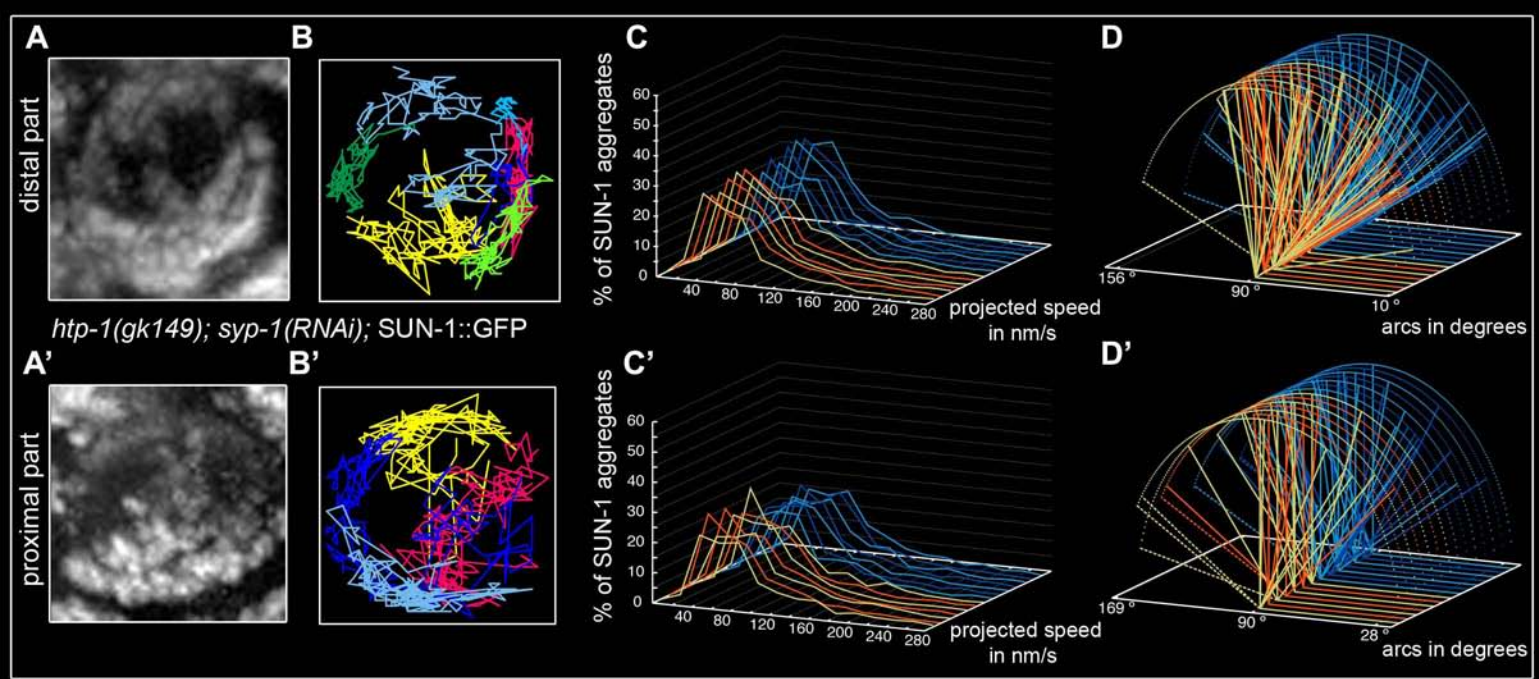


Figure 5

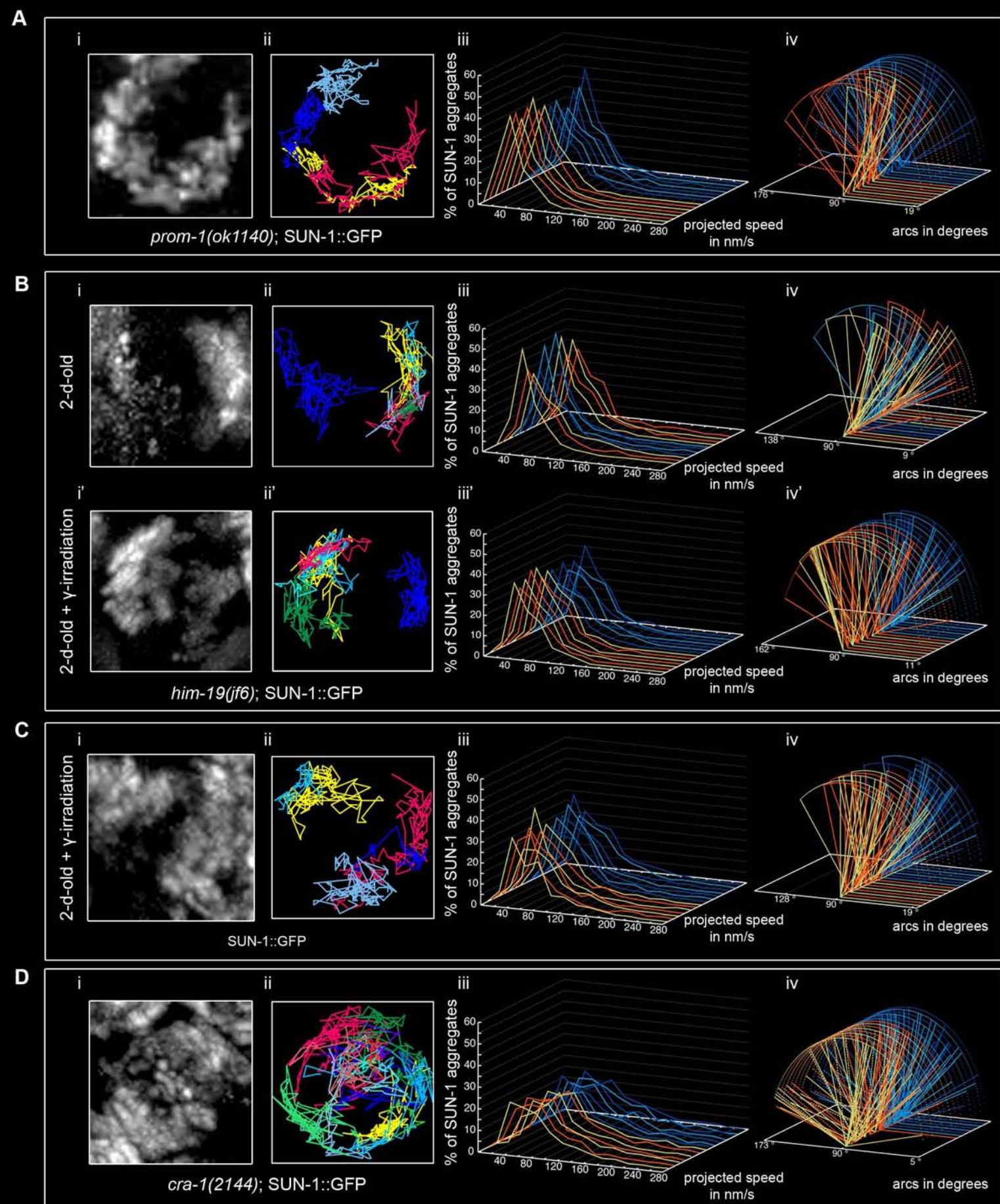


Figure 6

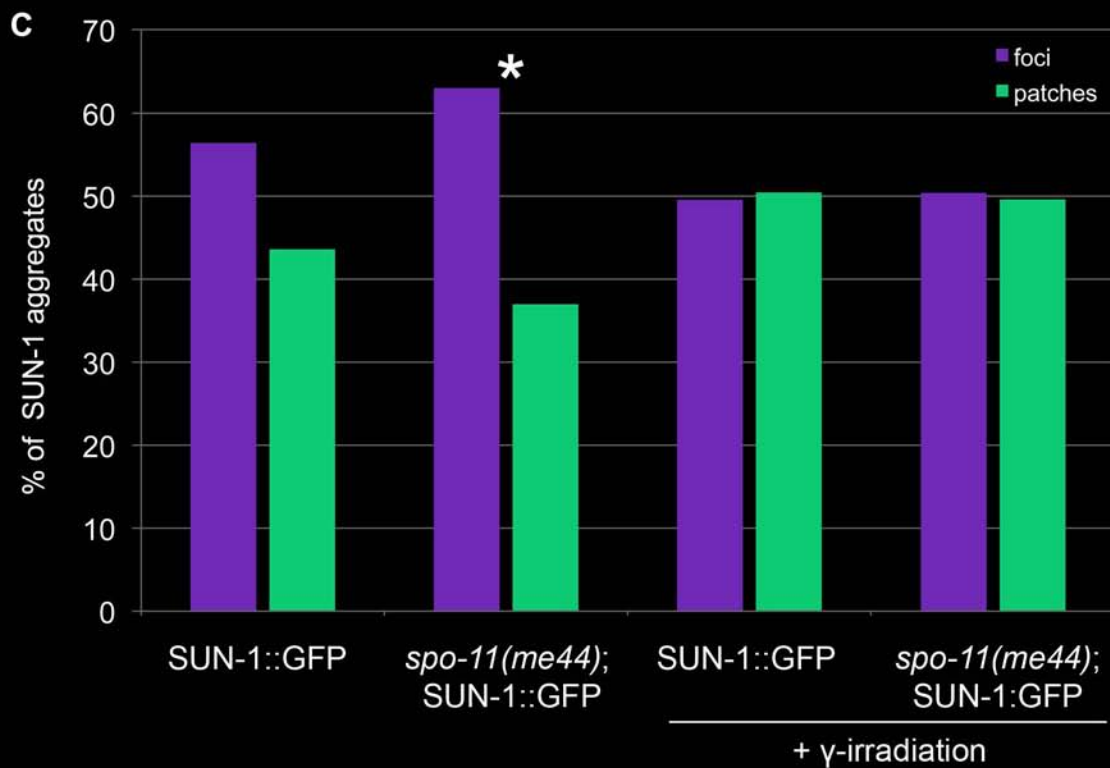
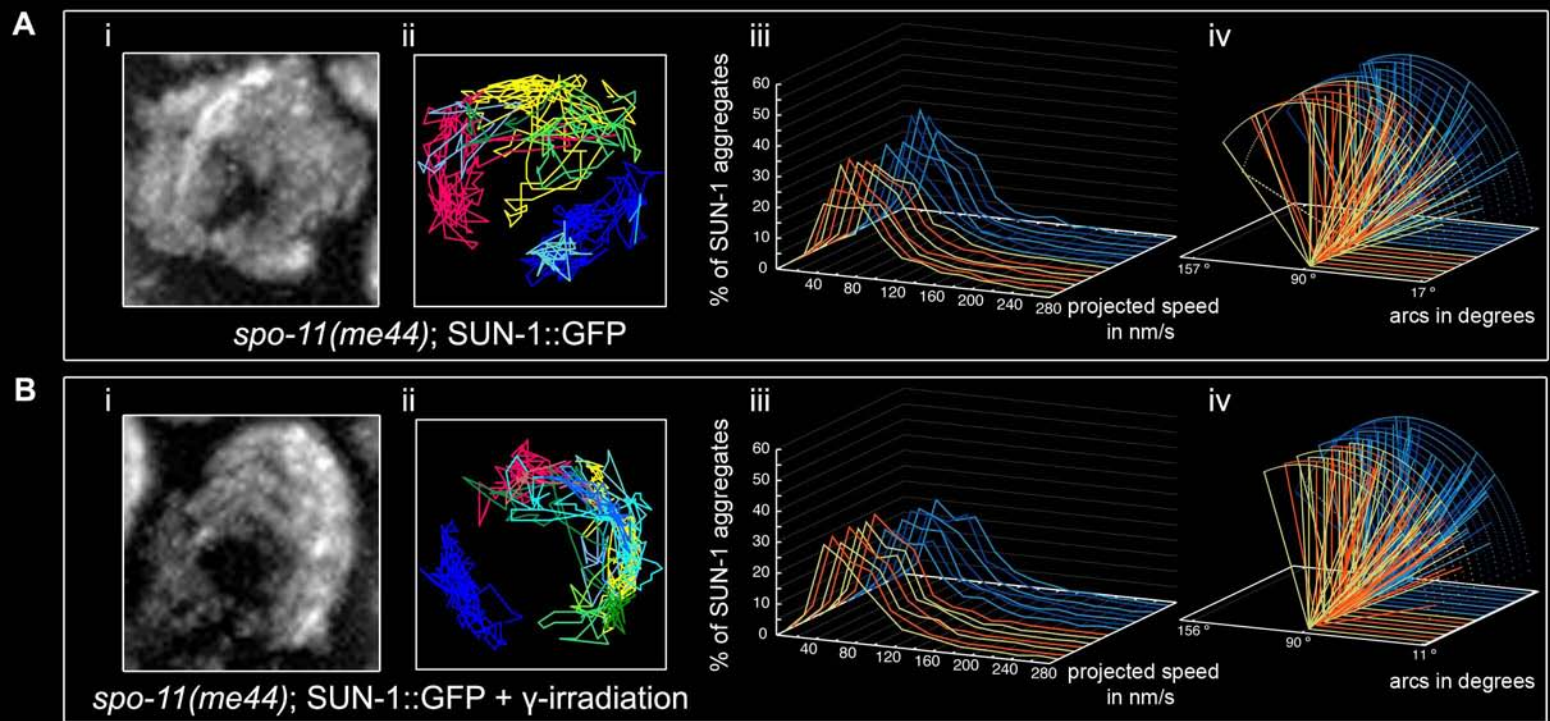


Figure 7

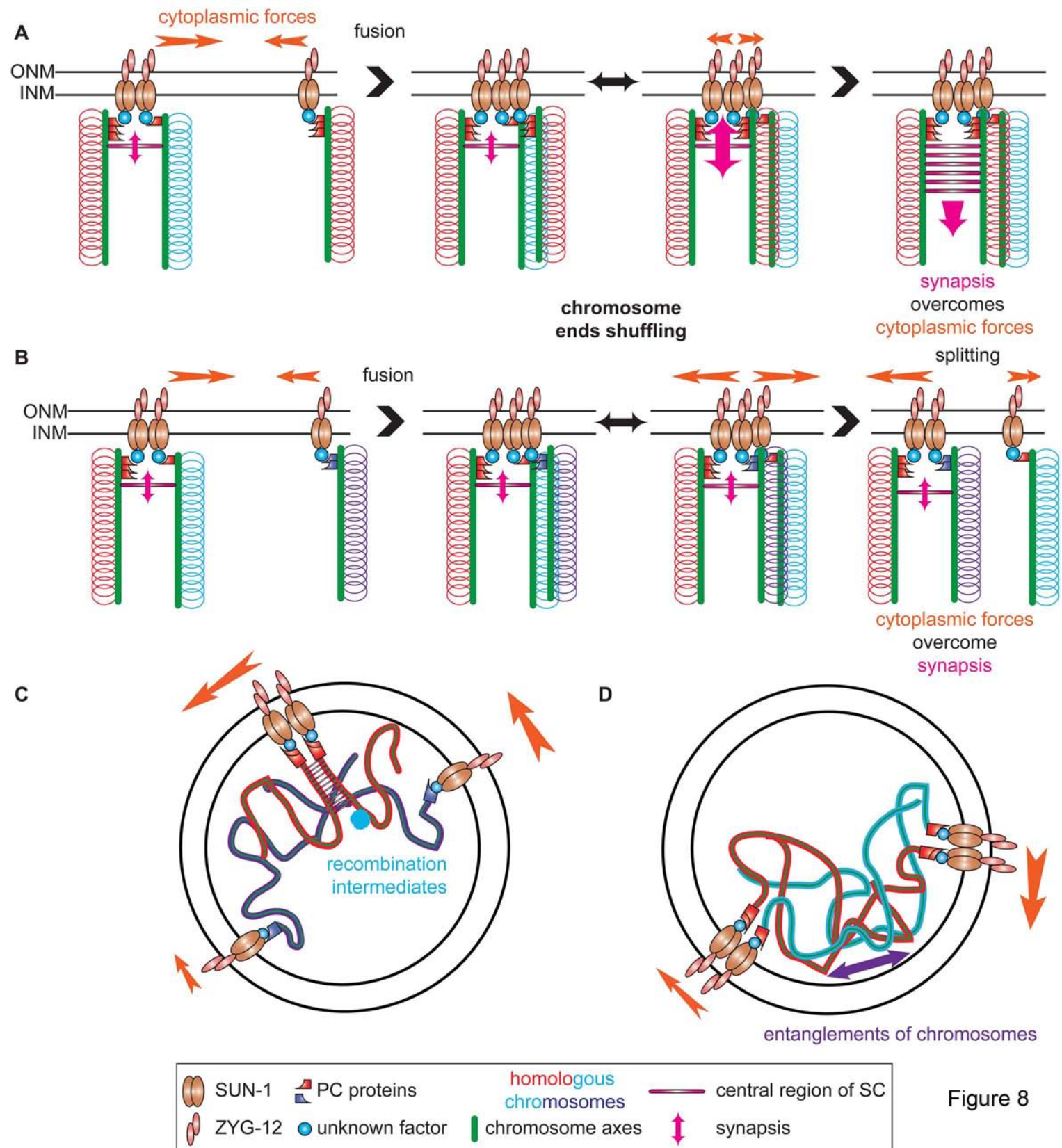


Figure 8

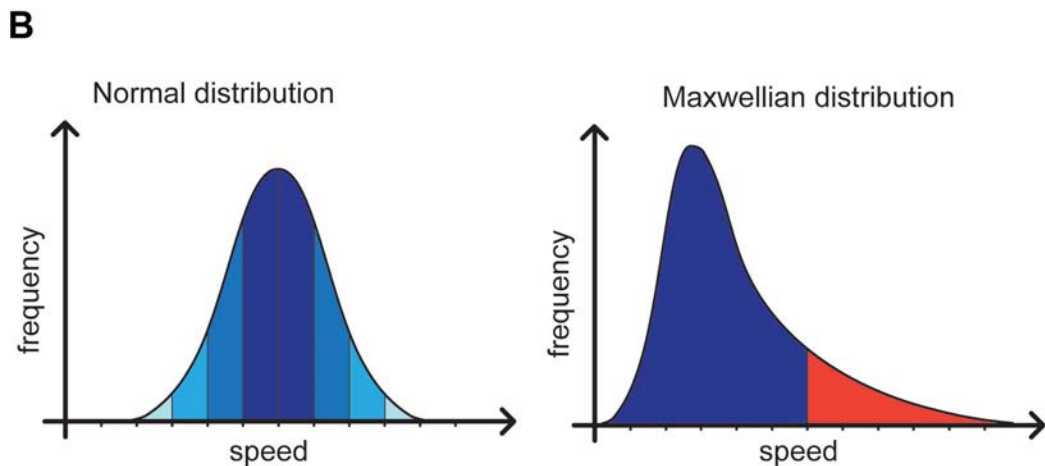
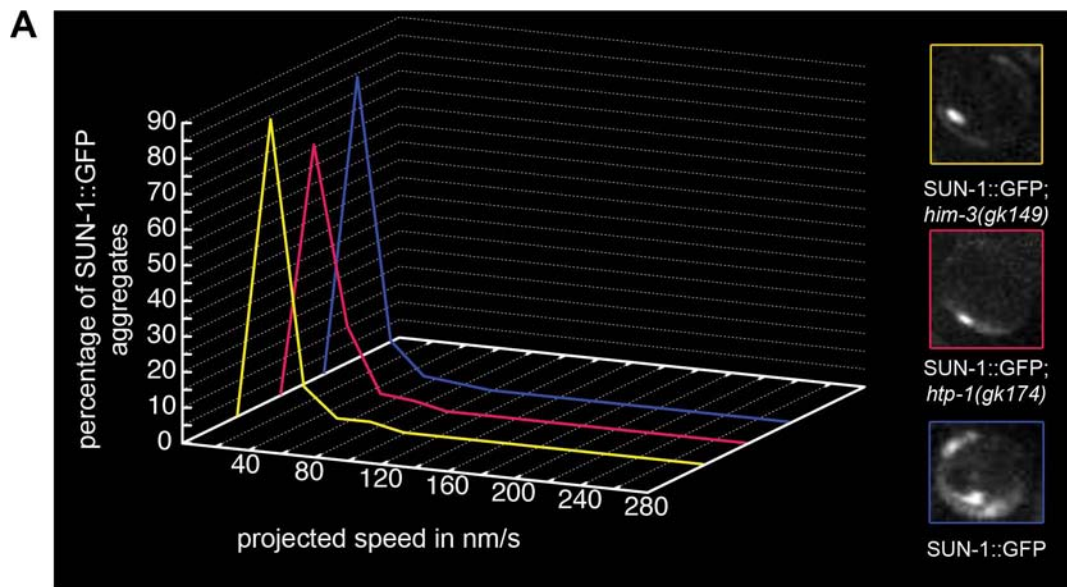
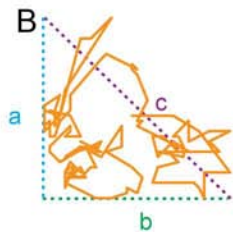
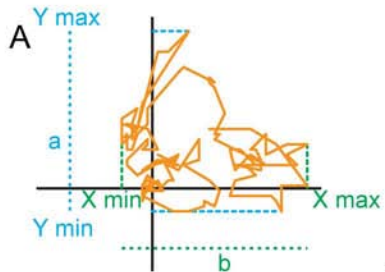


Figure S1

SUN-1::GFP

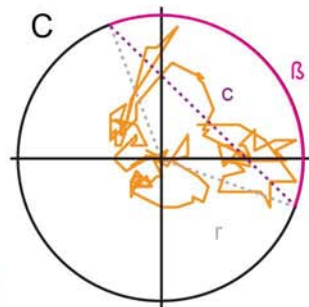


law of Pythagoras

$$c^2 = a^2 + b^2$$

law of Cosines

$$\cos(\beta) = \frac{2r^2 - c^2}{2r^2}$$



SUN-1(G311V)::GFP

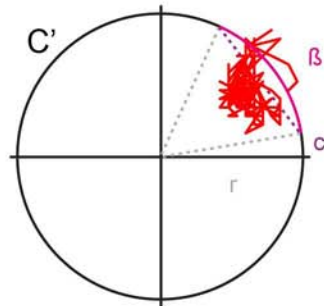
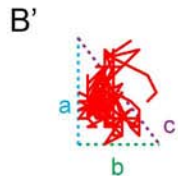
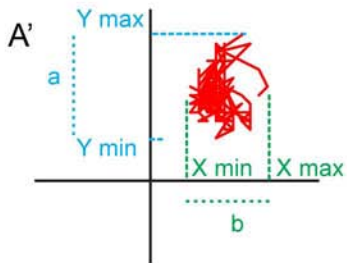


Figure S2

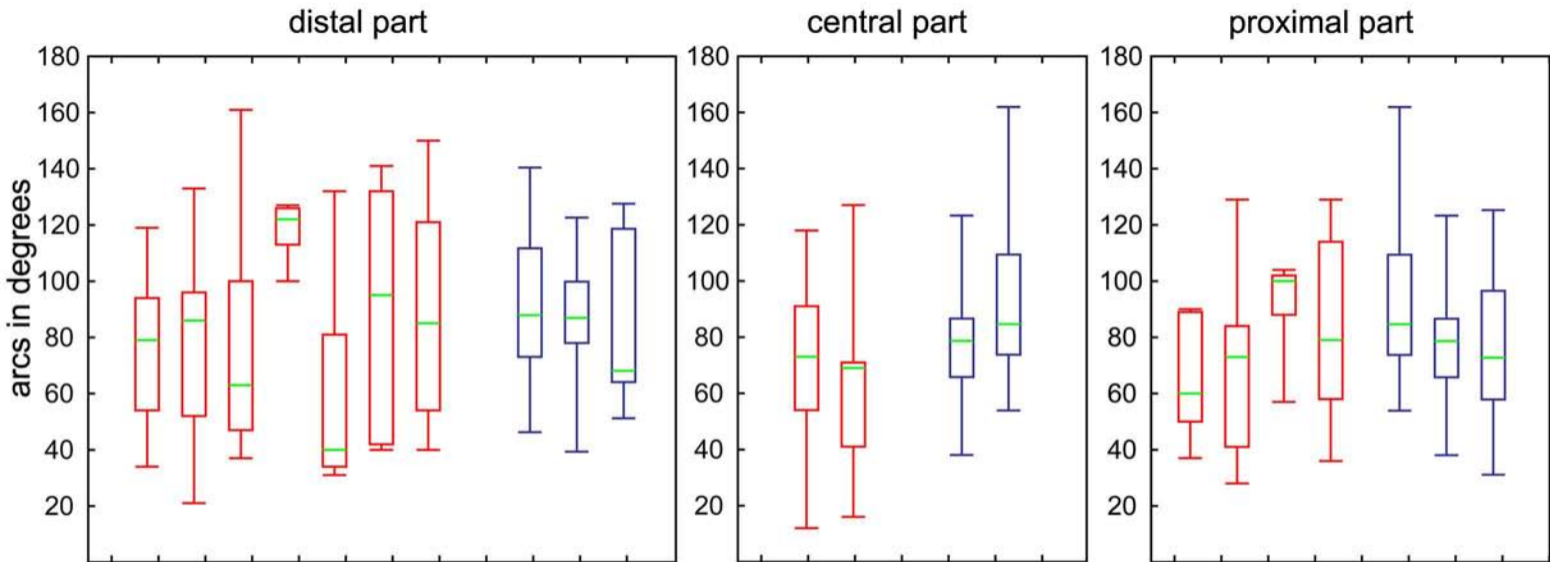


Figure S3

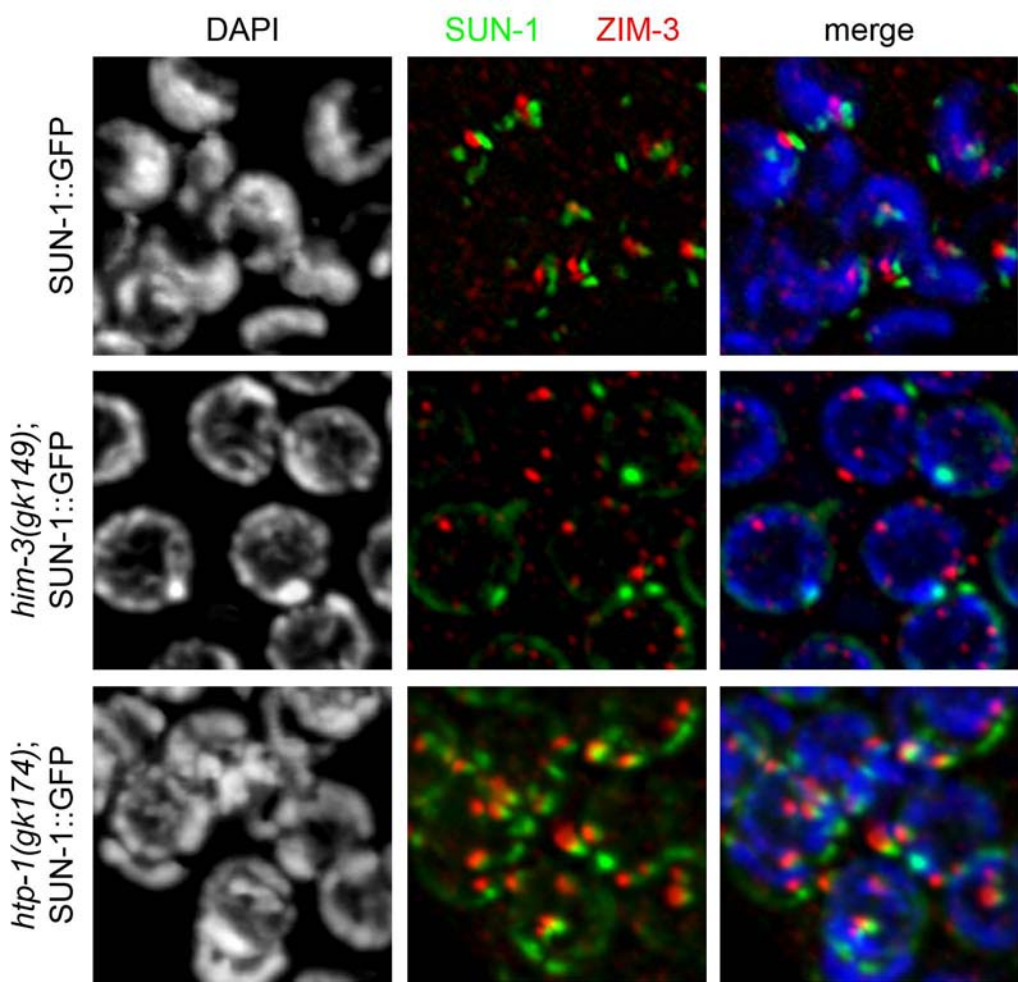


Figure S4

progression of meiosis

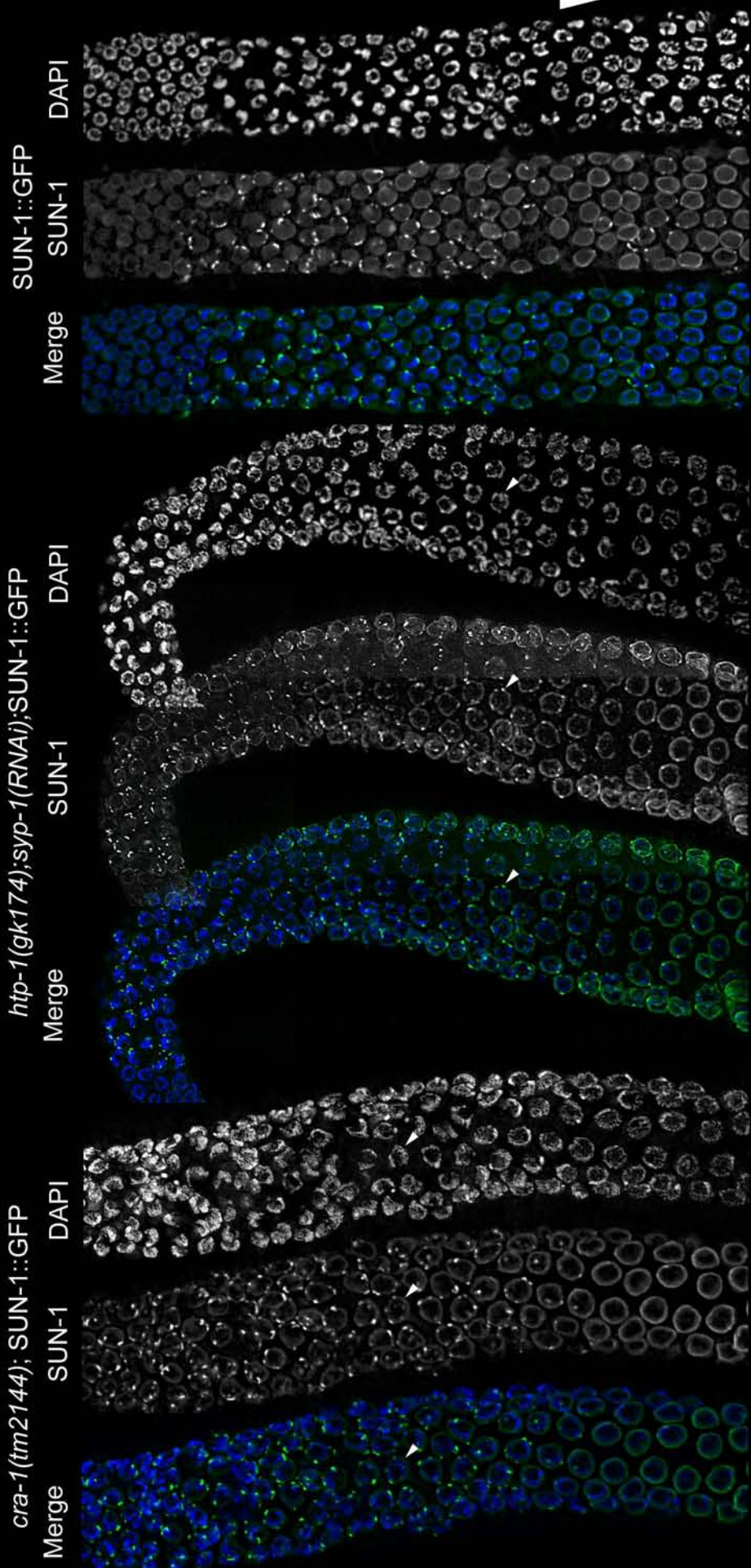


Figure S5

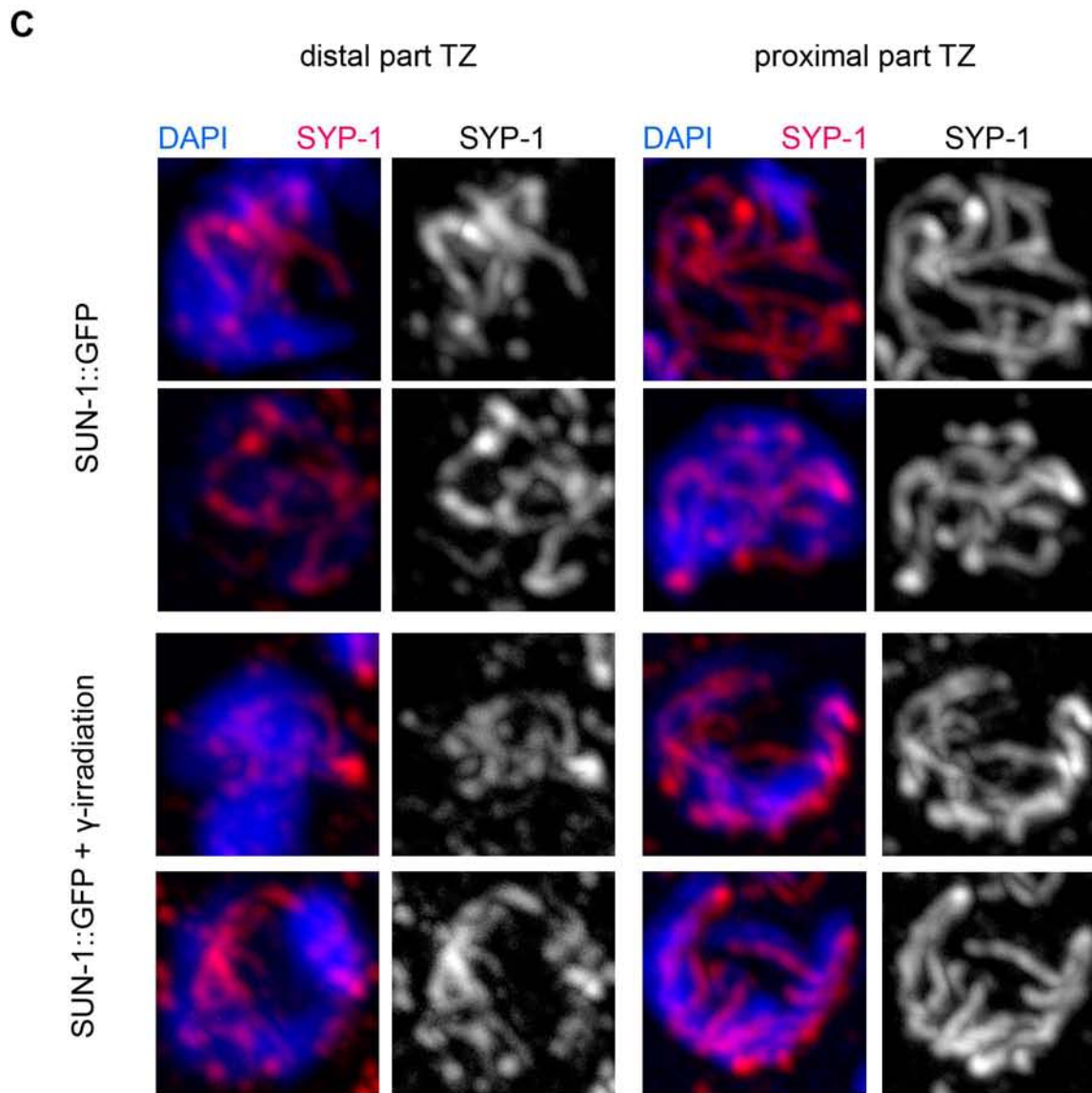
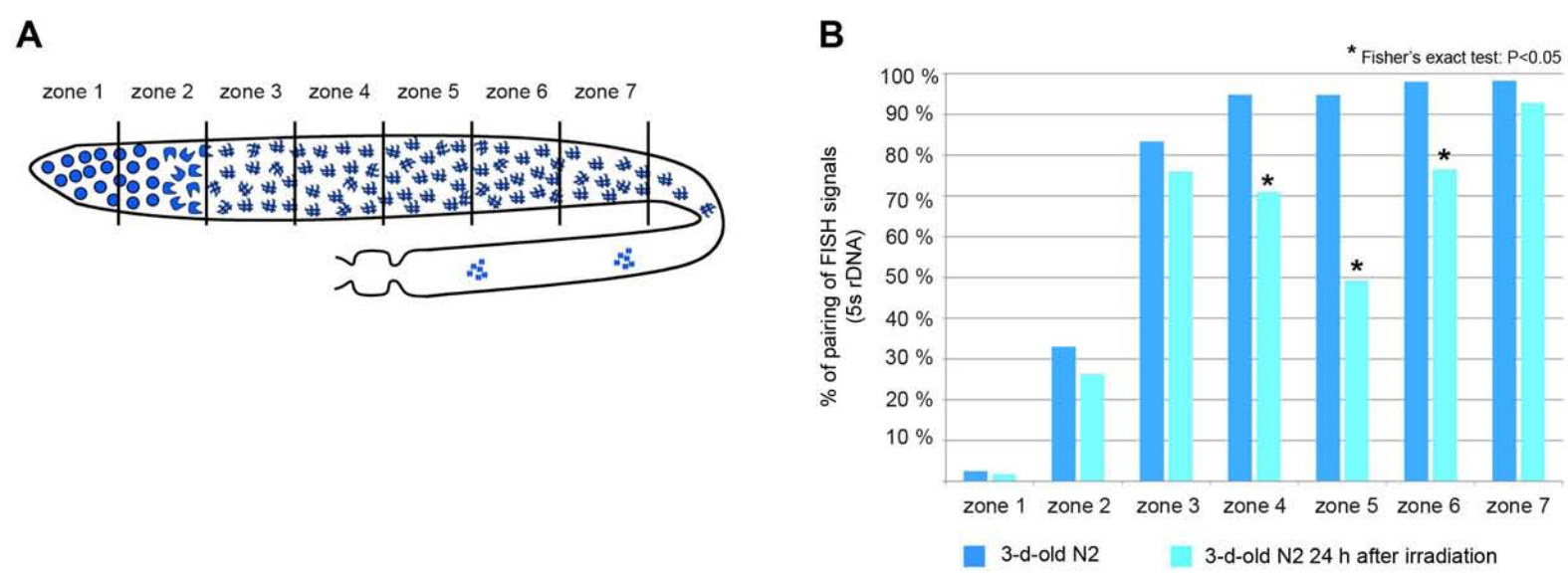


Figure S6

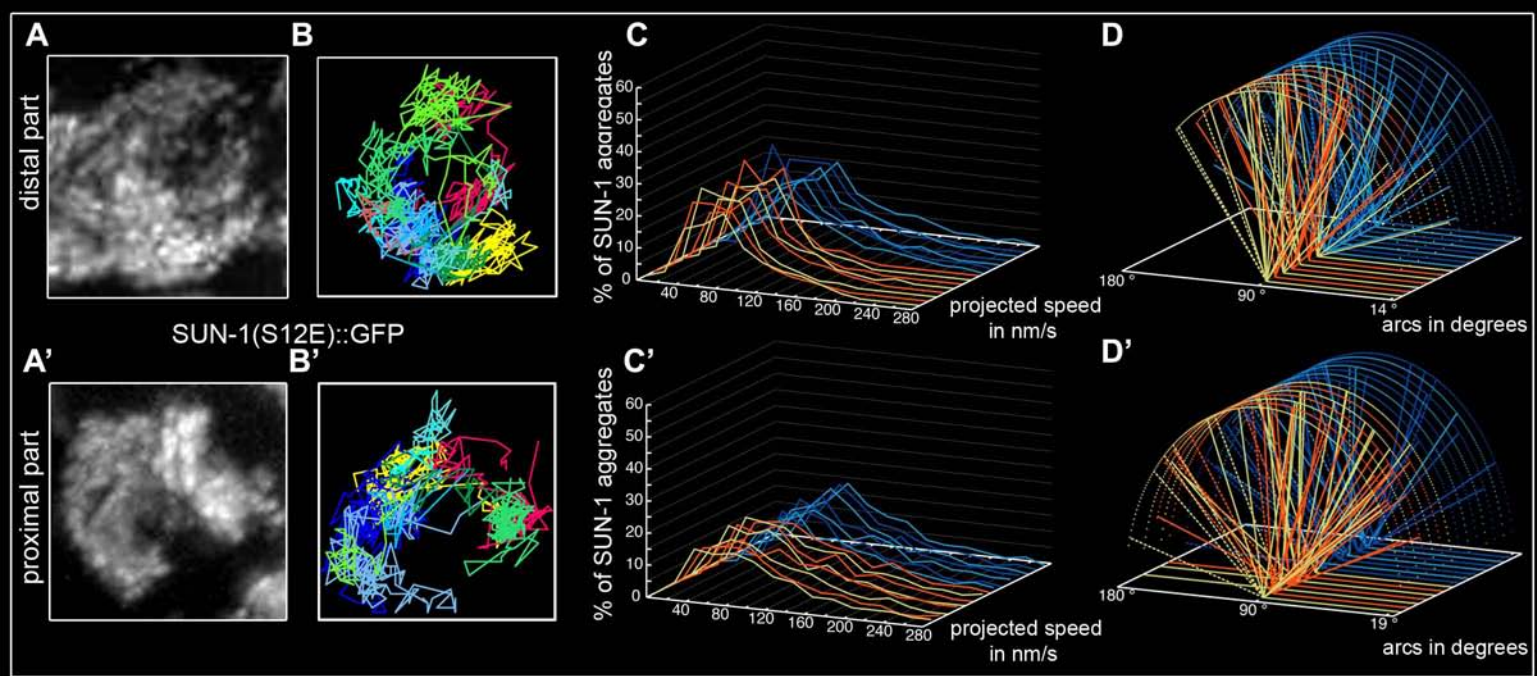
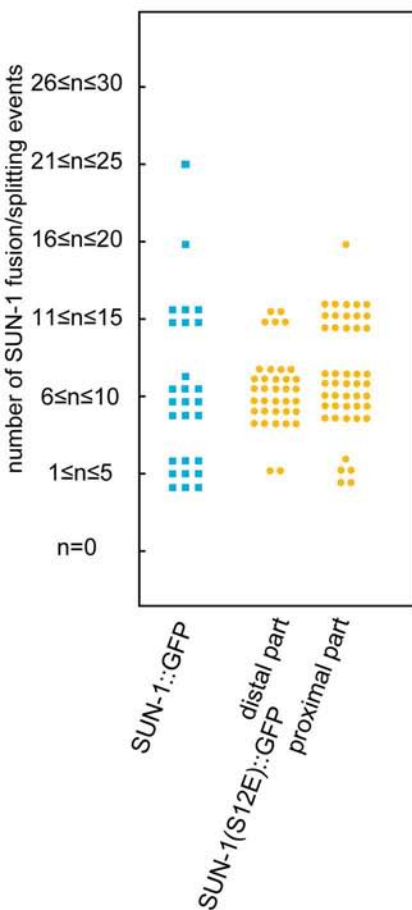
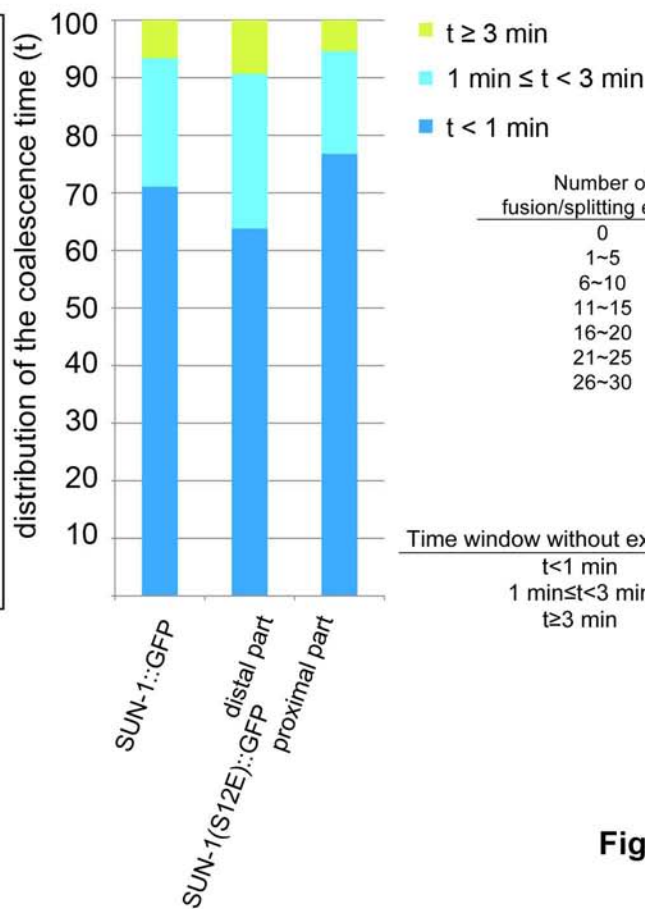


Figure S7

A

number of aggregates	SUN-1::GFP	SUN-1(S12E)::GFP	
	entire TZ	distal part of TZ	proximal part of TZ
average	3.9±1.4	3.7±1.3	4.3±1.3
minimum	2.4±1.1	2.8±1.2	2.3±1.1
maximum	6.1±2.8	5.0±1.5	5.9±2
n	27	43	25

B**C****D**

Number of fusion/splitting events	SUN-1(S12E)::GFP	SUN-1(S12E)::GFP
	distal part	proximal part
0	1	1
1~5	0,7988	0,3554
6~10	1	1
11~15	0,5036	1
16~20	0,6355	0,3409
21~25	1	1
26~30	1	0,4808

E

Time window without exchange (t)	SUN-1(S12E)::GFP	SUN-1(S12E)::GFP
	distal part	proximal part
t < 1 min	0.1138	0.1887
1 min ≤ t < 3 min	0.3475	0.6384
t ≥ 3 min	1	0.1751

Figure S8

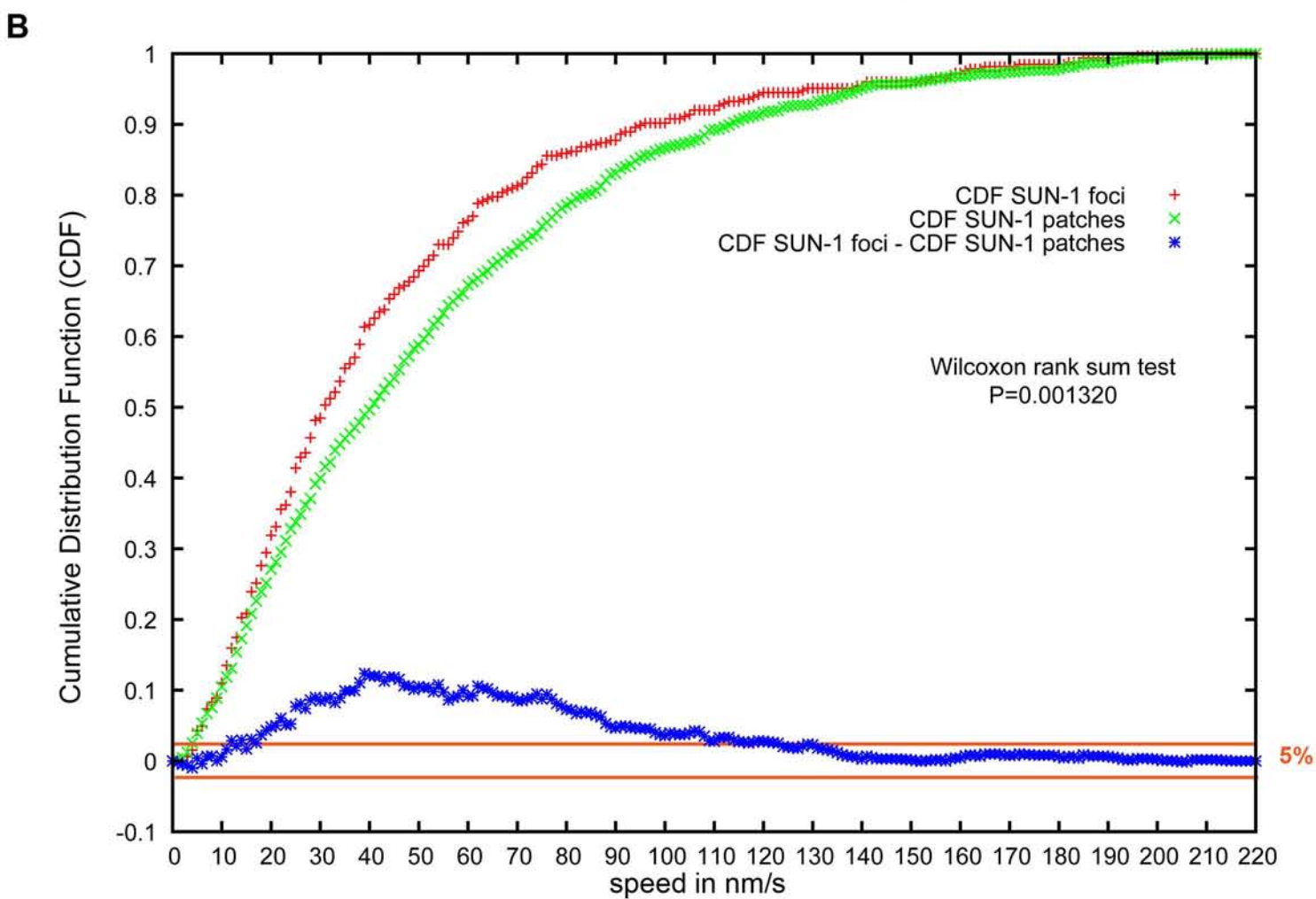
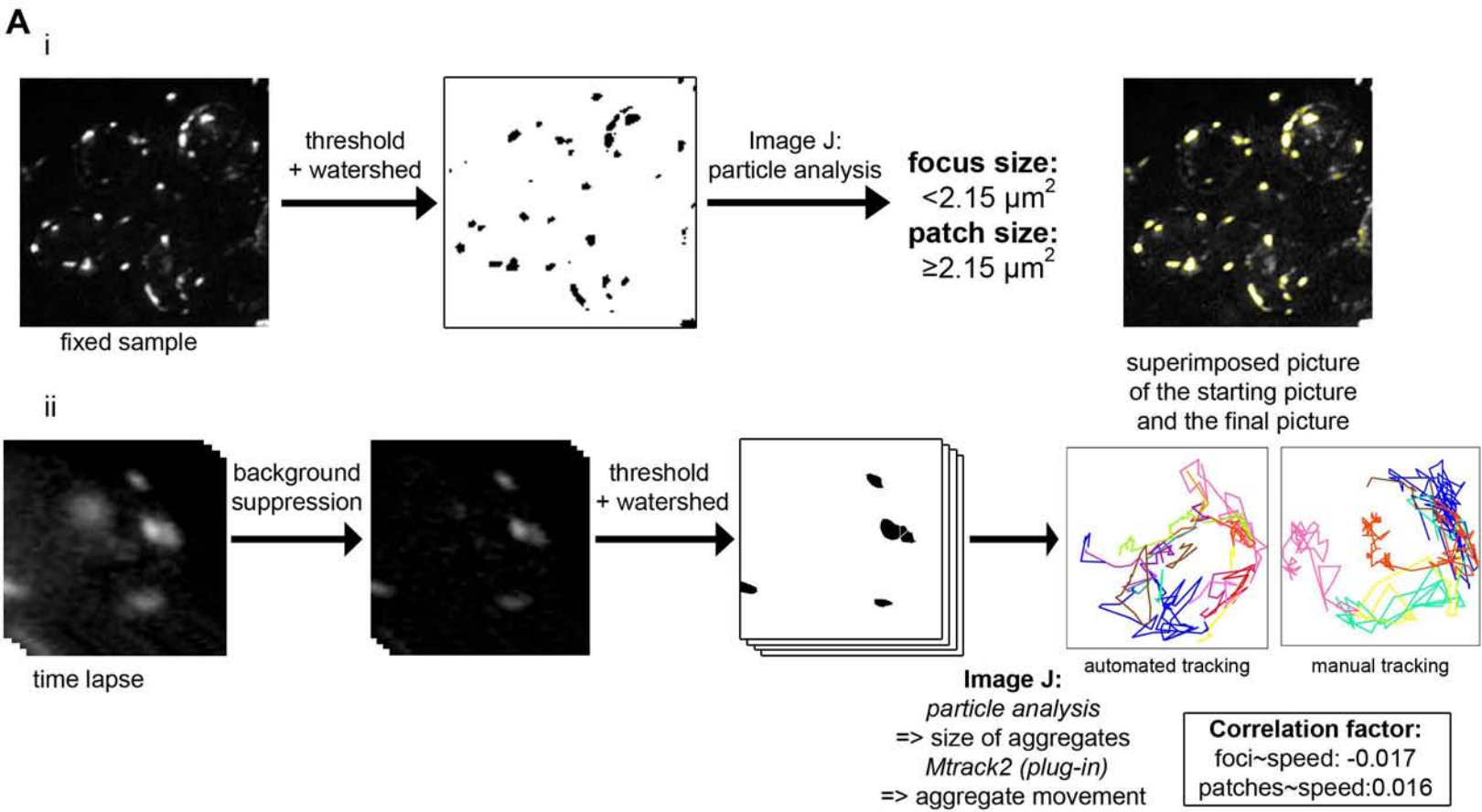


Figure S9

Chapter 6. A new Thermo-sensitive *smc-3(t2553)* Allele Reveals Involvement of Cohesion in Meiotic Repair in *C. elegans*.

first draft

A new Thermo-sensitive *smc-3* Allele Reveals Involvement of Cohesion in Meiotic Repair in *C. elegans*.

Antoine Baudrimont¹, Alexandra Penkner¹, Yasmine M. Mamnun¹, Margot Hulek¹, Kathrin Struck², Ralf Schnabel², Josef Loidl¹, Verena Jantsch^{1,*}

¹Department of Chromosome Biology, Max F. Perutz Laboratories, University of Vienna, 1030-Vienna, Austria; ²Technical University of Braunschweig, 38106-Braunschweig, Germany;

*Corresponding author

Key words: cohesin complex, SMC, DSB repair, meiosis

Short title: characterization of a thermosensitive allele of *C. elegans smc-3*

Abbreviations: DSB (double-strand break), SC (synaptonemal complex), nucleotide-binding domains (NBDs), CO (cross-over), SMC (structural maintenance of chromosomes), PC (pairing centre), sister chromatid repair (SCR)

Abstract

The cohesin complex is a major factor in the cohesion of sister chromatids which is required for their faithful segregation during mitosis and meiosis. Crossover recombination together with cohesion is essential for the disjunction of homologous chromosomes during the first meiotic division. In addition, cohesin has been implicated in facilitating recombinational repair of DNA lesions via the sister and in transcriptional regulation. Here we made use of a new temperature-sensitive mutation in the SMC-3 protein to study the role of cohesin in the repair of meiotic DNA double-strand breaks (DSBs) and hence in crossing over for the first time. We report that attenuated cohesin caused extensive SPO-11-dependent chromosome fragmentation, which represents unrepaired DSBs. Despite compromised axial element formation, homologue recognition and presynaptic alignment were normal. Notably, in spite of largely intact sister chromatid cohesion, backup DSB repair via the sister chromatid was mostly impaired. We also found that attenuated cohesin eliminates the need of MRE-11 and RAD-50 for DSB formation in *C. elegans*, which suggests a role for the MRX complex in making cohesin-loaded chromatin susceptible to meiotic DSBs. Additionally we found that mitotic repair of DSBs was also impaired. Altogether, our data suggest that recombinational DNA repair has higher demands on cohesion than chromosome segregation.

Introduction

Cohesins belong to the well-conserved group of structural maintenance of chromosomes (SMC) proteins (Wood et al., 2010). SMC proteins are involved in condensation, cohesion and repair. During mitosis replicated sister chromatids are held together by cohesins in metaphase and this cohesion permits the bipolar orientation of the spindle kinetochores allowing the microtubules to separate the sister chromatids into the two daughter cells (for review (Marston and Amon, 2004)). During meiosis chromosomes face a new challenge: separation of the homologues during meiosis I to halve the ploidy of the cell. During metaphase I, the monopolin complex supports the cohesins to establish co-orientated kinetochores of paired chromosomes linked by COs (Monje-Casas et al., 2007). This co-orientation leads to the separation of the homologous chromosomes in anaphase I. Co-orientation of kinetochores is further achieved by the two-step loss of cohesin during meiosis. During meiosis I in yeast, the conserved protein Shugoshin protects cohesin from cleavage by the active separase and allows segregation of the homologous chromosomes (Kitajima et al., 2004). In meiosis II, Shugoshin protection is lost and sister chromatids are disjoined into the daughter cells. In *C. elegans* meiosis I, protection of cohesins is shugoshin-independent and proper bivalent differentiation in response to a crossover is thought to ensure bipolar attachment of homologous chromosomes in metaphase I relying on the chromosome associated protein LAB-1 (de Carvalho et al., 2008).

Cohesin is a tetrameric complex made of two SMC subunits Smc1 and Smc3, and two non-SMC subunits, such as Scc1 and Scc-3 in yeast. SMC subunits bear nucleotide-binding domains (NBDs) at the amino and carboxyl termini of linked long coiled coil domains separated by a hinge domain. Each SMC protein folds on itself and forms a central region (coiled coil) with the hinge domain and the two NBDs at either end. SMC-1 and SMC-3 dimerize via the hinge domain and non-SMC subunits bind to the NBDs of the two SMC. This ring is closed by the non-SMC subunit Scc1, which belongs to the α -kleisin family. The kleisin Scc-1 belongs to the mitotic specific cohesin complex whereas during meiosis cohesin complexes include the meiotic specific kleisin Rec8 (Wood et al., 2010).

Homologues of these proteins have been identified in many eukaryotes. In *C. elegans* homologues of the cohesin complex are SMC-1/HIM-1 (Chan et al., 2003), SMC-3 (Chan et al., 2003), SCC-1/COH-2 (Mito et al., 2003), SCC-3 (Pasierbek et al., 2003) and REC-8 (Pasierbek et al., 2001). Surprisingly in *C. elegans* deletion alleles of SMC-1 and SMC-3 are able to reach the adult stage (Mclellan et al., 2009) but depleting SMC-1 and SMC-3 by RNAi resulted in embryonic lethality with complete penetrance (Mito et al., 2003) suggesting a maternal rescue in the deletion allele or the ability of SMC proteins to substitute for each other. The *C. elegans* genome encodes five different kleisins: COH-1, SCC-1/COH-2, COH-3, COH-4 and REC-8 (Pasierbek et al., 2001; Severson et al., 2009). COH-1 and SCC-1/COH-2 are found in the mitotic cohesin complex and the two kleisins seem to be involved in different processes during development of *C. elegans* (Mito et al., 2003). REC-8 was the first meiotic kleisin characterized in *C. elegans* (Pasierbek et al., 2001) and a recent study showed that COH-3 and COH-4 are also incorporated in the meiotic cohesin complex (Severson et al., 2009). Cohesins in addition to hold chromatids together during mitosis also delineate chromosomes axis during meiosis.

Chromosomes axis in meiosis correspond to the lateral elements of the tripartite synaptonemal complex (SC) (Colaiácovo, 2006). Lateral elements of the SC include the meiotic cohesin complex (SMC-1, SMC-3, REC-8, SCC-3), HIM-3 and HTP-1-3 that are zipped up by the central elements SYP-1-4 (Colaiácovo, 2006; Smolikov et al., 2009) in *C. elegans*. HIM-3 shares a HORMA domain with HTP-1-3 and additionally to being part of the chromosome axis restrains the repair of the programmed DSBs to the homologous chromosome (Couteau et al., 2004; Zetka et al., 1999). Him-Three Paralogs (HTPs) are found on chromosome axis and some of them have additional functions. Recently a requirement for HTP-3 to load cohesins onto chromosomes during meiosis was demonstrated (Severson et al., 2009). Additionally HTP-3 is involved in the formation of DSBs (Goodyer et al., 2008). HTP-1 licenses synapsis with the proper homologue (Couteau and Zetka, 2005; Martinez-Perez and Villeneuve, 2005). Indeed, in *htp-1* mutant synapsis is precocious and non homologous. Synapsis refers to the zipping of

homologous chromosomes driven by the polymerization of the central elements of the SC (SYP-1-4) between the chromosomes axis.

Whereas synapsis is dependent on the formation of DSBs by the endonuclease Spo11 in yeast (Keeney, 2001), in *C. elegans* synapsis is independent of formation of DSBs (Dernburg et al., 1998). As in other organisms, repair of DSBs entailing chiasmata takes place in the context of the SC (Colaiácovo et al., 2003). Repair of the DSBs requires the MRN complex to generate 5' to 3' resected DNA overhangs with covalently linked SPO-11 (Gerton and Hawley, 2005). This resection is necessary to allow loading of the strand invasion protein RAD-51. As in yeast, in worms the MRN complex is also needed for the formation of DSBs (Chin and Villeneuve, 2001). However, it was previously reported, that under conditions of weakened REC-8 function, DSBs could be formed in the absence of RAD-50 or MRE-11 (Hayashi et al., 2007), which are components of the MRN complex. Effective repair depends on the availability of another template namely the homologous chromosome since repair via the sister is inhibited by HIM-3, a constraint that is lost in late pachytene.

Here we report the isolation of a new thermo-sensitive *smc-3* allele with distinct reduced viability at the restrictive temperature (25°C). Our analysis reveals that *smc-3(t2553)* mutant worms form organized gonads but are defective in meiotic repair, with highly fragmented chromatin at diakinesis. We found that loading of the cohesin complex was reduced in *smc-3(t2553)* mutants and showed that the homologue search process starts with wild-type kinetics but defective synapsis cannot stabilize the pairing. We analyzed the repair defect observed in *smc-3(t2553)* during meiosis by epistasis analysis. Additionally we show that mitotic repair is also impaired. Our results suggest that successful cohesion is less sensitive to weakened cohesion than the repair of DSBs during mitosis and meiosis.

Results

t2553* is a new temperature-sensitive allele of the cohesin subunit *smc-3

t2553 was isolated as a temperature sensitive maternal effect lethal mutant. Mapping and complementation tests confirmed *t2553* as a new allele of *C. elegans smc-3*. Sequencing of the locus revealed a point mutation (a C to T transition) in the coding sequence of *smc-3* at the position 3241 resulting in the amino acid change (leucine (L) to phenyl-alanine (F) at position 1081). Alignment of SMC-3 proteins from various phyla revealed that this leucine was widely conserved (Figure 1.A). The L1081F mutation resides in a coiled coil region in proximity to the C-terminal ATPase domain.

L1 larvae displayed a reduced brood size in comparison to wild type when grown at 16°C (Figure 1.B). 88.9±3.1% of the *smc-3(t2553)* embryos hatched (wild type: 97.9±2.8%) and 3.6±2.2% of the viable offspring were males (wild type: 0%). The reduced brood size as well as the documented HIM (*high incidence of males*) phenotype are consistent with a chromosome segregation failure and a putative meiotic defect in *smc-3(t2553)* mutants. L1 larvae shifted to 25°C for ~55hrs displayed an even strongly reduced brood size (Figure 1.B) with a high embryonic lethality (hatch rate *smc-3(t2553)*: 2.2%, wild type: 98±3%). No obvious growth or morphological defects were observed in the surviving progeny. This is in stark contrast to homozygous *smc-3(ok1703)* deletion mutants, which display unorganized gonads. The *smc-3(t2553)* allele therefore allows for the first time the study of SMC-3 in the role of meiotic chromosome behavior.

Loading of the cohesin complex is reduced in *smc-3(t2553)*

First we compared loading of SMC-3 onto chromosome axis in *C. elegans* gonads of *t2553* worms with wild type. Whereas in the wild type effective loading of SMC-3 highlight chromosome axis in *smc-3(t2553)*, short and weakened extensions of SMC-3 are detectable in *smc-3(t2553)* mutant gonads (Figure 2.A). The point mutation thus leads to a reduced loading of SMC-3.

To further assess how loading of the cohesin complex was impaired in this mutant we next squashed the nuclei and looked under two different

conditions at the loading of the meiotic kleisin component REC-8 (untreated or washed with sarkosyl) (Figure 2.B). The addition of detergent leads to a strong removal REC-8 components in *smc-3(t2553)* (compare REC-8 immunodetection with and without sarkosyl in Figure 2.B). We concluded that introduction of the point mutation displayed defective loading of meiotic cohesin resulting in the instability of the complex.

Applying the same procedure of detergent washes on nuclei spreads, we asked whether HTP-3 loading was also impaired. Indeed proper loading of the cohesin complex requires HTP-3 to be effectively loaded first (Severson et al., 2009). Even strong detergent washes did remove HTP-3 neither from wild type nor *smc-3(t2553)* mutant squashed nuclei. (Figure 2.C).

Furthermore, we subjected *syp-2(ok307)* squashed nuclei to the same assays (REC-8 and HTP-3 staining with and without Sarkosyl) to control the reliability of the assay. Deletion of SYP-2, an SC central element component, results in unsynapsed chromosomes (Colaiacovo et al., 2003). No decreased in REC-8 or HTP-3 immunostainings were observed after washing with Sarkosyl in the *syp-2(ok307)* mutant (Figure S1.B). This reinforces the specificity of the assay, as lack of synapsis could not account for the decrease in REC-8 loading that we observed after washing with Sarkosyl. Similarly no defect in SMC-3 loading was detectable after depletion of SYP-2 (Figure S1.A)

Altogether these results reinforce the idea that defective loading of cohesin is caused by the L1081F mutation in *smc-3(t2553)* rendering the cohesion complex instable.

Stabilization of homologue pairing is compromised in *smc-3(t2553)*

We next looked at the pairing of homologous chromosomes. Homologous synapsis involves chromosome-bound pairing center (PC)-binding proteins that associate with the integral nuclear envelope components Matefin/SUN-1/ZYG-12 thereby linking chromosome ends to cytoplasmic motive forces (Penkner et al., 2009; Penkner et al., 2007; Sato et al., 2009). In leptotene/zygotene, when homologous contacts are established in wild type, Matefin/SUN-1 forms aggregates (foci and patches, likely representing

chromosomal attachment plaques), which is accompanied by SUN-1 phosphorylation at its N-terminus (Penkner et al., 2009).

Immunodetection of the pairing center protein ZIM-3 revealed that PCs were properly localized at the nuclear periphery of *smc-3(t2553)* mutant meiotic nuclei and homologous PCs were juxtaposed (Figure 3.A). Additionally, in *smc-3(t2553)* gonads as in wild type, Matefin/SUN-1 aggregate formation and phosphorylation of SUN-1 Ser8 could be observed upon entry into meiosis (Figure 3.B). We therefore conclude that *smc-3(t2553)* mutants are still proficient in the loading of PC-binding proteins, the phosphorylation of SUN-1 and the formation of Matefin/SUN-1 aggregates and show no defect in progression after meiotic entry.

We next investigated the pairing behavior of the X chromosome marked by the PC protein HIM-8 (Phillips et al., 2005) and of the autosome V highlighted by FISH of the 5SrDNA region. To this end, the hermaphrodite gonad was subdivided into 6 zones of equal length and for each zone the pairing status of the respective chromosome was assessed. In *smc-3* mutants pairing levels of the X chromosome are comparable to the wild-type situation (Figure 3.C). Only in late pachytene (zone 6) pairing levels decrease significantly compared to wild type. Although pairing of the autosome V initiates in time (Figure 3.D), only about 50% of the chromosomes are paired in later stages of meiosis comparable to mutants lacking SC central element components (MacQueen et al., 2002; Colaiacovo et al., 2003; Smolikov et al., 2007). Additionally more than two HIM-8 signals were detectable in the mitotic zone (zone 1) in *smc-3(t2553)* suggesting that cohesion in some cells is defective (Figure S.4).

These data demonstrate that the initial search process for the homologous partner is not compromised in *smc-3* mutants and suggests that the initial pairing is not stabilized.

Synapsis is compromised in *smc-3(t2553)*

The integrity of the meiotic chromosome axis is a prerequisite for the proficient elongation of the synaptonemal complex (SC) central element composed of proteins, such as SYP-1-4 (Couteau et al., 2004; Couteau and

Zetka, 2005; Martinez-Perez and Villeneuve, 2005; Colaiacovo et al., 2003). In wild type, SYP-1 is first detectable in the transition zone as foci and eventually as short linear structures (figure 3.E) and is fully polymerized along the entire length of paired homologous chromosomes in pachytene (Figure 3.E, left inset).

In *smc-3(t2553)* hermaphrodite gonads SYP-1 is detectable in the first nuclei displaying the polarized configuration of chromatin suggesting that it is expressed in time. However, the protein primarily concentrated in aggregates (polycomplexes) adjacent to the DNA instead of foci and short linear structures as seen in the wild type. Only a subpopulation of SYP-1 associates with the chromatin where SYP-1 is forming foci and very short stretches, which elongate as nuclei progress through meiotic prophase I (Figure 3.E, right inset). As long as SYP-1 polycomplexes are present, the chromatin remains in a clustered configuration, which is characteristic for mutants lacking SC central components. Full SYP-1 polymerization between bivalents is accompanied with chromatin redistribution (MacQueen et al., 2002; Colaiacovo et al., 2003; Smolikov et al., 2007).

In accordance with previous observations, the reduced loading of chromosome axis components in *smc-3(t2553)* mutants affected the polymerization of the SC (Severson et al., 2009). Indeed HIM-3 loading is strongly reduced in *smc-3(t2553)* mutants (Figure S2) but to an extent, which still permits the formation of the attachment plaques (ZIM-3 is properly loaded and SUN-1 is phosphorylated).

The observed defect in homologous pairing is most likely due to the failure in SC development and the resulting impaired stabilization of pairing.

***smc-3(t2553)* mutants are deficient in proper meiotic DSB repair**

In contrast to DAPI-stained wild-type hermaphrodite gonads the mutants displayed a prolonged zone of nuclei exhibiting a clustered configuration of chromatin (Figure 4.A, left, white arrows). At diakinesis of *smc-3(t2553)* worms instead of 6 DAPI-stained bodies, chromatin masses of varying numbers and size could be seen (Figure 5.A.i, bottom). The numerous small chromatin structures in diakinesis nuclei of *smc-3(t2553)*

hermaphrodites are indicative of persisting DNA fragments which have previously been observed for DNA repair deficient mutants (Pasierbek et al., 2001; Colaiacovo et al., 2003; Penkner et al., 2007b).

To study meiotic DNA repair in more detail, nuclei of hermaphrodite gonads were stained with antibodies specifically detecting the strand-invasion protein RAD-51 (Alpi et al., 2003; Colaiacovo et al., 2003). Gonads were divided into 6 zones of equal lengths and the number of RAD-51 counted per nuclei. In wild type, RAD-51 foci are observed from early-pachytene until mid-pachytene (figure 4.A, left) with a maximum number of 7-12 RAD-51 foci in zone 4 (Figure 4.A, right). In *smc-3(t2553)* mutants, first RAD-51 signals are seen earlier when compared to the wild type (Figure 4.B, left). The number of RAD-51 foci rose from entry into meiosis (zone 2) until late pachytene (zone 6) and accumulated (more than 12 foci in 70% of nuclei in zone 6, Figure 4.B, right). Few RAD-51 foci can even be found in diplotene and diakinesis (not shown).

Next we tested whether SPO-11 could account for the accumulation of RAD-51 during the meiotic progression. Depletion of SPO-11 in *smc-3(t2553)* mutant abolished RAD-51 loading (Figure 4.C, left). Indeed in the double mutant *smc-3(t2553), spo-11(ok79)* a maximum of 1~2 RAD-51 foci can be observed during the time course (Figure 4.C, right). Moreover, depleting the SPO-11 endonuclease suppressed the formation of chromatin fragments in diakinesis (Figure 5.A.ii, bottom). In 49 diakinesis nuclei of *spo-11(ok79);smc-3(t2553)* double mutants, 12 DAPI-positive structures could be seen on average (S.D.=0.2). Smaller chromatin fragments were completely absent.

Taken together these data support the conclusion that faithful meiotic DNA repair is affected in *smc-3(t2553)* mutant worms resulting in the accumulation of recombination intermediates.

The *smc-3(t2553)* mutation suspends the requirement of MRE-11 and RAD-50 for DSB formation

The MRN complex (MRE11–RAD50–NBS1) is involved in the resection process of the strand to which SPO-11 is covalently linked. This step is necessary for the strand invasion required for the formation of chiasma. In *C.*

elegans MRE-11 is needed for the formation of DSBs (Chin and Villeneuve, 2001).

Accordingly, in the absence of MRE-11, 12 univalents were observed at diakinesis (Figure 5.A.iii, top). We constructed the double mutant *smc-3(t2553), mre-11(ok179)* and scored the loading of RAD-51 foci (Figure 4.D, left). Until late pachytene (before zone 6) the number of RAD-51 foci was similar to the number observed in *smc-3(t2553), spo-11(ok79)* whereas in late pachytene a significant increase in the number of RAD-51 foci was found with a maximum of 7~12 foci (Figure 4.D, right). In addition, at diakinesis, instead of 12 univalents as observed in *smc-3(t2553), spo-11(ok79)*, an increase in the fragmentation of the chromosomes was detected (Figure 5.iii, bottom; see below for detailed analysis of fragmentation).

We next tested whether this excess appearance of RAD-51 foci in *smc-3(t2553), mre-11(ok179)* depends on breaks introduced by SPO-11. In the triple mutant *smc-3(t2553), spo-11(ok79), mre-11(ok179)* the number of RAD-51 foci was similar to what we observed in *smc-3(t2553), spo-11(ok79)* (Figure 4.E, left) and no increase in the number of RAD-51 foci could be seen during the time course (Figure 4.E, right). Furthermore in the triple mutant fragmentation at diakinesis was lost (Figure S3). It is also worth mentioning that the prolongation of the meiotic zone displaying a clustered configuration of chromatin is still seen in all these mutants (Figure 4, region between white arrows).

We found that in *smc-3(t2553), mre-11(ok179)* fragmentation of DNA was increased at diakinesis (Figure 5.A.iii, bottom). We investigated how much repair was impaired and quantified the fragmentation observed at diakinesis. To avoid artifacts generated by projections of pictures, this quantification was done on the stack of pictures (see Materials and Methods for detailed explanation). In wild type 6 DAPI structures form the bivalents (Figure 5.A.i, top and 5.B). In *smc-3(t2553)* DNA fragmentation is observed at diakinesis (Figure 5.A.i, bottom and 5.B).

The quantification showed that fragments and masses are the 2 most represented classes in *smc-3(t2553)* mutant despite some variation inside the samples (Figure 5.B). Suppression of DSBs resulted in the formation of 12

DAPI structures at diakinesis (Figure 5.A.ii, bottom). The quantification method is able to detect in the best cases 12 univalents (Figure 5.B). The number of DAPI structures detected was 11 ± 0.8 (SD, $n=9$). Quantification confirmed that fragmentation was increased in *smc-3(t2553)*, *mre-11(ok179)* in comparison to the *smc-3(t2553)* single mutant (Figure 5.B).

Sister chromatid repair is reduced but effective in *smc-3(t2553)* mutants.

HIM-3 is a major constituent of the lateral element of the SC and exerts an inhibitory effect on sister chromatid repair (SCR) (Couteau et al., 2004; Zetka et al., 1999). In the double mutant *smc-3(t2553)*, *him-3(gk149)* the fragmentation at diakinesis is still present (Figure 5.A.iv, bottom) but quantification revealed that fragmentation was decreased and the number of univalents increased (Figure 5.B). Allowing repair of DSBs via the sister chromatid reduced some of the fragmentation at diakinesis, suggesting that despite weakened cohesion in *smc-3(t2553)* mutants some repair can take place via SCR.

To test if an 'open conformation of the chromatin' could account for the effective but reduced repair via the sister chromatid observed in *smc-3(t2553)*, *him-3(gk149)* we constructed the double mutant *smc-3(t2553)*, *him-17(ok424)*. In *him-17(ok424)* worms the formation of DSBs is greatly reduced (Reddy and Villeneuve, 2004; Tsai et al., 2008). It was shown that when the chromatin is in an 'open conformation' (as reported in the *dpy-28(s399)*, *him-17(ok424)* double mutant, (Tsai et al., 2008)) the inhibitory chromatin status of *him-17* leading to a lack of DSBs is reversed by *dpy-28*. Depleting HIM-17 in *smc-3(t2553)* resulted in an increase in univalents and bivalents together with a diminution of fragmentation (Figure 5.a.v, bottom). Quantification confirmed that fragmentation was nearly lost in *smc-3(t2553)*, *him-17(ok424)* whereas formation of bivalents was increased. We concluded that an open conformation of the chromatin could not account for the fragmentation at the diakinesis observed in *smc-3(t2553)* mutants. It is unlikely that the few fragments and the slight restoration in bivalent numbers observed result from an open conformation of the chromatin as in *him-17(ok424)* mutants DSBs formation is reduced, but not completely abolished. Indeed in *him-17(ok424)*

the number of DAPI structure at the diakinesis ranges from 9 to 12 (Tsai et al., 2008).

These results reinforce the idea that *smc-3(t2553)* mutants are able to deal with a reduced number of DSBs most probably via SCR or the non-homologous end joining (NHEJ) repair pathway.

The NHEJ repair pathway is involved in the fragmentation at diakinesis.

Next we asked whether the NHEJ repair pathway was processing some of the DSBs made in *smc-3(t2553)*. To this aim we looked at the diakinesis of the double mutant *smc-3(t2553), lig-4(ok716)*. LIG-4 encodes a DNA ligase IV that is involved in the NHEJ repair pathway (Martin et al., 2005). In the double mutant *smc-3(t2553), lig-4(ok716)* fragmentation is decreased (Figure 5.A.vi, bottom) but surprisingly masses of DNA were observed at diakinesis. Quantification confirmed that in comparison to *smc-3(t2553)* there were overall more masses observed at diakinesis in *smc-3(t2553), lig-4(ok716)* (Figure 5.B). This suggests that the NHEJ repair pathway apparently influences the formation of fragmentation at the diakinesis in *smc-3(t2553)* mutants.

Meiotic cohesion is effective in *smc-3(t2553)* mutants

The presence of 12 univalents instead of 24 sister chromatids in *spo-11;smc-3* diakinesis (Figure 5.A.ii, bottom) clearly argues in favor of intact sister chromatid cohesion in this mutant background. To test this assumption, cohesin loading was further reduced by RNAi-mediated depletion of the cohesin subunit REC-8. Indeed, diakinesis nuclei of *spo-11(ok79);smc-3(t2553); rec-8(RNAi)* triple mutants constantly showed more than 20 signals (n=26 diakinesis nuclei of 8 independent gonads) which would be consistent with the expectation of 24 isolated sister chromatids in cohesion deficient mutants (Figure 5.A.vii). *spo-11(ok79); rec-8(RNAi)* control worms also displayed more than DAPI-positive 20 structures (n=15 diakinesis nuclei of 5 independent gonads; not shown). The reduced amount of cohesins loaded is therefore still sufficient for the establishment of functional cohesion but it is not sufficient for proficient DNA repair.

The mutation in *smc-3(t2553)* also affects mitotic repair

To test if repair of DSBs was specific to meiosis we designed an assay to test the proficiency of mitotic repair. Briefly, worms were allowed to lay eggs at restrictive (25°C) and permissive temperatures (16°C). Next, eggs were irradiated (5, 10 and 15 Gy) and the hatch rates were assayed.

At the permissive temperature (16°C) without irradiation *smc-3(t2553)* displayed a slightly reduced hatch rate compared to the wild type (Figure 6.A). After 5 Gy irradiation at the non-restrictive temperature the hatch rate of *smc-3(t2553)* mutant eggs dropped to 77% whereas the hatch rate of wild type eggs was unaffected. Increasing the irradiation dosage up to 10 and 15 Gy showed no impact on the *smc-3(t2553)* hatch rate (77% and 76% respectively). As the hatch rates of *smc-3(t2553)* eggs were impaired at dosages not affecting wild type worms, we concluded that repair of DSBs in *smc-3(t2553)* mutants is already reduced at the permissive temperature (16°C).

At the restrictive temperature (25°C) impairment of DSB repair in *smc-3(t2553)* was more pronounced (Figure 6.B). Without irradiation, the hatch rate of *smc-3(t2553)* eggs was reduced compared to wild type. At restrictive temperature after 5 Gy irradiation the hatch rate of *smc-3(t2553)* eggs dropped to 77%, similar to 16°C (compare Figure 6.A and 6.B, 5Gy). Wild type worms were unaffected at this dosage. Increasing the irradiation dosage to 10 Gy reduced the hatch rate of *smc-3(t2553)* eggs to 51% whereas wild type worms were slightly affected (hatch rate: 92%). At 15 Gy the hatch rate of *smc-3(t2553)* eggs was not further reduced in contrast to the hatch rate of wild type worms, which was reduced to 83%.

Overall these results lead us to the conclusion that repair was even more affected in *smc-3(t2253)* mutants at restrictive temperature. Surprisingly a plateau in the viability of *smc-3(t2553)* eggs was observed for irradiation above 5 Gy at the non-restrictive temperature and above 10 Gy at the restrictive temperature.

Discussion

We isolated a partial loss of function mutant of the cohesin component SMC-3 and showed that reduced cohesin loading mainly impairs repair of DSBs in mitosis and meiosis. The mutation (L1081F) in the newly identified thermo-sensitive allele *smc-3(t2553)* is located in the coiled coil region close to the NBDs. In human Hela cells Smc1 is phosphorylated in the coiled coils region (serine 957, serine 966) after introduction of DSBs in an ATM dependent manner (Kim et al., 2002; Yazdi et al., 2002). Two similar sites of phosphorylation (serine 1067, serine 1083) are found in the coiled coil region close to the NBDs of SMC-3. Recently phosphorylation of Smc3 at serine 1083 has been shown to take place in response to DNA damage (Watrin and Peters, 2009).

From our analysis it appears that the mutation introduced in the *t2553* allele (L1081F) leads to a reduce loading of the cohesin complexes on chromosome arms during meiosis. Indeed, the cohesin components (REC-8) can be washed away by addition of the detergent (Sarkosyl) in *smc-3(t2553)* mutants. It suggests that stable association of cohesin with chromatin is reduced, yet sister chromatid cohesion is still robust. Indeed *smc-3(t2553)* mutants form organized gonads at the restrictive temperature (25°C) and almost no mitotic defect (polyploidy) was detectable in the mitotic zone of *smc-3(t2553)* gonads. In addition in *smc-3(t2553)*, *spo-11(ok79)* 12 DAPI structures are found at the diakinesis whereas 24 DAPI structures are observed after inactivation of REC-8 in this double mutant. This is in accordance with a recent report that reduction in functional cohesin rings by 87% does not notably affect cohesion in yeast (Heidinger-Pauli et al., 2010).

Nevertheless, this *smc-3* mutant displays defects in meiotic and radiation-induced mitotic DSB repair. It is known that cohesion supports DSB repair, presumably by connecting the damaged site to the sister template in mitosis (Covo et al., 2010; Ström et al., 2007). Additionally introduction of DSBs have been shown to recruit cohesin complexes not only at the site of the DSB but on regions extending up to several kilobases (Kim et al., 2010; Ström et al., 2007; Unal et al., 2008). The reduced stability of the cohesin complex in *smc-3(t2553)* mutant could explain the sensitivity to DNA damage

observed in this mutant during mitosis. Indeed sufficient cohesion might not be recruited at the site of the DSBs due to the instability of the complex and therefore impeding the repair of introduced DSBs.

Holding together sister chromatids in meiosis might in fact be unproductive when DSB-carrying DNA strands should detach from their sisters in order to undergo repair via the homologue. In addition it has been proposed that cohesins inhibit the repair via the homologous chromosome (Covo et al., 2010). Therefore, in meiosis, the requirement for cohesin seems to be different, and primarily serves the purpose to create the platform for lateral element assembly/backbone of the synaptonemal complex (Klein et al. 1999; Pasierbek et al. 2001), for review see (Nasmyth and Haering 2009). The dramatic increase in RAD-51 signals and their persistence until later stages of meiotic prophase I in *smc-3(t2553)* argue for a defect in DNA repair downstream of the loading of RAD-51. We found that weakened SMC-3 does not allow DSB formation in the absence of HIM-17. Therefore the role of cohesion in supporting DSB generation by SPO-11 is distinct from that of HIM-17 which confers competence for meiotic DSB formation by the methylation of histone H3 (Reddy and Villeneuve 2004) and it demonstrates that the MRN complex and HIM-17 act in different pathways upstream of SPO-11.

In a double mutant of *smc-3(t2553)* with an *mre-11* deletion mutant, we observed pachytene chromosome fragmentation and RAD-51 foci as hallmarks of DSBs. In the absence of MRE-11 or RAD-50, DSBs are not normally observed (Chin and Villeneuve, 2001; Hayashi et al., 2007). It should be noted that the *rad-50* dependence for DSB formation is also partially abrogated in *htp-1* and *him-3* mutants, both mutants are defective in functions connected to axial elements (Hayashi et al., 2007). This points to weakened chromosome axes as the common cause for the dispensability of MRN for DSB formation. Weakened SMC-3 suspends the requirement for MRE-11 (or MRN) for DSB formation just as does weaken REC-8 (Pasierbek et al., 2001). Since both SMC-3 and REC-8 are components of meiotic cohesin, it is likely that weakening the cohesin complex as a whole promotes the generation of DSBs by SPO-11. It is conceivable that chromosome axis structure interferes

with the access or activity of SPO-11 and that this obstacle is locally and/or temporally released by the activity of MRN. This could be yet another layer in the control of meiotic recombination.

To summarize, this work reinforces the idea that cohesins are needed for effective repair of DSBs during mitosis and meiosis. The newly isolated temperature sensitive allele of *smc-3(t2553)*, represent a new tool to study the effect of weakened cohesion in worms.

Materials and Methods

Nematode strains, strain construction and culture conditions

All *C. elegans* strains were cultured using standard techniques (Brenner, 1974). The following *C. elegans* strains were used: N2 Bristol, AV276 *syp-2(ok307)* (Colaiácovo et al., 2003), AV106 *spo-11(ok79)* (Dernburg et al., 1998), AV112 *mre-11(ok179)* (Chin and Villeneuve, 2001), VC418 *him-3(gk149)* (Couteau et al., 2004), VC255 *him-17(ok424)* (Reddy and Villeneuve, 2004), RB873 *lig-4(ok716)* (Martin et al., 2005). Nematode strains were provided by the *Caenorhabditis Genetics Center*, which is funded by the NIH National Center for Research Resources (NCRR). GE4345 *smc-3(t2553)* was outcrossed 3 times.

Cytological preparation of gonads and immunostaining

Hermaphrodite gonads were dissected and fixed as described in (Martinez-Perez and Villeneuve, 2005). For chromatin staining, the preparations were mounted in Vectashield anti-fading medium (Vector Laboratories Inc., Burlingame, CA) containing 2 µg/ml 4'6-diamidino-2-phenylindole (DAPI).

For immunostaining, gonads were blocked in 3% BSA/1x PBS for 20 min. The primary antibodies were applied overnight at 4°C. Antibodies were diluted in 1x PBS/0.01% sodium azide as follows: anti-SUN-1 Ser8-Pi (Penkner et al., 2009) 1:700, anti-HIM-8 (Phillips et al., 2005) 1:500, anti-ZIM-3 (Tang et al., 2010) 1:100, anti-RAD-51 (Alpi et al., 2003) 1:300, anti-SYP-1 (MacQueen et al., 2002) 1:200, anti-HTP-3 (Goodyer et al., 2008) 1:500.

After 3 washes in 1x PBST (1x PBS, 0.1% Tween-20), secondary antibodies were applied for 2 hrs at RT. After washes in PBST, samples were mounted.

Fluorescence *in situ* hybridization (FISH)

The PCR-amplified 5S rDNA was used as a probe for the right arm of chromosome V. The 5S rDNA was labeled by PCR with digoxigenin-11-dUTP. FISH was performed as described in (Pasierbek et al., 2001). Hybridized digoxigenin-labeled probes were detected with FITC-conjugated anti-digoxigenin antibodies (1:100). Slides were mounted in Vectashield/DAPI.

Microscopy and evaluation

A Zeiss Axioskop epifluorescence microscope was used and images were recorded with a cooled CCD camera (Photometrics Ltd., Tucson, AZ). Evaluation of cytological phenotypes was performed in animals kept at 20°C, 18-24 hrs post L4. 3D stacks of images were taken (MetaVue software, Universal Imaging Co., Downingtown, PA), deconvolved (AutoDeblur software, AutoQuant Imaging Inc., Troy, NY) and projected (Helicon Focus software <http://helicon.com.ua/heliconfocus/>). Artificial coloring and merging were undertaken with Adobe Photoshop 7.0 software (Adobe Systems Incorporated).

RNA interference of *rec-8*

Double stranded RNA was produced by in vitro transcription and injected after (Pasierbek et al., 2001).

Mitotic repair assay

Ten young gravid worms for each genotypes (wild type, *smc-3(t2553)*) were allowed to lay eggs at the restrictive (25°C) and permissive temperatures (16°C) for 6 hours and 18 hours, respectively. Next, hermaphrodites were removed from the plates and the eggs were γ -irradiated with a dose of 5, 10, 15 and 60 Gy using a ¹³⁷Cs source. The hatch rate was then assayed after incubation at the two temperatures for 2-3 days.

Quantification of DNA fragmentation

Stack pictures from diakinesis were deconvolved (AutoDeblur software, AutoQuant Imaging Inc., Troy, NY). Volumes were quantified with the 3D Object Counter plugin using ImageJ (Abramoff, 2004). Care was taken to use the same parameters for all the pictures. Classes were defined by the volume occupied by the DAPI structures at the last diakinesis in WT (bivalents), in *spo-11(ok79)* (univalents). DAPI structure with a volume above the defined volume of bivalent was classified as masses. Every DAPI structure with a volume less than a univalent was defined as fragments. Graphing was done using Gnuplot (Thomas Williams, Colin Kelley et al. 2004, <http://www.gnuplot.info>). 3-dimensional projections of deconvolved pictures and counted volumes are provided for each genotype (Video S1-7)

Acknowledgments

We thank Christian Pflügl for technical assistance. We are grateful to Raymond Chan, Abby Dernburg, Anton Gartner, Anne Villeneuve and the Caenorhabditis Genetics Center for strains and antibodies. We are indebted to Monique Zetka for sharing unpublished results and discussion. We thank Alexander Schleiffer for discussion. This work was supported by grants from the FWF P-21107 and the WWTF LS05009.

Figure legends**Figure 1. *smc-3(t2553)*, a new allele.**

A. Alignment of SMC-3 sequences for *C. elegans* wild type, *C. elegans smc-3(t2553)* mutant, *C. briggsae*, *D. melanogaster*, *X. leavis*, *H. sapiens* and *M. musculus* highlights the conservation of the mutated Leucine (black arrow). B. Broodsize and hatch rate of wild type and *smc-3(t2553)* mutant worms at 16 and 25 °C.

Figure 2. Chromosomes axis are impaired in *smc-3(t2553)*.

A. Immunostaining of SMC-3 in wild type and *smc-3(t2553)* at 25°C. B. Squashed nuclei untreated and washed with Sarkozyl in wild type and *smc-3(t2553)* at 25°C in the TZ and pachytene stained against REC-8. C. Squashed nuclei washed with Sarkosyl stained against HTP-3 in wild type and *smc-3(t2553)* at 25°C in TZ and pachytene. Bar: 10 µm.

Figure 3. Active homologue search process in *smc-3(t2553)* but defective synapsis.

A. Immunostaining of the pairing centre protein ZIM-3 in wild type and *smc-3(t2553)* at 25°C (DAPI blue). B. Immunostaining of the SUN-1(S8Pi) in wild type and *smc-3(t2553)* at 25°C (DAPI blue). C. Time course for pairing of HIM-8 in wild type and *smc-3(t2553)* at 25°C. Gonads were subdivided in 6 zones of equal lengths. D. Time course for pairing of FISH probe (5s rDNA, chromosome V) in wild type and *smc-3(t2553)* at 25°C. Gonads were subdivided in 6 zones of equal lengths. E. Immunostaining of SYP-1 in wild type and *smc-3(t2553)* at 25°C with blow up of pachytene nuclei in inset (bar: 10 µm).

Figure 4. *smc-3(t2553)* mutants are defective in the repair of meiotic DSBs.

Left, immunostaining of RAD-51. Right, quantification of RAD-51 foci in wild type (A), *smc-3(tm2553)* (B), *smc-3(t2553); spo-11(ok79)* (C), *smc-3(t2553); mre-11(ok179)* (D) and *smc-3(t2553); spo-11(ok79); mre-11(ok179)* (E).

Gonads were divided in 6 zones of equal lengths for quantification. Bar: 10µm.

Figure 5. Fragmentation at diakinesis, a result of defective DSBs repair.

A. Representative DAPI structure found at the diakinesis of i: top: wild type, bottom: *smc-3(t2553)*, ii: top: *spo-11(ok79)* , bottom: *smc-3(t2553); spo-11(ok79)*, iii: top: *mre-11(ok179)*, bottom: *smc-3(t2553); mre-11(ok179)*, iv: top: *him-3(gk149)*, bottom: *smc-3(t2553), him-3(gk149)*, v: top: *him-17(ok424)*, bottom: *smc-3(t2553), him-17(ok424)*, vi: top: *lig-4(ok716)*, bottom: *smc-3(t2553), lig-4(ok716)* and vii: *smc-3(t2553); spo-11(ok79); mre-11(ok179)*. B. Quantification of fragmentation of DNA at the last diakinesis.

Figure 6. *smc-3(t2553)* mutants are also defective in mitotic repair.

Hatch rates with or without irradiation of the eggs in wild type and *smc-3(t2553)* at the permissive temperature (16°C, A) and restrictive temperature (25°C).

Supplemental information

Figure S1. Lack of synapsis could not account for a decrease in immunostaining after washing with Sarkosyl.

A. Immunostaining of SMC-3 in *syp-2(ok307)* mutant worms at 25°C. B. Squashed nuclei untreated and washed with Sarkosyl in *syp-2(ok307)* at 25°C in the TZ and pachytene stained against REC-8. C. Squashed nuclei washed with Sarkosyl stained against HTP-3 in *syp-2(ok307)* at 25°C in TZ and pachytene. Bar: 10 µm.

Figure S2. HIM-3 loading is strongly reduced in *smc-3(t2553)* mutants.

Immunostaining of HIM-3 (red) in wild type and *smc-3(t2553)* at 25°C. Bar: 10 µm.

Figure S3. No fragmentation is observed in the triple mutant *smc-3(t2553), spo-11(ok79), mre-11(ok179)*.

Quantification of number of DAPI structures observed at diakinesis in *smc-3(t2553), spo-11(ok79), mre-11(ok179)*. Inset shows 2 representative diakinesis of the triple mutant. Bar 5 µm.

Figure S4. Mitotic defect in *smc-3(t2553)* mutants worms.

Time course of HIM-8 pairing in wild type and *smc-3(t2553)* revealed the presence of 3 foci in the mitotic zone of *smc-3(t2553)* at 25°C.

Supplemental Videos

Video S1

3-dimensional projection of deconvolved stack pictures (left) and colored surface of the DAPI structures (right) in wild type.

Video S2

3-dimensional projection of deconvolved stack pictures (left) and colored surface of the DAPI structures (right) in *smc-3(t2553)*.

Video S3

3-dimensional projection of deconvolved stack pictures (left) and colored surface of the DAPI structures (right) in *smc-3(t2553); spo-11(ok79)*.

Video S4

3-dimensional projection of deconvolved stack pictures (left) and colored surface of the DAPI structures (right) in *smc-3(t2553); mre-11(ok179)*.

Video S5

3-dimensional projection of deconvolved stack pictures (left) and colored surface of the DAPI structures (right) in *smc-3(t2553), him-3(gk149)*.

Video S6

3-dimensional projection of deconvolved stack pictures (left) and colored surface of the DAPI structures (right) in *smc-3(t2553), him-17(ok424)*.

Video S7

3-dimensional projection of deconvolved stack pictures (left) and colored surface of the DAPI structures (right) in *smc-3(t2553), lig-4(ok716)*.

References

- Abramoff, M.D., Magelhaes, P.J., Ram, S.J. 2004. Image Processing with ImageJ. *Biophotonics International*. 11:36-42.
- Alpi, A., P. Pasierbek, A. Gartner, and J. Loidl. 2003. Genetic and cytological characterization of the recombination protein RAD-51 in *Caenorhabditis elegans*. *In Chromosoma*. Vol. 112. 6-16.
- Chan, R.C., A. Chan, M. Jeon, T.F. Wu, D. Pasqualone, A.E. Rougvie, and B.J. Meyer. 2003. Chromosome cohesion is regulated by a clock gene paralogue TIM-1. *In Nature*. Vol. 423. 1002-9.
- Chin, G.M., and A.M. Villeneuve. 2001. *C. elegans mre-11* is required for meiotic recombination and DNA repair but is dispensable for the meiotic G(2) DNA damage checkpoint. *In Genes Dev*. Vol. 15. 522-34.
- Colaiacovo, M., A. MacQueen, E. Martinez-Perez, K. McDonald, A. Adamo, A. La Volpe, and A. Villeneuve. 2003. Synaptonemal complex assembly in *C. elegans* is dispensable for loading strand-exchange proteins but critical for proper completion of recombination. *In Dev Cell*. Vol. 5. 463-74.
- Colaiácovo, M.P. 2006. The many facets of SC function during *C. elegans* meiosis. *In Chromosoma*. Vol. 115. 195-211.
- Colaiácovo, M.P., A.J. MacQueen, E. Martinez-Perez, K. McDonald, A. Adamo, A. La Volpe, and A.M. Villeneuve. 2003. Synaptonemal complex assembly in *C. elegans* is dispensable for loading strand-exchange proteins but critical for proper completion of recombination. *In Dev Cell*. Vol. 5. 463-74.
- Couteau, F., K. Nabeshima, A. Villeneuve, and M. Zetka. 2004. A component of *C. elegans* meiotic chromosome axes at the interface of homolog

alignment, synapsis, nuclear reorganization, and recombination. *In* *Curr Biol*. Vol. 14. 585-92.

Couteau, F., and M. Zetka. 2005. HTP-1 coordinates synaptonemal complex assembly with homolog alignment during meiosis in *C. elegans*. *In* *Genes Dev*. Vol. 19. 2744-56.

Covo, S., J.W. Westmoreland, D.A. Gordenin, and M.A. Resnick. 2010. Cohesin Is Limiting for the Suppression of DNA Damage-Induced Recombination between Homologous Chromosomes. *In* *PLoS Genet*. Vol. 6. e1001006.

de Carvalho, C.E., S. Zaaijer, S. Smolikov, Y. Gu, J.M. Schumacher, and M.P. Colaiácovo. 2008. LAB-1 antagonizes the Aurora B kinase in *C. elegans*. *In* *Genes Dev*. Vol. 22. 2869-85.

Dernburg, A.F., K. McDonald, G. Moulder, R. Barstead, M. Dresser, and A.M. Villeneuve. 1998. Meiotic recombination in *C. elegans* initiates by a conserved mechanism and is dispensable for homologous chromosome synapsis. *In* *Cell*. Vol. 94. 387-98.

Gerton, J.L., and R.S. Hawley. 2005. Homologous chromosome interactions in meiosis: diversity amidst conservation. *In* *Nat Rev Genet*. Vol. 6. 477-87.

Goodyer, W., S. Kaitna, F. Couteau, J.D. Ward, S.J. Boulton, and M. Zetka. 2008. HTP-3 Links DSB Formation with Homolog Pairing and Crossing Over during *C. elegans* Meiosis. *In* *Dev Cell*. Vol. 14. 263-74.

Hayashi, M., G. Chin, and A. Villeneuve. 2007. *C. elegans* Germ Cells Switch between Distinct Modes of Double-Strand Break Repair During Meiotic Prophase Progression. *In* *PLoS Genet*. Vol. 3. e191.

- Heidinger-Pauli, J.M., O. Mert, C. Davenport, V. Guacci, and D. Koshland. 2010. Systematic reduction of cohesin differentially affects chromosome segregation, condensation, and DNA repair. *In* *Curr Biol*. Vol. 20. 957-63.
- Keeney, S. 2001. Mechanism and control of meiotic recombination initiation. *In* *Curr Top Dev Biol*. Vol. 52. 1-53.
- Kim, B.-J., Y. Li, J. Zhang, Y. Xi, Y. Li, T. Yang, S.Y. Jung, X. Pan, R. Chen, W. Li, Y. Wang, and J. Qin. 2010. Genome-wide reinforcement of cohesin binding at pre-existing cohesin sites in response to ionizing radiation in human cells. *In* *J Biol Chem*. Vol. 285. 22784-92
- Kim, S.-T., B. Xu, and M.B. Kastan. 2002. Involvement of the cohesin protein, Smc1, in Atm-dependent and independent responses to DNA damage. *In* *Genes & Development*. Vol. 16. 560-70.
- Kitajima, T.S., S.A. Kawashima, and Y. Watanabe. 2004. The conserved kinetochore protein shugoshin protects centromeric cohesion during meiosis. *In* *Nature*. Vol. 427. 510-7.
- MacQueen, A.J., M.P. Colaiácovo, K. McDonald, and A.M. Villeneuve. 2002. Synapsis-dependent and -independent mechanisms stabilize homolog pairing during meiotic prophase in *C. elegans*. *In* *Genes Dev*. Vol. 16. 2428-42.
- Marston, A.L., and A. Amon. 2004. Meiosis: cell-cycle controls shuffle and deal. *In* *Nat Rev Mol Cell Biol*. Vol. 5. 983-97.
- Martin, J.S., N. Winkelmann, M.I.R. Petalcorin, M.J. McIlwraith, and S.J. Boulton. 2005. RAD-51-dependent and -independent roles of a *Caenorhabditis elegans* BRCA2-related protein during DNA double-strand break repair. *In* *Mol Cell Biol*. Vol. 25. 3127-39.

- Martinez-Perez, E., and A.M. Villeneuve. 2005. HTP-1-dependent constraints coordinate homolog pairing and synapsis and promote chiasma formation during *C. elegans* meiosis. *In Genes Dev.* Vol. 19. 2727-43.
- Mclellan, J., N. O'neil, S. Tarailo, J. Stoepel, J. Bryan, A. Rose, and P. Hieter. 2009. Synthetic lethal genetic interactions that decrease somatic cell proliferation in *Caenorhabditis elegans* identify the alternative RFC CTF18 as a candidate cancer drug target. *In Mol Biol Cell.* Vol. 20. 5306-13.
- Mito, Y., A. Sugimoto, and M. Yamamoto. 2003. Distinct developmental function of two *Caenorhabditis elegans* homologues of the cohesin subunit *Scs1/Rad21*. *In Mol Biol Cell.* Vol. 14. 2399-409.
- Monje-Casas, F., V.R. Prabhu, B.H. Lee, M. Boselli, and A. Amon. 2007. Kinetochores orientation during meiosis is controlled by Aurora B and the monopolin complex. *In Cell.* Vol. 128. 477-90.
- Pasierbek, P., M. Födermayr, V. Jantsch, M. Jantsch, D. Schweizer, and J. Loidl. 2003. The *Caenorhabditis elegans* SCC-3 homologue is required for meiotic synapsis and for proper chromosome disjunction in mitosis and meiosis. *In Exp Cell Res.* Vol. 289. 245-55.
- Pasierbek, P., M. Jantsch, M. Melcher, A. Schleiffer, D. Schweizer, and J. Loidl. 2001. A *Caenorhabditis elegans* cohesion protein with functions in meiotic chromosome pairing and disjunction. *In Genes Dev.* Vol. 15. 1349-60.
- Penkner, A., A. Fridkin, J. Gloggnitzer, A. Baudrimont, T. Machacek, A. Woglar, E. Csaszar, P. Pasierbek, G. Ammerer, Y. Gruenbaum, and V. Jantsch. 2009. Meiotic Chromosome Homology Search Involves Modifications of the Nuclear Envelope Protein Matefin/SUN-1. *In Cell.* Vol. 139. 920-33

- Penkner, A., L. Tang, M. Novatchkova, M. Ladurner, A. Fridkin, Y. Gruenbaum, D. Schweizer, J. Loidl, and V. Jantsch. 2007. The Nuclear Envelope Protein Matefin/SUN-1 Is Required for Homologous Pairing in *C. elegans* Meiosis. *In Dev Cell*. Vol. 12. 873-85.
- Phillips, C.M., C. Wong, N. Bhalla, P.M. Carlton, P. Weiser, P.M. Meneely, and A.F. Dernburg. 2005. HIM-8 binds to the X chromosome pairing center and mediates chromosome-specific meiotic synapsis. *In Cell*. Vol. 123. 1051-63.
- Reddy, K.C., and A.M. Villeneuve. 2004. *C. elegans* HIM-17 links chromatin modification and competence for initiation of meiotic recombination. *In Cell*. Vol. 118. 439-52.
- Sato, A., B. Isaac, C. Phillips, R. Rillo, P. Carlton, D. Wynne, R. Kasad, and A. Dernburg. 2009. Cytoskeletal Forces Span the Nuclear Envelope to Coordinate Meiotic Chromosome Pairing and Synapsis. *In Cell*. Vol 139. 907-919
- Severson, A.F., L. Ling, V. van Zuylen, and B.J. Meyer. 2009. The axial element protein HTP-3 promotes cohesin loading and meiotic axis assembly in *C. elegans* to implement the meiotic program of chromosome segregation. *In Genes Dev*. Vol. 23. 1763-78.
- Smolikov, S., K. Schild-Prüfert, and M.P. Colaiácovo. 2009. A yeast two-hybrid screen for SYP-3 interactors identifies SYP-4, a component required for synaptonemal complex assembly and chiasma formation in *Caenorhabditis elegans* meiosis. *In PLoS Genet*. Vol. 5. e1000669.
- Ström, L., C. Karlsson, H.B. Lindroos, S. Wedahl, Y. Katou, K. Shirahige, and C. Sjögren. 2007. Postreplicative formation of cohesion is required for repair and induced by a single DNA break. *In Science*. Vol. 317. 242-5.

- Tang, L., T. Machacek, Y.M. Mammun, A. Penkner, J. Gloggnitzer, C. Wegrostek, R. Konrat, M.F. Jantsch, J. Loidl, and V. Jantsch. 2010. Mutations in *Caenorhabditis elegans* *him-19* show meiotic defects that worsen with age. *In Mol Biol Cell*. Vol. 21. 885-96.
- Tsai, C.J., D.G. Mets, M.R. Albrecht, P. Nix, A. Chan, and B.J. Meyer. 2008. Meiotic crossover number and distribution are regulated by a dosage compensation protein that resembles a condensin subunit. *In Genes Dev*. Vol. 22. 194-211.
- Unal, E., J. Heidinger-Pauli, W. Kim, V. Guacci, I. Onn, S. Gygi, and D. Koshland. 2008. A Molecular Determinant for the Establishment of Sister Chromatid Cohesion. *In Science*. Vol. 321. 566.
- Watrin, E., and J.-M. Peters. 2009. The cohesin complex is required for the DNA damage-induced G2/M checkpoint in mammalian cells. *In EMBO J*. Vol. 28. 2625-35.
- Wood, A.J., A.F. Severson, and B.J. Meyer. 2010. Condensin and cohesin complexity: the expanding repertoire of functions. *In Nat Rev Genet*. Vol. 11. 391–404
- Yazdi, P.T., Y. Wang, S. Zhao, N. Patel, E.Y. Lee, and J. Qin. 2002. SMC1 is a downstream effector in the ATM/NBS1 branch of the human S-phase checkpoint. *Genes Dev*. 16:571-82.
- Zetka, M.C., I. Kawasaki, S. Strome, and F. Müller. 1999. Synapsis and chiasma formation in *Caenorhabditis elegans* require HIM-3, a meiotic chromosome core component that functions in chromosome segregation. *In Genes Dev*. Vol. 13. 2258-70.

A

	:: . . : : . . * * * . . * * : . : * : : : * * : * . * : * . ** * . : :	
<i>C. elegans</i>	QYMTASSQKEELTKRMAEQKKSIEDSIEELLKVLLENRKYEAIDLTFKQVKKNFEQVFKQLVPHGRGKMQMRA	1119
<i>C. elegans (t2553)</i>	QYMTASSQKEELTKRMAEQKKSIEDSIEELLKVLENRKYEAIDLTFKQVKKNFEQVFKQLVPHGRGKMQMRA	1119
<i>C. briggsae</i>	QYMTASTQKEELTKRMDEQKRSEASIEELLEVLLENRKFEAIDMTFKQVSKNFKEVFKQLVPHGSGKMTLKA	1062
<i>H. sapiens</i>	QFVNFSEQKEKLIKRRQEELDRGYKSIMELMNVLELRKYEAIQLTFKQVSKNFSEVFQKLVPGGKATLVMKK	1059
<i>M. musculus</i>	QFVNFSEQKEKLIKRRQEELDRGYKSIMELMNVLELRKYEAIQLTFKQVSKNFSEVFQKLVPGGKATLVMKK	1059
<i>X. laevis</i>	QFVNFSEQKEKLIKRRQEELDRGHKSIMELMNVLELRKYEAIQLTFKQVSKNFSEVFQKLVPGGKATLVMKK	1059
<i>D. melanogaster</i>	QFLSFSEQKEKLYRRKEELDIGDQKIHMLIQSLEMOKVEAIQFTFRQVAQNFTKVFKKLVPMGAGFLILKT	1058
<i>Athaliana</i>	QYVNFTEQREELQNRQAELDAGDEKIKELITVLDQRKDESIERTFKGVAHHFRDVFSELVQDGYGNLIIMK	1050
<i>S. pombe</i>	QFNNFTKQRDSLRLARREELRRSQESISELTTVLDQRKDEAIERTFKQVAKSFSEIFVKLVPAARGELVMNR	1047
<i>S. cerevisiae</i>	NFKKFNERRKDLAERASELDESKDSIQDLIVKLLKQKQVNAVDSTFQKVSENFQAVFERLVPRTAKLIIHR	1071

B

		N2	<i>smc-3(t2553)</i>
16°C	broodsize	258±25	188±38
	hatch rate	98±3	89±3
25°C	brood size	157±20	81±2
	hatch rate	98±3	2±2

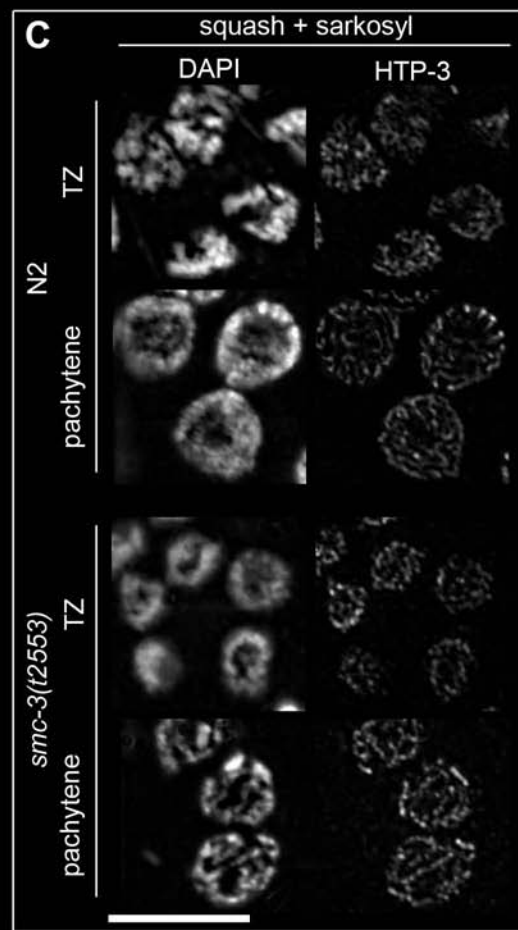
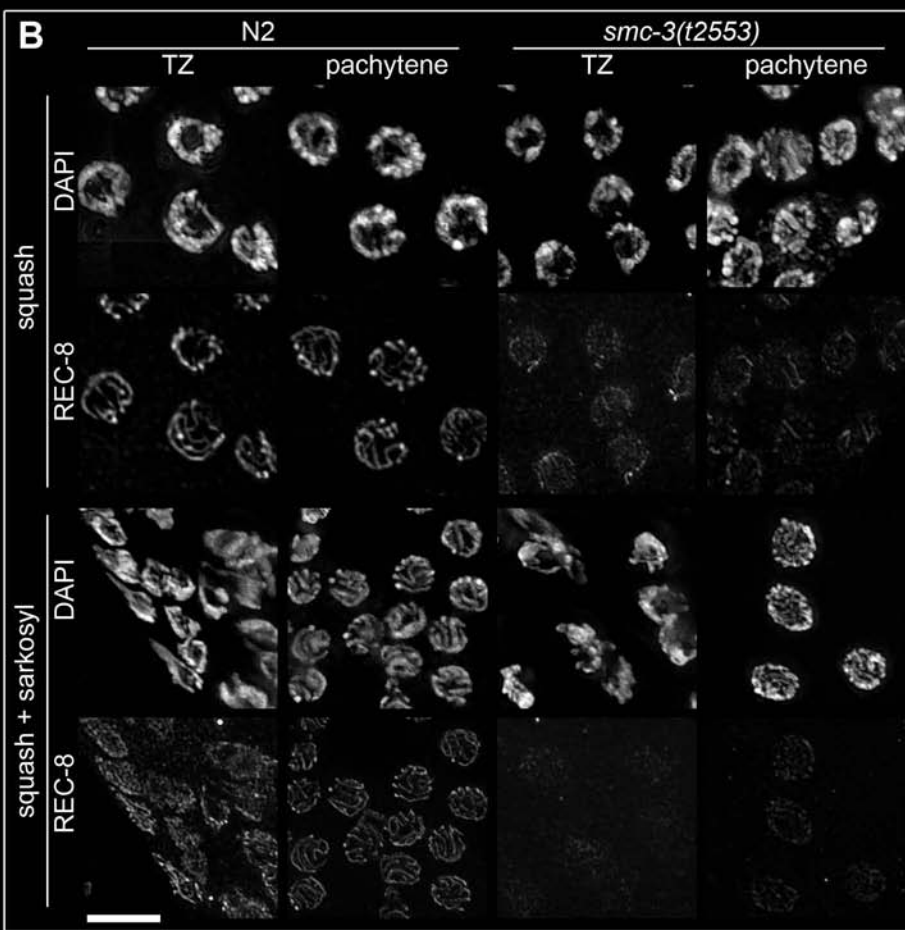
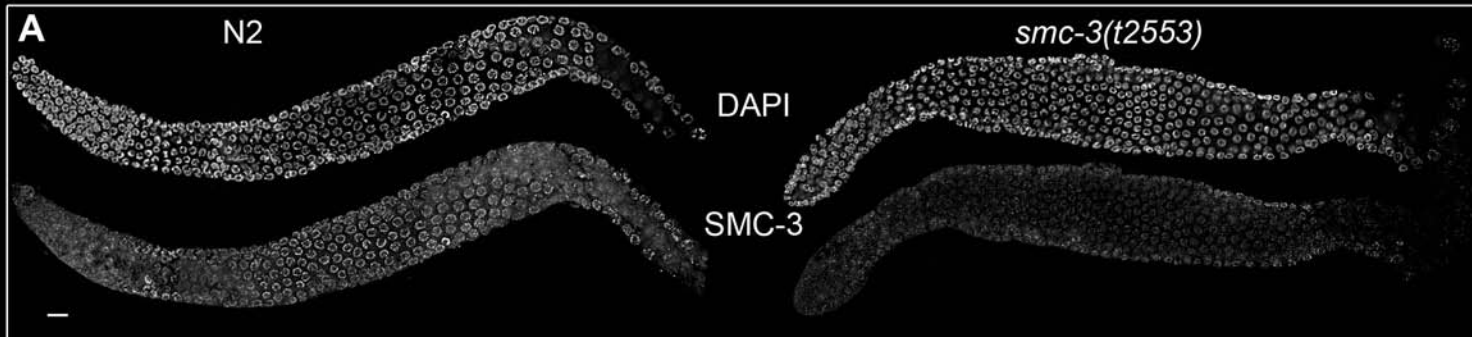
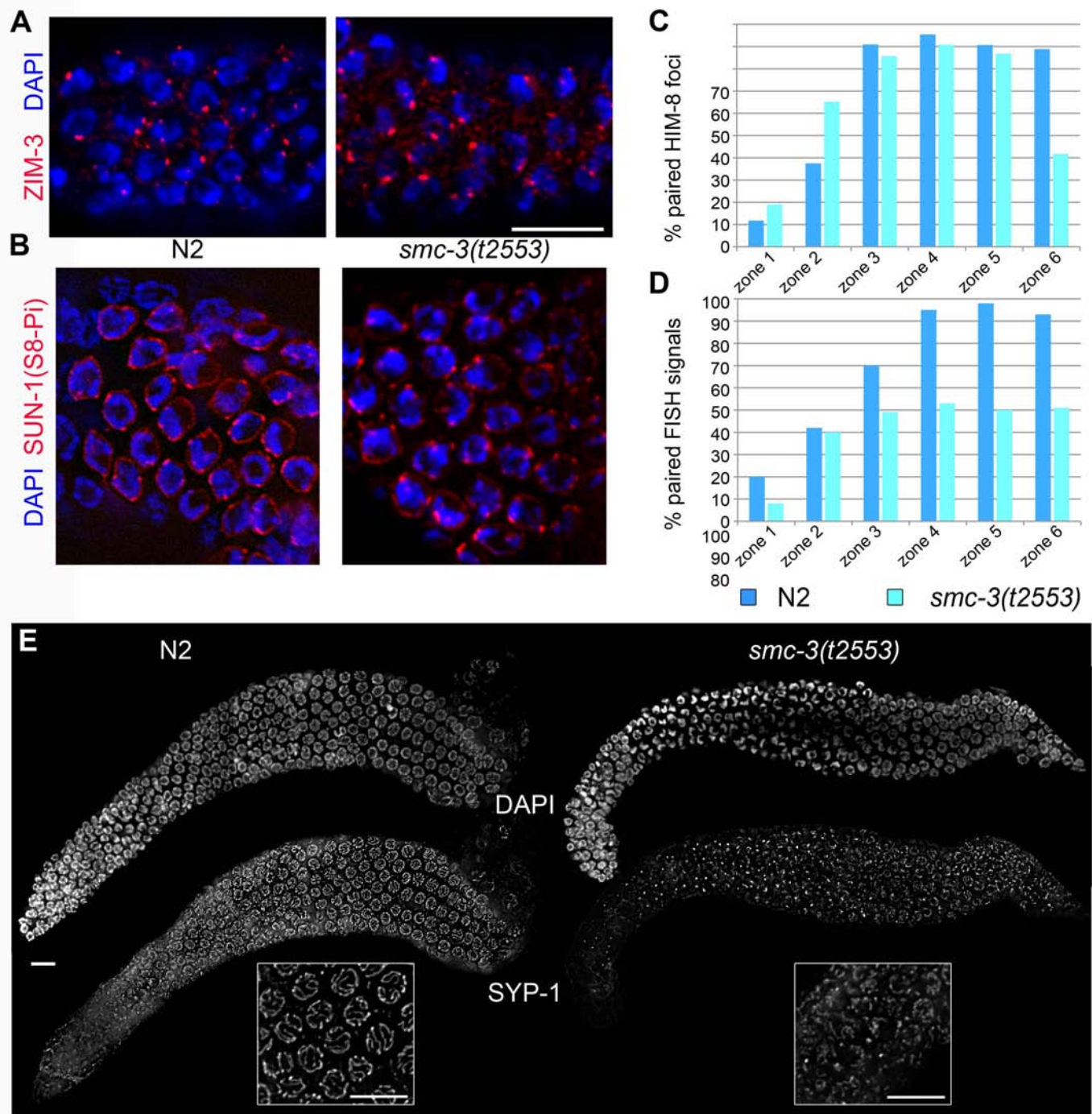
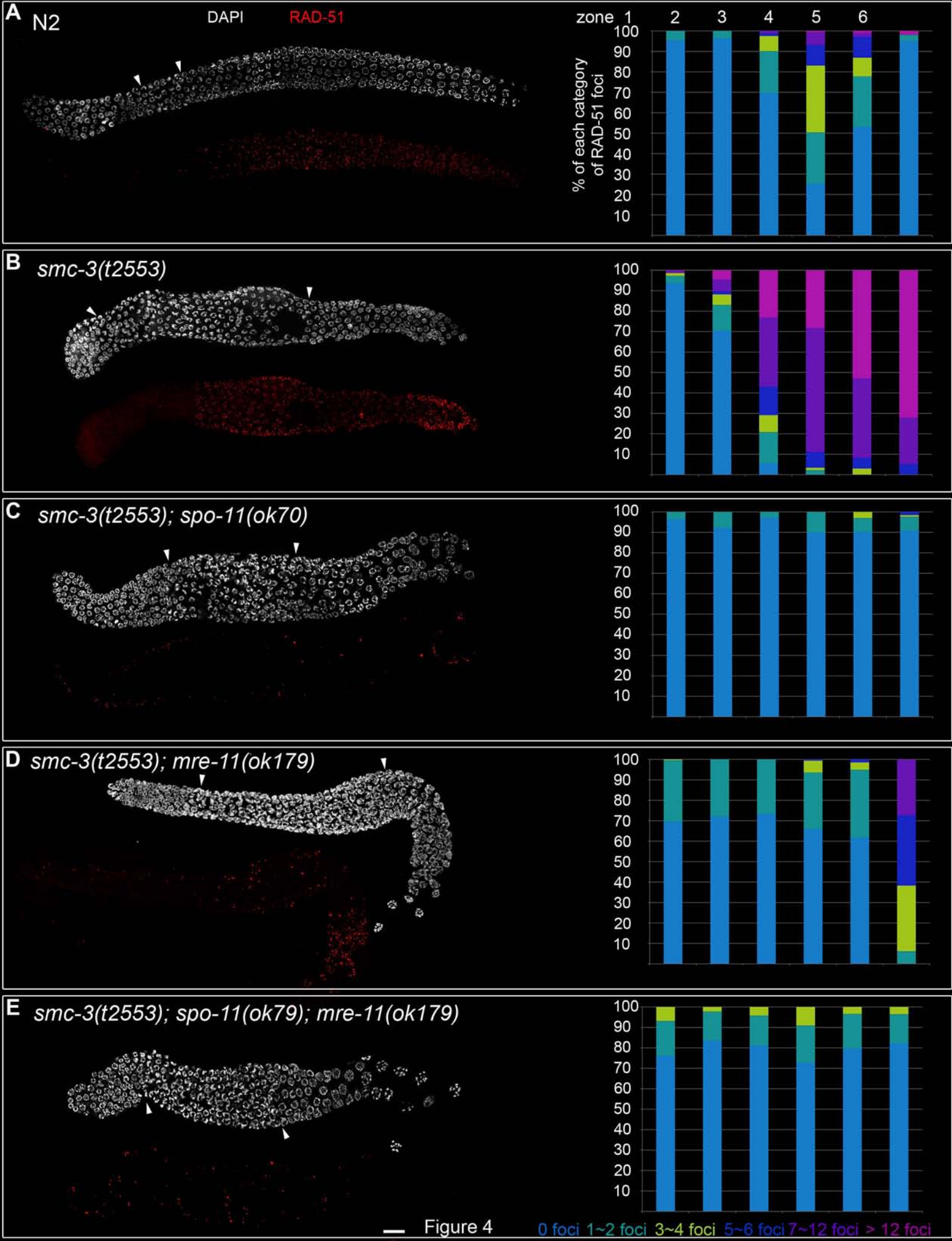


Figure 2





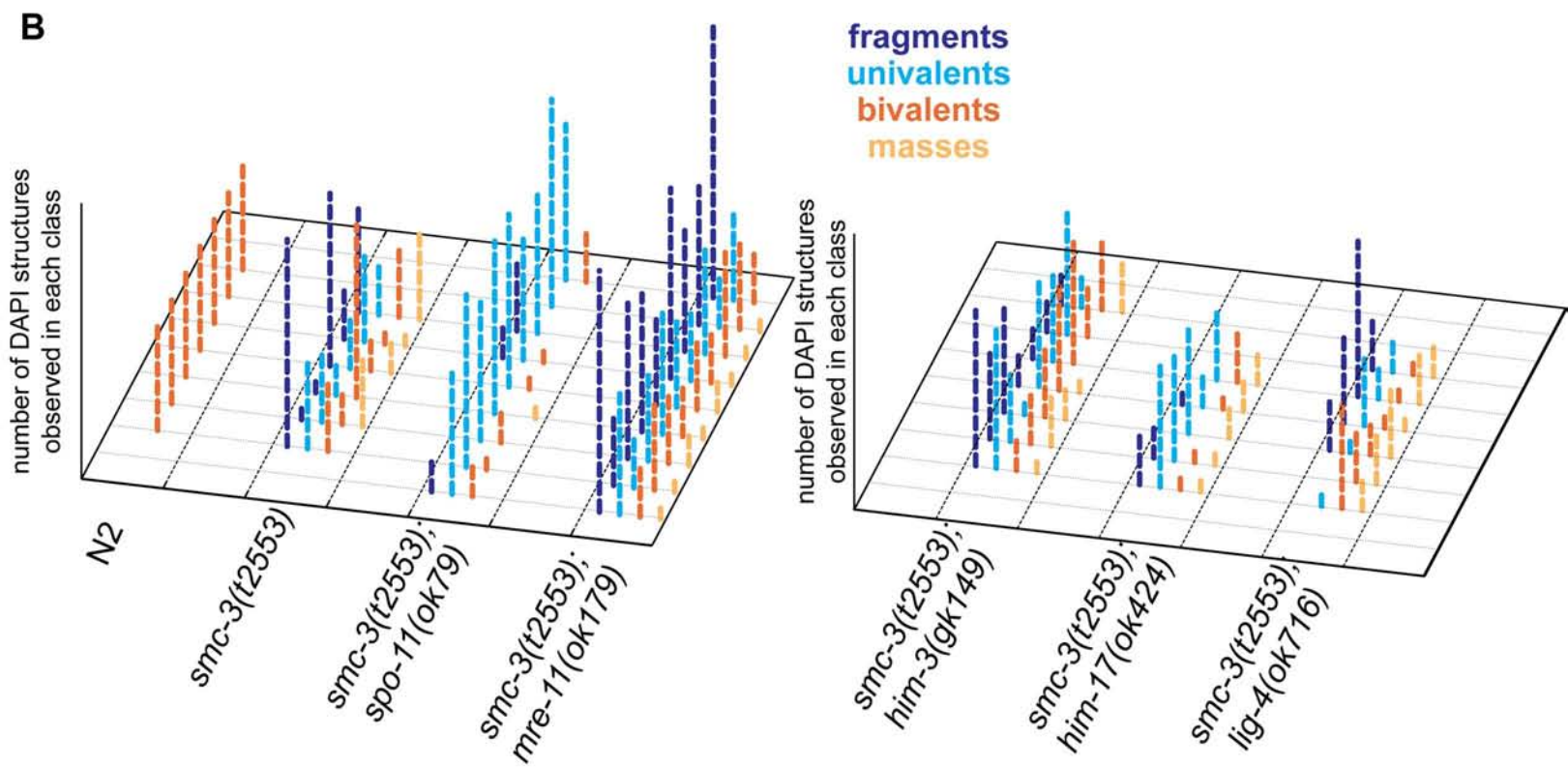
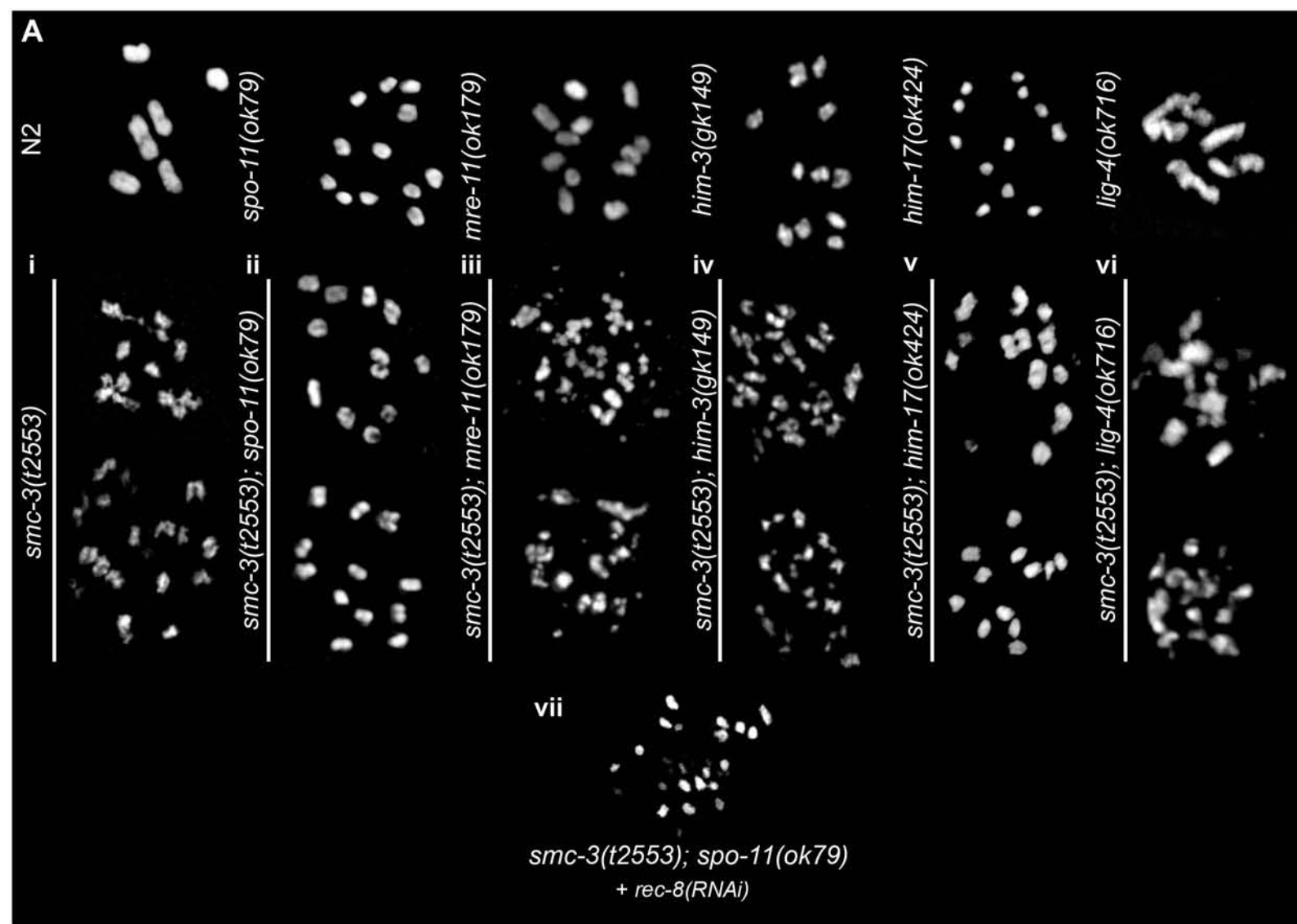


Figure 5

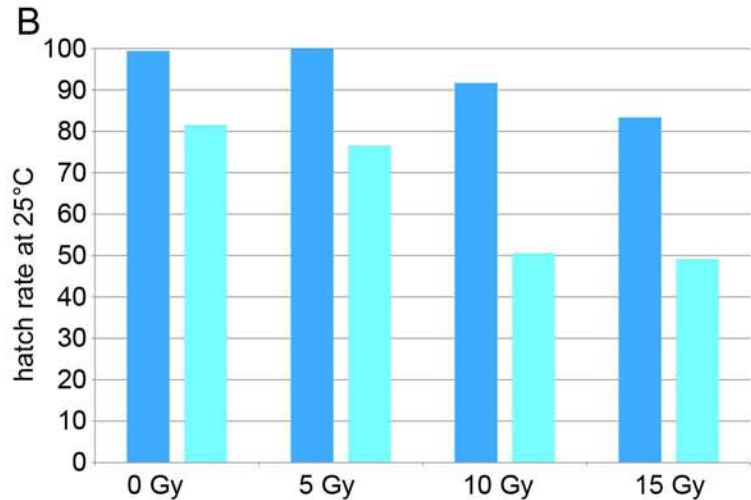
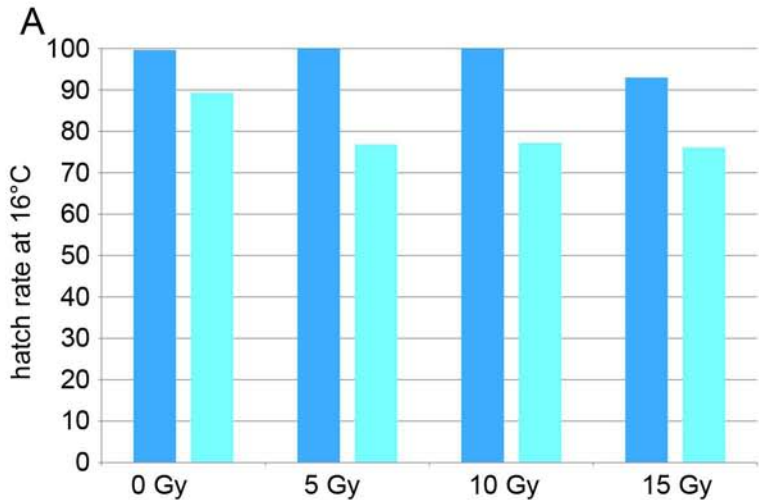
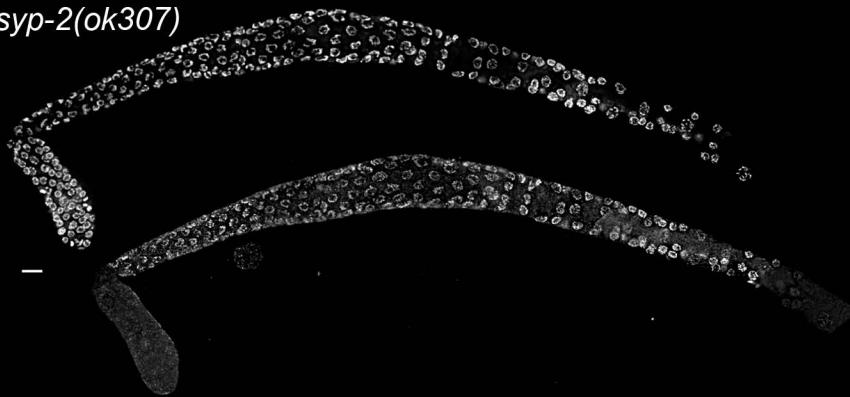
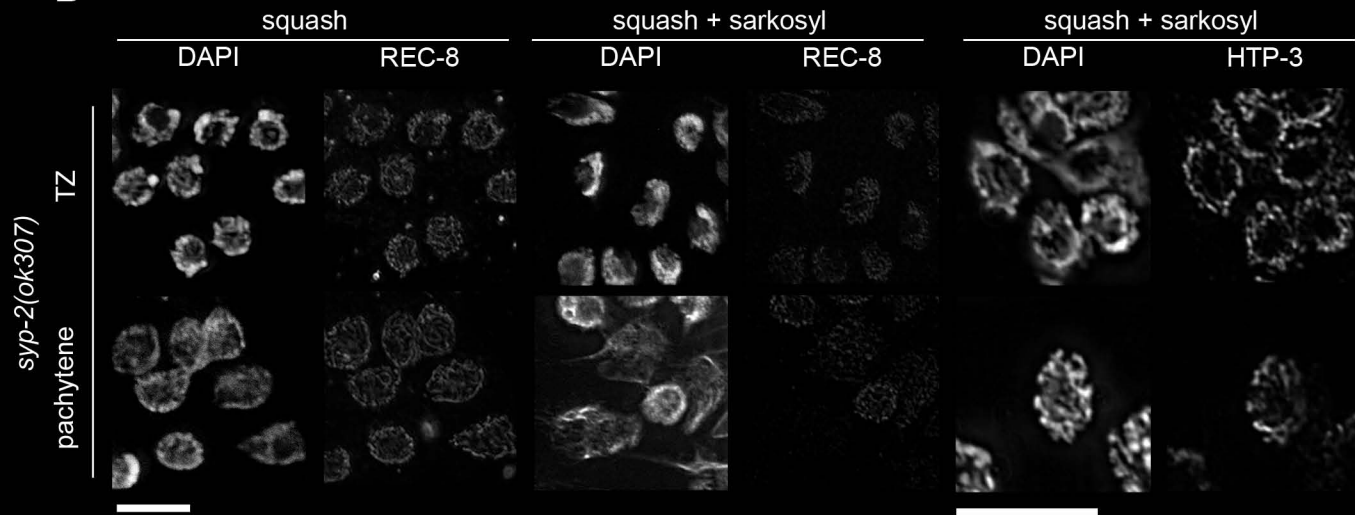


Figure 6

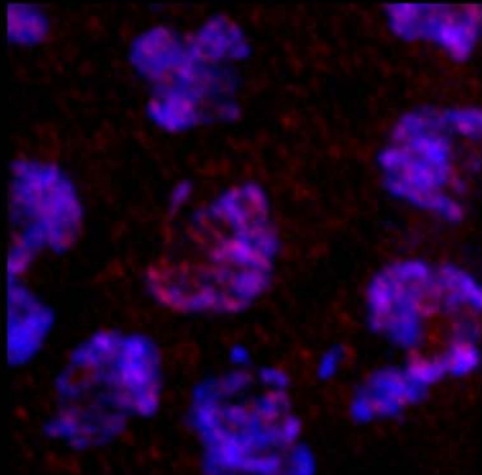
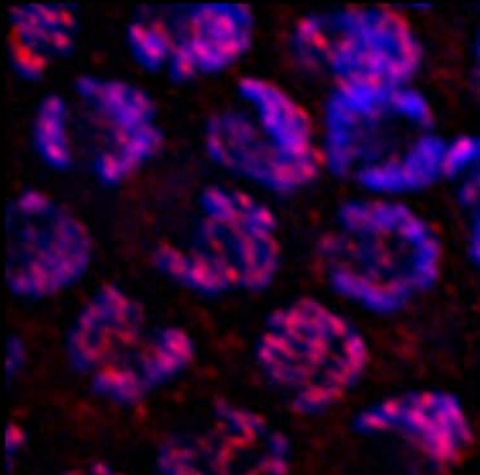
■ N2 ■ *smc-3(t2553)*

A*syp-2(ok307)***B****Figure S1**

N2

smc-3(t2553)

TZ



DAPI

HIM-3

pachytene

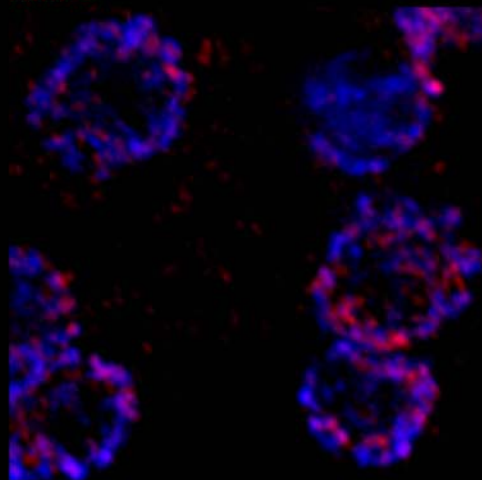
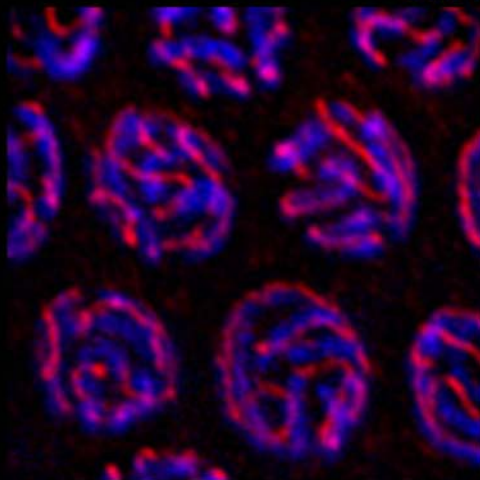


Figure S2

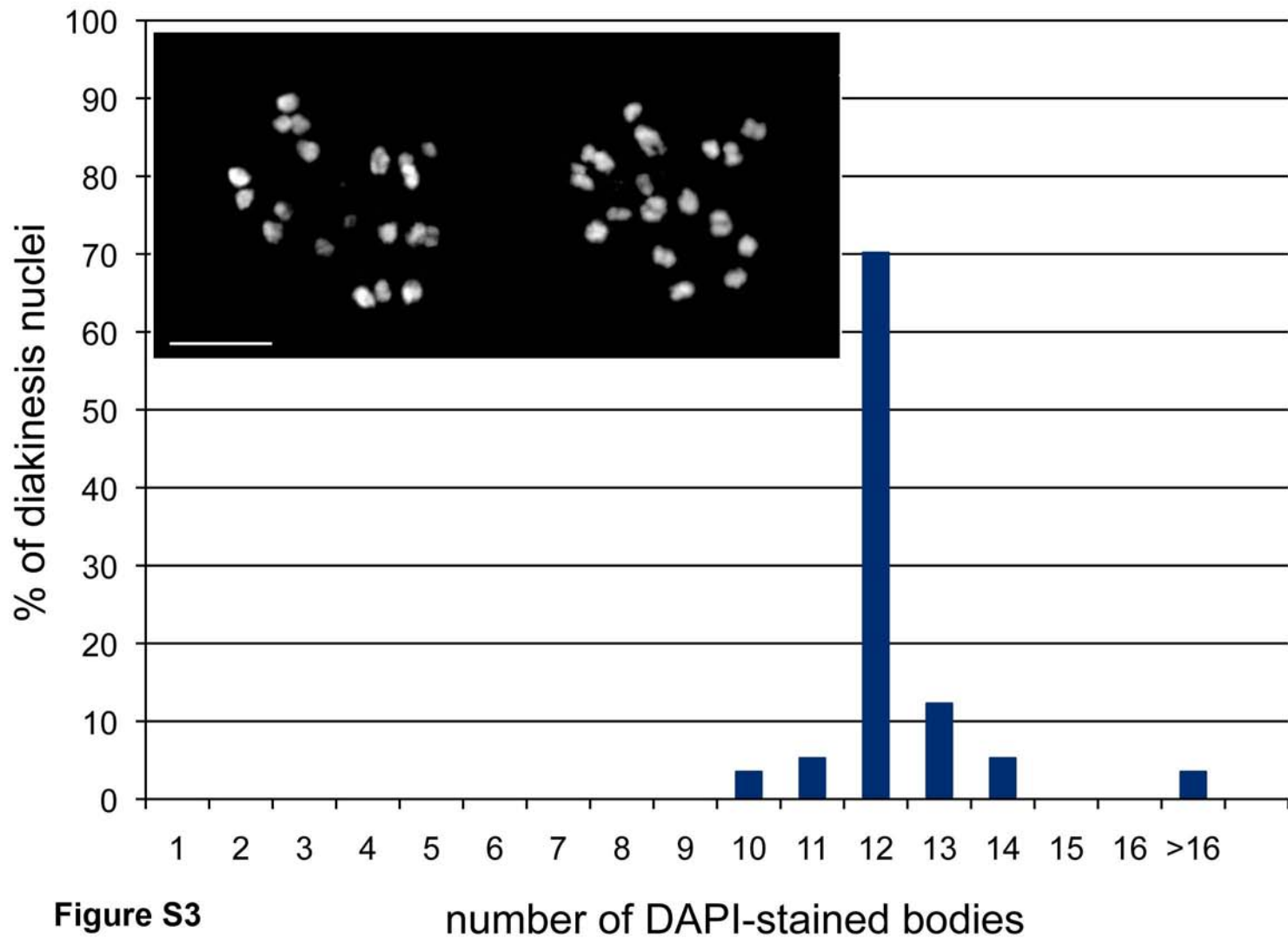


Figure S3

number of DAPI-stained bodies

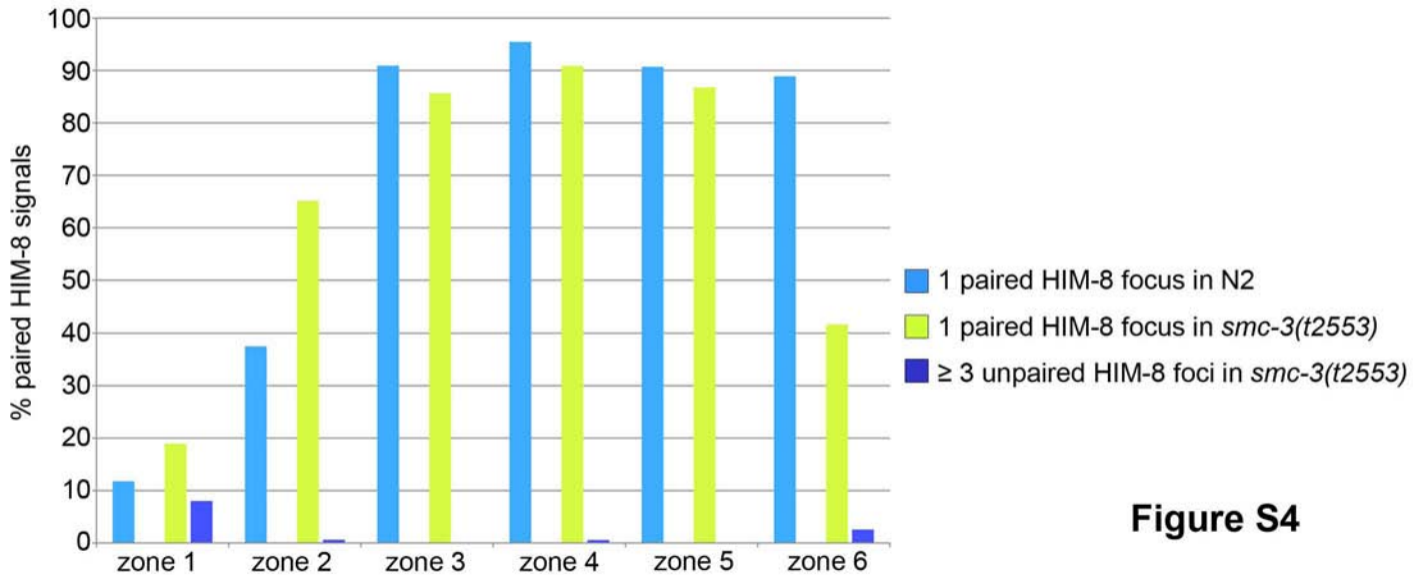


Figure S4

Methods

Suppressor screen

The suppressor screen is based on the worm's viability. Indeed *prom-1(ok1140)* mutant worms have a reduced viability. With the help of the controls (*prom-1(ok1140) unc-55(e402)* without mutagenesis and *unc-55(e402)*) the viability of the mutagenized worms was assayed by looking for plates overcrowded in the second generation (F2). The time line of the screen can be found in figure 26.

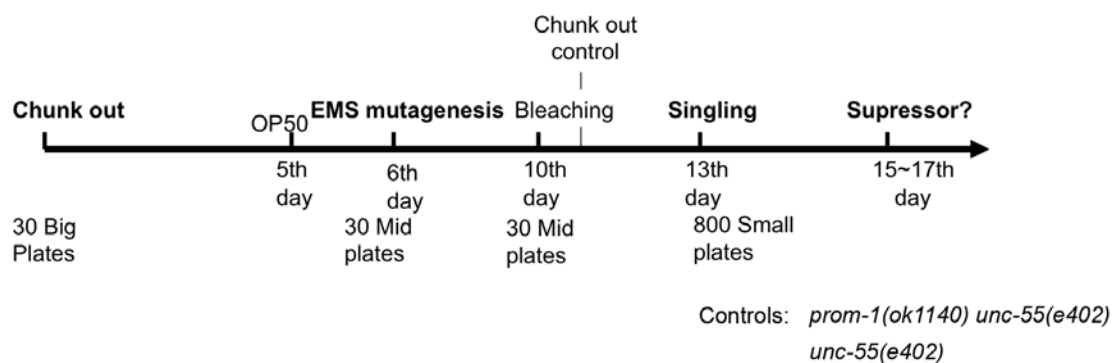


Figure 26. Overview of the suppressor screen time line.

Worms were grown on 30 big agar plates seeded with *E. coli* for 5 days. On the 5th day concentrated *E. coli* (OP50) was added to the plates to prevent worms from going into the dauer stage. On the next day worms were collected in M9 and washed 3 times in M9 to clean the worms from *E. coli*. Mutagenesis was carried out by the addition of EMS in the worm solution with a final concentration of 50 mM. After mutagenesis worms were allowed to recover until the 10th day and then they were bleached to synchronize the population. Eggs grown till the L4 stage and then singled on small agarose plates seeded with *E. coli*. The day after the bleaching, control worms (*prom-1(ok1140) unc-55(e402)* and *unc-55(e402)*) were chunked on agar plates seeded with *E. coli*.

This screen led to the isolation of 8 suppressor lines of *prom-1(ok1140)*.

Mapping

We crossed Hawaiian males with *psu-1(jf76); prom-1(ok1140) unc-55(e402)* hermaphrodites (Figure 27). In the F2 progeny, worms displaying the Unc maker phenotype and increased viability were lysed and 10 worms in the progeny were cut open to control that the mother was homozygous for *psu-1(jf76)*. Lysates were confirmed to be homozygous for *prom-1(ok1140)* by PCR.

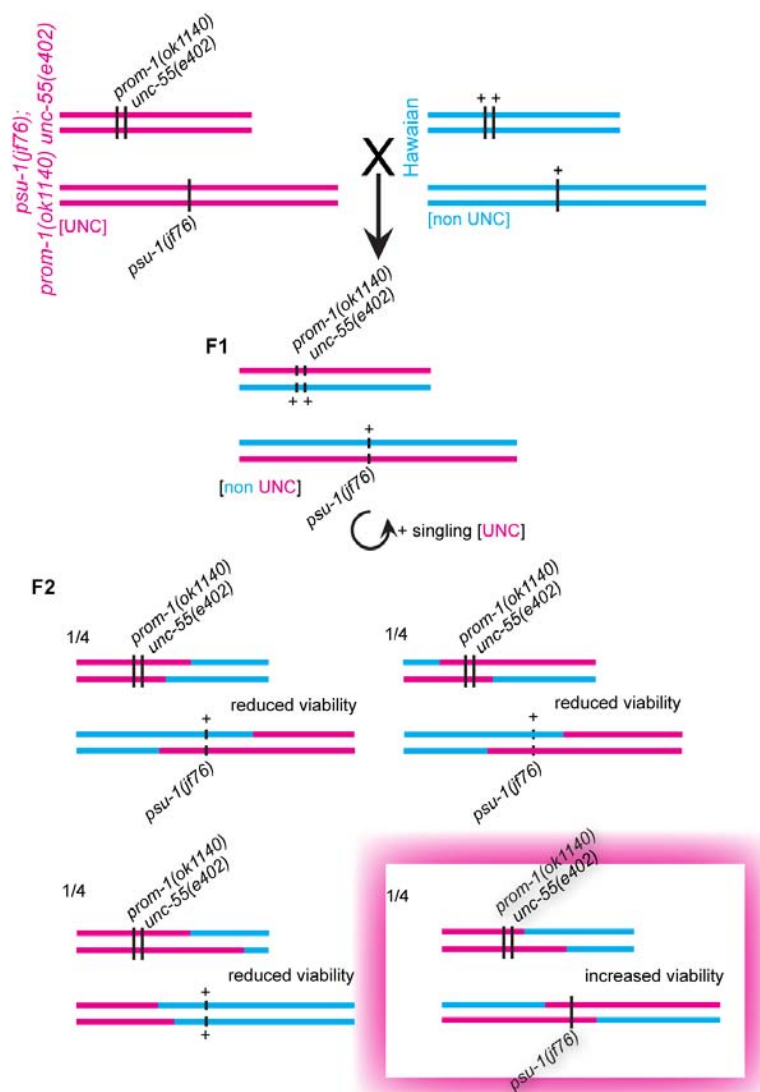


Figure 27. Mapping strategy of *psu-1(jf76)*.

psu-1(jf76); prom-1(ok1140) unc-55(e402) hermaphrodites were crossed with Hawaiian males. Progeny coming from successful cross (non [UNC]) were allowed to self and [UNC] F2

progeny were singled. ¼ of the progeny is homozygote for *prom-1(ok1140) unc-55(e402)* and *psu-1(jf76)* (pink shadow).

Primers and restriction enzymes used for the rough mapping are indicated in Table 3. The master mix for amplification by PCR of the region of interest is depicted in Table 1 and the PCR was done under these conditions (96°C for 4 min; 35 cycles (94°C for 40 sec, annealing temperature 50°C for 40 sec, elongation time 72°C for 1 min), last extension: 7 min). Table 2 summarizes the master mix used for overnight digestion of 10 µL of the PCR product.

Table 1. PCR master mix. From the condition for 1 sample a master mix for the 4 samples (*prom-1(ok1140) Unc-55(e402)* mutants, Hawaiian worms, siblings and F2 worms displaying increased viability and Unc phenotype) was prepared.

	(1 sample)	(4 samples)
10x Buffer	2.5	10
dNTPs	2	8
P1/P2	1	4
Template	0.5	
Dream Taq	0.2	0.8
dH2O	18.8	75.2
Final volume	25	100

Table 2. Master mix used for over night digestion of 10 µL of the PCR product with the corresponding restriction enzyme indicated in Table 3.

	(1 sample)	(4 samples)
PCR reaction	10	40
dH2O	7.7	30.8
10x Buffer	2	8
Restriction enzyme	0.3	1.2
Final Volume	20	80

Table 3. Pairs of primers and the corresponding restriction enzymes used for the rough mapping.

Chromosome	Position	Primer pairs (P1, P2)	Restriction enzyme
I	left	AAGCGAACCAATCAGCAG TCACGCCAAAATTAATGGG	DraI
	centre	ATGCAGGCATTCGACGAATC GTCGAAAAAGCGCACAATTC	DraI
	right	CACAAGTGGTTTGGAAGTACCG CAACAAAGGGATAGATCACGGG	HindIII
II	Left	AAGAGGTGTTCTTCTGCAGC ACCATCCACGCAGTTCATTC	DraI
	centre	TCCACACTATTTCCCTCGTG GAGCAATCAAGAACCGGATC	DraI
	right	AAAAGAGGGAGTTTTGGCAG GTTTGGAGATGAGGGTTGAG	SspI
III	left*	TTTAGCAGACCCAAGCTTACTG GTCATGTAAGCGACCTGAAAAC	DraI
	centre	AGCAGATGAAAGTTCCGACG CCCCGCTGTGGTTATTATAC	AccI
	right	CTAGGCACCAATCATTACAAGC TTTGTGCCCCTGATTTACATCC	TruI (65°C)
IV	left	GTCATTGTCAGCAGGTTTCCC TTCAAAGTCTTGATGGCTTCTG	HpaI
	centre	CCAAACAACCTACAGAAAATGC AAGATATTCATGCGTCGTAGTG	DraI
	right	GAATTCAGGTGTTGGAAGG TGCTCTGAAAAAATTGGCTG	DraI
V	left	CGGAAAATTGCGACTGTC ATTAGGACTGCTTGGCTTCC	DraI
	centre	GTGCTAATTCCAGAAATGATCC TAGTGTTCCATAGCATCCCATTG	DraI
	right	TTTATCCGCAGGGACTTGAC TCTCCTCTCCCTCATGGTTAAC	DraI
X	left	ATATGTGAGTTTACCATCACTGGG ACGTTTTGAAAAATTTGGTTGC	DraI
	centre	AGCAACAACAATGCAACTATGG TAAACAAGAGGGTACAAGGTATCG	DraI
	right	GCTGGGATTTTGAAGAGTTGTT CAGTGAATCATCCGTTGAATTT	DraI

Primers used to control that *prom-1(ok1140)* was homozygous are indicated below and were used under these PCR conditions (96°C for 4 min; 2 cycles (94°C for 45 sec, 54°C for 45 sec, 72°C for 1 min); 33 cycles (94°C for 45 sec, 56°C for 40 sec, 72°C for 1 min), last extension: 7 min) using the same PCR master mix as described above. Primers outside *prom-1(ok1140)* deletion allow checking if worms carry *prom-1(ok1140)* (PCR product: 796 bp) and primers inside *prom-1(ok1140)* deletion to check if worms are homozygous for the deletion (no PCR product in *prom-1(ok1140)* homozygous mutant).

Primers outside prom-1(ok1140) deletion:

P1: AACTAGACGATAACAGCCTGAAC

P2: TTCTTCGGAAGTTACCACGG

PCR product in wild type: 2025 bp

PCR product in *prom-1(ok1140)*: 796 bp

Primers inside prom-1(ok1140) deletion

P1: GGAAAGCGAGGCTAGATTGTCTGA

P2: TTCTTCGGAAGTTACCACGG

PCR product in wild type: 642 bp

PCR product in *prom-1(ok1140)*: 0 bp

Primers pairs and corresponding restriction enzymes used for fine mapping of *psu-1(jf76)* are given in Table 4.

Table 4. Primers pairs and corresponding restriction enzymes used for fine mapping.

Position on LG:III (bp)	Clone	Primer pair (P1, P2)	Restriction enzyme
8546	F10C5	GTACAGAAGAGCTATTGGTAGGG AGCTTCCTGATAGTAGAATAGAGC	Tru1I
8714	B0353	AGCTGCCGTAATCTACAAAGG GGTATGTGGATTCCAGAAGTGTC	NlaIII
11192	K02F3	CACAACATTGCATCAAGAGTGG TGGCAGAGTGTGTTTGAATAGG	ZraI
14042	W06E11	AACGGAGACTTCGAAAGATTAC CTACCGTAACCACAGATATTTCCG	BsmFI

14869	W02B3	CACCCTTGTACATTAGAAACACG TCAGAACCCAGGAAAATCATTC	Hin1L
19255	T17H7	ACCATCTGTTGACTGATGTCTC ATTGGACTCCTCATAAACAACACTACG	Hpy188I
20981	F42G9	CTCCCAGTAGGCAATATCGTTG TATCAATCTGAACAGCCTGACG	DraI
23658	C24A1	CAACTTCTGCTAGTGATGAAGC CGTACTTCAAGACCTTTTCTGC	PsiI
25580	B0412	TGATAGGCAACGACTCCTTCTC CAAGAATCTGGAGCCAATGAAG	XmnII

Sample preparation for solid sequencing

Strains (outcrossed multiple times) were grown for on 10 big plates for 5 days. Genomic DNA was then extracted by phenol extraction and the concentration evaluated by ethidium bromide staining (Figure 28). Sample 1 (*psu-1(jf76); prom-1(ok1140)*) and sample 2 (*prom-1(ok1140)*) were sent to the Solid sequencing facility of the University of Liverpool.

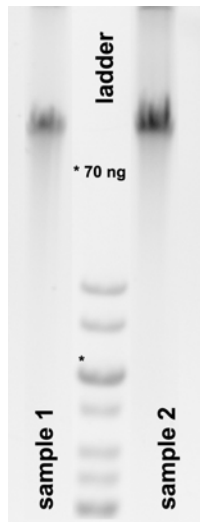


Figure 28. Quantification of genomic DNA of samples sent to Solid sequencing.

0.8% Agarose gel showing that sample 1 (*psu-1(jf76); prom-1(ok1140)*) and sample 2 (*prom-1(ok1140)*) have respectively a concentration of 90 ng/μl and 240 ng/μl.

Discussion and Outlook

Identification and characterization of *psu-1(jf76)*.

Catching the PROM-1 suppressor mutation *psu-1(jf76)*

A suppressor screen aimed at suppressing *prom-1* allowed me to recover 8 suppressor lines. The suppressor line (*psu-1(jf76); prom-1(ok1140) unc-55(e402)*) with the best viability (suppressor line UV24) was characterized and *psu-1(jf76)* mapped to chromosome III left. *psu-1(jf76)* rescued all the phenotypes of the *prom-1* deletion mutant with respect to viability, reintroduction of a TZ, bivalents and homologous synapsis). Identification of *psu-1* and its characterization are therefore crucial for our understanding of meiotic regulation and in particular the function of PROM-1. The nature of this mutant will hopefully instruct us to understand the requirements to timely exit meiotic entry.

Analysis of the results comparing the genomic sequences of *prom-1* with the suppressor line UV24 by Solid sequencing left us with 2 genes as potential candidates for *psu-1*. The next challenge will be to find a way to validate them. Confirming W02B3.3 as *psu-1* is difficult. Indeed no mutant/deletion of this allele exists precluding a simple evaluation of the double mutant. The best strategy would be to knock down the open reading frame by RNAi in the *prom-1* deletion allele. Gonads of the progeny of the RNAied worms would need to be dissected and screened for restoration of the TZ and bivalents at diakinesis. Care would have to be taken to release gonads of old worms as in gonads of young adult worms the extended MEZ is less prominent. In case W02B3.3 turned out as a candidate for *psu-1*, a deletion allele of this gene would have to be ordered at the *C. elegans* Gene Knockout Consortium for a more extensive study.

Validating the C29F9.5 open reading frame as *psu-1* would be more straightforward. Indeed the Hawaiian strain carries the niDF66 deletion. Therefore crossing the Hawaiian males into *prom-1(ok1140)* and singling the F2 progeny should allow the recovery of homozygous hermaphrodites carrying both the niDF66 deletion and *prom-1*. Worms should be checked with primers inside and outside the 2 deletions by PCR to find the 1/16 worms being homozygous for these 2 deletions. Once the double mutant is confirmed, as before, gonads have to be released and checked for the restoration of the TZ and the formation of bivalents at diakinesis. If C29F9.5 rescued the *prom-1* phenotype a deletion of this gene would have to be ordered at the *C. elegans* Gene Knockout Consortium. Indeed working with the deletion niDF66 would not be advisable as it deletes 5 additional open reading frames.

Function of *psu-1(jf76)* in meiosis

Once *psu-1* is isolated and a deletion mutant available this strain would be subjected to thorough cytological examination using markers highlighting the most important players of meiotic prophase I (REC-8, HIM-3, HTP-3, SYP-1, RAD-51, HIM-8, PC proteins and SUN-1). First we would start with examining the progression of meiosis by mere DAPI staining to assay whether there is a TZ? Would it be extended? Can one detect bivalents or univalents at diakinesis? These results would give us the first insights into the function of PSU-1 during meiosis.

Furthermore we would tag the open reading frame to determine its sub-cellular localization. Indeed, instead of transforming the worms by biolistic bombardment, I would use the new strategy based on the *mos* transposon insertion system (Frøkjær-Jensen et al., 2008). Once worms are successfully transformed, the transgene would be put into the deletion background and tested for functionality (for its ability to rescue the phenotype of *psu-1* deletion worms). This strain would allow us to immunoprecipitate the tagged version of *psu-1* and determine the protein complexes containing PSU-1 by mass

spectrometry. Depending on the nature of the open reading frame epistasis experiments with known meiotic mutants can be designed.

Gaining new insights into the process of chromosome pairing.

SUN-1 is definitely one of the key players involved in the process of homologous chromosome pairing. Our analysis left nonetheless some open questions.

Assaying the number of chromosome ends inside SUN-1 foci and patches.

We know that SUN-1 forms aggregates that can be classified according to their size: foci and patches. Foci are circular aggregates of SUN-1 whereas patches are bigger and mostly elongated in one direction (Penkner et al., 2009). We assumed that foci likely represent single ends of chromosomes and patches contained at least 2 chromosome ends.

These assumptions have to be confirmed assaying the number of chromosome ends located in SUN-1 aggregates. One approach would be to co-stain SUN-1 and one of the PC protein which binds to two different chromosomes (such as ZIM-1 or ZIM-3). This analysis should confirm that when only one ZIM-3 focus is detected in a cell, it always co-localizes with one SUN-1 patch.

In fact this experiment does not answer the question whether two different chromosome ends could be present in one SUN-1 focus. To answer this question we would need to probe at least two different chromosome ends

by FISH. This analysis should confirm that no more than two chromosomal ends co-localize with one SUN-1 focus.

Do paired homologues display different dynamics?

We showed in our analysis that we could not detect any difference in the behavior of SUN-1 aggregates upon pairing. This interpretation needs to be validated by simultaneous *in vivo* imaging of SUN-1 aggregates and a mCherry tagged chromosome end. ZIM-1 would be a good candidate since it only localizes to one chromosome.

Live imaging would have to be slightly adjusted to allow the recording of the two channels (GFP, RFP) in a short enough time interval so that the camera could do the Z-scan in less than 5 seconds (time lapse). Movies could be acquired under exposed and then exposure would be corrected using the FIJI software and the function “Maximum (3D)”. Then pictures could be projected (maximum intensity) to permit manual plotting of SUN-1 and ZIM-1 movement. Next movement of SUN-1 and ZIM-1 would have to be compared with the established tools (Baudrimont et al., in press).

Exit from the clustered chromatin conformation.

Polarization of the chromatin during the leptotene/zygotene stage was shown to depend on SUN-1 aggregate movement (Penkner et al., 2009). SUN-1 aggregates are involved in the process of pairing homologues but their dynamics of movement also reflect the process of repair of DSBs (Baudrimont et al., in press). In addition, upon entry into meiosis SUN-1 is phosphorylated at multiple positions. The inability of SUN-1 to be dephosphorylated at the

position serine 12 (S12) leads to an extension of the polarized conformation (revealed by the phosphomimetic SUN-1(S12E) mutant line). This suggests that dephosphorylation of S12 controls the exit of the polarized conformation. Identification of the triggers for the exit of the clustered conformation would be the next most appealing goal.

From previous work we know that there are at least 2 suspected triggers, namely completion of synapsis and repair of DSBs (Penkner et al., 2009). The identification of the particular recombination intermediate that governs activation of the SUN-1 directed phosphatase(s) will be the most interesting future goal for this project.

With the help of cytologically active SUN-1 phospho-antibodies raised against the phosphorylations 8, 12, 24, 43 we looked at the phosphorylations of SUN-1 in mutants in the mostly used meiotic repair pathway of homologous recombination (*rad-51(lg8701)*, *msh-5(me23)*, *zhp-3(jf61)*, *pph-4(tm1598)*, *spo-11(me44)*, *hel-308(tm2134)*; *rfs-1(ok2702)*). Loss of SUN-1 phosphorylation is disturbed in all those mutants. From this analysis it became evident that at least two populations of SUN-1 phospho-proteins exist. Therefore it will be very important to first understand the functional difference of the two classes of phospho-sites. Transgenic lines of SUN-1::GFP with S to A or S to E substitutions in all phospho-target sites will have to be generated, single substitutions and combinations of the different subclasses of target sites. The advances made with the new mos transformation system make me optimistic that this goal becomes realistic.

Recently I obtained results showing that different alleles of *htp-1* displayed distinct properties with respect to chromatin redistribution after TZ. In an *htp-1(gk149)*; *syp-1(RNAi)* double mutant polarization of the chromatin was extended whereas this polarization is absent in the *htp-1(gk149)* single mutant or the *htp-1(me84)* *syp-2* (please insert the allele) double mutant. This suggests that *htp-1* could play a role in the redistribution of chromatin. The phosphorylation status of SUN-1 in *htp-1(gk149)*, *htp-1(gk149)*; *syp-1(RNAi)* and *htp-1(m384)*; *syp-2(ok307)* has to be determined. One relevant

experiment, to confirm that HTP-1 is involved in the control of the redistribution of the chromatin, is to knock down HTP-1 and HTP-1/HTP-2 in the phosphomimetic strain S12E by RNAi. SUN-1 S12E shows an extended zone where polarization of the chromatin is observed and inactivating HTP-1/2 in this background could release the constraint imposed by constitutive phosphorylation of S12E on polarization of chromatin.

Extending live-imaging to other players of prophase I.

With *in vivo* imaging of the GFP tagged SUN-1 we could effectively contribute to the understanding of the process of homologous chromosome pairing in *C. elegans*. The amenability of *C. elegans* to live imaging thanks to its transparency make it attractive to look at the behavior of other players during prophase I of meiosis.

Some strains have already been made (HIM-3::GFP, SYP-3::GFP) (Merritt and Seydoux, 2010) and preliminary result show that SYP-3::GFP is amenable to live imaging. Recordings over 15 minutes showed that the process of synapsis due to the compaction of the chromatin in the TZ could not be resolved. Imaging of SYP-3::GFP in early pachytene reveals that chromosome movement is mostly absent at that stage. It has been proposed that the SC instead of being static could be quite dynamic (Wang et al., 2009). Improvements of time-lapse imaging could help us to follow *in vivo* how synapsis proceeds while chromosomes are in the process of pairing. The HIM-3::GFP line is not driven by its endogenous promoter as SYP-3::GFP, instead the *pie-1* promoter drives its expression. In other words HIM-3::GFP can only be detected after mid pachytene. It would be interesting to see if any chromosome movement is present in late pachytene (absent in early pachytene, SYP-3::GFP) when central elements of the SC are released from the chromatin in response to crossovers formation.

The length of the recording would have to be extended from 15 minutes to at least 3 hours to gain more insights into synapsis and chromosome movement. Indeed movement of one cell to the next cell row inside a gonad takes about 1 hour. To extend the recording time, worms should not be mounted in a drop of levamisole (10 mM) but instead in levamisole (0.5 mM) plus tricaine (0.4 mM). Indeed under these conditions worms survive better and recordings of movies up to 3 hours without affecting the viability are possible (Green et al., 2008). In addition it would be interesting once conditions were found to *in vivo* monitor nascent synapsis whether and how the kinetics of synapsis depends on SUN-1 mediated chromosome movement. To this end we could take advantage of the movement defective allele *sun-1(jf18)*.

References

- Frøkjær-Jensen, C., M.W. Davis, C.E. Hopkins, B.J. Newman, J.M. Thummel, S.-P. Olesen, M. Grunnet, and E.M. Jørgensen. 2008. Single-copy insertion of transgenes in *Caenorhabditis elegans*. *In Nature Genetics*. Vol. 40. 1375-83.
- Green, R.A., A. Audhya, A. Pozniakovsky, A. Dammermann, H. Pemble, J. Monen, N. Portier, A. Hyman, A. Desai, and K. Oegema. 2008. Expression and imaging of fluorescent proteins in the *C. elegans* gonad and early embryo. *In Methods Cell Biol.* Vol. 85. 179-218.
- Merritt, C., and G. Seydoux. 2010. The Puf RNA-binding proteins FBF-1 and FBF-2 inhibit the expression of synaptonemal complex proteins in germline stem cells. *In Development (Cambridge, England)*. Vol. 137. 1787-98
- Penkner, A.M., A. Fridkin, J. Gloggnitzer, A. Baudrimont, T. Machacek, A. Woglar, E. Csaszar, P. Pasierbek, G. Ammerer, and Y. Gruenbaum. 2009. Meiotic Chromosome Homology Search Involves Modifications of the Nuclear Envelope Protein Matefin/SUN-1. *In Cell*. Vol. 139. 920-933.
- Wang, C.-J.R., P.M. Carlton, I.N. Golubovskaya, and W.Z. Cande. 2009. Interlock formation and coiling of meiotic chromosome axes during synapsis. *In Genetics*. Vol. 183. 905-15.

Acknowledgements

First I would like to thank my thesis supervisor, Verena Jantsch, to give me the opportunity to get involve in so many successful projects during my thesis and her supervision through the last 4 years. Without her mentoring I would not be standing here at this point.

Second I would like to thank Joseph Loidl for introducing me in the department and making thus possible my first steps in the world of research. I am also grateful to Franz Klein and the interesting discussion in after 8 p.m. leading to new considerations of my results and how to present them. I am also thankful to Michael Jantsch and his helpful advices in cloning.

With alphabetical order (first name) I would like to thank the lab members of the last 4 years for making this lab such an enjoyable place to work: Alexander Woglar, Alexandra Penkner, Anahita Daryabeigi, Christian Pfuegl, Jiradet Gloggnitzer, Lois Tang, Lucia Riedman, Margot Hulek, Markus Ladurner, Martin Xaver, Michael Mueller, Susanna Portik, Thomas Machacek, Yasmin Mammun.

I would also thank my parents and family for their support through the last 4 years.

Last but not the least I would thank my Pillow (surname of my wife) who changed so many things in my life, is always here to cheer me up and open to discuss my results and the results of our common life. Я тебя люблю.

Curriculum Vitae

Name: BAUDRIMONT Antoine Marie
Date of birth: 12.01.1981
Gender: male
Nationality: French
Marital status: Married to Elena Shmanenko (Russian) on July 10th, 2009

Education:

- 2006 – present PhD in Microbiology and Genetics
University of Vienna, Austria
- 2004 – 2005 MASTER 2 Genomes, Cells, Development and Evolution,
option Evolution, University Paris Sud Orsay, France
- summer 2004 Summer session in Abstract algebra and Number theory
University of California, Berkeley, CA
- 2003 – 2004 MASTER 1 Molecular Genetics
University Victor Segalen Bordeaux II, France
- 2002 – 2003 LICENSE Biology Cellular and Physiology
University Victor Segalen Bordeaux II, France
- 2000 – 2002 DEUG Biology Life sciences
University Victor Segalen Bordeaux II, France

Professional experience

- **PhD**, University of Vienna
Department of Chromosome Biology, Dr. Verena Jantsch, Meiosis in
Caenorhabditis elegans

Research experience:

- time-lapse *in vivo* recording of SUN-1::GFP in wild type and most of *C. elegans* meiotic mutants. Defined requirements for SUN-1 aggregate formation. Documented influence of repair of DSBs for proper behavior of SUN-1 aggregates.

- Study of meiotic prophase I events in spermatogenesis in *rrf-3* mutant . Showed that meiotic chromosome axes morphogenesis and repair of DSBs were normal despite chromosome fragmentation and DNA bridge (collaboration with Dr. Andrew Fire's laboratory).
 - Isolation and characterization of a new *smc-3* allele. Showed that 1) repair of meiotic DSBs is impaired whereas cohesion is normal, 2) primary defect: partial loading of cohesin complex
 - Isolation and characterization of genetic suppressors of *prom-1* (suppressor screen). Suppresses meiotic arrest, entails proper loading of SC proteins. Mapped suppressor mutation to left arm of chromosome III.
- **Master studies**, University of Vienna
Department of Chromosome Biology, Dr. Joseph Loidl, *Schizosaccharomyces pombe*
Research experience:
 - Confirmation of irregular meiosis in *pat-114* mutant with respect to linear element formation

Publications

- *Leptotene/zygotene chromosome movement via the SUN/KASH protein bridge in C. elegans.*

Antoine Baudrimont, Alexandra Penkner, Alexander Woglar, Thomas Machacek, Christina Wegrostek, Jiradet Gloggnitzer, Alexandra Fridkin, Franz Klein, Yosef Gruenbaum, Pawel Pasierbek, Verena Jantsch
PLoS genetics, under revision.

- *Meiotic chromosome homology search involves modifications of the nuclear envelope protein Matefin/SUN-1.*

Penkner AM, Fridkin A, Gloggnitzer J, **Baudrimont A**, Machacek T, Woglar A, Csaszar E, Pasierbek P, Ammerer G, Gruenbaum Y, Jantsch V.
Cell. 2009 Nov 25;139(5):920-33.

- *A Caenorhabditis elegans RNA-directed RNA polymerase in sperm development and endogenous RNA interference.*

Gent JI, Schwarzstein M, Villeneuve AM, Gu SG, Jantsch V, Fire AZ, **Baudrimont A**.

Genetics. 2009 Dec;183(4):1297-314

- *Caenorhabditis elegans prom-1* is required for meiotic prophase progression and homologous chromosome pairing.

Jantsch V, Tang L, Pasierbek P, Penkner A, Nayak S, **Baudrimont A**, Schedl T, Gartner A, Loidl J.

Mol Biol Cell. 2007 Dec;18(12):4911-20

Manuscript in preparation

- A new thermo-sensitive *smc-3(t2553)* allele reveals involvement of cohesin in meiotic repair in *C. elegans*.

Antoine Baudrimont, Yasmine M. Mamnun, Alexandra Penkner, Margot Hulek, Alexander Schleiffer, Ralf Schnabel, Josef Loidl, Verena Jantsch.

Posters

- *In Vivo Writing Using Two-Photon-Polymerization as an Enabling Technology for Making Use of Bioinspired Structures*

J. Torgersen, **A. Baudrimont**, N. Pucher, K. Stadlmann, K. Cicha, C. Heller, R. Liska, J. Stampfl

August 24-26, 2010, Materials Science & Engineering (abstract accepted)

- *Phosphorylation events of the nuclear envelope protein Matefin/SUN-1 during C.elegans meiosis I*

Woglar Alexander, **Baudrimont Antoine**, Penkner Alexandra, Machacek Thomas, Fridkin Sasha, Gruenbaum Josef and Jantsch Verena

June 12-13, 2010, Gordon Research Conference, Meiosis (abstract accepted)

- *Matefin/SUN-1 Is Required for Homologous Chromosome Pairing in C. elegans Meiosis.*

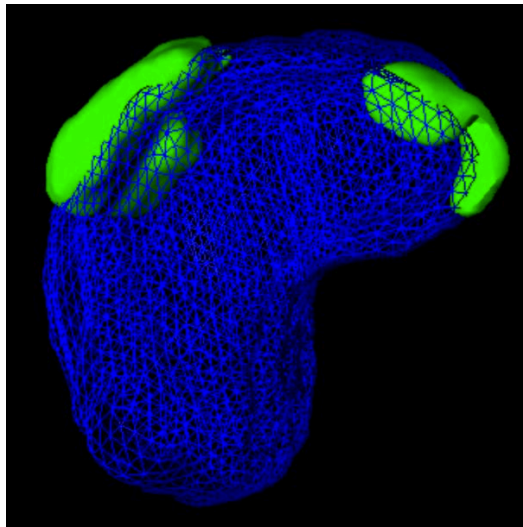
Alexandra Penkner, Jiradet Gloggnitzer, Alexandra Fridkin, **Antoine Baudrimont**, Pawel Pasierbek, Yosef Gruenbaum, Verena Jantsch.

2008 Development & Evolution Meeting.

- *Search For Interacting Partners of C. elegans prom-1, a Gene Involved in Meiotic Prophase Progression and Homologous Chromosome Pairing.*

Antoine Baudrimont, Lucia Riedmann, Markus Ladurner, Lois Tang, Pawel Pasierbek, Alexandra Penkner, Sudhir Nayak, Tim Schedl, Anton Gartner, Josef Loidl, Verena Jantsch.

2007 International Worm Meeting.



3-dimensional model of a nucleus stained for DAPI (blue) and SUN-1 (green).

